Acceleration and Heating of Metal Particles in Condensed Matter Detonation

by

Robert C. Ripley

A thesis
presented to the University of Waterloo
in fulfillment of the
thesis requirement for the degree of
Doctor of Philosophy
in
Mechanical Engineering

Waterloo, Ontario, Canada, 2010

I hereby declare that I am the sole author of this thesis. This is a true copy of the thesis, including any required final revisions, as accepted by my examiners.

I understand that my thesis may be made electronically available to the public.

Abstract

For condensed explosives containing metal particle additives, interaction of the detonation shock and reaction zone with the solid inclusions leads to non-ideal detonation phenomena. Features of this type of heterogeneous detonation are described and the behaviour is related to momentum loss and heat transfer due to this microscopic interaction. For light metal particles in liquid explosives, 60–100% of the post-shock velocity and 20–30% of the post-shock temperature are achieved during the timescale of the leading detonation shock crossing a particle. The length scales corresponding to particle diameter and detonation reaction-zone length are related to define the interaction into three classes, bound by the small particle limit where the shock is inert, and by the large particle limit dominated by thin-detonation-front diffraction. In particular, the intermediate case, where the particle diameter is of similar order of magnitude to the reaction-zone length, is most complex due to two length scales, and is therefore evaluated in detail.

Dimensional analysis and physical parameter evaluation are used to formalize the factors affecting particle acceleration and heating. Examination of experimental evidence, analysis of flow parameters, and thermochemical equilibrium calculations are applied to refine the scope of the interaction regime. Timescales for drag acceleration and convective heating are compared to the detonation reaction time to define the interaction regime as a hydrodynamic problem governed by inviscid shock mechanics. A computational framework for studying shock and detonation interaction with particles is presented, including assumptions, models, numerics, and validation. One- and two-dimensional mesoscale calculations are conducted to highlight the fundamental physics and determine the limiting cases. Three-dimensional mesoscale calculations, with up to 32 million mesh points, are conducted for spherical metal particles saturated with a liquid explosive for various particle diameters and solid loading conditions. Diagnostic measurements, including gauges for pressure, temperature, and flow velocity, as well as mass-averaged particle velocity and temperature, are recorded for analysis.

Mesoscale results for particle acceleration and heating are quantified in terms of shock compression velocity and temperature transmission factors. In addition to the density ratio of explosive to metal, the solid volume fraction and the ratio of detonation reaction-zone length to the particle diameter are shown to significantly influence the particle acceleration and heating. A prototype heterogeneous explosive system, consisting of mono-disperse spherical aluminum particles saturated with liquid nitromethane explosive, is studied to develop fitting functions describing the shock compression transmission factors.

Results of the mesoscale calculations are formulated into a macroscopic physical model describing an effective shock compression drag coefficient and Nusselt number. The novel models are explored analytically and are then applied to two challenging sets of test cases with comparison to experiment. Heterogeneous detonation is considered for aluminum particles saturated with liquid nitromethane, and inert particle dispersal is studied using a spherical explosive charge containing steel beads saturated in nitromethane. Finally, discussion of practical considerations and future work is followed by concluding remarks.

Acknowledgements

I am indebted to Dr. Fue-Sang Lien, who first formally introduced me to gas dynamics 13 years ago, and has remained supportive and engaged in my research topics including the fields of multiphase flow and condensed matter detonation. I am grateful for his teaching, supervision, and advice, which helped shape my academic and professional career.

I owe my deepest gratitude to Dr. Fan Zhang, who suggested this topic and joined UW as an adjunct professor to supervise this project. I am very fortunate to have learned from such a knowledgeable mentor and outstanding teacher. He inspired and challenged me to reach a higher level of thinking and achieve a deeper understanding of the physics.

I am grateful to Defence R&D Canada and Martec Limited for financial support of this project. This thesis would not have been possible without access to significant computing resources including the DRDC Suffield "Quantum" cluster, Public Safety Canada "Wildfire" cluster, Martec computer facilities, and Martec software.

I would like to thank the official committee members for their efforts, constructive comments, and helpful suggestions during the comprehensive exam and thesis review processes. I would like give special mention to Dr. Gordon Stubley, who I have known since my undergraduate CFD years, as I very much appreciated his suggestion of exploring dimensional analysis in this work.

It is a pleasure to thank my colleagues at Martec for their ongoing support and encouragement. In particular, I wish to thank Laura Donahue for helpful scientific discussions and technical review of my thesis, and Jeff Leadbetter for discussion of physical and numerical models. I would also like to thank David Whitehouse, who was continually supportive of my academic endeavors and provided much needed flexibility in my work schedule during my studies. Finally, I appreciate many years of assistance from everyone in the Combustion Dynamics Group who were involved in the Chinook code.

I would like express my gratitude to Dr. David Frost for his interest in this project, useful discussion of my work, interpretation of related experimental results, and permission to use his figures in this thesis. I would also like to thank Dr. Yukio Kato for his helpful comments on my results and kind use of his experimental data. I have benefited from many discussions with professors, colleagues, and leading scientists, for whom I have great regard; I apologize that I could not mention everyone individually.

I would like to express my sincere thanks to my parents, family, and friends for their genuine interest, optimism, and encouragement throughout this process. Of particular

significance, I extend special appreciation to my father, for his valuable editorial, proofreading, and technical review of my dissertation.

Last, and most importantly, I wish to thank my wife Caroline for her boundless patience, love, and support. It would have been impossible to complete this work without her confidence, encouragement, and understanding.

Contents

List of Tables

List of Figures

Nomenclature

Roman Characters

Symbol	Description
a	speed of sound
A	frequency factor (Arrhenius pre-exponential)
A_p	frontal area of a particle
B	body force vector
Bi	Biot number
c	compression factor
c_p	specific heat capacity at constant pressure
c_s	specific heat capacity of solid
c_v	specific heat capacity at constant volume
C	shock Hugoniot parameter
C_d	drag coefficient
d_p	particle diameter
D, D_0	detonation, or shock, velocity
e	internal energy
E	total energy
E_a	activation energy
F	force
F_d	drag force
F_p	momentum transfer source term
F, G, H, I, J	temperature fitting constants
h	convective heat transfer coefficient
ΔH_{det}	heat of detonation

J	mass exchange source term
k	thermal conductivity
ℓ	integration path length
L	length physical dimension in pi theorem
L_R	reaction-zone length
m_p	particle mass
M	mass physical dimension in pi theorem
M_0	Mach number
n_p	particle number density
N	number counter
N_p	particle number density source
Nu	Nusselt number
p	pressure
Pr	Prandtl number
q	conductive heat transfer vector component
Q	energy source term
Q_c	convective heat transfer
Q_p	energy exchange source term
Q_R	reaction energy source
r	cylindrical and spherical radius
R	gas constant
R_0	charge radius
Re	Reynolds number
s	inter-particle spacing
S	shock Hugoniot parameter
t	time
T	temperature
T	time physical dimension in pi Theorem
T_M	melting temperature
T_V	boiling temperature
u, v, w	Cartesian velocity components
V	volume
W	molecular weight
x, y, z	Cartesian coordinates
X, Y, Z	Cartesian grid resolution

Y	material mass fraction
Z	shock impedance

Greek Characters

Symbol	Description
α	velocity transmission factor
β	temperature transmission factor
δ	ratio of particle diameter to detonation reaction-zone length ($\delta = d_p/L_R$)
Δ	boundary-layer thickness
ε	solid surface emissivity
γ	isentropic exponent ($\gamma \equiv c_p/c_v$)
ϕ	volume fraction
Γ	Grüneisen gamma
Π	dimensionless group
ρ	density
σ	mass concentration ($\sigma \equiv \rho\phi$)
σ_B	Stefan-Boltzmann constant
λ	reaction progress variable
μ	molecular viscosity
ν	specific volume ($\nu \equiv \rho^{-1}$)
τ	timescale
τ_{ij}	stress tensor
τ_B	particle reaction timescale
τ_D	detonation reaction timescale
τ_R	radiation exchange timescale
τ_S	shock interaction timescale
τ_T	thermal relaxation timescale
τ_V	velocity relaxation timescale
θ	temperature physical dimension in pi theorem
ω	reaction rate

Subscripts

Symbol	Description
CJ	Chapman-Jouguet state
c	convection
d	drag
f	fluid phase
freeze	freezing temperature
$\mathcal{F}$	fuel material
g	gas phase
H	Hugoniot state
i, j, k	indices
$\mathcal{I}$	inert material
mix	mixture
n	normal component
oxi	oxidiser
p	particle phase
$\mathcal{P}$	particle material
s	solid material
S	shock
VN	von Neumann state
x, y, z	Cartesian component
0	initial state
1	shocked state

Abbreviations

Acronym	Description
1D	one-dimensional
2D	two-dimensional
3D	three-dimensional
AUSM	Advection Upstream Splitting Method
BKW	Becker-Kistiakowski-Wilson
CDPI	Critical Diameter for Particle Ignition

CEA	Chemical Equilibrium with Applications
CFD	Computational Fluid Dynamics
CFL	Courant-Freidrich-Lewey number
CJ	Chapman-Jouguet
CPU	Central Processing Unit
CRT	Constant Reaction Time
DETA	diethylenetriamine, a chemical sensitiser
DSD	Detonation Shock Dynamics
DDT	deflagration-to-detonation transition
EOS	equation of state
HOM	homogeneous equation of state
HLLC	Harten, Lax, van Leer flux solver
ID	inner diameter
JWL	Jones-Wilkins-Lee
MPI	Message Passing Interface
PMMA	polymethyl methacrylate
PVC	polyvinyl chloride
RVE	Representative Volume Element
TEA	triethylamine, a chemical sensitiser
TVD	Total Variation Diminishing
VN	von Neumann
ZND	Zel'dovich-von Neumann-Döering

Common Explosives

Explosive	**Common Name**
AN	ammonium nitrate
ANFO	ammonium nitrate fuel oil
AN/HZ	ammonium nitrate / hydrazine (tradename Astrolite)
AP	ammonium perchlorate
DEGN	diethylene glycol dinitrate
HMX	cyclotetramethylene tetranitramine
IPN	isopropyl nitrate
NG	nitroglycerin

NQ	nitroguanidine
NM	nitromethane
PETN	pentaerythritol tetranitrate
RDX	cyclotrimethylene trinitramine
TATB	triaminotrinitrobenzene
TNM	tetranitromethane
TNT	trinitrotoluene

Chapter 1

Introduction

High explosives, since they were discovered, have become commonplace in both constructive and destructive applications. The rapid chemical energy release and ability of expanding gases to perform useful work is unparalleled by other means. Metal particles are commonly added to explosives to enhance the overall performance—chief among them is aluminum powder. Scientists are charged with understanding the fundamentals of such metalized explosives, yet diagnostic techniques are limited and many questions remain unsolved. While experiments have inarguably demonstrated the phenomenology of this class of explosives, there is a need for a quantitative description of the underlying mechanisms for detonation interaction with particle additives. The goal of this work is to develop novel physics-based descriptions to help understand and explain key detonation phenomena. This involves exploring detonation behaviour using numerical studies at a mesoscopic scale. In particular, the acceleration and heating of metal particles in a high explosive detonation are studied to quantify the resultant physical behaviour. Based on this detailed examination of detonation interaction with metal particles, global models are proposed which capture the essential underlying physics. These high-level descriptions are suitable for practical problems involving metalized explosives and shock propagation in systems containing dense particles.

1.1 Brief theory of detonation

A detonation wave consists of a leading shock wave supported by chemically-reacting flow. An ideal one-dimensional detonation structure is the Zel'dovich-von Neumann-Döering

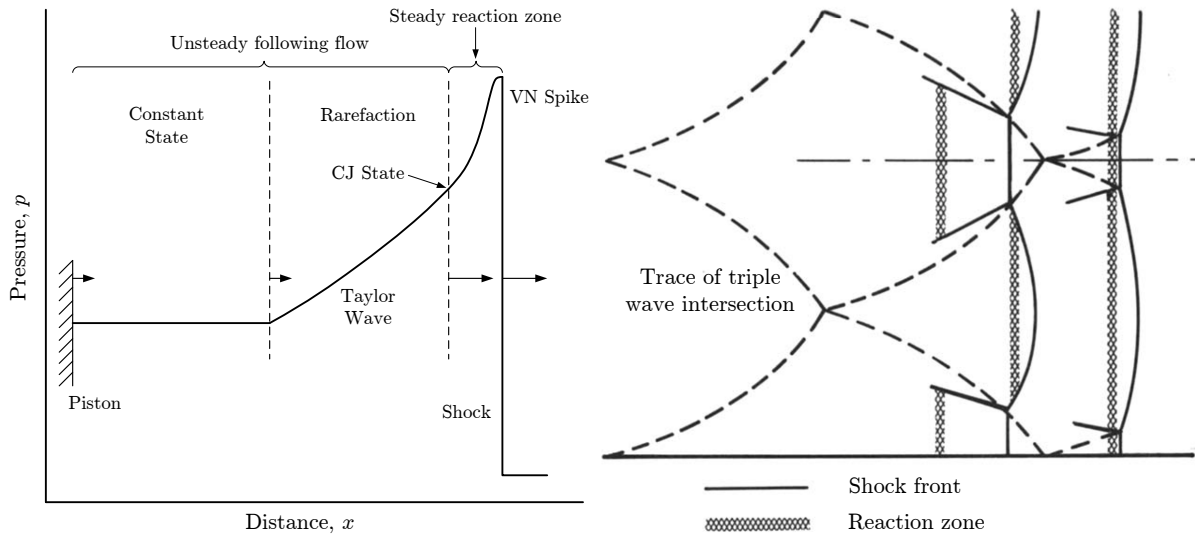

Figure 1.1: Structure of homogeneous detonation: (left) one-dimensional ZND wave adapted from [64]; and, (right) transverse wave structure and triple points in cellular detonation [205].

(ZND) wave (see Fickett and Davis [64]). The ZND model of a detonation was developed independently by Zel'dovich (1940) [224], von Neumann (1942) [209], and Döering (1943) [48]. It involves a thin shock followed by a finite reaction zone, where the flow is steady in the frame of reference attached to the shock. For a planar detonation wave to be self propagating at a steady velocity, simple detonation theories rely on a condition postulated by Chapman [37] and Jouguet [102], known as the CJ condition. The CJ condition states that an unsupported detonation will propagate at a minimum velocity where a sonic point terminates the reaction zone.

Detonation in condensed explosives typically features wave propagation speeds from 6 to 9 mm/μs and peak pressures from 10 to 50 GPa, where the leading shock front is often modeled by the von Neumann (VN) spike in the ZND wave. Behind the reaction zone, there is an unsteady expansion commonly called the Taylor wave [64]. The one-dimensional detonation wave structure is illustrated in Figure 1.1. In reality, detonation in most homogeneous explosives features an unsteady three-dimensional structure characterized by transverse waves (Figure 1.1).

Detonation theory, applicable to solids, liquids, and gases, is often treated in self-contained chapters in combustion texts (e.g., Glassman [81, 82], Strehlow [192], and Williams [218]). Full texts on the subject are also available (e.g., Zel'dovich [224], Fickett and Davis [64], and Fickett [63]). Detonation of condensed matter (solids and liquids) is the subject of this thesis. Specific details for condensed matter are treated by Taylor

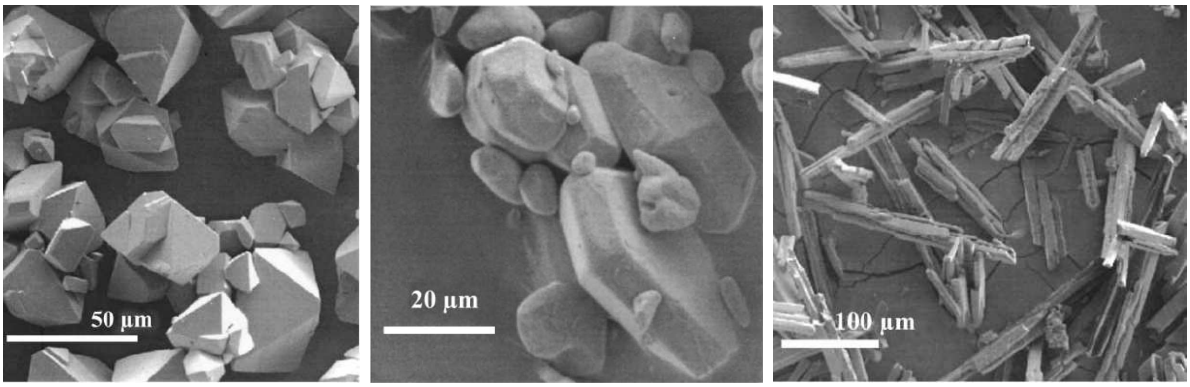

Figure 1.2: Microstructure of heterogeneous explosives from Baer [6]: (left) HMX crystals; (centre) TATB platelets; and, (right) PETN needles. Reprinted with permission of Elsevier.

[201], Zel'dovich and Kompaneets [225], Johansson and Persson [100], Mader [132, 133], and Dremin [51].

1.2 Heterogeneous explosive matter

Ideal detonation involves prompt and complete decomposition or oxidation of the explosive molecules forming condensed matter. Strictly speaking, homogeneous explosives are limited to pure liquids and single solid crystals, which in practise are only utilized in laboratory tests. Therefore most condensed-phase explosives are, in fact, heterogeneous mixtures of solids, or mixtures of solids and liquids. Whereas homogeneous explosives are presumedly formed from a single-molecule liquid or solid, or a liquid mixture of fuels, oxidizers, and sometimes sensitizers mixed at the molecular level, heterogeneous explosive matter often consists of one or more grain-scale or discrete components.

At the microscopic level, heterogeneous explosives include crystals, binders, plasticizers, solid particles, and voids. In some cases, the additives may be non-energetic but participate mechanically in the detonation process. The inhomogeneities introduce a number of physical phenomena that are characterized by the length scale of the microscopic material. Figure 1.2 illustrates some examples of components used in heterogeneous explosive matter.

A common example of a heterogeneous explosive is ammonium nitrate fuel oil (ANFO), which consists of solid oxidizer particles (NH_4NO_3) and a liquid hydrocarbon fuel. Aluminum powder is often added to increase both the detonability and explosive power. In general, the reaction of aluminum provides 18–31 MJ/kg-Al of energy release compared with 5–6 MJ/kg-explosive of detonation energy. Tritonal (80/20 TNT/aluminum) is

a standard military explosive that employs the aluminum energy release to improve underwater performance.

Due to the random packing and orientation of the explosive grains and additives, the detonation propagation is typically characterized by an irregular structure with transverse waves. The propagation is affected by local concentration gradients and density discontinuities at material interfaces. Waves reverberate within the solid matter, but also in the gaps and voids, producing a microscopic oscillation feature in the resulting shock pressure. The detonation interacts with material interfaces that include metal particle additives, voids, and the free boundary at the explosive-air interface. The main features of heterogeneous detonation include: detonation velocity deficit; altered sensitivity and initiation effects; decreased critical diameter for detonation failure; microscopic pressure fluctuations; and, increased detonation reaction-zone length.

The heterogeneous detonation features are strongly influenced by localized energy concentrations that form so-called hot spots. In homogeneous explosives, hot spots may form naturally due to instabilities in the wave structure (transverse waves). Hot-spot theory for condensed explosives is treated by Campbell et al. [33] and Mader [131]. Davis [44] reviews the mechanisms responsible for hot spots: material jetting between explosive grains; impact of material thrown across a void during collapse; viscous heating in material near the surface of a collapsing void; interaction of shocks around a high-impedance inclusion; friction between crystallites; and, internal shear (slippage) within crystallites. The addition of heterogeneities, such as metal particles, into condensed explosives introduces microscopic interactions between the detonation shock and the particles which artificially produce localized hot spots due to shock reflection, focusing, and transmission. Kato and Brochet [103] were among the first to visualize the hot spots in liquid explosives with particles.

1.3 Slurry detonation phenomena

A particular class of heterogeneous explosives called 'slurry' explosives includes wetted powders, emulsions, and aqueous gels. In general, a slurry is defined as a liquid that contains very finely dispersed solid particles. The solid particles are usually completely saturated by the liquid, filling all interstitial voids. The most common metal fuel used in slurry explosives is aluminum [41]; at the microscopic level, these powders may be flaked or spherical. Figure 1.3 shows scanning electron microscope photographs of various types

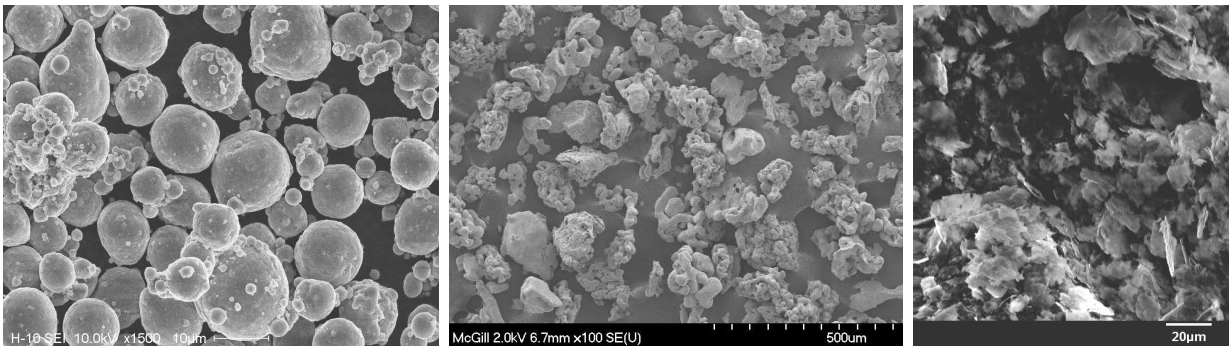

Figure 1.3: Micrographs of metal powders: spherical [227], conglomerated [72], and flaked [222] particle shapes. Images used with permission from the original authors.

of metal particles commonly used in slurry explosives.

Particles saturated with liquid explosives form a convenient system for fundamental studies of detonation. Examples of liquid explosives include nitroglycerin, isopropyl nitrate, nitromethane, tetranitromethane, trinitrotoluene (above 81°C), ammonium nitrate / hydrazine (trade name Astrolite), and diethylene glycol dinitrate (see Fordham [65] and Dobratz and Crawford [47] for details of manufacture, properties, and performance). Inert particle additives include microballoons (air voids), glass/silica beads, talcum powder (magnesium silicate), carborundum (silicon carbide), and corundum (aluminum oxide). Microscopic elemental metal powders commonly studied in scientific experiments include aluminum, copper, magnesium, titanium, tungsten, and zirconium; metal particles are often chosen based on their solid density, impedance matching, and reactivity. Detonation of slurry explosives is reviewed in a book chapter by Frost and Zhang [76].

The effect of a large volume fraction of metallic particle additives on the detonation properties of slurry explosives has been investigated by a number of researchers. In general, adding particles reduces the detonation velocity below that of the neat explosive (called a velocity deficit), since some of the chemical energy released goes into heating and, in particular, accelerating the particles. Detonation velocity deficit in liquid explosives containing heterogeneities have been observed experimentally by Engelke [58], Baudin et al. [18], Haskins et al. [94], Zhang et al. [234], and Kato et al. [107]. They related the bulk propagation speed to the particle properties, morphology, and loading ratio. For example, pure liquid explosives (e.g., nitromethane and TNT) have very little velocity deficit in tubes much larger than the critical diameter; whereas Lee et al. [126, 127] showed large velocity deficits (from 1 to 20%) when particles are added to nitromethane.

Figure 1.4 illustrates a typical heterogeneous detonation of a long cylindrical explosive

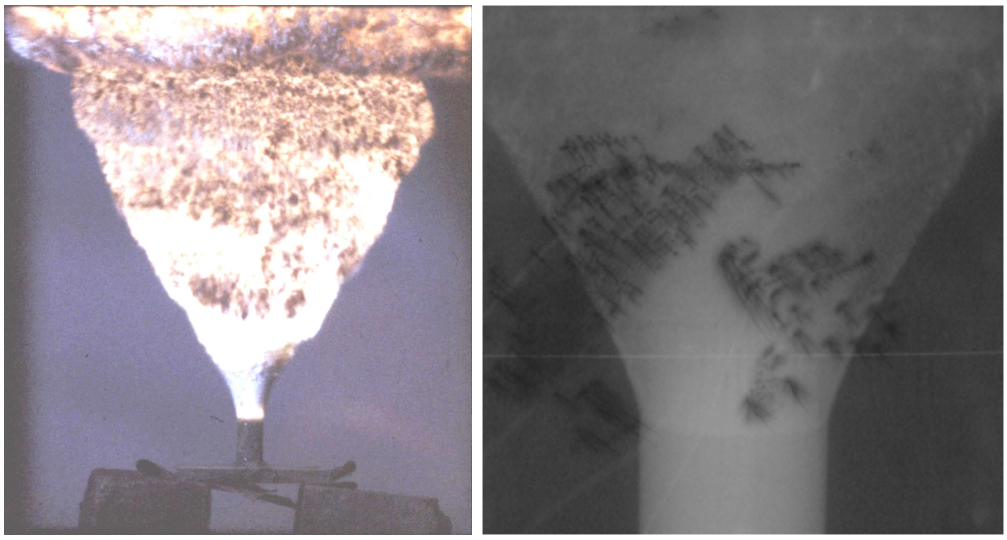

Figure 1.4: Cylindrical slurry detonation: (left) NM/Al explosive in a glass cylinder – high-speed photograph from Haskins et al. [94], reprinted with permission from the American Institute of Physics; and, (right) IPN/Al in a thin PVC tube – flash x-ray radiograph from Zhang et al. [234], image courtesy of Dr. Fan Zhang.

from the work of Haskins et al. [94] and Zhang et al. [234], which shows the detonation shock traveling from top to bottom and the expanding products flow. The explosive reaction-zone length is much smaller than the charge dimensions (length and diameter).

Experiments involving long cylindrical explosives, such as those shown in Figure 1.4, are also known as rate stick experiments, and are used to measure the detonation velocity as a function of charge diameter. The interaction of the detonation front with the free boundary alters the wave speed to accommodate the flow divergence. This results in a curved detonation shock front, an elongated reaction zone, and a corresponding detonation velocity deficit. Detonation front curvature theory was proposed by Eyring et al. [61] and by Bzdil [19]. Decreasing the charge diameter both increases the detonation curvature and radial expansion rate, and reduces the shock pressure and velocity that eventually leads to detonation failure. The critical charge size for detonation failure is known as the failure diameter, which is one of many explosive characterization metrics.

The solid particles in slurry explosives increase the detonation reaction-zone length due to momentum and heat losses to the particles; however, particles also form hot spots that sensitize the explosive. For cylindrical slurry explosives, the failure diameter depends on the competing effects of the explosive sensitization due to the formation of hot spots near the particles and the increasing detonation reaction length with momentum and energy

absorbed into the particles, apart from the detonation front curvature effect caused by the lateral expansion. Engelke [58] and Lee et al. [126, 127] extensively studied the critical diameter of nitromethane containing silica glass beads. They observed the detonation propagation and failure transition from large to small bead regimes for a 1.2 mm particle size, which is considerably larger than the estimated reaction-zone length of sensitized nitromethane (*ca.* 10 μm).

Kurangalina [118], Frost et al. [74], and Kato and Murata [105, 106] studied nitromethane detonation failure with aluminum powders. Unlike small concentrations of inhomogeneities that tend to increase detonation sensitivity, Kurangalina [118] found that large concentrations of powder decreased the sensitivity of liquid explosive slurries. Pure nitromethane has a failure diameter of 16.2 mm; when silica is added to nitromethane, the failure diameter is reduced to 9.6 mm [58]. Frost et al. [74] and Kato and Murata [105, 106] showed a U-shaped detonation failure diameter curve as a function of particle diameter for packed beds of aluminum particles saturated with nitromethane, thus suggesting a strong dependence on particle diameter. In particular, the charge diameter for detonation failure increases for the smallest particles.

In slurry explosives, particle ignition delay and reaction times are typically greater than the explosive detonation reaction timescale, and the resulting metal particle combustion heat release occurs predominantly behind the sonic point in the detonation. The products of detonation usually contain CO_2 and H_2O with the potential to oxidize metal particle additives. Baudin et al. [18] suggested for spherical aluminum particles as small as 100 nm, there is insufficient time for particles to react within the detonation reaction zone; this is consistent with Gogulya et al. [85], Haskins et al. [94], and Zhang et al. [234] who reported detonation velocity deficits using nanometric aluminum particles.

Kato et al. [107] and Kato and Murata [106] showed in time-resolved detonation profiles that aluminum reaction contributes to the nitromethane detonation only for particles smaller than 2 μm. Figure 1.5 gives the results of Kato et al. [107] that illustrate some of the slurry detonation behaviours for a nitromethane/aluminum mixture compared with a baseline pure liquid explosive pressure profile. The smallest particle size (3 μm) resulted in a pressure increase due to aluminum reaction inside the detonation zone. For the 5 μm particle size, the abrupt pressure rise beginning 3 μs after the leading shock indicates a subsequent aluminum reaction behind the detonation reaction zone. The pressure histories involving larger particle sizes show extended steady zones, a feature that was also shown numerically by Milne [144]. Baer [6] also demonstrated that highly-fluctuating stress states persist over several particle diameters. This feature is believed to apply for packed particle

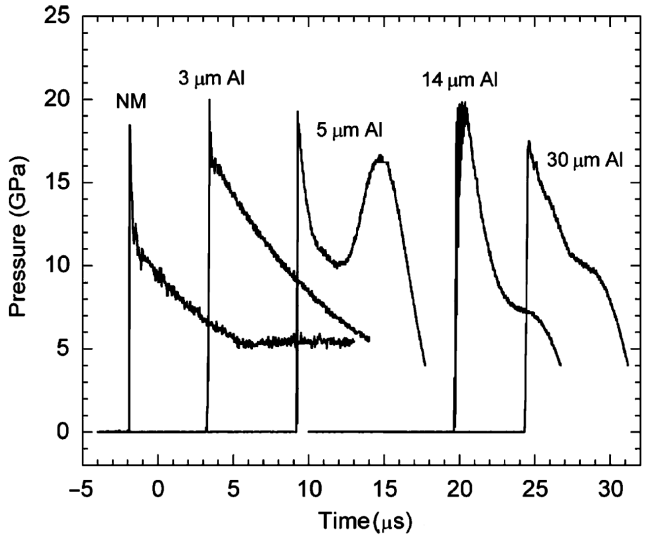

Figure 1.5: Time-resolved detonation profiles of NM and NM/Al recorded in a PMMA plate. Data of Kato and Murata [105], used with kind permission from Dr. Yukio Kato.

beds in which the solid sound speed is comparable to the bulk detonation velocity. Clearly, the pressure-time profiles in Figure 1.5 strongly depend on particle size.

Reaction of particles is contingent on heating, melting, and vaporization of the metal, in addition to availability of oxidizing gases. The results of Yoshinaka et al. [222] for 30 μm aluminum particles showed that particle melting did not occur within a 13 – 30 GPa shock compression environment in condensed matter, although there was damage and breakup of the aluminum particles. Thus, micrometric metal particles can usually be considered inert within the condensed detonation reaction zone. The interaction between the particles and explosive is therefore dominated by shock interactions in addition to momentum and heat transfer.

Figure 1.6 illustrates the cylindrical detonation of nitromethane/aluminum from the work of Frost et al. [74]. The later dispersal of particles into shock-heated air exhibits no reaction of the aluminum particles, since the charge diameter is below a critical value. Combinations of small cylindrical charge diameters with large-diameter particles showed no reaction of the dispersed particles due to insifficient particle heating time and rapid cooling in expanding gases. Frost et al. [77] introduced a second critical charge diameter, the critical diameter for particle ignition (CDPI), above which the dispersed particles ignite and react. For aluminum, the CDPI has a U-shaped dependence on particle diameter (Frost et al. [74]). It has been hypothesized that the particle size dependence of CDPI is influenced by the mechanisms responsible for the similar U-shaped failure diameter curve [164].

Figure 1.6: Cylindrical heterogeneous detonation and inert particle dispersal of 114 μm aluminum particles in a 19 mm diameter tube from Frost et al. [74, 76]. Five instances in time shown with 114 μs between frames. High-speed photographs from Defence R&D Canada – Suffield, courtesy of Dr. David Frost.

1.4 Particle dispersal phenomena

Lanovets et al. [120] modeled the dispersion of chemically-inert solid inclusions in the detonation products from a spherical condensed explosive charge. During detonation, they remarked that the particles entrained by the detonation wave acquire a high velocity and are grouped in the region adjacent to the leading front. The mechanism for accelerating the particles in the detonation flow was explained as a simple drag force. Lanovets et al. [120] numerically predicted that, for a certain range of particle size and density, the particles could penetrate the shockwave; this was confirmed experimentally by Zhang et al. [226]. Lanovets et al. [120] further stated that the particles destabilize the contact surface as they cross out of the fireball.

Figure 1.7 shows high-speed radiographs of the initial dispersal of iron beads in a centrally-initiated, glass-cased, spherically-symmetric charge. Although the gaseous detonation products and air shock are not visible in the radiographs, the particle front and glass fragments can be seen clearly. Analysis of these results by Frost et al. [75] notes that at 43 μs, a 1 mm thick particle layer has separated from the particle surface, in a similar fashion to spallation physics. The subsequent dispersal process shows strong spherical symmetry of the particle cloud, despite the detonation products fireball typically

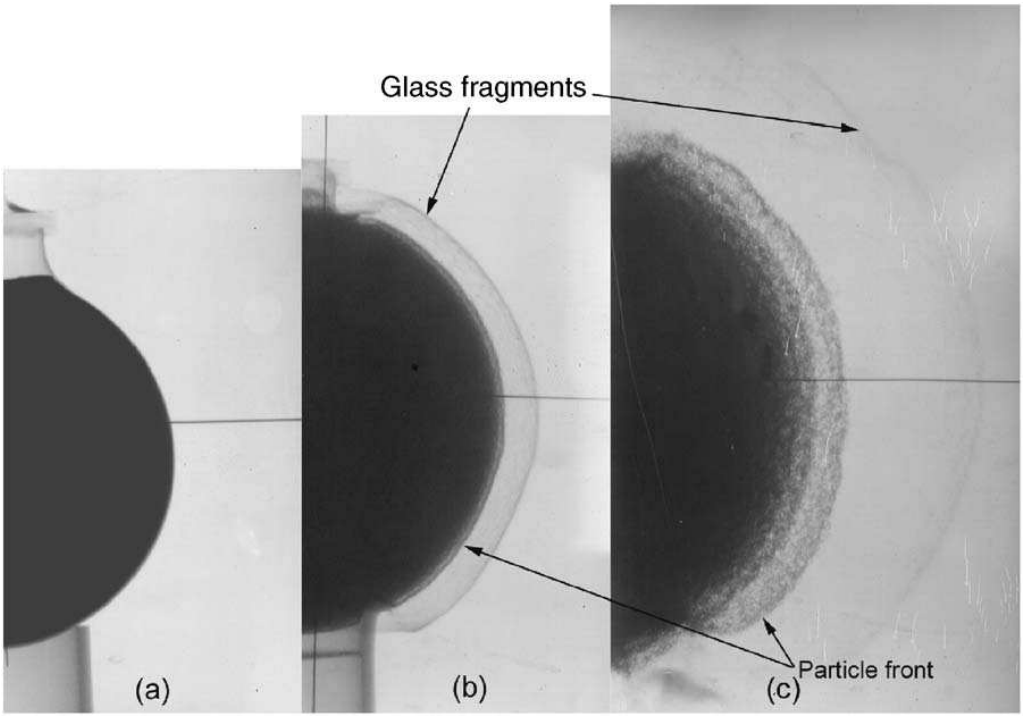

Figure 1.7: Radiographs of particle dispersal for an 11.8 cm diameter, glass-cased, spherical charge containing sensitized nitromethane and steel beads: (a) initial configuration at 0 μs; (b) dispersal of 275 μm iron particles at 43 μs; and, (c) dispersal of 463 μm particles at 75 μs. Figure from Frost et al. [75] and Zhang et al. [226]. Images from Defence R&D Canada – Suffield, courtesy of Dr. David Frost.

featuring large-scale Rayleigh-Taylor instabilities and small-scale turbulence at later times. As suggested by Zhang et al. [226], this indicates that the acceleration of particles at the outer edge of the charge occurs during the very initial stage of the particle dispersal.

In the experiment of Zhang et al. [226], the initial volume fraction of particles was $62 \pm 1\%$ (mass fraction $92 \pm 1\%$). After 43 and 75 μs (corresponding to times shown in Figure 1.7), the average volume occupied by the particles decreased to 35% and 10% respectively, although locally the volume fraction is lower. Below 8% volume fraction, the particle flow is considered dilute where the boundary layers on individual particles no longer interact (Rudinger [176]). For spherical explosions, the dense-to-dilute transition occurs very rapidly (under 100 μs in this example) and within an expansion of one charge radius. As evidenced by larger heavy particles, high momentum dominates the dispersal at nearly constant velocity until the particle passes the air shock. Frost et al. [75] showed for 463 μm steel particles that the velocity of the leading edge of the particle front was 1.280 km/s for 600 μs. Figure 1.8 shows the late-time dispersal process.

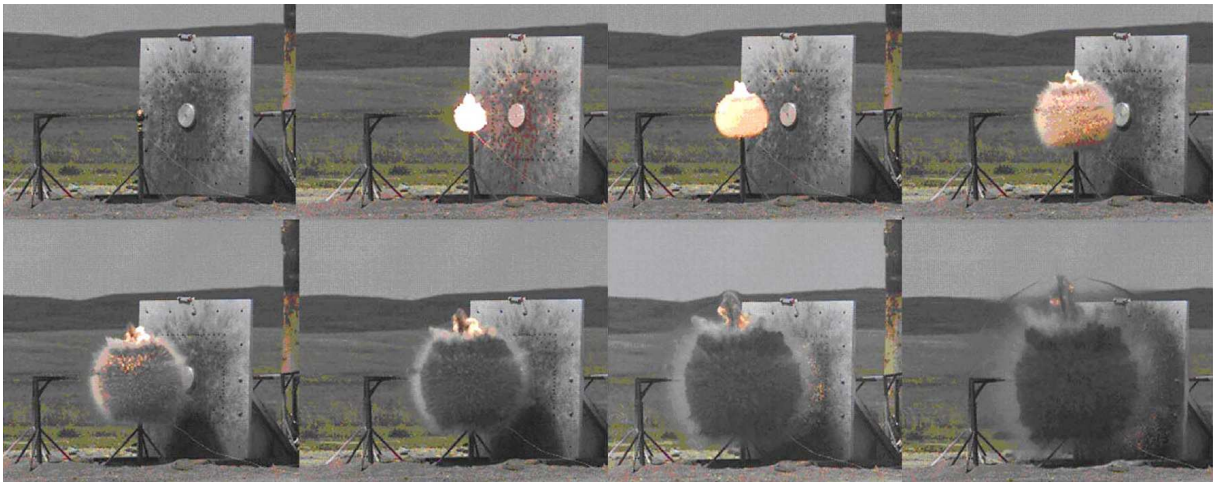

Figure 1.8: High-speed photograph of explosive dispersal of 275 μm inert particles in an 11.8 cm diameter, glass-cased, spherical charge from Frost et al. [75]. Times are 0, 40, 80, 160, 240, 360, 560, and 840 μs, respectively. High-speed photographs from Defence R&D Canada – Suffield, courtesy of Dr. David Frost.

Most models for shock/particle interaction are based on empirical drag and heat transfer laws developed for a single particle in steady isothermal flow. These models perform relatively well for dilute particle conditions in low-pressure gas flows. Successful simulation of dusty-gas experiments include Saito [178], Elperin et al. [56], and Rogue et al. [172] for particles of glass and Nylon. Rudinger [173, 174] gives drag coefficients for shock interaction in gas experiments. For dense particle conditions in condensed media, such as during detonation and early explosion expansion flow, the traditional momentum and heat exchange correlations are no longer valid. In fact, Zhang et al. [226] showed an empirical drag enhancement factor was required to correctly model the dispersed particle front crossing the shock. A momentum enhancement factor of 6 applied during the first 0.4 ms of dispersal from a constant-volume explosion state provided good agreement with experimental data. In similar dispersal modeling, Tanguay et al. [195] varied the particle velocity using 0, 0.5, 1, and 1.5 km/s as the detonation shock passes. Engelhardt [57] initialized particle velocity using a modified Gurney velocity ranging from 0 to 2.3 km/s as a function of radius. These *ad hoc* approaches have been employed to mimic the physical processes that occur at the detonation reaction zone and particle scale. Physical models are required for predictive modeling of particle dispersal for use in engineering applications.

1.5 Multiscale physics modeling

The scientific understanding of condensed explosives falls into two broad categories: initiation and detonation. Both are multiscale physical phenomena that begin at the atomic level where molecular excitation and then molecular vibration, chemical decomposition, and recombination lead to an increase in kinetic energy that increases the temperature and pressure. This produces waves that coalesce and amplify to support the detonation shock front, which accelerates and heats the explosive molecules (see Tarver [197, 198] and Baer [5]). Atomistic modeling includes first principles methods, such as quantum mechanics and *ab initio* molecular dynamics. At the microscopic scale, the structural arrangement of molecules into liquids, solids, and crystals includes directional-dependent microstructure and imperfections such as dislocations, cracks, inclusions, and oxide coatings on the individual constituents. At a much larger scale, the macroscopic scale widely used for engineering simulation, the explosive behaves as a continuous medium. In between the microscale and macroscale is the mesoscopic scale, or so-called mesoscale, which is characterized by heterogeneous components at the granular scale of the explosive. The mesoscale, however, cannot capture subgranular features such as microstructural crystal lattice defects or thin oxide coatings on metal particles. Figure 1.9 illustrates the modeling regimes for various length and time scales. The mesoscale is essentially a continuum system and typically covers geometric length scales of 0.1 μm – 1 mm and time horizons of 1 ns – 1 ms.

Although there is general agreement on the continuum theory (see Drumheller [55]) and conservation laws governing the multiphase flow (see Baer and Nunziato [10] and Powers et al. [160]), closure of the exchange terms between phases remains a challenge (see Bdzil et al. [21], Zhang et al. [226, 229], and Baer [6]). Considering a macroscopic control volume typically containing 10^2 – 10^4 physical particles (Figure 1.10), the complex process of shock and detonation interaction with the individual particles cannot be resolved at the macroscopic scale. Instead, the interaction occurs at a sub-grid scale where the momentum and heat transfer may be viewed as a process occurring over a shock-particle interaction timescale.

Studies of detonation interaction with particles at the sub-grid scale are required to develop new physical models. While experimental methods can provide information on the bulk detonation response, the diagnostics available today do not have the resolution required to record individual particle behaviour. On the other hand, direct numerical simulation using mesoscale modeling approaches is a practical alternative to gain insight

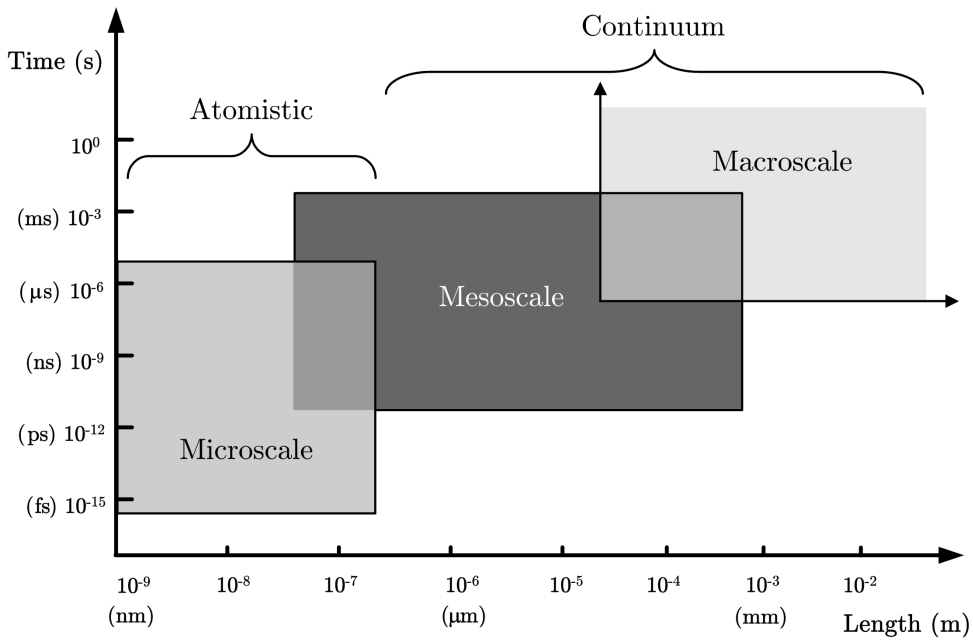

Figure 1.9: Length and time scales for physical modeling.

into detonation at the grain scale (0.1 μm – 1 mm) in condensed heterogeneous matter, where very high resolutions (Figure 1.10) are required to capture the small geometric features and shock interaction.

Modeling this range of physical mechanisms is a multiple length-scale problem. From a macroscopic viewpoint, Baer and Nunziato [10] and Baer et al. [9] have developed a macroscopic multiphase fluid dynamics model applicable to dense fluid-solid flow involving chemical reaction. These types of models average over the heterogeneities by using a mesh resolution much coarser than the particle size, where frozen shock interaction is assumed, in which the particle velocity and temperature are unaffected during the shock passage, and drag behind the shock accounts for the momentum transfer. Numerical simulation of particle dispersal by Zhang et al. [226] indicated that momentum transfer far beyond the standard drag magnitude is required for heterogeneous or granular explosives and the dense flow that follows detonation. Unfortunately, physical models describing the momentum and heat transfer between the explosive and particles have yet to be established.

Homogenization of the physical behaviour at one scale can be used to develop models for use at a larger scale (see Baer [5]). In this thesis, mesoscale simulation results for shock and detonation interaction are used to develop models at the macroscale. There are two approaches for entering the mesoscale: upscale from the microscopic level, or downscale

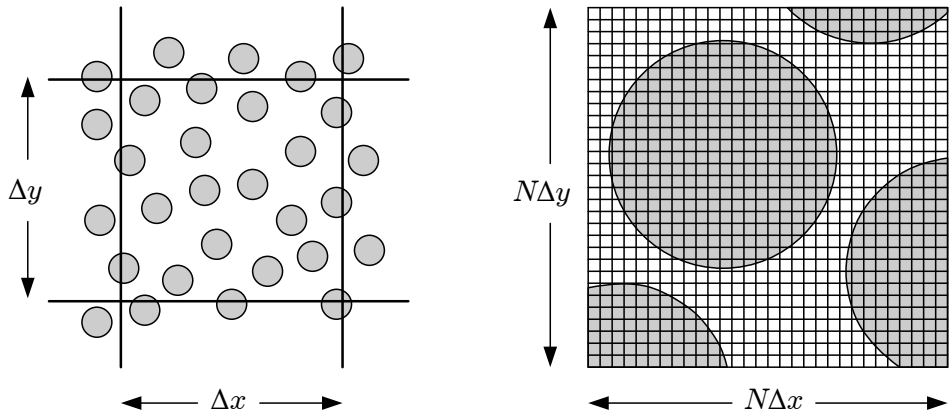

Figure 1.10: Comparison of particle and mesh size for the macroscale (left) and mesoscale with $N \gg 1$ (right). Two dimensions illustrated for simplicity.

from the macroscale. Both approaches inherit the same methods from their parent scale. Upscaling from the microscopic level involves adding more 'particles' (molecules or atoms) and looking at a larger section of matter; downscaling from the macroscale involves using finer mesh resolutions and focusing on a smaller piece of multi-component matter. Both methods are limited by computational power. Continuum approaches are adopted in this thesis to leverage the available macroscale framework.

1.6 Shock interaction at the mesoscale

Shock interactions, and related momentum and heat transfer from the explosive to the particles within the detonation zone, are important mechanisms associated with macroscopic detonation initiation, propagation, stability, and failure phenomena. On the other hand, the detonation transmits a strong shock into the solid particles that rapidly accelerates and heats the material as the wave passes. Internal wave reflections and external interactions with neighbouring particles dominantly affect the particle velocity and temperature due to shock compression, before viscous interaction takes over. Thus, the acceleration and heating of particles within the detonation shock compression regime will significantly determine the particle dynamics from the explosive dispersal and the subsequent reaction of the dispersed particles. Zhang et al. [230, 229] showed that light metal particles, such as aluminum, beryllium, and magnesium, achieve 60–100% of the shocked fluid velocity immediately behind the shock front. They demonstrated that the initial material density ratio of the explosive to solid particle was the most significant

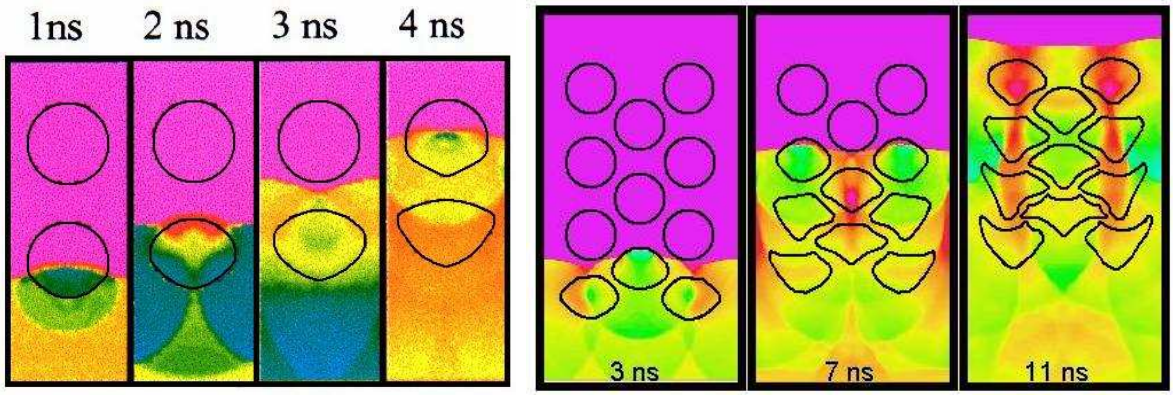

Figure 1.11: Two-dimensional mesoscale inert shock interaction with cylindrical particle matrices. Shock traveling from bottom to top. Figure enhanced from Zhang et al. [229], used with permission from the author.

factor affecting particle acceleration. Further, the influence of other parameters affecting particle acceleration and heating have been studied including particle matrix properties and explosive reactivity (see Ripley et al. [166, 169, 170]).

Mader [132] conducted some of the pioneering work in mesoscale modeling using 2D simulation of shock interaction with single air spheres and aluminum cylinders to study shock initiation of heterogeneous explosives. Following this early work, microstructural heterogeneities were typically modeled in 2D using ordered matrices of packed circles or simple polygons (e.g., [14, 24, 219]). Milne [144] used 2D domains to study nitromethane detonation in heterogeneous mixtures containing glass beads, aluminum particles, and steel particles. To simulate layers of particles, Milne's geometry consisted of stacked particles surrounded by either a rigid cylindrical wall or by toroidal 'particles' to simulate the increased detonation path length expected from real geometries. Zhang et al. [230, 229] used 2D mesoscale calculations involving single spherical particles and matrices of cylindrical 'particles' (see Figure 1.11) to quantify the acceleration of particles during the inert shock interaction. Two-dimensional calculations have provided fundamental knowledge of mesoscale physics using systematic studies; even though the real geometries are 3D, these models allowed finer meshes and shorter run times than possible in 3D.

Mader and Kershner [135, 136] were perhaps the first to employ 3D mesoscale modeling, as an extension of earlier 2D calculations. Their original simulation of 3D reaction zones in heterogeneous explosives, consisting of a solid explosive containing a small void fraction, aimed to study hot-spot formation and detonation initiation. The voids were modeled as spherical holes regularly spaced in a 3D matrix of continuous media, requiring only a single

material to describe a heterogeneous microstructure. The resolution used was 2 – 6 cells across each void, although they noted that three cells are sufficient.

Modern 3D mesoscale calculations typically employ at least 10^7 computational cells and contain $\mathcal{O}(100)$ particles. Multiple materials are required to describe the heterogeneous condensed matter. Baer [6] performed 3D numerical simulations using the Eulerian CTH shock physics code [141] which includes the effects of material strength, thermal dissipation, and reaction on shock loading behaviour at the mesoscale. Statistical interrogation has been performed on this extensive data with the goal to develop continuum-level descriptions of the fluctuating shock fields [11]. Cooper et al. [40] demonstrated 3D CTH mesoscale results for an energetic mixture of randomly oriented RDX cubes, aluminum platelets and IPN liquid filling the interstitial sites. This complex calculation illustrated high shear and subsequent breakup of the aluminum flakes behind the detonation.

In general, only a very small material sample (up to millimeter size) can be modeled using mesoscale simulation; a noteworthy exception is Baer [6] who modeled a one-centimeter disk of material in 3D, requiring 1.3×10^9 mesh points and the use of 4500 CPU computing in parallel. Recently, mesoscale simulation has gained wide-spread use since computing power increased, where it has been used to develop constitutive models, and to design and interpret experiments.

1.7 Motivation and state of the art

The scope of the present work is limited to liquid explosive / metal powder systems. While the effect of the particles on hot-spot sensitization, detonation wave structure, and propagation velocity is phenomenologically characterized, a theoretical description has not been developed. Furthermore, the commensurate effects of particle acceleration and heating on the detonation are not completely established. Whereas hot spots formed by particles are presumed to sensitize the explosive, momentum and heat transfer to the particles can provide a competing desensitizing effect. This desensitizing effect has not been properly quantified; hence, it has not been adequately considered in the explanation of particle size effects on critical diameter for detonation failure and particle ignition. In the case of detonation failure, the momentum loss within the detonation reaction zone further exacerbates the strong free-edge expansion for small cylindrical and spherical charge diameters. For particle reaction, heating during the detonation stage may contribute to subsequent ignition. The reviewed literature pertaining to slurry detonation and

subsequent particle acceleration, heating, and reaction during dispersal suggests strong a dependence on the size of particles. However, particle size needs to be considered in the context of other length scales present in the problem.

Knowledge of the acceleration and heating imparted on metal particles in condensed matter during explosive detonation remains a significant gap. Enhancement factors and *ad hoc* corrections have indicated that insufficient momentum and heat transfer are represented by current models in the literature. Physics-based models for shock compression particle acceleration and heating are therefore required. These physical models are necessary to further explore and understand the mechanisms responsible for the detonation and explosive dispersal phenomena observed in experiments.

The state-of-the-art mesoscale studies of momentum transfer of Zhang et al. [230, 229] have clearly demonstrated the effects of density ratio for a single particle and indicated the importance of volume fraction for clusters of particles subjected to a shock wave; their work has paved the way for quantitative accounting of the shock transmission. However, work remains to be conducted for a quantitative description of the acceleration and heating of particles in a matrix subjected to a shock wave and, particularly, a detonation wave. Extension of the original works of Milne [144] and Zhang et al. [230, 229] requires full three-dimensional effects and sufficient resolution of the detonation reaction zone to be included. Finally, development of the mesoscale results into macroscale models remains to be conducted.

1.8 Objective and plan of thesis

The objective of this thesis is to develop novel physical models for acceleration and heating of metal particles in condensed explosive detonation. A more quantitative description of the resultant momentum and heat transfer is sought in conjunction with determination of the principal shock interaction mechanisms. This is achieved using a theoretical dimensional analysis to identify key parameters, applying 3D mesoscale continuum modeling of packed particle matrices saturated with liquid explosive to understand the mechanisms and behaviour of the key parameters, and by compiling results into transmission factors that quantify the momentum and heat transfer from the explosive to the particles. The transmission factors are then incorporated into momentum and heat exchange source terms developed for the macroscopic computational fluid dynamics framework, which is suitable for modeling detonation shock compression in metal particles-condensed explosive systems.

Finally, the new models are applied and validated against macroscopic experimental test cases involving slurry detonation and dense particle dispersal.

This thesis is organized as follows:

Chapter 2 reviews fundamental considerations for the fluid-particle interaction regimes.

Chapter 3 presents a formal dimensional analysis with a discussion of the resulting parameter groups.

Chapter 4 provides the methodology adopted for mesoscale calculation, including assumptions, models, and validation.

Chapter 5 presents the mesoscale results for shock and detonation interaction, followed by compilation and reduction of the resulting velocity and temperature transmission factors.

Chapter 6 formulates the macroscopic physical models and applies the shock compression models to detonation and dispersal test cases with comparison to experiment.

Chapter 7 addresses final discussion and concluding points.

Chapter 2

Regimes for fluid-particle interaction in detonation and explosion flow

Particles involved in multiphase detonation and explosive dispersal are subject to a wide range of interaction regimes. Figure 2.1 schematically illustrates the wave processes and particle trajectory during the detonation of a spherical slurry explosive and early dispersal of particles. The detonation is centrally initiated ($r = 0$) and the detonation wave travels radially outward, followed by a Taylor expansion wave. When the detonation shock reaches the edge of the explosive, it transmits a strong shock into the air, while a rarefaction wave travels back into the explosive. The air shock is driven by the expanding detonation products interface (commonly called the fireball) at the contact surface. Particles contained in the explosive are stationary until the arrival of the detonation shock, which during the interaction, promptly imparts a velocity to the particles due to shock compression momentum transfer. Subsequently, the Taylor expansion slows the particles, particularly those closer to the centre of the charge. Near the outer edge of the charge, the strong edge expansion rapidly accelerates the particles, most significantly at the outermost particle layers. Depending on the particle size and solid density, the particles may escape the fireball and pierce through the primary shock wave (Lanovets et al. [120] and Zhang et al. [226]).

The flow field can be categorized into three major regimes by spatially dividing the radial flow. A proposed working description of the regimes is illustrated in Figure 2.2. For each regime, the force acting on particles in the flow, F_d, is normalized by the aerodynamic force on a single sphere, $F_{d,S}$. Regime I is the detonation flow regime, which is contained within one charge radius. Regime II is the dense particle flow regime and extends from

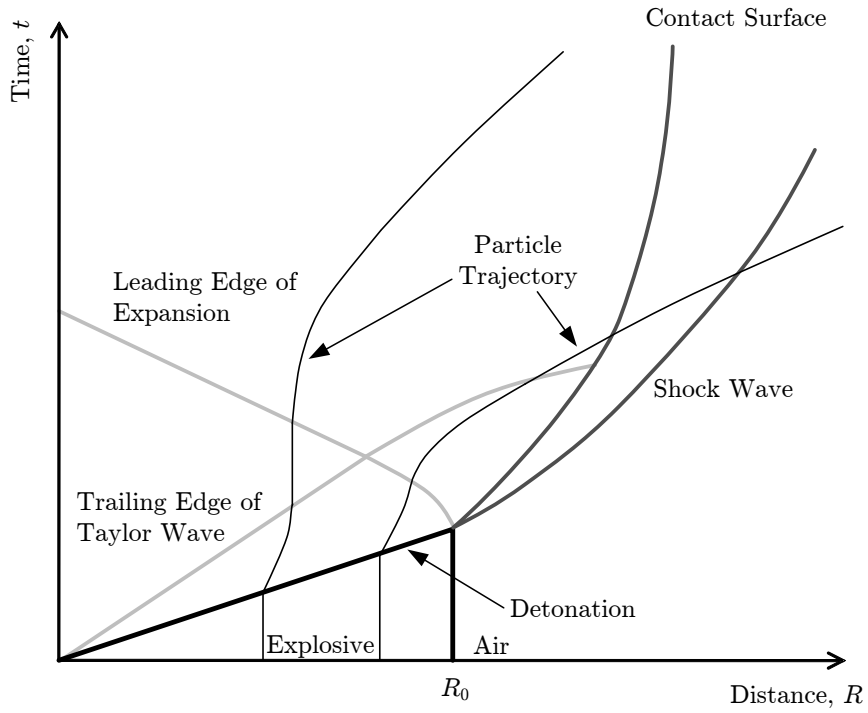

Figure 2.1: Schematic $x-t$ diagram for spherical detonation and early dispersal of particles (R_0 = charge radius).

the outer edge of the charge to a distance between two and three charge radii. Beyond the dense particle flow regime is the dilute particle flow in the far field, denoted as Regime III. The transition from dense to dilute particle flow is smooth. In contrast, the transition from the detonation to the dense particle flow regime contains a discontinuity caused by the abrupt detonation termination and expansion at the edge of the explosive.

The main features of these regimes as they pertain to particle acceleration and heating are briefly discussed in the following sections. For the generalized fluid-solid flow description that follows, subscript f denotes the fluid (gas or liquid) and p denotes the particle (solid). Additional nomenclature is given on Page xxi.

2.1 Dilute particle flow regime

Dilute particle-gas flow is well established in the literature (e.g., Soo [188] and Rudinger [176]), and is reviewed first since it is the most fundamental and to serve as a prerequisite for later discussion of the dense and detonation flow regimes. The primary interaction mechanisms between the two phases are acceleration, heating, and reaction. For the present

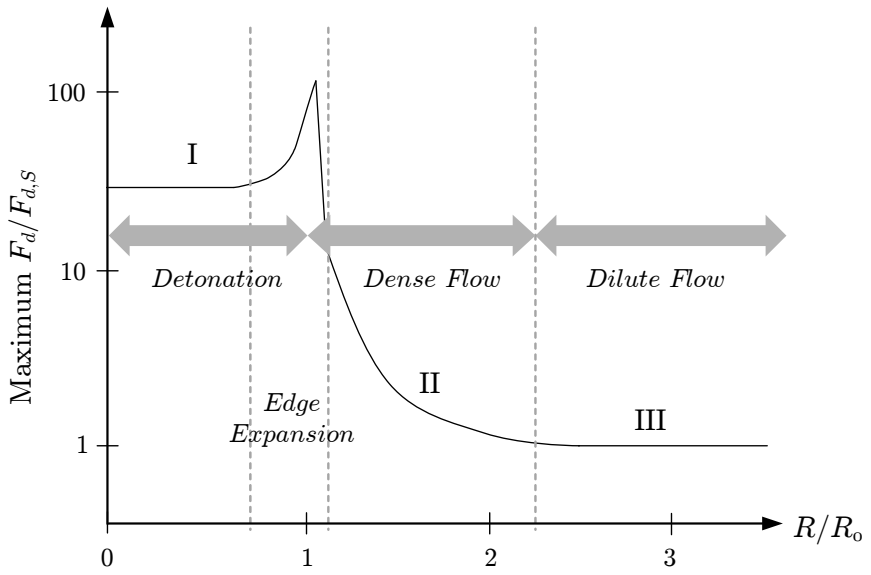

Figure 2.2: Flow regimes for spherical multiphase explosion (R_0 = charge radius).

analysis, the particles are assumed to be inert without evaporation, and therefore, mass transfer is not considered.

In the dilute limit, the particles are far apart and it is assumed that neither the particles nor the flow fields around each particle interact with each other. The dilute flow regime therefore consists of individual particles that exchange momentum and energy with the surrounding fluid. Therefore, the following discussion considers only a single particle, but is approximately applicable to a collection of non-interacting particles by multiplying by the number of particles. For gas-solid interaction where $\rho_s \gg \rho_f$, there are only very weak shock waves near the solid sound speed transmitted into the particle. Frozen interaction can be assumed, where the particle does not respond to gas shocks until after the wave passes the particle. Basically, there are only relaxation processes due to drag and heat transfer, between the particle and the shocked flow.

2.1.1 Particle acceleration

Acceleration of the particle occurs any time when there is a relative velocity between the fluid and particle, commonly defined as the slip velocity: $u_{slip} = u_f - u_p$. For spherical particles, Newton's law of motion can be used to define the interaction:

$$\frac{\pi d_p^3}{6}\rho_s \frac{\mathrm{d}u_p}{\mathrm{d}t} = C_d \frac{1}{2}\rho_f (u_f - u_p)|u_f - u_p|\frac{\pi d_p^2}{4} \tag{2.1}$$

where ρ is the density, u is the velocity, d_p is the particle diameter, and C_d is the drag coefficient. In Equation (2.1), $\mathrm{d}u_p/\mathrm{d}t$ is the particle acceleration in the Eulerian frame (fixed laboratory coordinates), and is related to the particle acceleration in the Lagrangian frame (attached to the particle), $\partial u_p/\partial t$, as follows:

$$\frac{\mathrm{d}u_p}{\mathrm{d}t} = \frac{\partial u_p}{\partial t} + u_p \frac{\partial u_p}{\partial x} \tag{2.2}$$

The drag coefficient, C_d, is defined in terms of the dynamic head of the relative flow and the frontal area of the particle:

$$C_d = \frac{F_d}{\frac{1}{2}\rho_f (u_f - u_p)^2 A_p} \tag{2.3}$$

where F_d is the drag force acting on the particle, including both viscous and pressure drag, and A_p is the frontal area of the particle (for spheres, $A_p = \pi \mathrm{d}_p^2/4$). Based on Reynolds' principle of dynamic similarity, C_d is a function of the Reynolds number and the Mach number in a compressible fluid (Schlichting [181]).

The particle Reynolds number, Re, and Mach number, M, are defined using the relative slip velocity:

$$Re = \frac{\rho_f d_p |u_f - u_p|}{\mu_f}, \quad M = \frac{|u_f - u_p|}{a_f} \tag{2.4}$$

where μ_f is the dynamic viscosity (i.e., the molecular viscosity) of the fluid and a_f is the speed of sound in the fluid.

Equation (2.1) can be re-written for the particle acceleration as:

$$\frac{\mathrm{d}u_p}{\mathrm{d}t} = \frac{3 C_d \rho_f}{4 d_p \rho_s} (u_f - u_p) |u_f - u_p| \tag{2.5}$$

For $u_f \neq u_p$, there is a drag force (defined on the RHS of Equation 2.1) that causes the fluid and particle velocity to approach an equilibrium value over a mechanical relaxation time. The particle acceleration can be expressed in discrete form:

$$\frac{\mathrm{d}u_p}{\mathrm{d}t} = \frac{u_f - u_p}{\tau_V} \tag{2.6}$$

where τ_V is the velocity relaxation time. Equating (2.5) and (2.6) yields the velocity relaxation time:

$$\tau_V = \frac{4 d_p \rho_s}{3 C_d \rho_f |u_f - u_p|} \tag{2.7}$$

Rudinger [173, 175] determined that the drag coefficients for particles in a gaseous shock flow have a steeper dependence on Reynolds number when compared to the drag coefficients in steady flow. Several numerical investigations of the unsteady drag coefficient on cylinders and spheres have been conducted, including Ripley et al. [167] and Sun et al. [193], which show the drag coefficient in a gaseous shock flow is greater than the steady value.

The Basset, Boussinesq, and Oseen (BBO) equation (see Soo [188], Rudinger [176]), given in Equation (2.8), is applicable to unsteady flow mainly in the dilute regime. The BBO equation is used to further analyze the contributions to the drag force magnitude using a more general unsteady form of the drag force.

$$\begin{aligned} \frac{\pi d_p^3}{6} \rho_s \frac{\mathrm{d}u_p}{\mathrm{d}t} &= C_d \frac{1}{2} \rho_f (u_f - u_p) |u_f - u_p| \frac{\pi d_p^2}{4} \\ &- \frac{\pi d_p^3}{6} \frac{\partial p}{\partial x} \\ &+ \frac{1}{2} \frac{\pi d_p^3}{6} \rho_f \frac{\mathrm{d}}{\mathrm{d}t} (u_f - u_p) \\ &+ \frac{3}{2} d_p^2 \sqrt{\pi \rho_f \mu_f} \int_{t_0}^{t} \frac{(\mathrm{d}/\mathrm{d}t')(u_f - u_p)}{\sqrt{t - t'}} \mathrm{d}t' \\ &+ F_a \end{aligned} \tag{2.8}$$

Examining the various force contributions on the RHS of Equation (2.8), the first term is the viscous drag force for steady flow (cf. Equation 2.1). The second term accounts for the pressure gradient in the flow acting on the particle. The third term is the added mass term, which is the force required to accelerate the virtual mass of fluid surrounding the particle; the apparent added mass is equal to one-half of the particle volume of the displaced mass of fluid. The fourth term is the Basset history force, or Basset integral, which represents the additional resistance due to unsteady motion; it considers the history of the force caused by deviation from the steady flow as a correction to the first term. The last term, F_a, represents external forces such as gravity.

The Basset force term addresses the temporal delay in boundary layer development as the relative velocity changes with time [176]. Thomas [202] studied the significance of

the Basset history force on particle drag in oblique aerodynamic shocks; Sommerfield and Decker [187] evaluated the Basset history force for planar shocks. Thomas [202] showed that in the immediate vicinity of the shock, the Basset integral can be many times larger than the viscous drag; however, the overall Basset force can be neglected when considering the overall particle motion.

2.1.2 Particle heating

The unsteady energy equation describing heat transfer (convection and radiation) to a spherical particle is given in Equation (2.9), which is valid below the solid melting point and assumes a constant specific heat capacity:

$$\frac{\pi d_p^3}{6}\rho_s c_s \frac{\mathrm{d}T_p}{\mathrm{d}t} = \left[h(T_f - T_p) + \varepsilon_s \sigma_B (T_f^4 - T_p^4)\right] \pi d_p^2 \tag{2.9}$$

where T is the temperature, c_s is the solid heat capacity, h is the convective heat transfer coefficient, ε_s is the emissivity of the particle, and σ_B is the Stefan-Boltzmann constant ($\sigma_B = 5.6704 \times 10^{-8}$ W/m^{2}T^4).

In Equation (2.9), $\mathrm{d}T_p/\mathrm{d}t$ is the particle heating rate in the Eulerian frame of reference, which is related to heating in the Lagrangian frame as follows:

$$\frac{\mathrm{d}T_p}{\mathrm{d}t} = \frac{\partial T_p}{\partial t} + u_p \frac{\partial T_p}{\partial x} \tag{2.10}$$

and the convective heat transfer coefficient in Equation (2.9) is defined as:

$$h = \frac{Nu k_f}{d_p} \tag{2.11}$$

where Nu is the Nusselt number and k_f is the fluid thermal conductivity. The Nusselt number is a function of the Mach number, Reynolds number, and Prandtl number: $Nu = f(M, Re, Pr)$, where the Prandtl number is defined by $Pr = c_p \mu_f / k_f$, with c_p being the fluid specific heat capacity at constant pressure. A wide range of empirical correlations for the Nusselt number are available in the literature, cf., Oseen [154], Knudsen and Katz [113], Drake [50], and White [216]. The effect of compressibility was considered in Nusselt number correlations by Fox et al. [67] and Sauer [180], but the Mach number correction mostly affects low Reynolds numbers ($Re < 100$).

Equation (2.9) can be re-written for the particle heating rate:

$$\frac{\mathrm{d}T_p}{\mathrm{d}t} = \frac{6(T_f - T_p)}{d_p \rho_s c_s} \left[\frac{Nu k_f}{d_p} + \varepsilon_s \sigma_B (T_f^2 + T_p^2)(T_f + T_p) \right] \tag{2.12}$$

Introducing the timescales for thermal equilibrium by convection, τ_T, and radiation, τ_R, the particle heating rate simplifies to:

$$\frac{\mathrm{d}T_p}{\mathrm{d}t} = (T_f - T_p) \left(\frac{1}{\tau_T} + \frac{1}{\tau_R} \right) \tag{2.13}$$

Convection and radiation can be considered independently by evaluating the dominant timescale when they are disparate. Evaluating the convective heat transfer timescale using Equations (2.12) and (2.13) and assuming $\tau_T \ll \tau_R$ shows:

$$\tau_T = \frac{\rho_s d_p^2 c_s}{6 k_f Nu} \tag{2.14}$$

Similarly, evaluating the radiation timescale assuming $\tau_\mathrm{R} \ll \tau_\mathrm{T}$ gives:

$$\tau_R = \frac{d_p \rho_s c_s}{6 \varepsilon_s \sigma_B (T_f^2 + T_p^2)(T_f + T_p)} \tag{2.15}$$

In general, convective heat transfer is the dominant energy exchange mechanism for small particles.

In addition to the unsteady heat transfer between the fluid and particle, the temperature distribution within the particle may be non-uniform. The Biot number, Bi, is the ratio of convective heat transfer from the fluid to the conductive heat transfer within the solid particle:

$$Bi = \frac{h d_p}{6 k_s} = \frac{Nu}{6} \left(\frac{k_f}{k_s} \right) \tag{2.16}$$

The Biot number can be used to judge the uniformity of the internal temperature distribution. For $Bi < 0.1$ the temperature distribution inside the particle is generally assumed to be uniform and a lumped capacitance method (see Incropera and DeWitt [98]) can be used to describe the heat transfer at the particle surface. Figure 2.3 plots Bi (Equation 2.16) for various metal particles in high-temperature gaseous detonation products. The Nusselt number correlation of Knudsen and Katz [113] is used, where $Nu =$

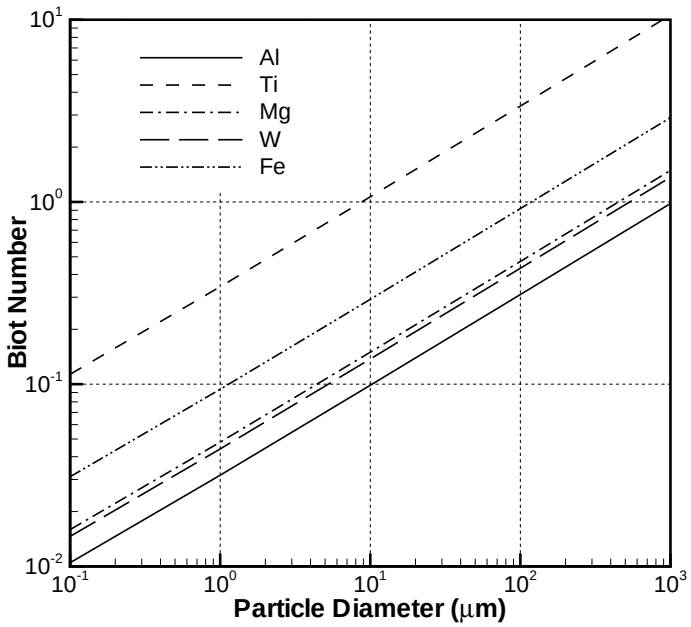

Figure 2.3: Biot number for various particle diameters and metals. Gas thermal conductivity is approximated from CO_2 at unexpanded detonation products temperature (3000 K) and density (1.535 g/cc). Relative flow velocity of 1.775 mm/μs assumed.

$2 + 0.6Re^{0.5}Pr^{0.33}$. For large particles or metals having low thermal conductivity, $Bi > 0.1$ and the unsteady temperature distribution inside the particle needs to be considered. Figure 2.3 shows that aluminum, magnesium, and tungsten can reasonably be represented by the lumped capacitance model for $d_p < 10$ μm.

2.2 Dense particle flow regime

The dense particle flow regime is characterized by a high volume fraction of solid particles, $\phi_p = V_p/(V_p + V_f)$, where V is the volume occupied by the particles or fluid phase. The extreme limit of granular flow occurs for $\phi_p \geq \phi_{packed}$, where particles are tightly packed. Above the packing limit, forces are exerted on the particles by direct contact with the neighbouring particles and also by the gas pressure in the pores [226]. Resistance to changes in the packing configuration is called compaction [10], which is caused by a competition between the contact forces and compression deformation. For $\phi_p \geq 0.49$, the flow behaves more like a solid [158], where the pressure and sound speed of the flow approach those of the solid itself.

In the dense particle flow regime, the particles interact with one another through random elastic collisions. However, unlike molecular kinetic theory, the dense particle regime features additional interaction forces due to the surrounding fluid flow. Since particle wakes occupy much more volume than the particles themselves [181], particle-wake interactions are much more likely than particle-particle collisions. Xu et al. [221, 220] have studied the turbulent wake interaction and collision in dense flows of particles ($\phi_p = 0.25$). Close-proximity particles in supersonic gas flow also introduce the interaction of shock wave structures (see Laurence et al. [121] and Zarei et al. [223]). In the dense particle flow regime, therefore, the flow pressure and sound speed are not satisfactorily described by theory. A heuristic model for compressible dense solid flow is discussed by Zhang et al. [226].

The transition from dense to dilute flow occurs when the boundary layers between neighbouring particles no longer interact. A particle volume fraction of 0.08 corresponds to a one-particle-diameter spacing between mono-sized spherical particles. The particles and flow fields are completely independent for volume fractions below 0.02, as suggested by Steinoir (1944) as cited in Soo [188], or below 0.05, as observed by Kaye (1962) and cited in Soo [188], depending on Reynolds number. The dilute limit is generally assumed for $\phi_p \leq 0.01$, as in [226].

For low-density gas flow, Figure 2.4 shows photographs of high-volume-fraction particle layers from the experiment of Rogue et al. [172]. Acceleration is dominated by the drag behind the shock front since $\rho_f \ll \rho_s$. Rogue et al. estimated that the drag was higher than that given by dilute correlations.

Several drag correlations for high volume fractions are available in the literature (e.g., Zuber [235], Soo [188], Smirnov [186], and Tam [194]). For example, the Smirnov correlation is given in Equation (2.17), which is valid for $1.5 < Re < 10^5$. Figure 2.5 plots the drag coefficient from the Smirnov correlation over a wide range of Reynolds number with a volume fraction range of $0.1 \leq \phi_p \leq 0.6$. The resulting C_d has an order-of-magnitude spread at a given Re for various ϕ_p. The high-volume-fraction drag coefficient relative to the single drag coefficient is plotted in the ratio $C_d/C_{d,s}$ in Figure 2.5, assuming $C_{d,s} = C_d(\phi_p = 0)$. For $\phi_p = 0.1$, $C_d/C_{d,s}$ ranges from 1 to 1.28; in comparison, for $\phi_p = 0.6$, $C_d/C_{d,s}$ ranges from 13.8 to 30.7 depending on Reynolds number.

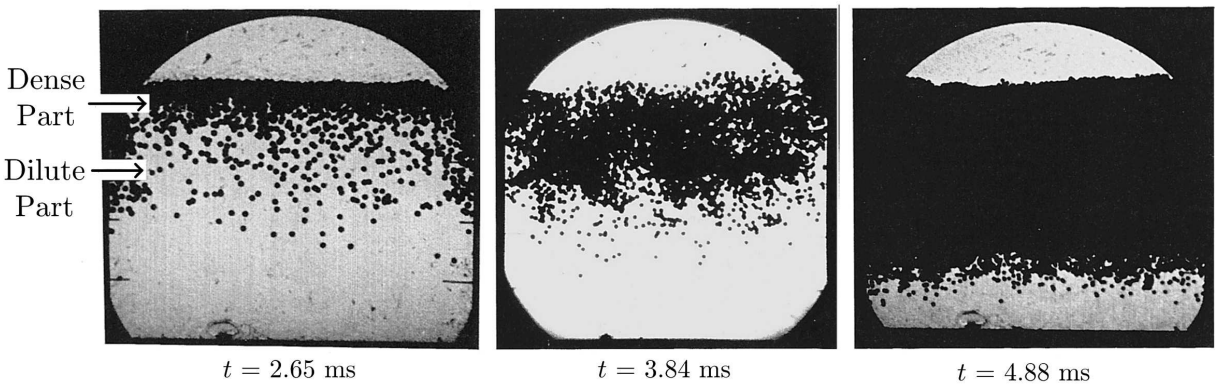

Figure 2.4: Photographs of high-volume-fraction particle flow accelerated by a Mach 1.3 air shock from Rogue et al. [172]. Results for three different configurations: a thin layer of 2 mm glass spheres (left); a double layer of 2 mm glass spheres (centre); and, a thick bed of 1.5 mm glass spheres (right). Reprinted with kind permission from Springer Science.

$$C_d = \begin{cases} C_1 = \dfrac{24}{Re} + \dfrac{4.4}{Re^{0.5}} + 0.42 & \phi_p \leq 0.08 \\ C_2 = \dfrac{4}{3(1-\phi_p)}\left(\dfrac{7}{4} + \dfrac{150\phi_p}{(1-\phi_p)Re}\right) & \phi_p \geq 0.45 \\ \dfrac{(\phi_p - 0.08)C_2 + (0.45 - \phi_p)C_1}{0.37} & 0.08 < \phi_p < 0.45 \end{cases} \tag{2.17}$$

Convective heat transfer correlations for high volume fractions are generally limited to low-Reynolds-number flow such as in heat exchangers and fluidized beds.

In addition to featuring a high volume fraction of solid particles, the dense particle flow regime may also consist of dense gas flow and unsteady wave dynamics such as in the near-field expansion of condensed-phase detonation. Real dense gas flow should consider molecular collision effects to correct the molecular transport coefficients, including viscosity and conductivity, as well as accounting for shock transmission into the particles (this issue is discussed further in §2.3.2).

2.3 Detonation regime

The above discussion demonstrates that the dilute and dense particle flow regimes are well characterized and generally understood from a variety of experimental and numerical investigations. As such, both the dilute and dense fluid-particle interactions can be

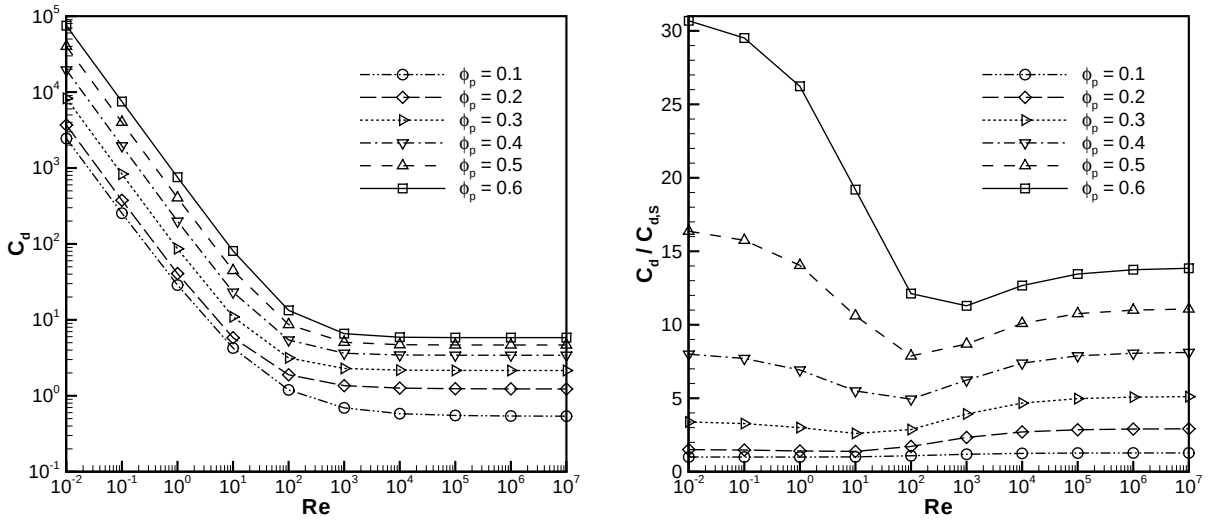

Figure 2.5: Plot of the high-volume-fraction correlation for drag coefficient based on the equation in Smirnov [186].

quantified in terms of standard drag coefficients and heat transfer correlations, $C_d = f(Re, M, \phi_p)$ and $Nu = f(Re, Pr, M, \phi_p)$. When considering the detonation regime and subsequent transition to dense flow, momentum and heat transfer become dominated by *shock compression interaction*, rather than aerodynamic forces.

In the 1D detonation model, the detonation zone contains a shock wave followed by a reaction zone. Behind the reaction zone, there is an unsteady flow region. Relevant physical considerations for these zones are reviewed in this section. Before considering the interaction of the detonation wave with particles, additional background on homogeneous detonation theory is presented first.

2.3.1 Homogeneous detonation

Theories for homogeneous detonation in gases and high explosives must satisfy the Rankine-Hugoniot equations, given in Equation (2.18), which are conservation laws for mass, momentum and energy across a shock front traveling with velocity D (see Figure 2.6). The Rankine-Hugoniot equations are as follows:

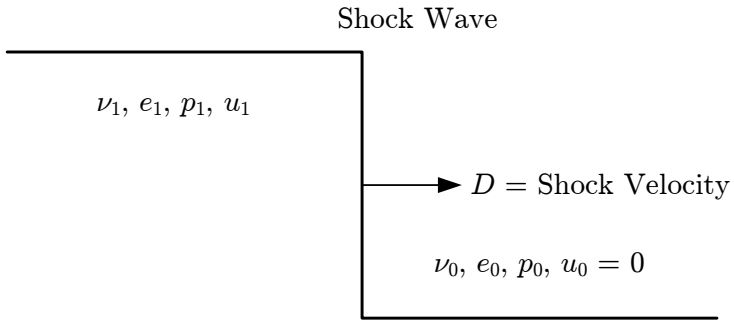

Figure 2.6: Schematic of a shock Hugoniot.

$$u_1 = D\left(1 - \frac{\nu_1}{\nu_0}\right) \tag{2.18a}$$

$$\rho_0^2 D^2 = (p_1 - p_0)/(\nu_0 - \nu_1) \tag{2.18b}$$

$$e_1 - e_0 = \frac{1}{2}(p_1 + p_0)(\nu_0 - \nu_1) \tag{2.18c}$$

The line determined by Equation (2.18b) is called Rayleigh line; the curve obtained from Equation (2.18c), given an equation of state, is called the Hugoniot curve.

In the 'Simplest Theory' of detonation [64], the reaction is completed in a single discontinuity that includes both the shock and reaction zone. Fickett and Davis state "the simplest theory assumes the following:

1. The flow is one-dimensional (laminar).

2. The plane detonation front is a jump discontinuity, a shock in which the chemical reaction is assumed to be completed instantaneously. The material emerging from the discontinuity is assumed to be in thermochemical equilibrium, and is thus described by a thermodynamic equation of state.

3. The jump discontinuity is steady (independent of time), so that the state of the material emerging from the front is independent of time. The flow following this point may be time-dependent" [64].

Detonation waves represented by the simplest theory have no initiation transients and are self-similar in time with a constant reactive shock velocity.

For a planar detonation wave to be self-propagating at a steady velocity, the simple detonation theories rely on the Chapman-Jouget (CJ) condition. The CJ condition states

that an unsupported detonation will propagate at a minimum velocity found where the Rayleigh line has the least slope while remaining tangent to the detonation products Hugoniot curve. This minimum velocity is uniquely defined as the CJ velocity.

Figure 2.7 illustrates the CJ point and Rayleigh line in the $p-\nu$ plane. Hugoniot curves are loci of possible end states for adiabatic shock compression ($Q = 0$ for no chemical reaction or heat losses); Hugoniot curves in Figure 2.7 are denoted as lines of $\mathcal{H} = 0$. The initial condition (State 0) and von Neumann point (VN state) are both found on the unreacted Hugoniot curve. Dashed lines are partial reaction Hugoniot curves proceeding from unreacted ($\lambda = 0$) to completely reacted ($\lambda = 1$). Rayleigh lines, denoted by $\mathcal{R} = 0$, have slopes proportional to the square of the detonation velocity, D. Detonation velocities below that of a CJ wave, e.g., D_2 in Figure 2.7, do not intersect the completely reacted ($\lambda = 1$) Hugoniot curve, consistent with the CJ postulate. For detonation velocities D_1 greater than the CJ velocity, called overdriven detonations, two possible intersections with the detonation products Hugoniot are possible corresponding to strong (S) and weak (W) detonations. For completeness, lines of constant products flow velocity are shown in Figure 2.7 through the CJ, S and W points. Depending on the rear boundary condition, the final state may end at the CJ point, or follow an isentrope in a rarefaction.

The Zel'dovich-von Neumann-Döering (ZND) model of detonation involves a thin shock followed by a finite reaction zone, where the flow is steady in the frame of reference attached to the shock. The ZND detonation is shown schematically in Figure 1.1. For the ZND model, Fickett and Davis state "the explicit assumptions are as follows:

1. The flow is one-dimensional,
2. The shock is a jump discontinuity, because transport effects (heat conduction, radiation, diffusion, viscosity) are neglected,
3. The reaction rate is zero ahead of the shock and finite behind, and the reaction is irreversible (proceeds in the forward direction only),
4. All thermodynamic variables other than the chemical composition are in local thermal thermodynamic equilibrium everywhere" [64].

The final state occurs where the reaction approaches equilibrium, and is identical for both the simplest theory (unresolved reaction zone and infinite reaction rate) and the ZND theory (finite reaction rate). The final state only depends on the explosive

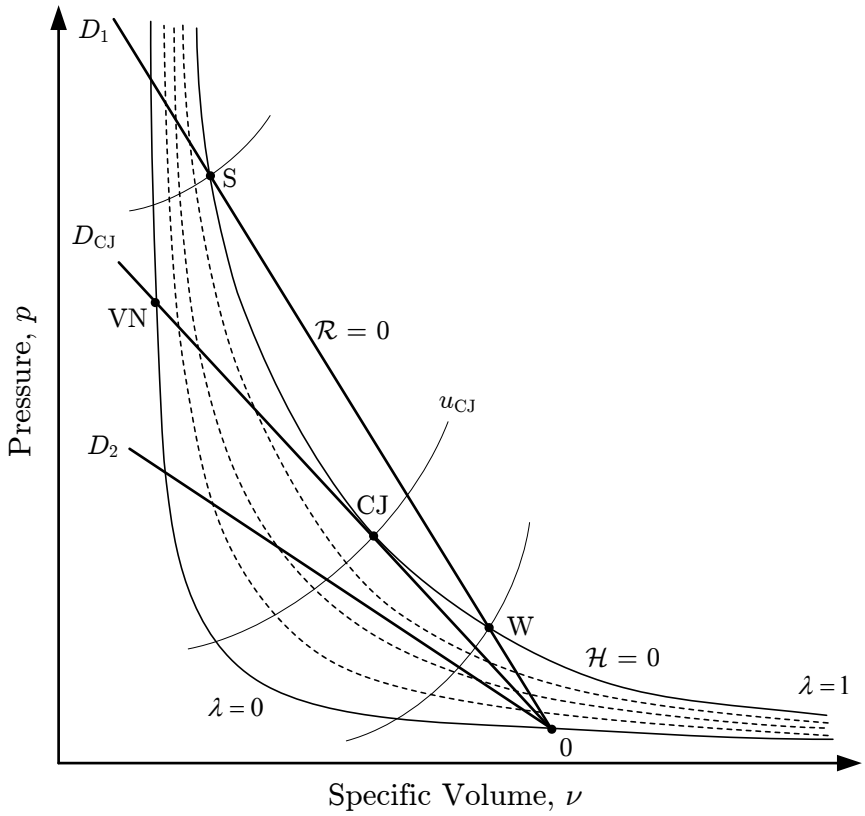

Figure 2.7: Detonation Hugoniot curves illustrated in the $p - \nu$ plane. Figure adapted from Fickett and Davis [64].

products composition and equation of state, and consists of detonation products that are in thermochemical equilibrium.

Cheetah is a thermochemical equilibrium code designed to analyze energetic materials (see Fried et al. [68]). It employs predefined gas species libraries and balances chemical potentials using Gibb's free-energy minimization. Cheetah version 2.0 was produced in 1999 at the University of California, Lawrence Livermore National Laboratory. Cheetah was used in this work for various purposes, including determining the equilibrium CJ state for detonation, thermodynamic properties of the detonation products, and the detonation velocity. Furthermore, Cheetah was used to compute the adiabatic expansion of detonation products with equation-of-state parameter fitting. Finally, Cheetah was used to determine the heat of detonation of the explosive decomposition.

Some liquid explosives in particular, namely nitroglycerin, dinitroglycerin, tetranitromethane and 87/13 nitromethane/benzene, have apparently one-dimensional detonation

fronts (Dremin et al. [54]). In reality, the homogeneous detonation structure is three-dimensional. Instabilities in the shock front result in a regular 3D cellular structure with transverse waves and natural hot spots (see Erpenbeck [60], Shchelkin [184], and Urtiew [205]). The present focus is on the primary detonation flow pressure and temperature interaction with particles, and therefore the disturbances induced by natural cellular instability will not be treated within the context of this thesis. Instead, significant disturbances and strong interactions are dominated by the detonation interaction with the particles.

2.3.2 Dilute heterogeneous detonation

Figure 2.8 schematically illustrates detonation in a heterogeneous mixture of reactive fluid and inert particles. The distance between particles is sufficient for dilute flow where the particles and particle flows are not interacting. The particle diameter is much greater than the shock thickness. For the conditions depicted in Figure 2.8, the detonation reaction-zone length (L_R) is much larger than the particle diameter; however, the situation may be reversed for large particles or small reaction-zone lengths.

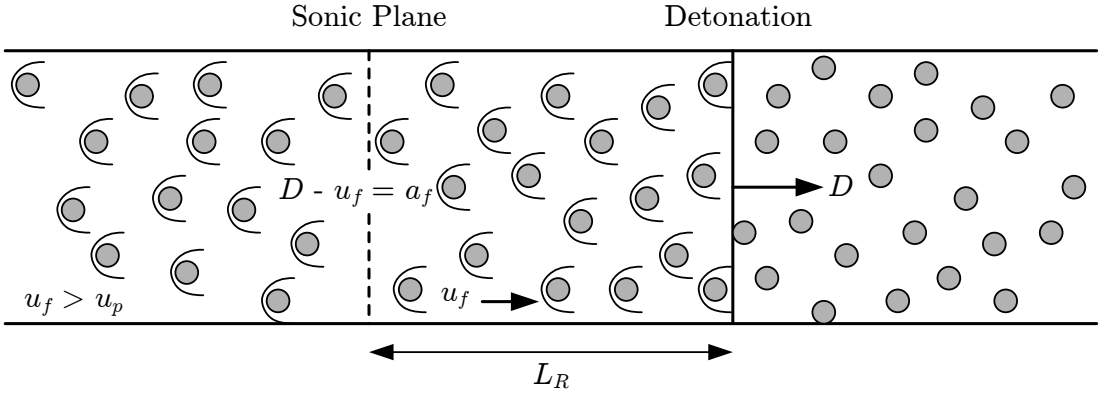

Figure 2.8: Heterogeneous detonation with dilute conditions ($\phi_p \approx 0.05$). Figure adapted from Zhang et al. [231].

In detonation in dense heterogeneous flow, the shock impedance of each material ($Z = \rho D$) become comparable in magnitude, and therefore, the detonation shock transmits a strong shock into the particle. The jump condition across this transmitted shock provides a large velocity and temperature discontinuity that in turn provides the initial acceleration and heating. Depending on the impedance ratio between the explosive and particles, there is usually a wave speed mismatch between the shock in the fluid passing over the particle

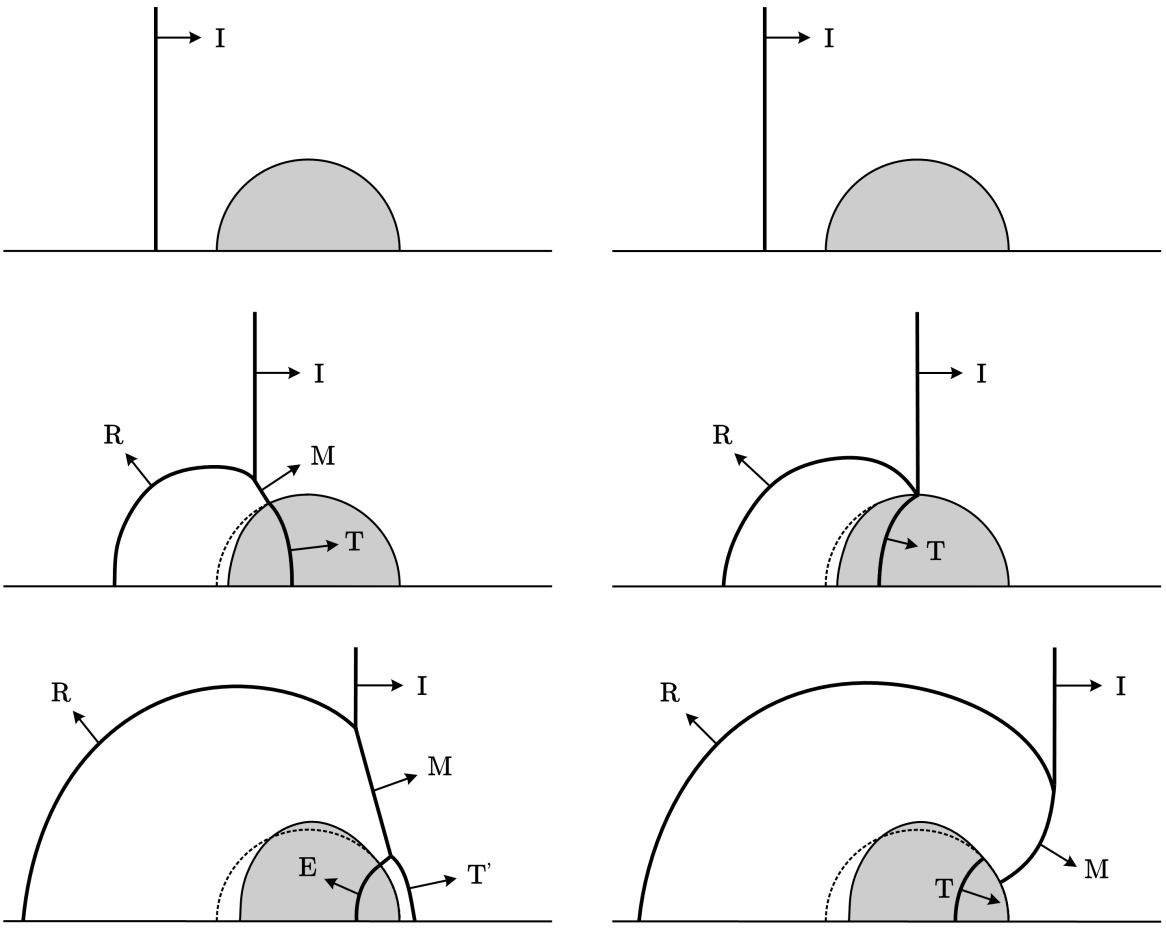

Figure 2.9: Condensed shock interaction with a solid metal particle: (left) high impedance ratio; and, (right) low impedance ratio. Nomenclature: I, incident shock; R, reflected shock; M, Mach shock; T, transmitted shock; T', re-transmitted shock; and E, head of expansion wave. Dashed line denotes undeformed particle shape.

surface and the shock traveling within the particle. For shock impedance ratios differing from unity, the shock reflects and diffracts from the curved particle surface, inhibiting the shock propagation in the vicinity of the particle. The transmitted wave and the interaction with the surrounding waves provide a shock compression effect that is mainly responsible for the particle acceleration and heating, and occurs primarily within the timescale of the detonation shock crossing the particle diameter. The process for a single particle is illustrated schematically in Figure 2.9. When densely-packed particles are considered, multiple reflections further complicate the shock interactions.

2.3.3 Dense heterogeneous detonation

Figure 2.10 schematically illustrates heterogeneous detonation in a slurry of liquid explosive saturating dense-packed particles. The particles are compressed by the shock as the detonation crosses the particles. In Figure 2.10, the detonation reaction-zone length (L_R) is much larger than the particle diameter; however the situation may be reversed for large particles or small reaction-zone lengths. Behind the detonation shock and reaction zone in the explosive, there is mechanical and thermal relaxation due to viscous drag effects.

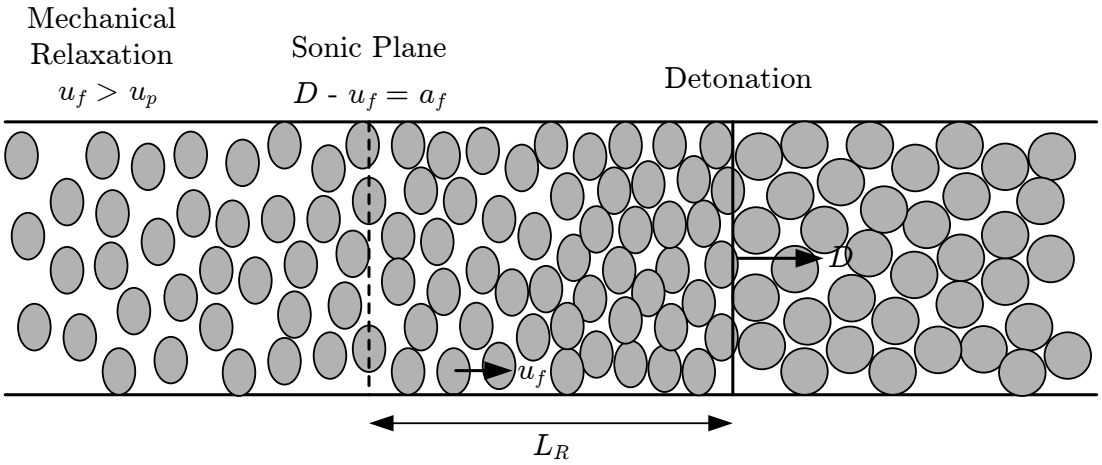

Figure 2.10: Heterogeneous detonation in dense conditions ($\phi_p \approx 0.5$).

The presence of multiple particles increases the complexity of the condensed shock interaction. Figure 2.11 illustrates the shock interaction process in the vicinity of a pair of particles. In both the dilute and dense heterogeneous detonation conditions, hot spots are formed at the particle leading edges due to the strong wave reflection. For dense packing in particular, hot spots are also formed during the shock wave collapse in the concave or convex regions between neighbouring particles [45]. For high-impedance metal particles, the shock interaction downstream of the particles forms hot spots in the void region between the particles. Alternatively, for low-impedance metal particles, the hot spots are formed directly behind the particles. Figure 2.11 also illustrates the transverse wave structure that is established with regularly sized and spaced particles. High pressure fluctuations are expected due to complex wave interactions, which are dependent on the size and spacing of the particles.

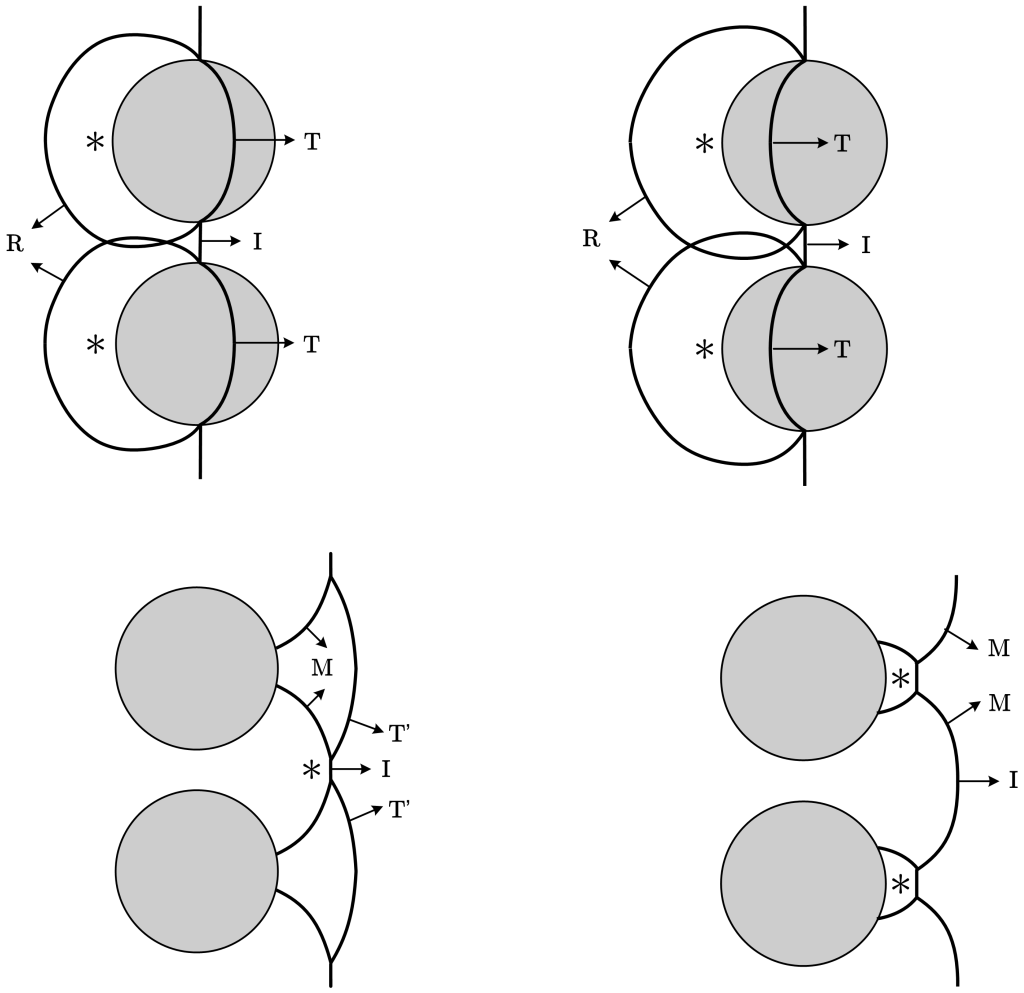

Figure 2.11: Shock interaction near particles in dense heterogeneous detonation: (left) high-impedance metal particle; and, (right) low-impedance particle. Nomenclature: I, incident shock; R, reflected shock; M, Mach shock; T, transmitted shock; and, T', re-transmitted shock. Particle deformation omitted in schematic. * denotes hot-spot location.

2.4 Detonation-to-dense flow transition

Figure 2.12 schematically illustrates the shock interaction process at the edge of the charge, where the detonation shock transmits into an air shock and forms a strong rarefaction wave that travels back into the charge. This relief wave accelerates the particles layer by layer beginning at the outermost layer. The interaction is the strongest at the free edge of the charge, which imparts the highest velocities in the outermost layer.

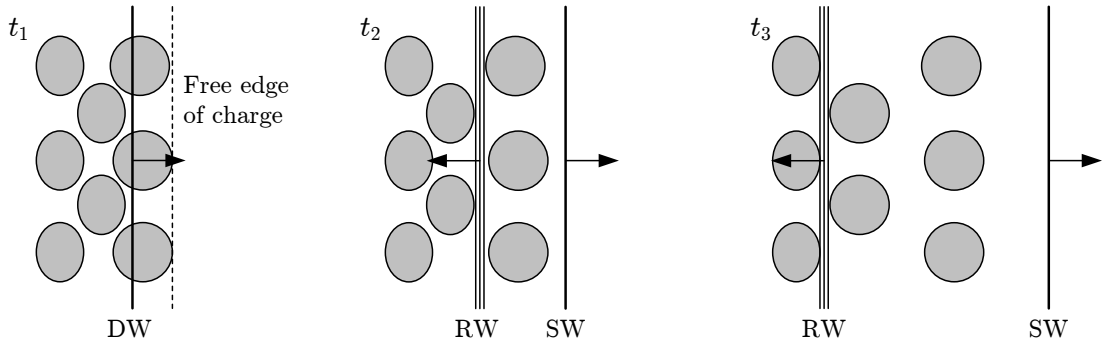

Figure 2.12: Schematic of edge expansion: (left) time t_1 prior to detonation shock reaching free-edge of the charge; (centre) time t_2 immediately after detonation shock exits the free edge of the charge and rarefaction wave travels back into the charge; and, (right) later time t_3. Figure nomenclature: DW = detonation wave; SW = shock wave in air; and, RW = head of rarefaction wave.

Figure 2.13 shows radiographs of the very early phases of a spherical explosion, from the experiments of Zhang et al. [226]. As discussed in Section 1.4, the dense-to-dilute transition occurs within a dispersal and expansion distance of one charge radius. Assuming a uniform distribution of particles within the expanding cloud, one charge radius of dispersal corresponds to a solid volume fraction change from 0.62 to 0.08. However, the dispersed volume of particles is not uniform, rather the particles are most significantly accelerated by the rarefaction wave travelling inwards beginning at the outer edge of the charge.

2.5 Regimes for detonation interaction with particles

The remainder of this chapter focuses on the acceleration and heating within the detonation regime. The main features of the detonation interaction regimes are discussed in terms of the characteristic length scales. The detonation interaction is considered during a shock interaction timescale, defined as the time required for the leading shock front to cross a

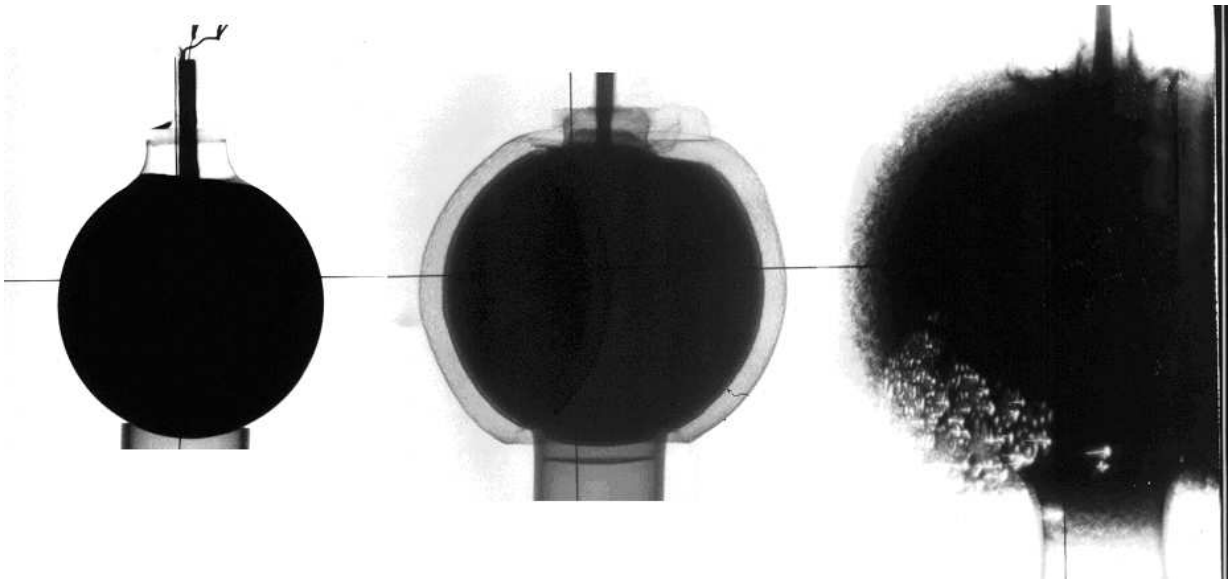

Figure 2.13: Radiographs of early particle dispersal from an 11.8 cm spherical charge: (left) $t = 0$ μs, $\phi_p = 0.62$; (centre) $t = 43$ μs, $\phi_p = 0.41$; and, (right) $t = 102$ μs, $\phi_p = 0.25$. Figure from Zhang et al. [226], used with permission from Defence R&D Canada – Suffield, courtesy of Dr. Fan Zhang.

particle: $\tau_S = d_p/D_0$. Three interaction classes can be identified according to the ratio of the characteristic particle size, d_p, to the detonation reaction-zone thickness, L_R, illustrated schematically in Figure 2.14.

2.5.1 Case 1: small particle limit ($d_p/L_R \ll 1$)

At the limit of $\delta = d_p/L_R \to 0$, the detonation front is considered inert (i.e., the von Neumann shock) during the early interaction, which can then be represented by a Heaviside step function. Within the shock interaction time, the detonation reaction-zone length is no longer a parameter and the response is represented by a single length scale of the particle diameter. For an inert planar shock crossing a particle, the dynamic response of the particle and the surrounding fluid at any given time can be scaled by the particle diameter using geometric similarity when employing inviscid governing equations and rate-independent material models (see Zhang et al. [229]). Thus, the computational results for a system of liquid explosive containing particles of a given size can be scaled to systems of the same liquid explosive with any diameter particles within the small particle limit. This means that only a single particle diameter needs to be computed in numerical experiments.

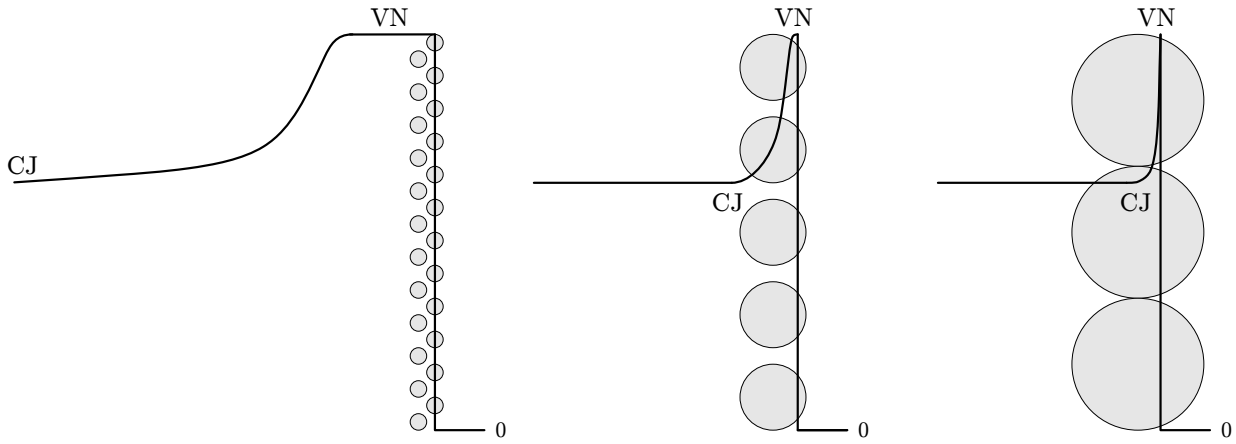

(a) $d_p/L_R \ll 1$ (b) $d_p/L_R \approx 1$ (c) $d_p/L_R \gg 1$

Figure 2.14: Schematic of a ZND-type detonation superimposed on particle matrices to illustrate the relative length scales.

Chemical equilibrium analyses, such as those performed in the Cheetah code (see Fried et al. [68]), assume the small particle limit where the particles are represented as individual molecules ($d_p \to 0$). In this limit, mechanical and thermal equilibrium are assumed throughout the inert shock and reacting expansion flow up to the CJ point.

2.5.2 Case 2: large particle limit ($d_p/L_R \gg 1$)

For $\delta = d_p/L_R \to \infty$, the reaction-zone length becomes negligibly small and the detonation wave can therefore be considered as a discontinuity of the Chapman-Jouguet (CJ) front, separating the fresh explosive from its detonation products. The interaction consists of diffraction of a thin CJ detonation front dictated by the curved boundary of the particle, followed by unsteady expanding products flow controlled by the rear boundary. The particle acceleration and heating are then characterized by the single length scale of the particle diameter, similar to the small particle limit ($d_p/L_R \ll 1$).

Detonation shock dynamics (DSD) (see Stewart and Bdzil [190], and Bdzil and Stewart [22]) has been applied to the large particle regime by assuming $L_R \to 0$. Frost et al. [70] used 2D cylinders to measure the detonation velocity deficit in a model slurry explosive by studying the propagation path length. Recently, Stewart and Bdzil [191] used 3D DSD simulations of packed matrices of spheres, representative of a heterogeneous explosive. These approaches do not consider the shock inside the particle, but qualitatively reproduce a detonation velocity deficit.

In the classical detonation theory for the CJ condition, the steady reaction zone following the shock wave is terminated at the sonic point. For two-phase flow, there are two characteristic sound speeds (i.e., one for the fluid and one for the particle), creating the potential for multiple points. For $\delta \gg 1$, the particle length exceeds the reaction-zone length. Transmitted shock waves traveling inside the particles can propagate past the CJ point in the explosive, if the solid sound speed exceeds the detonation speed, thereby extending the steady zone behind the detonation wave. For $\delta \gg 1$, the resulting steady zone is then proportional to the particle size. This was observed by Milne [144] for the case of close-packed aluminum particles in nitromethane, where the steady zone was shown to be up to $10d_p$ long.

2.5.3 Case 3: intermediate regime ($d_p/L_R \sim 1$)

The case of $d_p/L_R \sim 1$ lies between the above two limits and is therefore most complex due to two characteristic length scales. The detonation reaction-zone length is similar to the particle size and both length scales play a role in the acceleration and heating. In this regime, the particle interacts with both the VN shock and the expanding reacting flow in the detonation reaction zone that terminates at the CJ point. Locally, the reaction zone is affected by the particle presence, resulting in a decreased reaction-zone length at hot spots and an increased reaction-zone length in the expansion flow around the particle.

2.6 Transmission factors for shock and detonation

In order to describe the effect of the acceleration of solid particles in shock and detonation of a condensed explosive, a velocity transmission factor, α, is defined as the ratio of the particle mass-averaged velocity, u_p, after an interaction time, τ, over the shocked fluid velocity, u_{f1}:

$$\alpha = u_p(\tau)/u_{f1} \tag{2.19}$$

In general, the velocity transmission factor varies between 0 for perfect reflection at a rigid body to 1 for perfect transmission into a particle with the same material properties as the fluid. Similarly, a temperature transmission factor, β, is defined as the ratio of the particle mass-averaged temperature, T_p, after an interaction time, τ, over the shocked fluid temperature, T_{f1}:

$$\beta = T_p(\tau)/T_{f1} \tag{2.20}$$

where $0 \leq \beta \leq 1$. In both cases, the $f1$ state represents the post-shock fluid condition. The particle velocity and temperature are measured following the shock interaction time defined as follows.

In Equations (2.19) and (2.20), $\tau = \mathcal{O}(\tau_S)$ with $\tau_S = d_p/D_0$. The characteristic shock interaction time, τ_S, is used for a single particle in condensed matter. For a dense solid particle-fluid system, transmission factors are measured after $\tau = 2\tau_S$ such that the immediate effect of wave reflections both within particles and in the voids between neighbouring particles is included. This comprises the majority of the acceleration and heating due to primary shock transmission, while subsequent internal waves further influence the final velocity and temperature achieved during shock compression. This timeframe also accounts for the influence of transverse wave reflections and upstream/downstream particle reflections in a densely-packed matrix. The factors affecting particle acceleration and heating are examined in the next chapter to understand the velocity and temperature transmission factors defined in Equations (2.19) and (2.20).

Chapter 3

Factors affecting particle acceleration and heating

In this chapter, the factors affecting particle acceleration and heating are investigated using a formal dimensional analysis. Dimensional reasoning was suggested by Euler (1765), Fourier (1822), and Rayleigh (1877); their ideas have provided the foundation for scaling laws and similarly conditions (White [217]). Similarity principles have been used more recognizably, for instance, in wind tunnel scale models, where geometrically-similar bodies and flow streamlines can be obtained with different fluids, flow velocity or dimensions. According to Reynolds' principle of similarity, dynamic similarity occurs between systems displaying the same Reynolds and Mach numbers (Schlichting [181]). Dimensional analysis has been used by scientists and engineers to reduce the number of physical parameters describing a system by defining dimensionless parameter groups. For the same wind tunnel example, lift, drag, and pressure coefficients form the dimensionless groups. Similarly, heat transfer analysis is founded on the dimensionless groups of Prandtl, Grashoff and Eckert (White [216]). Heat transfer data are traditionally further correlated into the dimensionless Nusselt number (Incropera and DeWitt [98]).

In the field of explosives, dimensional analysis has been used in both detonation and air blast. Sedov (1946) [182], Taylor (1950) [200], and von Neumann (1963) [210] applied similarity solutions to estimate the explosive energy release from pressure measurements. Air-blast scaling was originally proposed by Hopkinson (1915) and Sachs (1944) [177] (as discussed by Baker [12], Baker et al. [13], and Kinney and Graham [110]). Later, Oppenheim et al. (1972) [152] included the CJ detonation in the blast wave scaling. Recently, Stewart (2004) [189] investigated the miniaturization of explosives using scaling

considerations.

Mesoscale numerical experiments are necessary to determine the physical models for acceleration and heating of particles in condensed explosive detonation. To reduce the number of parameters that need to be varied in the numerical experiments, dimensional analysis of the drag force and heat transfer rate is conducted. Further, non-dimensionalization of the equations of motion is employed here to determine the importance of the factors affecting particle acceleration and heating. The physical parameters are reviewed using a literature survey; the range and significance of the resulting parameter groups are analyzed in this section.

3.1 Dimensional analysis using the Pi Theorem

The Buckingham Pi Theorem [31] is one method of determining a minimum set of dimensionless groups. The pi theorem makes use of Fourier's principle of dimensional homogeneity, which states "all the terms of a physical equation must have the same dimensions, or that every correct physical equation is dimensionally homogeneous" [66]. Therefore, physical laws are independent of the form of the units, and acceptable laws are homogeneous in all dimensions [31]. For a problem containing i physical variables defined by j primary dimensions, the equation relating all the variables will have $k = i - j$ dimensionless groups. Application of the pi theorem is described in general fluids textbooks (e.g., Schlichting [181] and White [216]).

Table 3.1 summarizes the physical variables and dimensions relevant to heterogeneous detonation, where M is the mass, L is the length, T is the time, and θ is the temperature. In the subsequent sections, the pi theorem is applied to physical laws for drag force and heat transfer rate to a particle in dense fluid-solid flow.

3.1.1 Drag force

Considering detonation of a liquid explosive containing dense solid particles, the drag force acting on a particle (F_d) is assumed to be a function of the relevant dimensional parameters:

$$F_d = f(d_p, D_0, \rho_{f0}, \rho_{s0}, \phi_{s0}, p_0, \mu_{f0}, L_R) \tag{3.1}$$

where d_p is the particle diameter, D_0 is the detonation velocity, ρ_{f0} is the initial fluid density, ρ_{s0} is the particle material density, ϕ_{s0} is the solid volume fraction, p_0 is the

Table 3.1: Physical variables and dimensions used in dimensional analysis.

Symbol	SI Units	Physical Dimensions	Description of Quantity
F_d	N	MLT^{-2}	Drag force
Q_c	W	ML^2T^{-3}	Heat transfer rate
d_p	m	L	Particle diameter
D_0	m/s	LT^{-1}	Detonation velocity
ρ_{f0}	kg/m^3	ML^{-3}	Fluid density
ρ_{s0}	kg/m^3	ML^{-3}	Solid density
ϕ_{s0}	-	-	Solid volume fraction
μ_{f0}	N-s/m^2	$ML^{-1}T^{-1}$	Fluid viscosity
k_{f0}	W/m-K	$MLT^{-3}\theta^{-1}$	Fluid thermal conductivity
c_p	J/kg-K	$L^2T^{-2}\theta^{-1}$	Fluid heat capacity
p_0	N/m^2	$ML^{-1}T^{-2}$	Reference pressure
T_0	K	θ	Reference temperature
L_R	m	L	Detonation reaction-zone length

ambient pressure, μ_{f0} is the molecular viscosity of the fluid, and L_R is the detonation reaction-zone length.

The proposed function in Equation (3.1) has nine variables, therefore $i = 9$. The definition and dimensions for each variable are given in Table 3.1. The number of primary dimensions contained in the variables is three (i.e., M, L, T) so that $j \leq 3$. There are at least three variables that cannot be combined into a dimensionless Π group (e.g., d_p, D_0, and ρ_{f0}); therefore, $j = 3$. The pi theorem requires that there will be exactly $k = i - j = 6$ dimensionless groups. One of these is ϕ_{s0} which is already dimensionless:

$$\Pi_6 = \phi_{s0} \tag{3.2}$$

Assuming d_p, D_0, and ρ_{f0} are independent variables among the nine parameters in the force expression (Equation 3.1), they are chosen for the repeating variables in the Π groups, which are determined as follows:

$$\Pi_1 = F_d \rho_{f0}^a D_0^b d_p^c = (MLT^{-2})(ML^{-3})^a (LT^{-1})^b (L)^c = M^0 L^0 T^0 \tag{3.3}$$

$$a = -1, b = -2, c = -2 \tag{3.4}$$

$$\Pi_1 = \frac{F_d}{\rho_{f0} D_0^2 d_p^2} = C_d \tag{3.5}$$

$$\Pi_2 = \mu_{f0}^{-1} \rho_{f0}^a D_0^b d_p^c = (ML^{-1}T^{-1})^{-1}(ML^{-3})^a(LT^{-1})^b(L)^c = M^0L^0T^0 \tag{3.6}$$

$$a = 1, b = 1, c = 1 \tag{3.7}$$

$$\Pi_2 = \frac{\rho_{f0} D_0 d_p}{\mu_{f0}} = Re \tag{3.8}$$

$$\Pi_3 = p_0^{-1} \rho_{f0}^a D_0^b d_p^c = (ML^{-1}T^{-2})^{-1}(ML^{-3})^a(LT^{-1})^b(L)^c = M^0L^0T^0 \tag{3.9}$$

$$a = 1, b = 2, c = 0 \tag{3.10}$$

Assuming $a_0^2 = \gamma p_0/\rho_{f0}$, where a_0 is the sound speed and $\gamma = c_p/c_v$ is the ratio of specific heats, then

$$\Pi_3 = \frac{\rho_{f0} D_0^2}{p_0} = \frac{\gamma D_0^2}{a_0^2} = \gamma M_0^2 \tag{3.11}$$

$$\Pi_4 = \rho_{s0}^{-1} \rho_{f0}^a D_0^b d_p^c = (ML^{-3})^{-1}(ML^{-3})^a(LT^{-1})^b(L)^c = M^0L^0T^0 \tag{3.12}$$

$$a = 1, b = 0, c = 0 \tag{3.13}$$

$$\Pi_4 = \frac{\rho_{f0}}{\rho_{s0}} \tag{3.14}$$

$$\Pi_5 = L_R^{-1} \rho_{f0}^a D_0^b d_p^c = (L)^{-1}(ML^{-3})^a(LT^{-1})^b(L)^c = M^0L^0T^0 \tag{3.15}$$

$$a = 0, b = 0, c = 1 \tag{3.16}$$

$$\Pi_5 = \frac{d_p}{L_R} = \delta \tag{3.17}$$

The final equation relating all the parameters describing F_d is of the form $\Pi_1 = f(\Pi_2, \Pi_3, \Pi_4, \Pi_5, \Pi_6)$:

$$C_d = f\left(Re, M_0, \frac{\rho_{f0}}{\rho_{s0}}, \frac{d_p}{L_R}, \phi_{s0}\right) \tag{3.18}$$

Therefore, the drag force for particles in a detonation flow can be entirely described by an "effective" drag coefficient, C_d, where Re is the Reynolds number and M_0 is the Mach number of the detonation shock. Note that the flow compressibility is represented by the shock Mach number, instead of the flow Mach number commonly used. Equation (3.18) also includes the density ratio of explosive to solid particles, ρ_{f0}/ρ_{s0}, the ratio of particle diameter to detonation reaction-zone length, d_p/L_R, and the solid volume fraction, ϕ_{s0}.

3.1.2 Heat transfer rate

The heat transfer rate to a particle (Q_c) during detonation in a solid particles-explosive system is assumed to be:

$$Q_c = f(d_p, D_0, \rho_{f0}, \rho_{s0}, \phi_{s0}, T_0, \mu_{f0}, k_{f0}, c_p, L_R) \tag{3.19}$$

where T_0 is the ambient temperature, k_{f0} is the thermal conductivity of the explosive, and c_p is the explosive fluid heat capacity. This function has eleven variables ($i = 11$); the definitions and dimensions for each variable are given in Table 3.1. The number of primary dimensions contained in the variables is four (i.e., M, L, T, θ) so that $j \leq 4$. There are at least four variables that cannot be combined into a dimensionless Π group (e.g., d_p, D_0, ρ_{f0}, and T_0); therefore, $j = 4$. The pi theorem requires that there will be exactly $k = i - j = 7$ dimensionless groups. One of these is ϕ_{s0} which is already dimensionless:

$$\Pi_7 = \phi_{s0} \tag{3.20}$$

Using the four independent variables that do not form a dimensionless group (d_p, D_0, ρ_{f0} and T_0) for the repeating variables in the Π groups, the dimensionless groups are found as follows:

$$\Pi_1 = \mu_{f0}^{-1}\rho_{f0}^a D_0^b d_p^c T_0^d = (ML^{-1}T^{-1})^{-1}(ML^{-3})^a(LT^{-1})^b(L)^c(\theta)^d = M^0L^0T^0\theta^0 \tag{3.21}$$

$$a = 1, b = 1, c = 1, d = 0 \tag{3.22}$$

$$\Pi_1 = \frac{\rho_{f0} D_0 d_p}{\mu_{f0}} = Re \tag{3.23}$$

$$\Pi_2 = c_p^{-1}\rho_{f0}^a D_0^b d_p^c T_0^d = (L^2T^{-2}\theta^{-1})^{-1}(ML^{-3})^a(LT^{-1})^b(L)^c(\theta)^d = M^0L^0T^0\theta^0 \tag{3.24}$$

$$a = 0, b = 2, c = 0, d = -1 \tag{3.25}$$

Noting that for an ideal gas $c_p = \gamma R/(\gamma - 1)$ and $a_0^2 = \gamma R T_0$, where R is the gas constant, then

$$\Pi_2 = \frac{D_0^2}{c_p T_0} = \frac{D_0^2(\gamma - 1)}{\gamma R T_0} = M_0^2\,(\gamma - 1) \tag{3.26}$$

$$\Pi_3 = k_{f0}^{-1}\rho_{f0}^a D_0^b d_p^c T_0^d = (MLT^{-3}\theta^{-1})^{-1}(ML^{-3})^a(LT^{-1})^b(L)^c(\theta)^d = M^0L^0T^0\theta^0 \tag{3.27}$$

$$a = 1, b = 3, c = 1, d = -1 \tag{3.28}$$

$$\begin{aligned}
\Pi_3 &= \frac{\rho_{f0} D_0^3 d_p}{k_{f0} T_0} \\
&= \frac{\rho_{f0}\gamma R D_0^3 d_p}{k_{f0} a_{f0}^2} \\
&= \frac{\rho_{f0} c_p M_0^2(\gamma - 1) D_0 d_p}{k_{f0}} \\
&= \frac{Pr\,\rho_{f0} D_0 d_p M_0^2(\gamma - 1)}{\mu_{f0}} \\
&= Pr\,Re\,M_0^2(\gamma - 1) \\
&= Pr\,\Pi_1\Pi_2
\end{aligned} \tag{3.29}$$

where the Prandtl number, $Pr = \mu_{f0} c_p / k_{f0}$, has been introduced.

$$\Pi_4 = Q_c \rho_{f0}^a D_0^b d_p^c T_0^d = (ML^2T^{-3})(ML^{-3})^a (LT^{-1})^b (L)^c (\theta)^d = M^0 L^0 T^0 \theta^0 \tag{3.30}$$

$$a = -1, b = -3, c = -2, d = 0 \tag{3.31}$$

$$\begin{aligned} \Pi_4 &= \frac{Q_c}{\rho_{f0} D_0^3 d_p^2} \\ &= \frac{Q_c}{\mu_{f0} Re D_0^2 d_p} \\ &= \frac{Q_c c_p}{k_{f0} Pr Re D_0^2 d_p} \\ &= \frac{Q_c}{k_{f0} Pr Re M_0^2 T_0 (\gamma - 1) d_p} \\ &= \frac{Nu}{Pr Re M_0^2 (\gamma - 1)} \\ &= \frac{Nu}{\Pi_3} \end{aligned} \tag{3.32}$$

where the Nusselt number, $Nu = Q_c / k_{f0} T_0 d_p$, has been introduced.

$$\Pi_5 = \rho_{s0}^{-1} \rho_{f0}^a D_0^b d_p^c T_0^d = (ML^{-3})^{-1} (ML^{-3})^a (LT^{-1})^b (L)^c (\theta)^d = M^0 L^0 T^0 \theta^0 \tag{3.33}$$

$$a = 1, b = 0, c = 0, d = 0 \tag{3.34}$$

$$\Pi_5 = \frac{\rho_{f0}}{\rho_{s0}} \tag{3.35}$$

$$\Pi_6 = L_R^{-1} \rho_{f0}^a D_0^b d_p^c T_0^d = (L)^{-1} (ML^{-3})^a (LT^{-1})^b (L)^c (\theta)^d = M^0 L^0 T^0 \theta^0 \tag{3.36}$$

$$a = 0, b = 0, c = 1, d = 0 \tag{3.37}$$

$$\Pi_6 = \frac{d_p}{L_R} = \delta \tag{3.38}$$

The final equation relating all the parameters describing Q_c is of the form $\Pi_1 = f(\Pi_2, \Pi_3, \Pi_4, \Pi_5, \Pi_6, \Pi_7)$. Rearranging the Π terms shows that the heat transfer rate can be entirely described by an "effective" Nusselt number, Nu:

$$Nu = f\left(Re, M_0, Pr, \frac{\rho_{f0}}{\rho_{s0}}, \frac{d_p}{L_R}, \phi_{s0}\right) \tag{3.39}$$

The resulting dimensionless groups for Re, Pr, M_0 are standard parameter groups in fluid mechanics. The additional groups for ϕ_{s0}, ρ_{f0}/ρ_{s0} and d_p/L_R represent physical properties of the slurry explosive mixture. For dilute particles-gas flow ($\phi_{s0} \ll 1; \rho_{f0}/\rho_{s0} \ll 1$), with a small particle limiting scale ($d_p/L_R \ll 1$), the drag coefficient function (Equation 3.18) and Nusselt number function (Equation 3.39) approach the well established classic forms of $C_d = f(Re, M_0)$ and $Nu = f(Re, Pr, M_0)$.

In general, the dimensionless groups obtained using the pi theorem are not unique and their physical meaning depends on the choice of dimensionless parameters. Furthermore, the pi theorem does not indicate the relative importance of each parameter.

3.2 Non-dimensionalization of the governing equations

The dimensionless parameters are further investigated using non-dimensionalization of the flow equations. The basic equations that govern the flow are considered first. The conservation equations for a compressible material in the Eulerian frame are given in tensor notation as follows:

Conservation of mass:

$$\frac{\partial \rho}{\partial t} + \frac{\partial \rho u_i}{\partial x_i} = J \tag{3.40}$$

Conservation of momentum:

$$\rho \frac{\partial u_i}{\partial t} + \rho u_j \frac{\partial u_i}{\partial x_j} - \frac{\partial \tau_{ij}}{\partial x_j} = B_i \tag{3.41}$$

Conservation of energy:

$$\rho\frac{\partial E}{\partial t} + \rho u_j \frac{\partial E}{\partial x_j} - \tau_{ij}\frac{\partial u_i}{\partial x_j} - \frac{\partial q_i}{\partial x_i} = Q \tag{3.42}$$

where ρ is the density, u_i is the velocity vector, E is the total specific energy, τ_{ij} is the stress tensor, q_i is the conductive heat transfer vector, x_i is the Cartesian coordinate vector, and t is the time. The right-hand side of the governing equations contains volumetric source terms, where J is a mass source, B_i is a body force vector, and Q represents energy sources.

In the continuum theory for granular flows, the solid *flow* mass concentration and pressure, σ_p and p_p, respectively, are assumed to be equal to the solid *material* density and pressure, ρ_s and p_s, respectively, times the solid volume fraction, ϕ_s (Baer and Nunziato [10] and Powers et al. [160]):

$$\sigma_p = \rho_s \phi_s \tag{3.43}$$

$$p_p = p_s \phi_s \tag{3.44}$$

Similarly, the fluid volume fraction is used to define the mass concentration for the fluid phase:

$$\sigma_f = \rho_f \phi_f \tag{3.45}$$

where the saturation constraint (i.e., conservation of volume) is: $\phi_s + \phi_f = 1$.

Non-dimensionalization of the governing equations can also be used to obtain the dimensionless parameter groups controlling the flow in addition to indicating the importance of each parameter. Without losing generality, 2D conservations equations are examined in the non-dimensional analysis. Each physical variable (both dependent and independent) needs to be made dimensionless by dividing them by constant reference properties, and then substituting into the governing equations (Equations 3.40 – 3.42). Reference length and time scales are chosen that are appropriate to the relevant problem physics. The characteristic length dimension is the particle diameter, d_p, and the characteristic velocity is the detonation velocity, D_0. Dimensionless variables are denoted by an asterisk, which are defined as follows:

$$
\begin{aligned}
x^* &= \frac{x}{d_p} & y^* &= \frac{y}{d_p} & u^* &= \frac{u}{D_0} & v^* &= \frac{v}{D_0} \\
t^* &= \frac{tD_0}{d_p} & \rho_f^* &= \frac{\rho_f}{\rho_{f0}} & \rho_s^* &= \frac{\rho_s}{\rho_{s0}} & p_f^* &= \frac{p_f}{p_0} \\
\phi_s^* &= \frac{\phi_s}{\phi_{s0}}
\end{aligned}
\tag{3.46}
$$

3.2.1 Conservation of mass

The 2D mass conservation equations for two-phase fluid-solid flow, where J_p is the mass transfer from the solid to the fluid, are:

$$
\frac{\partial \sigma_f}{\partial t} + \frac{\partial \sigma_f u_f}{\partial x} + \frac{\partial \sigma_f v_f}{\partial y} = -J_p \tag{3.47}
$$

$$
\frac{\partial \sigma_p}{\partial t} + \frac{\partial \sigma_p u_p}{\partial x} + \frac{\partial \sigma_p v_p}{\partial y} = J_p \tag{3.48}
$$

Summing Equations (3.47) and (3.48) gives the phase-conservative continuity equation, in which the mass transfer source term has been eliminated:

$$
\frac{\partial \left[\phi_f \rho_f + \phi_s \rho_s\right]}{\partial t} + \frac{\partial \left[\phi_f \rho_f u_f + \phi_s \rho_s u_s\right]}{\partial x} + \frac{\partial \left[\phi_f \rho_f v_f + \phi_s \rho_s v_s\right]}{\partial y} = 0 \tag{3.49}
$$

Substituting the saturation constraint, $\phi_f = 1 - \phi_s$, gives:

$$
\frac{\partial \left[(1-\phi_s) \rho_f + \phi_s \rho_s\right]}{\partial t} + \frac{\partial \left[(1-\phi_s) \rho_f u_f + \phi_s \rho_s u_s\right]}{\partial x} + \frac{\partial \left[(1-\phi_s) \rho_f v_f + \phi_s \rho_s v_s\right]}{\partial y} = 0 \tag{3.50}
$$

Substituting the dimensionless groups from Equation (3.46) gives:

$$
\begin{aligned}
\frac{\rho_{f0} D_0}{d_p} \frac{\partial \rho_f^*}{\partial t^*} \quad &- \quad \frac{\rho_{f0} \phi_{s0} D_0}{d_p} \frac{\partial \rho_f^* \phi_s^*}{\partial t^*} + \frac{\rho_{s0} \phi_{s0} D_0}{d_p} \frac{\partial \rho_s^* \phi_s^*}{\partial t^*} \\
&+ \quad \frac{\rho_{f0} D_0}{d_p} \frac{\partial \rho_f^* u_f^*}{\partial x^*} - \frac{\rho_{f0} \phi_{s0} D_0}{d_p} \frac{\partial \rho_f^* \phi_s^* u_f^*}{\partial x^*} + \frac{\rho_{s0} \phi_{s0} D_0}{d_p} \frac{\partial \rho_s^* \phi_s^* u_s^*}{\partial x^*} \\
&+ \quad \frac{\rho_{f0} D_0}{d_p} \frac{\partial \rho_f^* v_f^*}{\partial y^*} - \frac{\rho_{f0} \phi_{s0} D_0}{d_p} \frac{\partial \rho_f^* \phi_s^* v_f^*}{\partial y^*} + \frac{\rho_{s0} \phi_{s0} D_0}{d_p} \frac{\partial \rho_s^* \phi_s^* v_s^*}{\partial y^*} = 0
\end{aligned}
\tag{3.51}
$$

Dividing by $\rho_{f0}D_0/d_p$, the following non-dimensional equation is obtained:

$$\frac{\partial \rho_f^*}{\partial t^*} + \frac{\partial \rho_f^* u_f^*}{\partial x^*} + \frac{\partial \rho_f^* v_f^*}{\partial y^*} - \underbrace{\phi_{s0}}_{\text{I}} \left(\frac{\partial \rho_f^* \phi_s^*}{\partial t^*} + \frac{\partial \rho_f^* \phi_s^* u_f^*}{\partial x^*} + \frac{\partial \rho_f^* \phi_s^* v_f^*}{\partial y^*} \right) + \phi_{s0} \underbrace{\frac{\rho_{s0}}{\rho_{f0}}}_{\text{II}} \left(\frac{\partial \rho_s^* \phi_s^*}{\partial t^*} + \frac{\partial \rho_s^* \phi_s^* u_s^*}{\partial x^*} + \frac{\partial \rho_s^* \phi_s^* v_s^*}{\partial y^*} \right) = 0 \quad (3.52)$$

Terms I and II represent the dimensionless groups ϕ_{s0} and ρ_{s0}/ρ_{f0}, respectively. Note that Term II is the inverse of Π_4 in Equation (3.14) for the ratio of explosive to solid particles.

3.2.2 Conservation of momentum

The conservation of linear momentum equations for two-dimensional flow are as follows:

x-direction:

$$\frac{\partial \sigma_f u_f}{\partial t} + \frac{\partial (\sigma_f u_f^2 + p_f \phi_f)}{\partial x} + \frac{\partial \sigma_f u_f v_f}{\partial y} + \frac{\partial}{\partial x}\left[-\frac{4}{3}\mu_f \frac{\partial u_f}{\partial x} + \frac{2}{3}\mu_f \frac{\partial v_f}{\partial y} \right] + \frac{\partial}{\partial y}\left[\mu_f \left(\frac{\partial u_f}{\partial y} + \frac{\partial v_f}{\partial x} \right) \right] = -J_p u_p - F_{px} \quad (3.53a)$$

y-direction:

$$\frac{\partial \sigma_f v_f}{\partial t} + \frac{\partial \sigma_f u_f v_f}{\partial x} + \frac{\partial (\sigma_f v_f^2 + p_f \phi_f)}{\partial y} + \frac{\partial}{\partial x}\left[\mu_f \left(\frac{\partial v_f}{\partial x} + \frac{\partial u_f}{\partial y} \right) \right] + \frac{\partial}{\partial y}\left[-\frac{4}{3}\mu_f \frac{\partial v_f}{\partial y} + \frac{2}{3}\mu_f \frac{\partial u_f}{\partial x} \right] = -J_p v_p - F_{py} \quad (3.53b)$$

where F_{px} and F_{py} are the phase interaction force components in the x- and y-directions, respectively. For non-dimensionalization of the two-dimensional flow equations, the conservation of linear momentum is analyzed in the x-direction for the fluid phase. Analysis of the y-direction momentum equation follows a similar procedure and yields the same dimensionless groups, hence the y-direction has been omitted in the remainder of this section.

Applying the the saturation constraint to Equation (3.53a) gives:

$$\frac{\partial \rho_f(1-\phi_s)u_f}{\partial t} + \frac{\partial \rho_f(1-\phi_s)u_f^2}{\partial x} + \frac{\partial p_f(1-\phi_s)}{\partial x} + \frac{\partial \rho_f(1-\phi_s)u_f v_f}{\partial y} + \frac{\partial}{\partial x}\left[\frac{2}{3}\mu_f\frac{\partial v_f}{\partial y} - \frac{4}{3}\mu_f\frac{\partial u_f}{\partial x}\right] + \frac{\partial}{\partial y}\left[\mu_f\left(\frac{\partial u_f}{\partial y} + \frac{\partial v_f}{\partial x}\right)\right] = F_{px} \quad (3.54)$$

Additional dimensionless groups in addition to Equation (3.46) are:

$$\mu_f^* = \frac{\mu_f}{\mu_{f0}} \qquad F_{px}^* = \frac{F_{px}d_p^3}{F_0} \qquad F_{py}^* = \frac{F_{py}d_p^3}{F_0} \quad (3.55)$$

where μ_{f0} is a reference viscosity and F_0 is a reference force in Newtons. Note that F_{px} and F_{py} are volumetric forces with units of $\mathrm{N/m^3}$.

Substituting the dimensionless groups from Equations (3.46) and (3.55) gives:

$$\begin{aligned}&\frac{\rho_{f0}D_0^2}{d_p}\frac{\partial \rho_f^* u_f^*}{\partial t^*} + \frac{\rho_{f0}D_0^2}{d_p}\frac{\partial \rho_f^* {u_f^*}^2}{\partial x^*} + \frac{p_0}{d_p}\frac{\partial p_f^*}{\partial x^*} + \frac{\rho_{f0}D_0^2}{d_p}\frac{\partial \rho_f^* u_f^* v_f^*}{\partial y^*} \\ &- \frac{\rho_{f0}\phi_{s0}D_0^2}{d_p}\frac{\partial \rho_f^*\phi_s^* u_f^*}{\partial t^*} - \frac{\rho_{f0}\phi_{s0}D_0^2}{d_p}\frac{\partial \rho_f^*\phi_s^* {u_f^*}^2}{\partial x^*} - \frac{p_0\phi_{s0}}{d_p}\frac{\partial p_f^*\phi_s^*}{\partial x^*} - \frac{\rho_{f0}\phi_{s0}D_0^2}{d_p}\frac{\partial \rho_f^*\phi_s^* u_f^* v_f^*}{\partial y^*} \\ &+ \frac{\mu_{f0}D_0}{d_p^2}\frac{\partial}{\partial x^*}\left[\frac{2}{3}\mu^*\frac{\partial v_f^*}{\partial y^*} - \frac{4}{3}\mu^*\frac{\partial u_f^*}{\partial x^*}\right] + \frac{\mu_{f0}D_0}{d_p^2}\frac{\partial}{\partial y^*}\left[\mu^*\left(\frac{\partial u_f^*}{\partial y^*} + \frac{\partial v_f^*}{\partial x^*}\right)\right] = \frac{F_0}{d_p^3}F_{px}^* \quad (3.56)\end{aligned}$$

Dividing by $\rho_{f0}D_0^2/d_p$, the following is obtained:

$$\begin{aligned}&\frac{\partial \rho_f^* u_f^*}{\partial t^*} + \frac{\partial \rho_f^* {u_f^*}^2}{\partial x^*} + \frac{\partial \rho_f^* u_f^* v_f^*}{\partial y^*} + \underbrace{\frac{p_0}{\rho_{f0}D_0^2}}_{\mathrm{I}}\frac{\partial p_f^*}{\partial x^*} \\ &- \underbrace{\phi_{s0}}_{\mathrm{II}}\left\{\frac{\partial \rho_f^*\phi_s^* u_f^*}{\partial t^*} + \frac{\partial \rho_f^*\phi_s^* {u_f^*}^2}{\partial x^*} + \frac{\partial \rho_f^*\phi_s^* u_f^* v_f^*}{\partial y^*}\right\} - \underbrace{\phi_{s0}\frac{p_0}{\rho_{f0}D_0^2}}_{\mathrm{III}}\frac{\partial p_f^*\phi_s^*}{\partial x^*} \\ &+ \underbrace{\frac{\mu_{f0}}{d_p\rho_{f0}D_0}}_{\mathrm{IV}}\left\{\frac{\partial}{\partial x^*}\left[\frac{2}{3}\mu^*\frac{\partial v_f^*}{\partial y^*} - \frac{4}{3}\mu^*\frac{\partial u_f^*}{\partial x^*}\right] + \frac{\partial}{\partial y^*}\left[\mu^*\left(\frac{\partial u_f^*}{\partial y^*} + \frac{\partial v_f^*}{\partial x^*}\right)\right]\right\} \\ &= \underbrace{\frac{F_0}{\rho_{f0}d_p^2D_0^2}}_{\mathrm{V}}F_{px}^* \quad (3.57)\end{aligned}$$

The dimensionless groups in the momentum conservation equation are summarized as follows:

Term I can be simplified using the ideal gas law:

$$\frac{p_0}{\rho_{f0} D_0^2} = \frac{a_0^2}{\gamma D_0^2} = \frac{1}{\gamma M_0^2} \tag{3.58}$$

Term II is the solid volume fraction, ϕ_{s0}. Term III is the product of Terms I and II.

Term IV is the inverse Reynolds number:

$$\frac{\mu_{f0}}{d_p \rho_{f0} D_0} = \frac{1}{Re} \tag{3.59}$$

Term V is the definition of drag coefficient:

$$\frac{F_0}{\rho_{f0} d_p^2 D_0^2} = C_d \tag{3.60}$$

3.2.3 Conservation of energy

The momentum conservation equation confirmed four of the dimensionless groups: C_d, ϕ_{s0}, Re, and M_0. The energy equation for viscous chemically-reacting flow is analyzed to determine the remaining dimensionless groups. The two-dimensional energy equation is:

$$\begin{aligned} \frac{\partial \rho_f \phi_f E_f}{\partial t} + \frac{\partial \rho_f \phi_f u_f E_f}{\partial x} + \frac{\partial \phi_f p_f u_f}{\partial x} + \frac{\partial}{\partial x}\left(u_f \tau'_{xx} + v_f \tau_{xy} + q_x\right) \\ + \frac{\partial \phi_f p_f v_f}{\partial y} + \frac{\partial}{\partial y}\left(u_f \tau_{yx} + v_f \tau'_{yy} + q_y\right) \\ = F_{px} u_p + F_{py} v_p + Q_p + Q_r \end{aligned} \tag{3.61}$$

The stress tensor components, which have been used to keep the equations more compact, are defined as follows (prime denotes hydrostatic pressure removed from normal stress component):

$$\tau'_{xx} = \frac{4}{3}\mu \frac{\partial u}{\partial x} - \frac{2}{3}\mu \frac{\partial v}{\partial y} \tag{3.62a}$$

$$\tau_{xy} = \mu\left(\frac{\partial u}{\partial y} + \frac{\partial v}{\partial x}\right) \tag{3.62b}$$

$$\tau_{yx} = \mu\left(\frac{\partial v}{\partial x} + \frac{\partial u}{\partial y}\right) \tag{3.62c}$$

$$\tau'_{yy} = \frac{4}{3}\mu \frac{\partial v}{\partial y} - \frac{2}{3}\mu \frac{\partial u}{\partial x} \tag{3.62d}$$

The conduction heat flux components are defined as follows:

$$q_x = -k\frac{\partial T}{\partial x} \tag{3.63a}$$

$$q_y = -k\frac{\partial T}{\partial y} \tag{3.63b}$$

where T is the temperature. The source terms Q_p and Q_r on the RHS of Equation (3.61) represent the particle heat transfer and fluid chemical reaction, respectively. They are defined as follows:

$$Q_p = \pi d_p^2 n_p h \left(T_f - T_p\right) \tag{3.64}$$

$$Q_r = \rho_f \omega \Delta H_{det} \tag{3.65}$$

Additional dimensionless variables need to be defined in order to complete the non-dimensionalization of the energy equation:

$$\begin{aligned}
E^* &= \frac{E}{D_0^2} & \Delta H^* &= \frac{\Delta H}{D_0^2} & \omega^* &= \omega\frac{L_R}{D_0} \\
k^* &= \frac{k}{k_{f0}} & T^* &= \frac{T}{T_0} & h^* &= \frac{h}{h_0} \\
\tau^* &= \frac{\tau d_p}{\mu_{f0} D_0} & q^* &= \frac{q d_p}{k_{f0} T_0} & n_p^* &= n_p d_p^3
\end{aligned} \tag{3.66}$$

Substituting dimensionless groups (Equations 3.46, 3.55, and 3.66) and $\phi_f = 1 - \phi_s$ into Equation (3.61), and re-arranging the terms, gives:

$$
\begin{aligned}
&\frac{\rho_{f0}D_0^3}{d_p}\left(\frac{\partial \rho_f^* E_f^*}{\partial t^*}+\frac{\partial \rho_f^* u_f^* E_f^*}{\partial x^*}+\frac{\partial \rho_f^* v_f^* E_f^*}{\partial y^*}\right)\\
&\quad-\frac{\rho_{f0}\phi_{s0}D_0^3}{d_p}\left(\frac{\partial \rho_f^* \phi_s^* E_f^*}{\partial t^*}+\frac{\partial \rho_f^* \phi_s^* u_f^* E_f^*}{\partial x^*}+\frac{\partial \rho_s^* \phi_s^* v_f^* E_f^*}{\partial y^*}\right)\\
&\quad+\frac{p_0 D_0}{d_p}\left(\frac{\partial p_f^* u_f^*}{\partial x^*}+\frac{\partial p_f^* v_f^*}{\partial y^*}\right)-\frac{p_0\phi_{s0}D_0}{d_p}\left(\frac{\partial p_f^* \phi_s^* u_f^*}{\partial x^*}+\frac{\partial p_f^* \phi_s^* v_f^*}{\partial y^*}\right)\\
&\quad+\frac{\mu_{f0}D_0^2}{d_p^2}\left(\frac{\partial}{\partial x^*}\left[u_f^* {\tau'_{xx}}^* + v_f^* {\tau_{xy}}^*\right]+\frac{\partial}{\partial y^*}\left[u_f^* {\tau_{yx}}^* + v_f^* {\tau'_{yy}}^*\right]\right)\\
&\quad-\frac{k_{f0}T_0}{d_p^2}\left(\frac{\partial q_x^*}{\partial x^*}+\frac{\partial q_y^*}{\partial y^*}\right)\\
&\quad=\frac{F_0 D_0}{d_p^3}\left(F_{px}^* u_p^* + F_{py}^* v_y^*\right)+\frac{h_0 T_0}{d_p}\pi {d_p^*}^2 n_p^* h^*\left(T_f^*-T_p^*\right)+\frac{\rho_{f0}D_0^3}{L_R}\rho_f^*\omega^*\Delta H_{det}^*
\end{aligned}
\tag{3.67}
$$

Dividing by $\rho_{f0}D^3/d_p$, the following is obtained:

$$
\begin{aligned}
&\frac{\partial \rho_f^* E_f^*}{\partial t^*}+\frac{\partial \rho_f^* u_f^* E_f^*}{\partial x^*}+\frac{\partial \rho_f^* v_f^* E_f^*}{\partial y^*}+\underbrace{\frac{p_0}{\rho_{f0}D_0^2}}_{\text{I}}\left(\frac{\partial p_f^* u_f^*}{\partial x^*}+\frac{\partial p_f^* v_f^*}{\partial y^*}\right)\\
&-\underbrace{\phi_{s0}}_{\text{II}}\left(\frac{\partial \rho_f^* \phi_s^* E_f^*}{\partial t^*}+\frac{\partial \rho_f^* \phi_s^* u_f^* E_f^*}{\partial x^*}+\frac{\partial \rho_f^* \phi_s^* v_f^* E_f^*}{\partial y^*}\right)-\underbrace{\phi_{s0}\frac{p_0}{\rho_{f0}D_0^2}}_{\text{III}}\left(\frac{\partial p_f^* \phi_s^* u_f^*}{\partial x^*}+\frac{\partial p_f^* \phi_s^* v_f^*}{\partial y^*}\right)\\
&+\underbrace{\frac{\mu_{f0}}{\rho_{f0}D_0 d_p}}_{\text{IV}}\left(\frac{\partial}{\partial x^*}\left[u_f^* {\tau'_{xx}}^* + v_f^* {\tau_{xy}}^*\right]+\frac{\partial}{\partial y^*}\left[u_f^* {\tau_{yx}}^* + v_f^* {\tau'_{yy}}^*\right]\right)-\underbrace{\frac{k_{f0}T_0}{\rho_{f0}d_p D_0^3}}_{\text{V}}\left(\frac{\partial q_x^*}{\partial x^*}+\frac{\partial q_y^*}{\partial y^*}\right)\\
&\quad=\underbrace{\frac{F_0}{\rho_{f0}D_0^2 d_p^2}}_{\text{VI}}\left(F_{px}^* u_p^* + F_{py}^* v_y^*\right)+\underbrace{\frac{h_0 T_0}{\rho_{f0}D_0^3}}_{\text{VII}}\pi {d_p^*}^2 n_p^* h^*\left(T_f^*-T_p^*\right)+\underbrace{\frac{d_p}{L_R}}_{\text{VIII}}\rho_f^*\omega^*\Delta H_{det}^*
\end{aligned}
\tag{3.68}
$$

The dimensionless groups in the energy conservation equation are summarized as follows. Term I is the inverse square of Mach number:

$$
\frac{p_0}{\rho_{f0}D_0^2}=\frac{1}{\gamma M_0^2} \tag{3.69}
$$

Term II is the solid volume fraction, ϕ_{s0}. Term III is the product of Terms I and II.

Term IV is the inverse Reynolds number:

$$
\frac{\mu_{f0}}{\rho_{f0}d_p D_0}=\frac{1}{Re} \tag{3.70}
$$

Term V is the inverse of Π_3 in Equation (3.29):

$$\frac{k_{f0}T_0}{\rho_{f0}d_pD_0^3} = \frac{1}{PrReM_0^2(\gamma-1)} \tag{3.71}$$

Term VI is the definition of drag coefficient, which identical to Π_1 in Equation (3.5):

$$\frac{F_0}{\rho_{f0}D_0^2d_p^2} = C_d \tag{3.72}$$

Term VII is equivalent to Π_4 in Equation (3.32):

$$\frac{h_0T_0}{\rho_{f0}D_0^3} = \frac{Nu}{PrReM_0^2(\gamma-1)} \tag{3.73}$$

Term VIII is the ratio of particle size to detonation reaction-zone length, as found in Π_6 in Equation (3.38):

$$\frac{d_p}{L_R} = \delta \tag{3.74}$$

The energy equation provides additional dimensionless groups: Nu, Pr, and δ. The final form of the non-dimensional energy equation is as follows:

$$\begin{aligned}
&\frac{\partial\rho_f^*E_f^*}{\partial t^*} + \frac{\partial\rho_f^*u_f^*E_f^*}{\partial x^*} + \frac{\partial\rho_f^*v_f^*E_f^*}{\partial y^*} + \left[\frac{1}{\gamma M_0^2}\right]\left(\frac{\partial p_f^*u_f^*}{\partial x^*} + \frac{\partial p_f^*v_f^*}{\partial y^*}\right) \\
&- [\phi_{s0}]\left(\frac{\partial\rho_f^*\phi_s^*E_f^*}{\partial t^*} + \frac{\partial\rho_f^*\phi_s^*u_f^*E_f^*}{\partial x^*} + \frac{\partial\rho_f^*\phi_s^*v_f^*E_f^*}{\partial y^*}\right) \\
&- \left[\phi_{s0}\frac{1}{\gamma M_0^2}\right]\left(\frac{\partial p_f^*\phi_s^*u_f^*}{\partial x^*} + \frac{\partial p_f^*\phi_s^*v_f^*}{\partial y^*}\right) \\
&+ \left[\frac{1}{Re}\right]\left(\frac{\partial}{\partial x^*}\left[u_f^*{\tau'_{xx}}^* + v_f^*{\tau_{xy}}^*\right] + \frac{\partial}{\partial y^*}\left[u_f^*{\tau_{yx}}^* + v_f^*{\tau'_{yy}}^*\right]\right) \\
&- \left[\frac{1}{PrReM_0^2(\gamma-1)}\right]\left(\frac{\partial q_x^*}{\partial x^*} + \frac{\partial q_y^*}{\partial y^*}\right) \\
&= [C_d]\left(F_{px}^*u_p^* + F_{py}^*v_p^*\right) + \left[\frac{Nu}{PrReM_0^2(\gamma-1)}\right]Q_p^* + \left[\frac{d_p}{L_R}\right]Q_r^*
\end{aligned} \tag{3.75}$$

Thus, Equations (3.52), (3.57), and (3.75) provide the dimensionless parameters of Re, Pr, M_0, ϕ_{s0}, ρ_{f0}/ρ_{s0}, δ, C_d, and Nu. The same result can be obtained by an analysis of the 3D momentum and energy equations.

In both the non-dimensional analysis and the pi theorem, the dimensionless group $\gamma = c_p/c_v$ was introduced in an equation of state, or so-called closure relationship, to

arrive at the sound speed, a_0, used in the Mach number. In the pi theorem, this could be avoided by simply assuming a_0 is a dimensional parameter in Equations (3.1) and (3.19). However, employing a_0 as the characteristic velocity in the non-dimensional analysis (Equations 3.46, 3.55, and 3.66) results in the flow Mach number, rather than the shock Mach number, for the dimensionless group representing compressibility. Since the shock Mach number is traditionally used to characterize the explosive detonation velocity, the additional dimensionless group for γ was retained. Therefore, the ratio of specific heats was used in both the non-dimensional analysis and the pi theorem for consistency.

Whereas the pi theorem did not provide the relative importance of each parameter group, the non-dimensionalization of the governing equations shows an inverse relationship for Re and Pr, and an inverse-squared dependence on M_0. Therefore, for high Reynolds numbers, the flow is momentum dominated and viscous effects become less important. For high Mach numbers, the flow is convectively dominated, as opposed to low Mach numbers where the flow becomes pressure dominated.

Further inspection of the non-dimensional form of the governing equations can be used to evaluate the properties of the particles-explosive system. For high solid volume fractions ($\phi_{s0} > 0$), the fluid phase is diluted with a corresponding reduction in momentum and energy. For an increasing density ratio of explosive to solid particles ($\rho_{f0}/\rho_{s0} \rightarrow 1$), the individual phase conservation and fluxes of mass, momentum, and energy become apportioned by the volume fraction. For small particles or explosives with a long reaction-zone length ($d_p/L_R \rightarrow 0$), the initial chemical heat release becomes negligible and the flow can be assumed to be inert within the length scale of a particle diameter.

3.3 Analysis of the dimensionless parameter groups

The dimensionless parameters found in Sections 3.1 and 3.2, used to determine the force that accelerates the particles and heat transfer rate that increases the particle temperature (Equations 3.18 and 3.39), are summarized as follows:

a. Mach number, M_0

b. ratio of specific heats, $\gamma = c_p/c_v$

c. Reynolds number, Re

d. Prandtl number, Pr

e. volume fraction of solid particles, ϕ_{s0}

f. density ratio of explosive fluid to solid particle, ρ_{f0}/ρ_{s0}

g. ratio of particle diameter to detonation reaction-zone length, $\delta = d_p/L_R$

3.3.1 Mach number

The detonation performance of explosives is considered here to explore the range of detonation shock velocity and pressure. The detonation velocity depends on the initial density, temperature, and charge diameter. The values tabulated in Table 3.2 have been extrapolated for large charges (infinite diameter assumption). Pure high explosives have a detonation pressure range typically from 10 to 40 GPa; detonation pressures up to 50 GPa are possible for some specialty high explosives. In general, the range of detonation velocity for high explosives is from 6 to 9 mm/μs.

The detonation shock Mach number is defined by $M_0 = D_0/a_0$. Typically the detonation Mach number in condensed matter is less than that for gas detonation due to the higher solid/liquid sound speed. The sound speed in condensed matter has the added complexity of longitudinal and transverse components even in isotropic materials. The bulk sound speed, a_B, in isotropic materials (see Marsh [139], and Dobratz and Crawford [47]) is defined as:

$$a_B = \sqrt{a_L^2 - \frac{4}{3}a_T^2} \tag{3.76}$$

Table 3.2: Performance of pure high explosives in large charges (from Dobratz and Crawford [47]).

Explosive	Density, ρ_{f0} (g/cc)	Velocity, D_0 (mm/μs)	Pressure, P_{CJ} (GPa)
NM	1.13	6.35	12.5
TNM	1.6	6.4	14.4
TNT	1.59	6.95	21.0
NG	1.59	7.65	25.3
PETN	1.79	8.26	33.5
RDX	1.77	8.7	33.8
HMX	1.89	9.11	39.0

where a_L is the longitudinal sound velocity and a_T is the transverse shear wave speed. For homogeneous materials such as liquids, only a bulk sound velocity is reported from experiments. Table 3.3 summarizes the calculated detonation shock Mach number using the bulk sound speed (i.e., $a_0 = a_B$).

The detonation shock Mach number of solid and liquid explosives at their theoretical maximum density has a narrow range of $2.5 < M_0 < 4$ in general. Shock velocity and pressure effects were investigated in a previous work (see Zhang et al. [229]) by varying the inert shock pressure from 5 to 20 GPa. While the resulting momentum transfer to the particles remained proportional to the shocked fluid velocity, the variation in velocity transmission after the shock interaction was less than 10% for the resulting shock velocity range of 4 – 9 mm/μs for metal particles in RDX explosives.

3.3.2 Ratio of specific heats

The ratio of specific heats depends on the gas composition and the temperature. The ratio of specific heats of the gaseous detonation products at the CJ plane can be obtained using the thermochemical equilibrium code, Cheetah (Fried et al. [68]). Table 3.4 summarizes the CJ flow conditions including the ratio of specific heats. The CJ flow Mach number is also calculated in the fixed (laboratory) frame of reference.

In the frame of reference attached to the detonation shock, the detonation products flow at the CJ plane is sonic, where $M_0 = (D_0 - u_{CJ})/a_{CJ} = 1$. Considering that particles are frozen – that is, not moving within the shock – they are subject to subsonic flow behind the detonation shock. The range of flow Mach number is remarkably narrow for

Table 3.3: Shock Mach number calculated using detonation shock velocity and sound speed for pure explosives at their theoretical maximum density.

Explosive	Density, ρ_{f0} (g/cc)	Detonation Velocity, D_0 (mm/μs)	Sound Speed, a_0 (mm/μs)	Shock Mach, M_0
HMX	1.90	9.15	3.07 [(a)]	2.97
HMX (PBX-9501)	1.891	9.11	2.97 [(b)]	3.08
NM	1.128	6.612	1.648 [(c)]	4.01
NQ	1.81	8.74	3.54 [(a)]	2.47
PETN	1.78	8.59	2.98 [(a)]	2.88
RDX	1.80	8.75	3.095 [(c)]	2.83
RDX	1.77	8.7	2.65 [(b)]	3.28
TATB	1.94	8.00	2.00 [(b)]	4.00
TNT (crystal)	1.654	6.97	2.20 [(b)]	3.17
TNT (molten)	1.47	6.48	2.1 [(a)]	3.09
TNT (liquid)	1.472	6.52	2.14 [(a)]	3.05
TNT (liquid)	1.447	6.58	2.00 [(c)]	3.29
AN	1.722	6.765	2.5 [(c)]	2.706

[(a)]Marsh [139], [(b)]Dobratz and Crawford [47], [(c)]Mader [133].

a wide range of explosives and in particular for liquid explosives. For frozen particles encountering the CJ flow conditions, the Mach number is typically less than 0.4, indicating subsonic flow conditions for frozen particles. This is the maximum relative Mach number that the particles are subjected to within the detonation zone. When considering particles accelerated during the shock interaction time, the post-shock velocity difference between the particle and flow will be even smaller, and the flow quickly becomes incompressible as the relative Mach number diminishes.

3.3.3 Reynolds number

An order-of-magnitude analysis can be used to estimate the Reynolds number range for particles in a detonation flow. The CJ condition can be used to estimate the frozen particles Reynolds number. Table 3.4 indicates that the CJ density ranges from 1 to 4 g/cc with a streaming flow velocity between 1 and 2 mm/μs for a wide range of condensed explosives. Aside from flow density and velocity, the Reynolds number depends on the host fluid viscosity and the particle size. In general, the molecular viscosity, $\mu = f(T, p)$, has high uncertainty in shock-compressed states and in the hot detonation products. Assuming the

Table 3.4: CJ flow Mach number for liquid and solid explosives calculated using the Cheetah BKWS library.

Explosive *	ρ_{CJ} (g/cc)	u_{CJ} (mm/μs)	a_{CJ} (mm/μs)	γ_{CJ}	$M_{CJ} = u_{CJ}/a_{CJ}$
Liquid Explosives					
DEGN (1.39)	1.865	1.836	5.374	1.328	0.342
IPN (1.036)	1.443	1.502	4.356	1.227	0.345
NG (1.594)	3.362	1.950	6.040	1.299	0.323
NM (1.128)	1.736	1.764	4.847	1.379	0.364
TNM (1.638)	2.128	1.252	4.192	1.300	0.299
TNT (1.447)	1.927	1.623	4.880	1.262	0.333
Solid Explosives					
HMX (1.905)	2.460	2.125	7.290	1.171	0.291
NQ (1.77)	2.244	1.796	6.712	1.265	0.268
PETN (1.778)	2.324	2.058	6.703	1.155	0.307
RDX (1.806)	2.348	2.078	6.922	1.175	0.300
TATB (1.937)	2.499	1.894	6.529	1.177	0.290
TNT (1.654)	2.175	1.734	5.502	1.155	0.315

* initial density in g/cc given in parenthesis.

viscosity for high temperature gases (but at standard pressure) is representative of the detonation products, the viscosity can be estimated for the dominant gas species present in the products of detonation. The CJ temperature for typical explosives ranges from 2500 to 4000 K, where the molecular viscosity of N_2, O_2, CO_2 and H_2O are in a narrow range of 10^{-5} – 10^{-4} kg/m-s, which may be verified using Sutherland's law. A weaker detonation strength corresponds to a lower CJ temperature and consequently a small molecular viscosity; similarly, a stronger detonation has a higher viscosity in its product gases. These two limits both result in a Reynolds number dependence of $Re = d_p \times 10^{11}$, where d_p is in metres. Therefore, as typical examples, a 1 μm particle has $Re = \mathcal{O}(10^5)$ and a 1 mm particle has $Re = \mathcal{O}(10^8)$.

The boundary layer thickness is important to consider as it defines the region where frictional effects are important. Outside the boundary layer, flow is dominated by inertia and it can often be represented as inviscid (frictionless). The ratio of laminar boundary layer thickness to particle diameter is: $\Delta/d_p = 2.12Re_d^{0.5}$. Choosing a typical Re in the laminar regime for CJ flow, the boundary layer thickness is 77 times smaller than the particle diameter for a 1 μm particle and 240 times smaller than a 10 μm particle. For larger particles, the boundary layer thickens and becomes turbulent; however, it is still

many times smaller than the particle size. For the particle size and flow conditions in a detonation, the flow may be represented as inviscid.

3.3.4 Prandtl number

The Prandtl number is the ratio of thermal diffusivity to momentum diffusivity. The thermal boundary layer thickness is directly related to the velocity boundary layer thickness by the Prantdl number ($Pr = a/\nu$, where $a = k/\rho c_p$ is the thermal diffusivity and $\nu = \mu/\rho$ is the kinematic viscosity). As a typical example, for particles subjected to the VN shock in NM, $Pr = 5.22$ and hence the thermal boundary layer is five times smaller than the velocity boundary layer. Conversely, for particles heated in the CJ flow of NM detonation products, $Pr = 0.758$ and the thermal boundary layer is 30% larger than the velocity boundary layer. In both cases, the velocity and thermal boundary layers are of the same order of magnitude. The thermal boundary layer can therefore be neglected, similar to the velocity boundary layer, since they are much smaller than the particle length scale as demonstrated in the previous section.

The foregoing discussion of velocity and thermal boundary layers in terms of Re and Pr did not include the effects of compressibility. In general, compressible flow has increased thermal and velocity gradients confined within thinner boundary layers. Highly compressible flow, in general, is treated as an inviscid and non-heat-conducting fluid flow (Bertin [25] and Anderson [1]).

3.3.5 Density ratio of explosive to solid particle

Table 3.5 summarizes the density ratio for common explosive mixtures used in experiments. The table has been sorted from largest to smallest density ratio of explosive to solid particle. Slight variations are expected depending on the initial density of the explosive and solid metal particles. For the range of experiments surveyed, the density ratio is typically $\rho_{f0}/\rho_{s0} < 1$. For liquid explosives in particular, an order of magnitude variation in the metal density changes the resulting explosive to solid density ratio by an order of magnitude. For example, for particles saturated with nitromethane, the density ratio ranges from $\rho_{f0}/\rho_{s0} = 0.748$ for silica to $\rho_{f0}/\rho_{s0} = 0.058$ for tungsten.

For a step shock wave passing a spherical metal particle in condensed matter, Zhang et al. [229] studied the velocity transmission factor, α, for a particle of magnesium, beryllium,

Table 3.5: Density ratio of explosive to solid from various sources.

Mixture (Explosive/Particle)	**Explosive Density, ρ_{f0} (g/cc)**	**Solid Density, ρ_{s0} (g/cc)**	**Density Ratio, ρ_{f0}/ρ_{s0}**
NM/Glass (Lee et al. [127])	1.160	$\sim$ 1.550	0.748
TNT/Al (Zhang and Wilson [232])	1.654	2.700	0.613
RDX/Al (Gonthier and Rumchik [86])	1.650	2.785	0.593
IPN/Mg (Frost et al. [77])	1.036	1.780	0.582
NM/Al (†)	1.128 – 1.160	2.700 – 2.785	0.405 – 0.430
NM/Al_2O_3 (Kuralingala [118])	1.128	3.9 – 4.1	0.289 – 0.275
NM/Ti (Frost et al. [71, 72])	1.128	4.528	0.250
NM/Zr (Frost et al. [71])	1.128	6.520	0.173
RDX/Pb (Mader [133])	1.800	11.34	0.159
NM/Fe (Zhang et al. [226]; Frost et al. [75])	1.128	7.860	0.144
NM/Cu (Kato et al. [107, 105])	1.128	9.920	0.114
HMX/W (Richards et al. [161])	1.900	19.25	0.099
RDX/W (Gonthier and Rumchik [86])	1.806	19.30	0.094
PBX/W (Kato et al. [104])	1.700	19.25	0.088
NM/W (‡)	1.128	19.30	0.058

†Kurangalina [118], Baudin et al. [18], Gogulya et al. [85], Haskins et al. [94], Frost et al. [74], and Kato et al. [107, 105, 106].

‡Kurangalina [118]; Frost et al. [75], and Kato et al. [104].

aluminum, nickel, uranium and tungsten subjected to a shock of 5 – 20 GPa in liquid NM and various solid RDX densities. The particle velocity after the shock interaction time, τ_S, was found to strongly depend on the initial density ratio of explosive to metal and can be expressed by:

$$\alpha = \frac{1}{a+b}\left(a + b\frac{\rho_{f0}}{\rho_{s0}}\right)\frac{\rho_{f0}}{\rho_{s0}} \tag{3.77}$$

where a and b are constants independent of the particle and explosive matter. The light-metal particle velocity for aluminum, beryllium, and magnesium achieved 60 – 100% of the shocked explosive velocity after the shock interaction time.

The density ratio also appears in the material impedance ratios. The acoustic impedance is defined as $Z_A = \rho_f a_f/\rho_s a_s$ and the shock impedance is defined as $Z_S = \rho_f D_f/\rho_s D_s$. Investigation by Zhang et al. [229] showed that the acoustic impedance and shock impedance do not significantly influence the velocity transmission within the shock Mach number range of condensed explosives.

3.3.6 Volume fraction of particles

The solid volume fraction is already a dimensionless parameter. It describes the volume occupied by the solid relative to the total volume of the mixture: $\phi_{s0} = V_{s0}/(V_{s0} + V_{f0})$. The solid volume fraction has a range of $0 \leq \phi_{s0} \leq 1$. Ordered packing of same-size spheres in lattice arrangements (simple cubic, body-centred cubic, and face-centred cubic packing) have solid volume fractions ranging from 0.52 to 0.74. Random packing of poly-disperse particles results in volume fraction ranges from 0.58 to 0.62. Loose powders typically have a volume fraction of 0.5. Table 3.6 summarizes the bulk density, solid mass fraction, and solid volume fraction range from a survey of experiments. Variations in the mixtures are a result of particle size distribution, particle shape and, occasionally, trapped gas pockets. In general, the solid volume fraction ranges from 0.35 to 0.65.

Slurry explosives employed for fundamental scientific investigations usually contain a high solid volume fraction near the maximum packing value due to the difficulty of uniformly suspending lower concentrations of particles in a liquid. In practice, the amount of metal particle additive is usually chosen to balance the overall explosive stoichiometry and fuel richness in explosives, and is often less than in the slurry explosives reviewed in Table 3.6. Mixtures of metal powders with solid explosives in widespread use have a volume fraction range from 0 to 0.25. For example, Tritonal (80/20 wt% TNT/Al) and

Table 3.6: Typical volume fractions calculated for experimental configurations with dense and packed particle beds saturated with nitromethane (ρ_{f0} = 1.093 – 1.16 g/cc).

Mixture (Explosive/Metal)	Bulk Density, ρ_{mix} (g/cc)	Solid Mass Fraction, Y_{s0}	Solid Volume Fraction, ϕ_{s0}
NM/Al (Frost et al. [74])	2.09 – 2.16	0.77 – 0.79	0.58 – 0.62
NM/Al (Kurangalina [118])	2.00	0.75	0.556
NM/Al (Kato et al. [107])	1.72 – 2.04	0.57 – 0.75	0.35 – 0.55
NM/Mg (Kato et al. [107])	1.42 – 1.48	0.57 – 0.70	0.46 – 0.60
NM/Cu (Kato et al. [107])	5.44 – 5.49	0.91 – 0.92	0.57 – 0.59
NM/Fe (Zhang et al. [226]; Frost et al. [75])	5.11 – 5.54	0.92 ± 0.01	0.61 ± 0.01
NM/Zr (Frost et al. [71])	2.97 – 3.04	0.755 ± 0.005	0.342 – 0.354
NM/Ti (Frost et al. [71, 72])	3.32 – 3.36	0.881 ± 0.003	0.641 – 0.654
NM/Al_2O_3 (Kurangalina [118])	2.24	0.70	0.40
NM/W (Frost et al. [75])	8.40	0.92	0.40

H-6 (45/30/20/5 wt% RDX/TNT/Al/wax) [132] are standard military formulations that have a metal volume fraction of 0.13. Aluminized ANFO for the mining industry typically contains 7 – 10% Al by weight, and potentially up to a maximum of 15% by weight (Kennedy [108]); this corresponds to a metal volume fraction range of 0.03 – 0.06.

3.3.7 Ratio of particle diameter to reaction-zone length

The smallest commercially-available particles are less than one micron in diameter, and are termed ultrafine or nanometric particles. Nanometric particle sizes of 20 – 200 nm are available from Argonide Corp [2] and their use in explosives is reviewed by Brousseau and Anderson [30]. Similarly, 50 nm particles from Technanogy and 100 nm particles from Nanotechnologies were studied by Gonthier and Rumchik [86]. Particles above one micron are more commonly used in scientific investigations. The most widely used micrometric aluminum particles are from Valimet Inc. [206]. Particle size distributions with designations Valimet H-2 (3 ± 1.5 μm) to H-95 (114 ± 40 μm) were used by Zhang et al. [234], Frost et al. [74], and Kato et al. [107, 105]; Valimet type X-81 (typ. 20 μm) has been used by Gonthier and Rumchik [86].

Other spherical beads used in fundamental studies are summarized here: Kurangalina [118] used alumina, aluminum, and tungsten in a size range of 1 - 50 μm; Frost et al. [75] used 149 μm tungsten particles; Frost et al. [71, 72] used 40 – 254 μm titanium particles;

Kato et al. [107, 105] used 9 – 350 μm copper particles; Frost et al. [77] used 60 – 520 μm magnesium particles; Zhang et al. [226] and Frost et al. [75] used 100 – 925 μm steel particles; and, Lee et al. [126, 127] used 66 μm – 2.4 mm spherical glass beads. Each particle size introduces an additional characteristic length scale making mesoscale study of all particle sizes, or particle sizes covering a wide distribution, prohibitive. From the above survey, an order of magnitude range for particle size is then $10^{-8} < d_p < 10^{-3}$ m.

In 1947, Eyring et al. [61] determined the reaction-zone length for high explosives to be about 1 mm long. Later, Engelke and Bdzil [59] remarked that condensed detonation reaction zones are typically 0.1 mm long. Dobratz and Crawford [47] surveyed the reaction-zone length of pure explosives from various sources and found it to be about 0.1 mm, but suggested it could vary by several orders of magnitude, depending on the high explosive. The detonation reaction zone can be as small as 0.01 mm for some sensitive explosives (Bdzil et al. [20]).

Table 3.7 summarizes the approximate reaction-zone length and product equilibrium times for liquid explosives. The reaction timescale is defined as: $\tau_{det} = L_R/D_0$, and is estimated using velocity-time or pressure-time histories in combination with observation of the detonation velocity. Large variations are expected due to the differences in the experimental configuration (charge diameter, casing material, and casing thickness). Furthermore, a variety of diagnostic techniques have evolved with improved resolution: embedded gauges (both pressure and particle velocity); electrical conductivity probes [95]; particle velocity using laser interferometry techniques such as VISAR [185] and Fabry-Perot [199]; laser Doppler velocimetry [27]; and, mass spectroscopy [26]. Reaction-zone lengths for a variety of condensed explosives are tabulated in a report of the Department of the Army [46], Dobratz and Crawford [47], and Cooper [41].

Nitromethane has been widely studied in a number of scientific experiments, where the reported reaction-zone length ranges from 0.03 to 1.6 mm, as demonstrated in Table 3.7. The reaction zone of NM can be reduced by the addition of diethylenetriamine (DETA) [211] or using triethylene amine (TEA). The reaction zone of NM can be increased by diluting it with acetone, which is miscible in any proportion [52, 53], or by dilution with nitroethane [157].

Without losing generality for the reaction-zone length in condensed explosives, solid explosives are also considered: HMX has a reaction-zone length of 0.5 – 0.7 mm [198]; RDX has a reported reaction-zone length of 0.826 mm [61] and 1.82 – 2.9 mm [47]; solid TNT has a reaction-zone length of 2.0 mm [119]; and, TATB has a reaction-zone length of 2.5 – 3 mm [198]. Ammonium perchlorate is a granular solid explosive with a reaction-

Table 3.7: Approximate reaction-zone length and reaction time for liquid explosives.

Explosive	Reaction-Zone Length, L_R (mm)	Reaction Time Scale, τ_{det} (ns)	Reference
NG	0.21	26.3*	Eyring et al. (1947) [61]
NM	0.03 – 0.036	5 – 6	Engleke (1979) [58]; Engelke and Bdzil (1983) [59]
Sensitized NM	0.05	7	Blais et al. (1997) [26]
NM	0.13 *	20	Hayes (1965) [95]
NM	0.12 – 0.16 *	19 – 25	Mallory (1976) [137]
NM	0.08 – 0.27	13 – 43 *	Campbell et al. (1955) [34]
NM	0.3	50	Sheffield et al. (2002) [185]
NM	0.3 – 0.6	50 – 100 *	Nahmani and Manheimer (1956) [149]
NM	0.6 – 0.9	100 – 150	Bouyer et al. (2009) [27]
NM/acetone 75/25	0.8 – 1.6	127 – 254 *	Dobratz and Crawford (1985) [47]
TNT liquid (at 100°C)	0.9 – 1.1	138 *	Igel and Seely (1955) [97]
TNT liquid	0.63 *	100	Hayes (1965) [95]
IPN	1.0	171 *	Zhang et al. (2002) [234]
TNM	1.6	250	Mochalova et al. (2009) [147]
TNM	2	500	Dremin et al. (1970) [54]

* Estimated using the CJ velocity

zone length of 6.3 – 10 mm [47]. Thus, the physical length scale describing the detonation reaction zone is $10^{-6} < L_R < 10^{-2}$ m for condensed explosives.

The above physical parameters can be combined to evaluate the ratio of the particle size to detonation reaction-zone length. As a typical example, 10 – 100 μm particles in an explosive with a 10 – 1000 μm reaction-zone length gives a ratio of $10^{-2} < \delta < 10^{1}$. However, the full range of particle diameter to detonation reaction-zone length needs to consider the particle size ranges discussed above and the explosive reaction-zone lengths summarized in Table 3.7. Therefore, a potential range of $10^{-6} < \delta < 10^{3}$ can be obtained assuming $10^{-6} < L_R < 10^{-2}$ m and $10^{-8} < d_p < 10^{-3}$ m as justified above.

3.4 Summary

The factors affecting particle acceleration and heating were established using dimensionless analysis approaches. Subsequently, the range and significance of each parameter were evaluated using data from the literature. For particles within the condensed matter detonation wave, the Reynolds number is sufficiently large that inviscid flow can be assumed and the Reynolds number, therefore, is not considered as a dominant parameter. Although the results are expected to depend on Mach number, the condensed detonation shock Mach number has a limited range and, therefore, does not need to be varied parametrically. Similarly, the specific heat ratio has a limited range and does not require further study. With regards to the particle heating, the Prandtl number is of an order of magnitude of one and is therefore be assumed not to be a dominant parameter.

The most important parameters influencing the particle acceleration and heating within a condensed matter detonation wave are the material density ratio of explosive to particle, the particle volume fraction, and the ratio of particle diameter to detonation reaction-zone length. While the material density ratio of explosive to particle has been studied previously (see Zhang et al. [229]), the effect of the volume fraction of solid particles, packing configuration in 3D, and the ratio of particle diameter to detonation reaction length are further investigated using a mesoscale modeling approach.

Chapter 4

Approach for shock and detonation interaction with particles

Computational modeling of shock compression physics was founded at the mesoscale, where details of the mechanics and chemistry can be resolved. Recently, mesoscale simulation has gained wide-spread use due to increases in computing power; it has been used to develop constitutive models, and to design and interpret experiments. Furthermore, it has been used to study dispersive waves (Baer and Trott [11]) and compaction wave profiles (Menikoff [143]) from impact in granular explosives, shock initiation of granular explosives (Mulford and Swift [148]), and characterization of the formation and propagation of detonation waves (Plaskin et al. [159]). The particular computational approach for a given application must be matched with the chemical and physical processes at hand, while maintaining sufficient numerical resolution to capture the essential features of the problem. The approach may be simplified by making a number of reasonable assumptions.

For shock and detonation interaction with metal particles in a condensed explosive, multiple materials describing reactive and inert components are required, where hydrodynamic wave transmission occurs between materials. For dense heterogenous detonation, representing the three-dimensional arrangement of packed beds of particles and spacing between particles is important. This work is focused on examining the mechanical and thermal interaction, rather than details of chemical reaction. This chapter presents the approach for studying shock and detonation interaction with particles.

4.1 Assumptions and justifications

Considerations that help simplify the modeling approach are made based on a survey of experimental evidence. The following assumptions are elaborated on in this subsection:

a. Shock compression temperature is based on specific volume change

b. Phase change of particles does not occur during shock compression

c. Particles are not mechanically broken by shock compression during shock and detonation interaction

d. Material strength can be neglected during shock interaction

e. Particles are inert within the detonation reaction zone

f. Particles are spherically shaped

g. Particles are mono-sized

h. Infinite charge diameter with a planar detonation front

4.1.1 Shock compression of metals

Unlike static compression measurements (e.g., Bridgman [28]), which are performed isothermally, shock wave compression tests employ high explosives to generate high pressure in the test specimens, where the resulting loading follows the Hugoniot curve. Walsh and Christian [212] transformed the pressure compression data for aluminum, zinc, and copper into compression temperature for shocks from 15 to 50 GPa using the conservation equations. The database was expanded by Walsh et al. [213] to include twenty-seven metals for shock compressions up to 60 GPa. McQueen and Marsh [142] further extended the pressure range up to 200 GPa for nineteen metals. The Hugoniot data from over 5000 experiments conducted at Los Alamos National Laboratories were compiled by Marsh [139].

Fitting to the various temperature data obtained using the Walsh and Christian technique results in a fourth-order polynomial of log specific volume [132]:

$$T_H = F_S + G_S(\ln\nu) + H_S(\ln\nu)^2 + I_S(\ln\nu)^3 + J_S(\ln\nu)^4 \tag{4.1}$$

The results from Equation (4.1) combined with the shock Hugoniot (Equation 2.18b) are plotted for common metals in Figure 4.1.

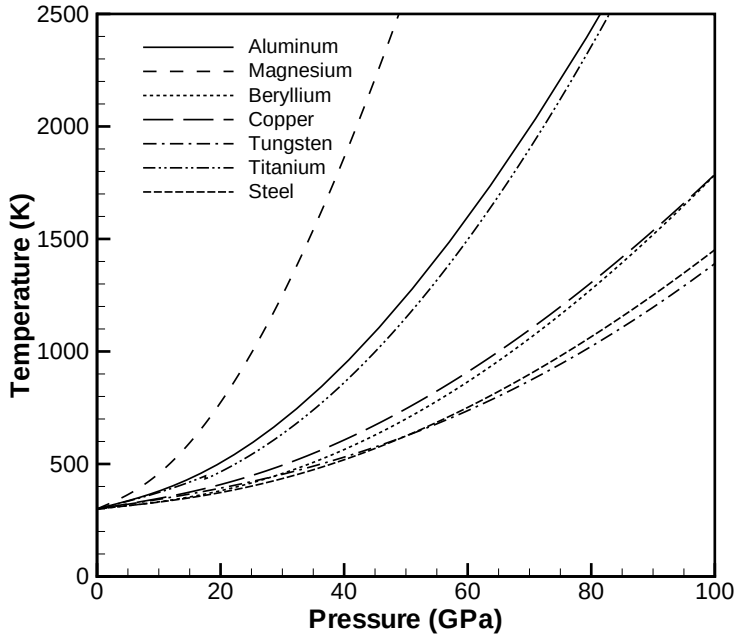

Figure 4.1: Shock compression temperature for several metals based on Walsh and Christian temperature fitting and using coefficients of Mader [133].

4.1.2 Melting temperature and phase change

The phase change temperature can be compared to the shock compression pressure on the temperature Hugoniots in Figure 4.1 to determine if melting or evaporation may occur. The phase change temperatures under ambient conditions are summarized in Table 4.1, where T_M is the melting temperature and T_V is the vaporization temperature. Magnesium and aluminum have nearly the same T_M; however, from the temperature Hugoniots, magnesium reaches the melting temperature at 23 GPa, while Al reaches it at 40 GPa. Inspection of the temperature Hugoniots and phase change temperature indicates that beryllium, copper, tungsten, and titanium are unlikely to melt under detonation pressure conditions. The low melting and vaporization temperatures of lead, tin, zinc, and phosphorus may lead to potential phase change under shock and detonation conditions. The latent heat necessary for phase change, and high-pressure effects on the phase change temperature, affect whether phase change occurs. Davydov et al. [45] used the formula of Johnson, which is strictly valid for low pressures, to estimate an unrealistically high melting temperature of 8000 K for aluminum at 10 GPa.

Table 4.1: Phase change temperatures at STP for various materials commonly used in fundamental explosive experiments.

Material	Solid Density, ρ_{s0} (g/cc)	Phase Change Temperature T_M (K) [4]	T_V (K)
Inert Metals			
Copper	8.96	1358	2835
Beryllium	1.85	1563	3243
Gold	19.3	1337	3080
Lead	11.34	600	2013
Tin	7.29	505	2543
Tungsten	19.25	3683	5705
Zinc	7.14	693	1180
Reactive Materials			
Aluminum	2.70	933	2740
Magnesium	1.74	923	1380
Phosphorus	1.83	317	550
Titanium	4.54	1941	3536
Zirconium	6.49	2125	4650

Gover [90] measured shock heating effects by studying the process of shock compression followed by adiabatic expansion. For aluminum with a melting temperature of 933 K, incipient melting (material reaching melting point) begins at a compression of 60 GPa and complete melting can be caused by pressure of 90 GPa. Similarly for other metals such as copper, gold, nickel, and titanium, the shock compression required for incipient melting is above 100 GPa. These pressures are unlikely to be achieved or sustained using liquid explosives and, therefore, phase change via detonation shock compression is not considered for slurry explosives.

4.1.3 Particle damage

Depending on the particle morphology, strong shocks and detonation pressure may significantly alter the metal particle during interaction [109]. It has been shown in experiments by Yoshinaka et al. [222] and in mesoscale simulations by Cooper et al. [40] that aluminum flakes are readily shattered during shock interaction. However, spherical particles may remain intact due to their high solid volume to surface area ratio. Some evidence is reviewed below.

Yoshinaka et al. [222] investigated Valimet H-30 spherical aluminum particles (36 μm mean diameter by mass) saturated with an inert oxygen-free liquid (i.e., heptane), which was shocked up to 29.3 GPa using a flyer plate impact test. Recovered specimens showed that the average particle size was not changed significantly, although the initial spherical shape became geodesic with evidence that the faceted surface was caused by shear. Fragmentation of the smaller particles was observed with probable removal of the oxide coating from the larger particles, but the majority of the particles remained intact. There was clearly no evidence of melting of either the oxide coating or the exposed aluminum core, indicating that the temperature achieved during shock compression was less than 933 K, and there was also no evidence of agglomeration.

Richards et al. [161] embedded spherical tungsten particles (37 μm mean size by mass) in castable HMX, and collected the resulting deformed particles after being subjected to a detonation wave (24.3 GPa CJ pressure and 4.8 mm/μs shock velocity). The post-detonation condition of the particles was heavily deformed (plastic deformation) and agglomerated by shock welding during particle-particle impacts. The relative softness of tungsten and the crystalline structure of HMX may have increased the particle damage.

Using the particle image velocimetry experiment described in Jenkins et al. [99], intact spherical aluminum particles were photographed in the dispersed particle flow, which indicated minimal damage during shock acceleration. However, these particles were loosely packed outside of an RDX-based explosive, rather than being mixed in an explosive matrix. Even for spherical glass particles in liquid nitromethane, post-detonation recovery of the dispersed beads showed intact spheres, although internal fracturing was observed [69]. Therefore, spherical particles can deform but are assumed to remain intact during detonation interaction.

4.1.4 Hydrodynamic assumption

Materials exhibit plastic stress-strain behaviour, like a fluid, if the shock pressure is above ten times the elastic limit (yield strength) [41]. In these cases, the material response can be assumed to be hydrodynamic, which is justified as follows. The incident shock pressures encountered in the detonation of condensed explosives are typically 10 – 50 GPa (see Table 3.2), which far exceed the yield strength of many pure metals. For example, aluminum particles from Valimet Inc. are 99.7% pure (Valimet [206]); the yield strength of 99% commercially pure Al is 0.035 GPa (Callister [32]). Therefore, Al is likely to behave plastically when shocked above 0.3 GPa.

The particle strength was addressed previously (see Zhang et al. [229] and Ripley et al. [168]) where it was shown that mesoscale modeling results without a constitutive strength model were in agreement with results computed using a finite element model for the spherical particle. In the current work, material strength has been neglected by assuming that only volumetric strain occurs in the particles during the shock interaction time.

4.1.5 Particle reactivity

For pure metal particles, oxidizing gas species are required for particle burning. The explosive decomposition occurs behind the leading shock and throughout the detonation reaction zone, producing oxidizing gas species. Small particles may react within the detonation reaction zone if they are heated, melted, and ignited before the CJ plane. Baudin et al. [18] showed that even 100 nm aluminum particles do not react in the NM detonation zone. In condensed heterogeneous explosives, shattering of the oxide coating or particle fragmentation may promote earlier reaction.

Shock compression heating alone is insufficient to reach the aluminum melting temperature; heating behind the shock is further responsible for bringing the particle to the required ignition temperature and overcoming the delay time. Whether or not particle ignition occurs also depends on a competition between particle heating in the detonation products and expansion cooling, which is dictated by the lateral confinement condition.

Cylindrical explosive tests provide an indication of the ignition delay time behind the detonation front for micrometric particles. Under thick steel tube confinement, Kato et al. [107] observed that the reaction of 8 μm spherical particles takes place at approximately 2.5 μs after the leading shock. For light casing confinement in thin-walled steel and aluminum tubes, Zhang et al. [233] showed the apparent ignition delay to be 13 – 18 μs for 13 μm particles and 26 – 63 μs for 54 μm particles. For low confinement in glass tubes, Haskins et al. [94] showed an ignition delay of 10 μs for 10.5 μm spherical particles and Frost et al. [74] showed the ignition delay for 63 ± 21 μm particles to be about 50 μs. Milne et al. [146] used numerical simulation to calibrate aluminum burn times to experimental cylindrical expansion (cylex) test data and showed that 5 – 10.5 μm particles have a burn time of 50 – 220 μs. In explosive dispersal, Grégoire et al. [91] showed aluminum ignition delay times greater than 100 μs.

For aluminum, the ignition delay for 1 – 100 μm particles is 1 – 100 μs (see Kato et al. [107], Zhang et al. [233], Haskins et al. [94], Frost et al. [74], Milne et al. [146], Grégoire

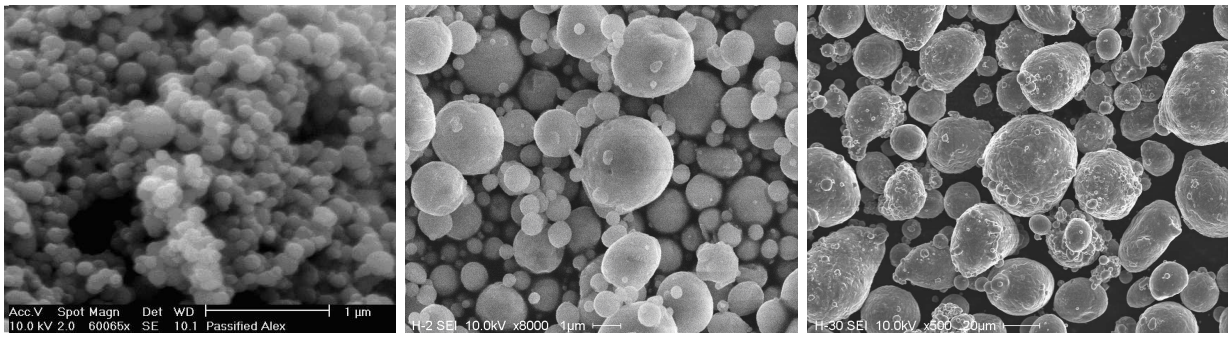

Figure 4.2: Micrographs of spherical aluminum particles: Argonide 100 nm Alex (left), Valimet H-2 (3 ± 1.5 µm) (centre), and Valimet H-30 (36 ± 14 µm) (right) from Zhang et al. [227].

et al. [91]), which is much greater than the shock interaction timescale ($\tau_s \ll 1$ µs). More importantly, for a detonation velocity of 6 – 9 mm/µs, the ignition delay is much greater than the reaction-zone length scale. Therefore, micrometric particles can be treated as inert within the shock interaction timescale and throughout most of the detonation reaction-zone length.

4.1.6 Particle shape and size distribution

In previous studies, the particle diameter has typically been adjusted parametrically to study various effects. Actual particle sizes span a wide range depending on the material and manufacturing technique. The exploding wire method produces nanometric particles with a narrow size distribution. For aluminum, 50 and 100 nm sizes are available from the Argonide Corp. [2]. Metal particles formed using the atomization process generally have a micrometric size range. Atomized aluminum particles are available from Valimet Inc. [206] in sizes from H-2 (3.0 ± 1.5 µm) to H-95 (114 ± 40 µm). The Valimet aluminum particles have been used extensively (e.g., [74, 228, 107, 105]). As shown in Figure 4.2, these types of aluminum particles are generally spherical.

Many other particles are non-spherical, including crystalline, flaked, fragmented, and agglomerated morphologies. Spherical particles are assumed in this work to avoid additional geometric length scales in describing the particles and their orientation. Further, spherical particles do not require strength and damage models as explained in Section 4.1.3. The characteristic dimension is therefore represented by the spherical diameter.

Each particle diameter introduces a new set of characteristic timescales (shock interaction, acceleration, heating, and reaction). The size of particles formed in a variety

of processes follow a natural, or log-normal, distribution. Typical atomized particle distributions span two orders of magnitude in size. These may be sieved for experiments requiring narrower diameter range representative of mono-sized particles. Nanometic particles more closely approximate monodisperse (single-sized), and millimeter-scale beads have a controlled narrow size distribution. Using monodisperse particles allows scaling of results based on the particle diameter. The monodisperse size assumption avoids dense collisions and frictional effects since all particles are subjected to the same wave interaction and resulting acceleration processes. A monodisperse size distribution of spherical particles is assumed for all calculations herein.

4.1.7 Infinite diameter assumption

At the macroscale, the detonation front in practical cylindrical or planar explosive charges has curvature. Increasing the charge diameter reduces the detonation front curvature; in the limit of an infinite diameter charge, the detonation front becomes planar. When considering a small but representative volume of the explosive for the mesoscale modeling domain, a region of the explosive near the centre of a charge is not influenced by the edge expansion (see Figure 4.3) within the timescale analyzed. Further, the mesoscale domain is approximately $3 - 4$ orders of magnitude smaller than a typical charge diameter; hence, the flow divergence is assumed to be negligible. Similarly, the detonation front curvature is much greater than the particle size, and can therefore be assumed to be planar within the mesoscale domain. The resulting model is thus representative of the infinite diameter condition, and detonation failure due to edge expansion is not considered.

4.2 Prototype heterogeneous system

A prototype heterogeneous system, consisting of metal particles saturated with liquid explosive, is studied in this work. Nitromethane (NM), CH_3NO_2, is considered for the condensed matter as it is a uniform, low-viscosity, liquid explosive and is assumed to follow the ZND detonation theory. Spherical aluminum particles are used for the solid phase. Nitromethane/aluminum mixtures form the prototype heterogeneous condensed explosive used in this work, since both NM and NM/Al mixtures have been intensively studied in experiments (e.g., [118, 18, 85, 94, 234, 74, 107, 105, 106]) that help gain physical insights and formulate models. This section discusses the thermophysical and detonation

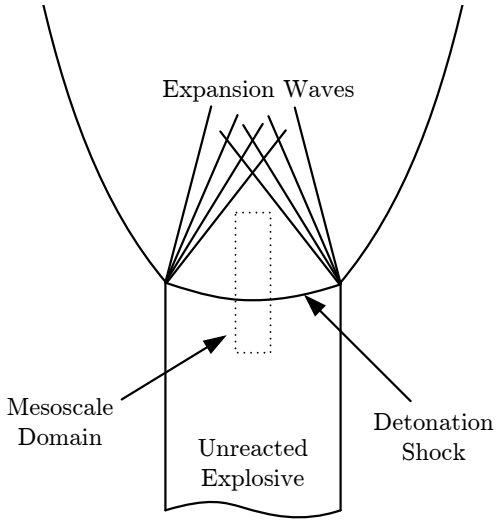

Figure 4.3: Schematic of mesoscale modeling domain relative to an explosive charge (cross section shown; not to scale).

properties of the constituents, develops parameters for the equations of state needed for modeling, and analyzes the timescales for shock interaction.

4.2.1 Thermophysical properties of nitromethane and aluminum

Pure liquid nitromethane is considered. The theoretical maximum density (TMD) of NM is 1.16 g/cc; however, standard temperature and pressure (STP) conditions give a density of 1.128 g/cc, representing 97.24% TMD. Pure aluminum has a solid density of 2.699 g/cc [4] to 2.703 g/cc [98]. The natural oxide coating on aluminum particles has significantly different properties, but it is only a few nanometers thick (Gertsman and Kwok [78], and Gonthier and Rumchik [86]). For micrometric aluminum particles, the oxide coating has a small influence on the thermophysical properties of the bulk material. For such passivated aluminum particles, the accepted nominal solid density is 2.785 g/cc. In some cases, properties of aluminum alloys ($\rho = 2.700 - 2.828$ g/cc [139]) are employed in the modeling. Selected thermophysical properties of the nitromethane/aluminum slurry constituents are tabulated in Table 4.2.

4.2.2 Linear Hugoniots of nitromethane and aluminum

The shock Hugoniot relating the shock velocity, D, to the material velocity, u_{f1}, is commonly expressed as a linear function, $D = C + Su_{f1}$, with the exception of phase change

Table 4.2: Thermophysical properties of the components of the prototype explosive system.

Property	Nitromethane	Aluminum
Density, ρ_0 (g/cc)	1.128	2.785
Molecular weight, W (g/mol)	61.04	26.98
Heat of formation, ΔH_{f0} (kJ/mol)	-112.59 [116]	0
Heat capacity, c (J/kg-K)	1741 (298 K) [214]	883 [98]
Thermal conductivity, k (W/m-K)	0.203 (300 K) [208]	238 [4]
Viscosity, μ (Pa-s)	6.2×10^{-4} (298 K) [214]	n/a

or microstructure change. The fitting coefficients C and S are experimentally determined; they can be found for common materials in Cooper [41] and Drumheller [55], and for unreacted explosives in Marsh [139], Gibbs and Popolato [79], Dobratz and Crawford [47], and Mader [133].

There is some variation in the C and S fitting coefficients in the literature. For nitromethane, Marsh [139] and Mader [133] cite $D = 1.647 + 1.637u_{f1}$ mm/μs for a wide range of shocks in unreacted liquid nitromethane. The data of Marsh and Mader are used in the present work to facilitate comparison to published numerical results. Figure 4.4 shows the shock Hugoniots for aluminum and nitromethane.

4.2.3 VN shock condition of nitromethane

The Rankine-Hugoniot relations (Equation 2.18) are used to calculate the von Neumann (VN) condition of the pure explosive. Using the linear Hugoniot for nitromethane, the shocked fluid velocity can be calculated for a given shock velocity. For $D = 6.612$ mm/μs from Cheetah, the resulting shocked fluid velocity is: $u_{f1} = 3.033$ mm/μs. For $\rho_0 = 1.128$ g/cc, and applying the continuity equation (Equation 2.18a) across a shock, $u_1 = D(1 - \nu_1/\nu_0)$, gives the post-shock density as $\rho_1 = 2.084$ g/cc or specific volume of $\nu_1 = 0.4798$ cc/g. Inserting the linear Hugoniot into the continuity and momentum equations (Equations 2.18a and 2.18b), and neglecting the p_0 term, yields $p_1 = \rho_0(Cu_1 + Su_1^2)$, which gives the VN pressure: $p_{\mathrm{VN}} = 22.62$ GPa. The temperature is calculated using $\nu_1 = 0.4798$ cc/g in the Walsh-Christian equation (Equation 4.1) with temperature fitting parameters for NM from [133]. Table 4.3 summarizes the von Neumann state and provides a comparison to numerical results with good agreement. Note that at the von Neumann shock, the NM is assumed to be inert.

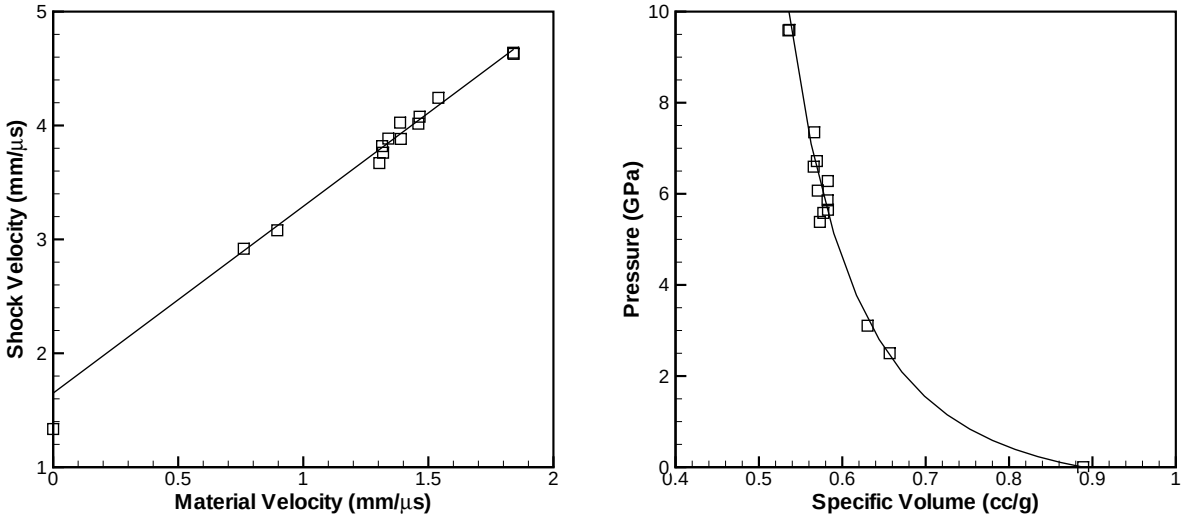

(a) nitromethane: $\rho_0 = 1.128$ g/cc, $C = 1.65$ mm/μs, and $S = 1.64$.

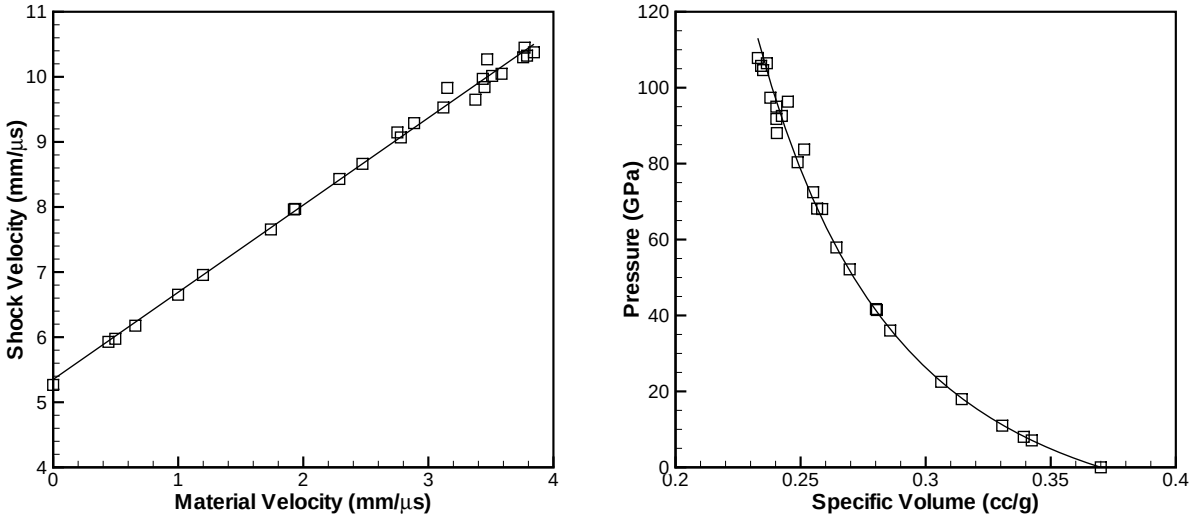

(b) 6061 aluminum: $\rho_0 = 2.703$ g/cc, $C = 5.35$ mm/μs, and $S = 1.34$.

Figure 4.4: Experimental shock Hugoniot data points and fitting curves. Data points and fitting coefficients from Marsh [139].

Table 4.3: The von Neumann shock condition in nitromethane calculated using the Rankine-Hugoniot relations with comparison to numerical results.

Shock Parameter	Analytical	Numerical [170]
Pressure (GPa)	22.62	22.80
Specific volume (cc/g)	0.4798	0.4796
Density (g/cc)	2.084	2.085
Temperature (K)	2768	2790
Shock velocity (mm/μs)	6.612	6.690
Particle velocity (mm/μs)	3.033	3.046

4.2.4 CJ equilibrium condition of nitromethane

In the detonation of liquid nitromethane, the monopropellant is presumed to decompose into a set of gaseous species, as follows:

$$CH_3NO_2 \rightarrow H_2O + CO_2 + CO + N_2 + CH_4 + H_2 + \ldots \tag{4.2}$$

The decomposition begins after the leading shock, and chemical equilibrium is assumed as the flow reaches the CJ point. The reaction products of NM can be estimated using Chemkin [130], CEA [87], or Cheetah [68].

An equation of state (EOS) for the detonation products is required to determine the CJ condition. For instance, the Becker-Kistiakowski-Wilson (BKW) equation of state (Kistiakowsky and Wilson [112]) is commonly used for detonation products. It is a based on a repulsive potential applied to the virial EOS (Mader [132]):

$$\frac{p\nu}{nRT} = 1 + x\exp(bx), \quad x = \frac{k}{\nu}(T+\theta)^a, \quad k = \kappa\Sigma_{i=1}^{n} X_i k_i \tag{4.3}$$

where a, b, κ, and θ are adjustable parameters in the EOS; X_i and k_i are the mole fractions and co-volumes of species i, respectively. Parameters for the BKW EOS for high explosives are given by Cowan and Fickett [43] and Mader [132]. For NM in the present analysis, the BKW parameters are: $a = 0.5$, $b = 0.298$, $\theta = 6620$ and $\kappa = 10.5$.

The particular species sets considered in the BKW EOS have been chosen based on performance comparison to experimental detonation results. In the Cheetah code, the BKWC library generally provides the best results for a wide range of explosives; however, it has only been tested for C-, H-, N-, O-, and F-based explosives [68]. The BKWS library

Table 4.4: The CJ condition for nitromethane detonation computed using Cheetah with various libraries and initial densities (in g/cc).

CJ State Parameter	BKWC ($\rho_{f0} = 1.16$)	BKWC ($\rho_{f0} = 1.128$)	BKWS ($\rho_{f0} = 1.16$)	BKWS ($\rho_{f0} = 1.128$)
Pressure (GPa)	11.89	11.34	13.85	13.16
Specific volume (cc/g)	0.628	0.644	0.634	0.650
Density (g/cc)	1.591	1.553	1.576	1.539
Energy (kJ/cc-explosive)	1.61	1.55	1.83	1.76
Temperature (K)	3669	3664	3621	3628
Shock velocity (mm/μs)	6.149	6.059	6.724	6.612
Particle velocity (mm/μs)	1.667	1.659	1.775	1.764
Speed of sound (mm/μs)	4.483	4.399	4.949	4.847
Gamma	2.690	2.651	2.788	2.748

contains an increased number of species (see Hobbs and Baer [96]) and is more appropriate for aluminized explosives.

The species list (in order of decreasing concentration) for NM decomposition using the BKWC library includes: H_2O, CO, N_2, CO_2, CH_4, H_2, C_2H_4, H_3N, CH_2O_2 CH_3OH, CH_2O, C_2H_6, CH_3, NO, O_2, NO_2, and C. The BKWS calculation resulted in detonation products containing 61 gas species. The CJ condition from Cheetah using the two libraries is shown in Table 4.4. The initial state for nitromethane is compared to the theoretical maximum density ($\rho_{f0} = 1.16$ g/cc). The largest differences are in the CJ pressure and shock velocity when comparing the two libraries.

The CJ condition is based on a one-dimensional detonation wave and, as such, represents the infinite diameter detonation parameters. The accepted nominal detonation velocity and pressure for nitromethane are 6.35 mm/μs and 12.5 GPa, respectively (Dobratz and Crawford [47]), which falls in between the results using the two libraries. The BKWS library was selected since the detonation velocity more closely matches the numerical results of Mader [132] ($D = 6.46 - 6.75$ mm/μs) and the experimental results for pressure $p = 14.1$ GPa given in Mader [132].

4.2.5 Equilibrium detonation of the prototype system

The prototype system consists of aluminum particles saturated with liquid nitromethane explosive. The Cheetah chemical equilibrium analysis code (see Fried et al. [68]) is used

to investigate the detonation velocity deficit and CJ flow temperature by including the presence of aluminum in the explosive mixture. Cheetah assumes a composition mixture at the molecular level and, therefore, the finite metal particle size is not considered. Full mechanical and thermal equilibrium are enforced in addition to the chemical equilibrium. The metal acts as a considerable momentum loss and heat sink for thermal energy. Aluminum is considered inert as justified in Section 4.1.5. In the limit of small particles, where molecular mixing can be assumed, the inert aluminum also acts as an explosive dilutant. Figure 4.5 illustrates the CJ flow velocity, temperature, pressure, density, sound speed, and detonation velocity for equilibrium conditions. As the mass fraction of Al increases, the detonation velocity and pressure decrease monotonically.

The equilibrium detonation represents the lower limit for detonation velocity, while an upper limit can be expressed by the neat NM detonation, where one can consider the phase interactions (mechanical and thermal exchanges) between the particles and NM reacting products as frozen. In reality, the detonation parameters in a heterogeneous system are higher than equilibrium predictions due to non-equilibrium phase interaction processes. The actual heterogeneous detonation lies in between the frozen and equilibrium interaction limits. Numerical modeling is ultimately required to fully resolve the non-equilibrium process of the two-phase flow between explosive and particles.

4.2.6 Analysis of the timescales

Various timescales can be evaluated based on the particle diameter alone by assuming all other flow parameters. A similar comparison was performed by Milne et al. [145]. Considering spherical aluminum particles in a nitromethane detonation, these timescales are evaluated at the CJ detonation shocked flow condition and the VN shocked flow condition by assuming frozen phase interaction within the shock. Both the CJ equilibrium detonation and VN shock state refer to neat nitromethane without aluminum particles.

The shock interaction timescale is defined as the time for the leading detonation shock to cross the particle diameter, $\tau_S = d_p/D_0$. Similarly, the detonation reaction timescale is defined using the reaction-zone length and the detonation velocity, $\tau_D = L_R/D_0$. The timescale for viscous relaxation, thermal relaxation and radiation heat transfer, duplicated from Section 2.1, are summarized here:

$$\tau_V = \frac{4\rho_s d_p}{3\rho_f C_d |u_f - u_p|}, \quad \tau_T = \frac{\rho_s d_p^2 c_s}{6k_f Nu}, \quad \tau_R = \frac{\rho_s d_p c_s |T_f - T_p|}{6\varepsilon_s \sigma_B (T_f^4 - T_p^4)} \tag{4.4}$$

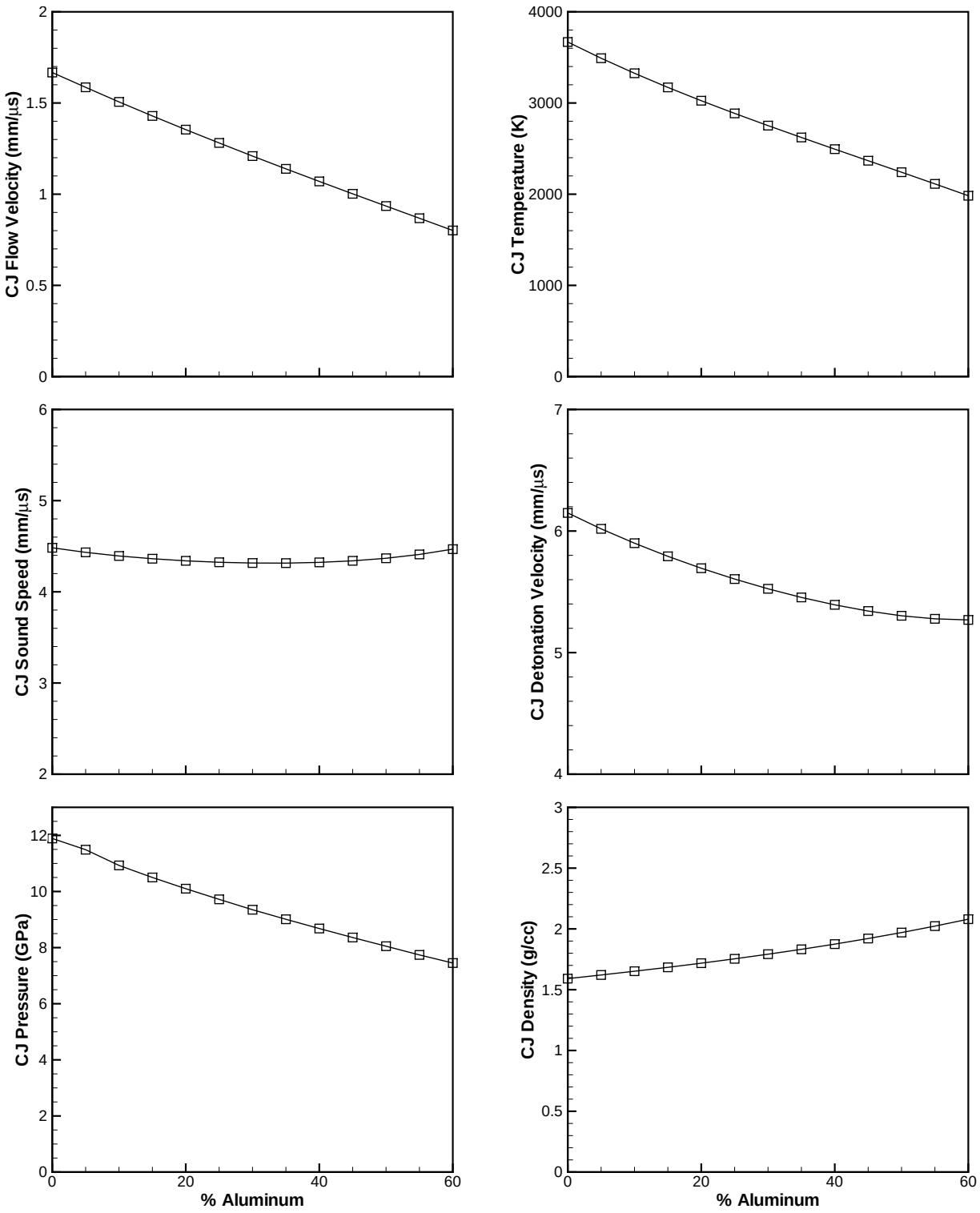

Figure 4.5: Effect of inert aluminum concentration in NM on the equilibrium CJ detonation condition.

Except for the shock interaction process, the timescales above represent the time to reach about 63% of the equilibrium value, since these are exponential processes with asymptotic behaviour.

For this post-shock flow analysis, empirical correlations are required for $C_d = f(M, Re)$ and $Nu = f(M, Re, Pr)$. For simplicity, dilute conditions ($\phi_{s0} \to 0$) are assumed and correlations for steady incompressible flow ($M < 0.3$) are chosen among numerous available options. For drag, the correlation of Gilbert et al. [80] was used:

$$C_d(Re) = 0.48 + (Re)^{-0.85} \tag{4.5}$$

For heat transfer, the Nusselt number correlation of Knudsen and Katz [113] was used:

$$Nu(Re, Pr) = 2 + 0.6 Re^{1/2} Pr^{1/3}, \quad Re < 2 \times 10^5 \tag{4.6}$$

The Reynolds number and Nusselt number for frozen particles in the VN shocked flow and the CJ detonation shocked flow are plotted in Figure 4.6. In the calculations, the thermodynamic properties for the VN shock use the values in Table 4.2. The Prandtl number of the VN state is then $Pr = \mu_f c_{pf}/k_f = 5.22$. For a spherical particle suddenly immersed in the CJ shocked flow, the conditions $u_{p0} = 0$ mm/μs, $u_{f1} = u_{\mathrm{CJ}}$ and $\rho_{f1} = \rho_{\mathrm{CJ}}$ are assumed. The Cheetah calculation gives $c_{pf,\mathrm{CJ}} = 3.7$ kJ/kg-K and $k_{f0} = 0.486$ W/m-K for gaseous detonation products dominantly with H_2O, N_2 and CO_2 ($T_{\mathrm{CJ}} = 3628$ K). There is an order of magnitude range in the molecular viscosity suggested in the literature (cf. Kopyshev et al. [114], Bastea [16], and Gordon and McBride [87]). A conservative estimate of the molecular viscosity of $\mu_f = 0.0001$ N-s/m^2 is selected for the analysis. The resulting CJ Prandtl number is then $Pr = 0.758$. Both the Re and Nu numbers in Figure 4.6 feature an increasing trend for increasing particle diameter. In both cases, there is less than an order of magnitude difference in the results between the CJ and VN shocked flows.

The burning time for particles is assumed to follow the diffusion-limited d^2 law following liquid-droplet combustion theory (Glassman [81]). In this case, infinite chemical kinetics are assumed for the gas-solid reaction, and the burn time is proportional to the initial surface area provided that the surface of the particle has melted:

$$\tau_B = \frac{\kappa d_{p0}^2}{Y_{oxi}^a} \tag{4.7}$$

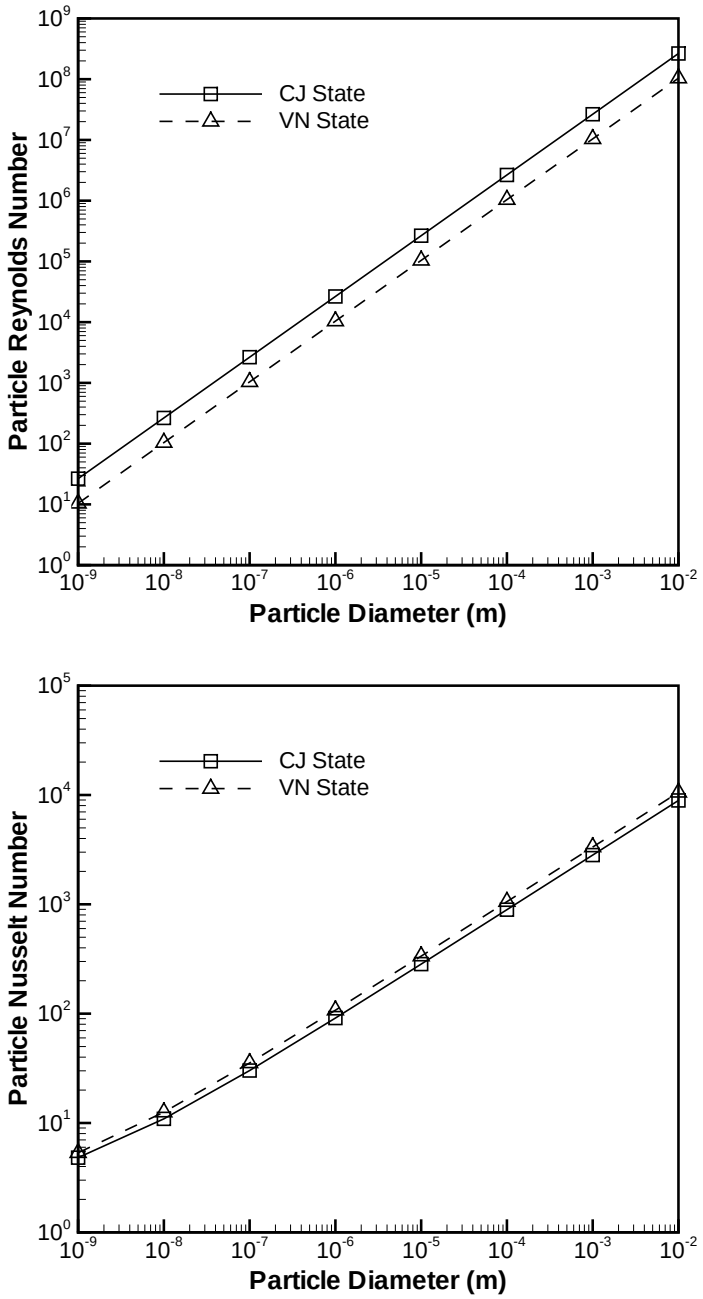

Figure 4.6: Frozen aluminum particles immersed in nitromethane VN shock and CJ detonation flow conditions: Reynolds number (upper) and Nusselt number (lower).

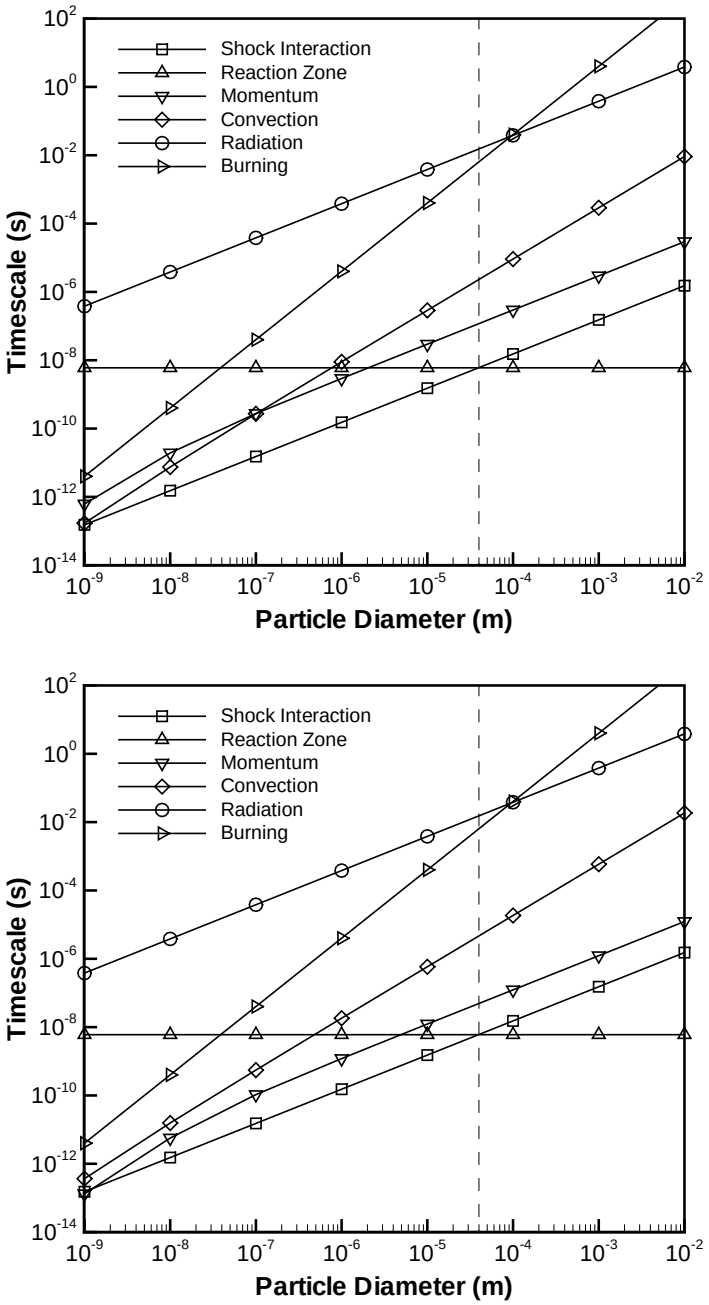

Figure 4.7: Timescales for interaction processes of frozen aluminum particles in a NM detonation. Frozen particles immersed in CJ flow conditions (upper) and immersed in VN shock conditions (lower).

where κ is a metal-dependent constant, a is dependent on the oxidizing gas type, and Y_{oxi} is the mass fraction of oxidizing gases (see Zhang et al. [227] for additional details).

Figure 4.7 shows the timescales as a function of particle diameter for the CJ and VN conditions. The shock interaction time, defined as the characteristic time for the leading shock to cross the particle, is directly proportional to the particle diameter. The timescales may be compared assuming $L_R = 40$ μm and $D = 6.6$ mm/μs for neat NM. For a particle size of 40 μm, the shock interaction timescale is the same as the reaction-zone timescale. Below $d_p = 40$ μm, the shock interaction timescale is less than the detonation reaction-zone timescale. Therefore, for particles $d_p \ll 40$ μm, the particle-detonation interaction falls into the small particle limit ($d_p/L_R \ll 1$) as defined in Chapter 2. For particles $d_p \gg 40$ μm, the particle-detonation interaction becomes in the large particle limit ($d_p/L_R \gg 1$). For particles in between (about 20 – 100 μm for $0.5 < \tau_S/\tau_D < 2.5$), the particles interact with the detonation in the intermediate regime ($d_p/L_R \sim 1$).

For very small particle diameters, the timescales for momentum and heating are proportional to d_p^2, due to low Reynolds numbers in the C_d and Nu correlations (Equations 4.5 and 4.6). Assuming the d-squared rate law for burning, the timescale is proportional to d_p^2 for all particle sizes. Employing empirical laws for drag and convection heating, and including Reynolds number in each, the characteristic timescales deviate from diameter squared, depending on the correlation used. For momentum, the timescale is proportional to d_p for particle sizes above 0.1 μm. For convection heat transfer, the timescale is proportional to $d_p^{1.5}$.

The radiation heat transfer timescale is proportional to d_p for all particle sizes. Using a surface emissivity of $\varepsilon = 0.33$ [98] for aluminum and the CJ temperature for nitromethane detonation, the radiative heat transfer timescale is about six orders of magnitude greater than the shock interaction timescale, and can therefore be safely neglected. The burn time can be used to determine if the particles behave as inert within the detonation interaction timescale. Even if ignition occurs within the explosive reaction zone, the particle burn time is several orders of magnitude greater than the reaction timescale. It is clear from Figure 4.7 that the timescale for burning is considerably longer than the shock interaction time, even when neglecting heating and melting time before burning starts.

The foregoing assumes the limiting case of no shock transmission into particles, where the particles are suddenly immersed in the VN or CJ shocked flow conditions with large impulsive velocity and temperature differences between the flow and particles. Assuming frozen particle/shock interaction (i.e., $u_{p1} = 0$ mm/μs and $T_{p1} = 300$ K), the ratio of shock interaction time to viscous interaction time is:

$$\frac{\tau_S}{\tau_V} = \frac{3\mu_f C_d Re}{4 d_p \rho_s D} = \left(\frac{3}{4}\right)\left(\frac{\rho_f}{\rho_s}\right)\left(\frac{u_f}{D}\right) C_d \tag{4.8}$$

Similarly, the ratio of shock interaction time to thermal heating time is:

$$\frac{\tau_S}{\tau_T} = \frac{6 k_f Nu}{d_p c_s \rho_s D} = \left(\frac{6}{Re}\right)\left(\frac{c_p}{c_s}\right)\left(\frac{\rho_f}{\rho_s}\right)\left(\frac{u_f}{D}\right) Nu \tag{4.9}$$

Inspection of the rearranged equations show all the bracketed terms are typically less than unity. The flow velocity behind a shock must be less than the shock speed. In general, the fluid density is less than the solid density for the range of materials considered. For particles larger than 0.1 μm, the drag coefficient assuming laminar flow approaches Newton's value ($C_d = 0.44$). Table 4.5 summarizes the calculated ratio of shock interaction time to viscous interaction time for aluminum particles in nitromethane.

Table 4.5: Ratio of shock interaction time to velocity and thermal relaxation times for aluminum particles (ρ_s = 2.7 g/cc).

Shock Condition	ρ_{f1} (g/cc)	u_{f1} (mm/μs)	D_0 (mm/μs)	τ_S/τ_V	τ_S/τ_T
10 GPa inert shock in NM	1.875	1.884	4.769	0.09	0.011
VN shock in NM detonation	2.085	3.046	6.612	0.12	0.014
CJ flow in NM detonation	1.538	1.742	6.612	0.05	0.019

For the nitromethane/aluminum system in particular, the shock interaction time is approximately one order of magnitude less than the viscous interaction time and two orders less than the thermal relaxation time. For denser particles, the viscous and thermal interaction timescale increase, further supporting the above conclusion. In lieu of a sensitivity study on the thermophysical properties, caution should be taken due to uncertainty in the thermophysical properties.

For all particle diameters of interest, the characteristic timescale for momentum and thermal exchange are greater than the shock interaction timescale (i.e., $\tau_S \ll \tau_V$ and $\tau_S \ll \tau_T$). Therefore, viscous and thermal relaxation effects can be neglected during the shock interaction timescale and the shock compression process is the dominant mechanism for the particle acceleration and heating. Viscosity and Reynolds number are not significant during the timescale for the leading shock to pass the particle diameter. Similarly, heat transfer by conduction and convection are negligible during the shock interaction process. Therefore, the prototype NM/Al system satisfies the assumptions of inviscid and non-heat-conducting flow during the shock interaction timescale.

4.3 Numerical model at the mesoscale

4.3.1 Governing equations for continuum modeling

Continuum modeling of the aluminum particles-liquid explosive media is conducted at the mesoscale, where the individual constituents occupy large uniform regions of the mesh to represent the packed particle beds. The aluminum material strength has been neglected, assuming that only volumetric strain occurs in the particles. Hence, neglecting viscosity and thermal conductivity as justified earlier, the hydrodynamic response of both the liquid nitromethane and solid aluminum particles can be computed using the three-dimensional inviscid Euler equations, given here in vector notation:

$$\frac{\partial}{\partial t}\begin{bmatrix} \rho_f \\ \rho_f u_f \\ \rho_f v_f \\ \rho_f w_f \\ \rho_f E_f \\ \rho_f Y_{\mathcal{F}} \\ \rho_f Y_{\mathcal{P}} \\ \rho_f Y_{\mathcal{I}} \end{bmatrix} + \frac{\partial}{\partial x}\begin{bmatrix} \rho_f u_f \\ \rho_f u_f^2 + p_f \\ \rho_f u_f v_f \\ \rho_f u_f w_f \\ u_f(\rho_f E_f + p_f) \\ \rho_f u_f Y_{\mathcal{F}} \\ \rho_f u_f Y_{\mathcal{P}} \\ \rho_f u_f Y_{\mathcal{I}} \end{bmatrix} + \frac{\partial}{\partial y}\begin{bmatrix} \rho_f v_f \\ \rho_f v_f u_f \\ \rho_f v_f^2 + p_f \\ \rho_f v_f w_f \\ v_f(\rho_f E_f + p_f) \\ \rho_f v_f Y_{\mathcal{F}} \\ \rho_f v_f Y_{\mathcal{P}} \\ \rho_f v_f Y_{\mathcal{I}} \end{bmatrix}$$
$$+\frac{\partial}{\partial z}\begin{bmatrix} \rho_f w_f \\ \rho_f w_f u_f \\ \rho_f w_f v_f \\ \rho_f w_f^2 + p_f \\ w_f(\rho_f E_f + p_f) \\ \rho_f w_f Y_{\mathcal{F}} \\ \rho_f w_f Y_{\mathcal{P}} \\ \rho_f w_f Y_{\mathcal{I}} \end{bmatrix} = \begin{bmatrix} 0 \\ 0 \\ 0 \\ 0 \\ \omega_f \Delta H_{det} \\ -\omega_f \\ \omega_f \\ 0 \end{bmatrix} \tag{4.10}$$

where u, v, and w are the Cartesian velocity components in the x, y and z directions respectively, E is the total energy, Y is the material mass fraction, ω is the mass-specific reaction rate, and ΔH_{det} is the chemical heat of NM detonation. In Equation (4.10) there are three material mass fractions denoted by $\mathcal{F}$ (fuel) for the liquid NM explosive, $\mathcal{P}$ (products) for the gaseous NM detonation products, and $\mathcal{I}$ (inert) for the solid Al particles treated as inert. Equations of state (EOS) for each material are described below.

4.3.2 Mixture theory for multiple materials

The mixture of unreacted explosive and detonation products within the detonation zone and the material boundaries at the metal particle surface are treated using continuum mixture theory rather than interface tracking. Assuming pressure equilibrium following Benson [24], the mixture density ρ_f in the governing equations (4.10) is expressed by $\rho_f = \sum \rho_j \phi_j$, where each material j ($j = \mathcal{F}$, $\mathcal{P}$, $\mathcal{I}$) has a material density and volume fraction. Mass fractions represent the relative amount of each material: $Y_j = \rho_j \phi_j / \rho_f$. Pressure equilibrium is assumed at any mesh point where more than one material is present, which is obtained iteratively by varying ρ_j and ϕ_j subject to the saturation constraint, $\Sigma \phi_j = 1$, and mass conservation, $\rho_j \phi_j = \rho_f Y_j$. Equations of state (described below) are used to solve for $p_j = f_{EOS}(\rho_j, E_j)$. Once a converged mixture pressure is obtained, the mixture sound speed can be determined using:

$$a_f = \left(\sum_j \frac{\rho_f \phi_j}{\rho_j a_j^2} \right)^{-\frac{1}{2}}, \quad a_j = \left(\frac{\partial p_j}{\partial \rho_j} + \frac{p_j}{\rho_j^2} \frac{\partial p_j}{\partial e_j} \right)^{\frac{1}{2}} \tag{4.11}$$

4.3.3 Equations of state

Two equations of state are used in this work: one to represent the condensed matter (solid particles and liquid explosive), and another for the gaseous detonation products.

Condensed Matter EOS

The unreacted nitromethane and the aluminum particles are modeled using the Mie-Grüneisen (M-G) EOS (see Mader [133]), which gives the expansion solution near the shock Hugoniot. Each material has a Grüneisen parameter, Γ_S, which is the negative of the log slope along an isentrope:

$$\Gamma_S = -\left(\frac{\partial \ln p}{\partial \ln \nu} \right)_S = -\frac{\nu}{p} \left(\frac{\partial p}{\partial \nu} \right)_S \tag{4.12}$$

For materials under compression, the Mie-Grüneisen EOS for pressure and temperature is:

$$p = \frac{\Gamma_S}{\nu} (e - e_H) + p_H, \quad T = \frac{(e - e_H)}{c_v} + T_H \tag{4.13}$$

where ν is the specific volume and e is the specific internal energy. The Hugoniot states (subscript H) are determined using the pressure relation:

$$p_H = \left(\frac{C}{\nu_0 - S(\nu_0 - \nu)} \right)^2 (\nu_0 - \nu) \tag{4.14}$$

The temperature Hugoniot was modeled using Equation (4.1) with fitting to the data of Walsh and Christian [212], as explained in Section 4.1.1. The temperature fitting coefficients (F_S, G_S, H_S, I_S, J_S) and the Hugoniot parameters used for nitromethane and aluminum are summarized in Table 4.6, which were selected from those available for several common materials (see Mader [133]). The shock Hugoniot parameters (C, S and Γ_S) are also available in Drumheller [55] for other metals and in Marsh [139], Gibbs and Popolato [79], and Dobratz and Crawford [47] for unreacted explosives.

Table 4.6: Material and shock Hugoniot parameters selected from Mader [133] for the Mie-Grüneisen EOS with Walsh and Christian temperature fitting.

Parameter	Nitromethane	Aluminum
ρ_0 (g/cc)	1.128	2.785
C (mm/μs)	1.647	5.350
S	1.637	1.350
Γ_S	0.6805	1.7
c_v (kJ/kg-K)	1.7334	0.9205
F_S	5.41	-14.24
G_S	-2.73	-95.75
H_S	-3.22	-155.2
I_S	-3.91	-102.9
J_S	2.39	-23.53

Gaseous detonation products EOS

Although the BKW EOS (see Section 4.2.4) is a proven EOS for detonation products, its power lies in the calculation of state points. Tracking the time evolution and spatial distribution of 61 species required for the BKW EOS is computationally prohibitive, particularly in 3D. Alternatively, a fitting EOS approach is used to represent the isentropic expansion of detonation products.

The expansion of the gaseous detonation products is represented by the Jones-Wilkins-Lee (JWL) EOS (see Lee et al. [124]),

$$p = A\exp(-R_1 V) + B\exp(-R_2 V) + C(V)^{-\omega-1} \tag{4.15}$$

where $V = \nu/\nu_0$ is the volume of detonation products relative to that of the unreacted explosive. In Equation (4.15), A, B, and C are linear fitting coefficients; R_1, R_2, and ω are nonlinear fitting coefficients. The fitting coefficients for many common explosives are tabulated in Dobratz and Crawford [47]. Alternatively, the fitting coefficients can be determined using the Cheetah thermochemical code (see Fried et al. [68]). Lee et al. [123] also published JWL parameters for nitromethane. Table 4.7 compares the Cheetah JWL parameters to the data of Lee et al., and demonstrates significant differences in the JWL coefficients. The JWL coefficients from Cheetah were used in this work.

Table 4.7: JWL parameters for nitromethane detonation products from Lee et al. [123] compared to Cheetah calculations (BKWS library with $\rho_0 = 1.128$ g/cc and $T_{\text{freeze}} = 2145$ K).

JWL Coefficient	Lee et al. [123]	Cheetah
A	209.2	277.2
B	5.689	4.934
C	0.770	1.223
R_1	4.4	4.617
R_2	1.2	1.073
ω	0.30	0.379

4.3.4 Reaction model for nitromethane

The NM detonation model follows the approach of Mader [132] who simulated reaction-zone lengths ranging from 0.24 to 70.5 μm using a single-step Arrhenius reaction law. Other more sophisticated reaction schemes are proposed in the literature, including: two-step Arrhenius (see Korobeinikov et al. [115], Nunziato et al. [151], Kipp and Nunziato [111], and Oran and Boris [153]), and three-step Arrhenius (see Cook et al. [39]); Ignition and Growth (see Lee and Tarver [125]); and, Forest Fire (see Mader and Forrest [134]) models. Simpler models, such as the constant reaction time (CRT) model [38], are insufficient as they are not dependent on temperature and, therefore, will not capture the hot-spot mechanism or detonation failure. Since the goal of this work is to study the mechanical and thermal interaction between the particles and the shock and detonation flow, a single-step Arrhenius reaction model is adequate.

The sensitivity of the nitromethane has been downplayed and it is presumed to react in an ideal manner. A single-step Arrhenius reaction model [3] was employed for the NM detonation:

$$\omega_f = \rho_f Y_{\mathcal{F}} A \exp\left(\frac{-E_a}{RT_f}\right) \tag{4.16}$$

Mader [132, 133] used $A = 1.27 \times 10^{12}$ s^{-1} and $E_a = 1.672 \times 10^5$ J/mol-K for a 7.75 μm long reaction zone. Milne [144] used a pre-exponential factor of $A = 6.9 \times 10^{10}$ s^{-1} and an activation temperature $T_f = 14400$ K from the data of Hardesty [92] for NM; however, this resulted in only five computational cells describing a reaction-zone length of about 10 μm. In the present work, the reaction-zone length is a parameter used in the ratio $\delta = d_p/L_R$, and a target reaction-zone length of 1.0 μm was sought for convenience in the nondimensional analysis. Mader's parameters were adjusted to shorten the reaction zone, using a pre-exponentional factor of $A = 8.0 \times 10^{12}$ s^{-1} while retaining the original activation energy, $E_a = 1.672 \times 10^5$ J/mol-K, which gives $L_R = 2.2$ μm. Similarly, by lowering the activation energy with the Arrhenius parameters $A = 2.0 \times 10^{12}$ s^{-1} and $E_a = 1.4644 \times 10^5$ J/mol-K, the target reaction zone was shortened to 1.8 μm. The reaction-zone length is measured from the leading edge of the VN spike to the sonic point (location where $D = u_f - a_f$), and is dependent on the mesh resolution. In this model, the reaction is 99.99% complete at the CJ point. A heat of detonation of $\Delta H_{det} = 5.725$ kJ/cc was determined using Cheetah [68]. Validation of this detonation reaction model, including the effect of mesh resolution and timestep sensitivity, is presented in Section 4.4.4.

4.4 Model validation

The above governing equations and models are implemented in the Chinook CFD code [140] (Martec Limited). The code is a fully explicit, second-order accurate, compressible flow code founded on a three-dimensional, unstructured mesh, adaptive grid, and parallel computing framework. Chinook employs AUSM [129] and HLLC [17, 203] approximate Riemann solvers, which are flux-vector splitting techniques among various Godunov-type methods (Godunov [84]). Unstructured three-dimensional Green-Gauss and Least-Squares gradients (Ottosen and Petersson [156]) are used in conjunction with multidimensional slope limiters, such as MinMod [207], van Leer [207], and Barth and Jesperson [15]. The above numerical methods, applicable to unstructured meshes, are reviewed in detail in [162].

In the present work, the unstructured mesh and adaptive grid technologies were not utilized in favour of regular uniform structured meshes (quadrilateral and hexahedral), which were used exclusively. The HLLC flux solver was used for all calculations since it is better at handling dense fluids with high sound speeds. This section provides a series of validation tests for multidimensional shock interaction and the detonation reaction model, in comparison to benchmark data. The effect of mesh resolution and solver settings are evaluated for each test case.

4.4.1 One-dimensional multi-component test

Mader [132] compares numerical results of the SIN Lagrangian code to the 2DE Eulerian code for a one-dimensional multi-component problem. These results are used as a validation test case for the present numerical framework, equations of state, and mixture model. The test problem consists of an 8.5 GPa shock in 0.04 cm of nitromethane interacting with a 0.016 cm thick slab of aluminum backed by 0.016 cm of air. The aluminum and air are initially at a pressure of one atmosphere. There are 40 cells across the aluminum slab. The spatial distribution of density is shown in Figure 4.8 at three different times. The pressure, specific volume, temperature, and velocity are compared to the benchmark solutions at the state locations indicated in Figure 4.8. The comparison is summarized in Table 4.8 with excellent agreement.

4.4.2 Solver order of accuracy

The numerical methods are implemented in a second-order TVD framework [93]. Slope limiters are employed to prevent oscillations in the reconstructed solution. Figure 4.9 illustrates the effect of solver order (compression factor) and solver type. The first-order solution is compared to second-order implementations of the MinMod limiter [207] (most dissipative) and Barth-Jesperson (B-J) limiter [15] (most aggressive). The results of the compression factor are compared between the range of $c = 0$ for piecewise constant and $c = 2$ for a piecewise linear solution. Although full compression ($c = 2$) represents a fully second-order solution on uniform meshes, the results in Figure 4.9(a) show undesirable 'overshoot' in the density solution and 'staircasing' in the pressure solution. Reducing the compression to $c = 1$ sharpens the discontinuities and material interfaces without significant numerical instability.

Table 4.8: Comparison of the present numerical results using Chinook to numerical results of the 2DE and SIN codes of Mader [132].

Parameter	**2DE Code (Eulerian)**	**SIN Code (Lagrangian)**	**Chinook (Eulerian)**
Nitromethane Shock (State 0)			
Pressure (GPa)	8.58	8.57	8.58
Specific Volume (cc/g)	0.5455	0.5455	0.5456
Temperature (K)	1146.2	1181.9	1180.6
Velocity (mm/μs)	1.710	1.710	1.710
Reflected Shock in Nitromethane (State 1)			
Pressure (GPa)	17.8	17.87	17.90
Specific Volume (cc/g)	0.4686	0.4858	0.4856
Temperature (K)	1365.5	1436.1	1434.4
Velocity (mm/μs)	0.967	0.964	0.963
Aluminum Shock (State 2)			
Pressure (GPa)	17.85	17.86	17.90
Specific Volume (cc/g)	0.3071	0.3070	0.3070
Temperature (K)	511.0	518.3	519
Velocity (mm/μs)	0.964	0.964	0.965
Aluminum Rarefaction (State 3)			
Pressure (GPa)	0.8	0.04	0.14
Specific Volume (cc/g)	0.3561	0.3603	0.3601
Temperature (K)	380.0	355.5	371
Velocity (mm/μs)	1.873	1.932	1.929

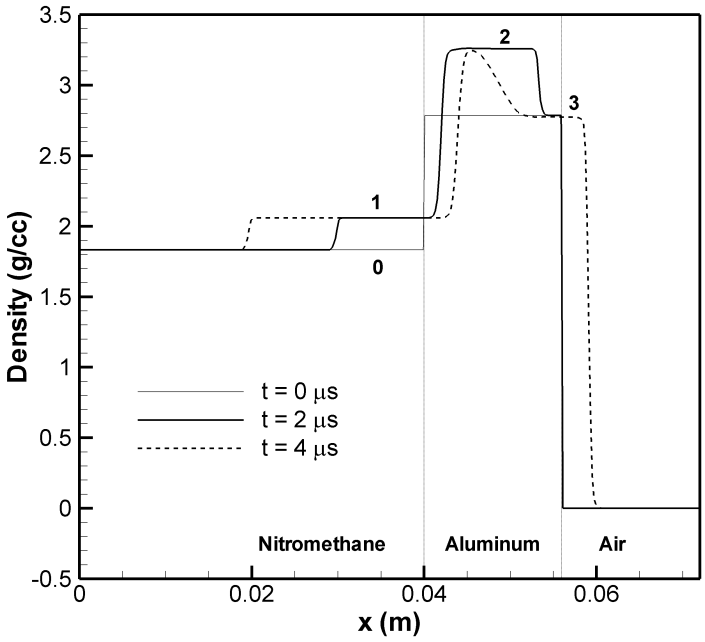

Figure 4.8: One-dimensional results for the multi-component validation problem of Mader [132]. States denoted in the plot: 0 is the nitromethane shock, 1 is the reflected shock in nitromethane, 2 is the transmitted shock in aluminum, and 3 is the rarefaction in aluminum.

4.4.3 Grid convergence study

A grid convergence study was performed using an inert nitromethane shock interacting with an aluminum particle, with results given in Figure 4.10. The results show that the first-order solution has greater error than the second-order methods, and that the higher compression had the smallest error. For velocity, the grid convergence is asymptotic for resolutions above 20 cells per particle diameter. The order of the scheme in the asymptotic convergence region based on velocity was 0.59, 0.93, and 1.70 for $c = 0$, 1, and 2, respectively. For temperature, the grid convergence is asymptotic for resolutions above 40 cells per particle diameter, where the order of the schemes was 0.88, 1.69, and 1.86 for $c = 0$, 1, and 2, respectively. Although the order of the schemes was less for velocity, the magnitude of error was lower for velocity. It should be noted that an error of 10^{-2} in velocity corresponds to a deviation in velocity transmission factor, α, of 0.006; an error of 10^{-2} in temperature corresponds to a deviation in temperature transmission factor, β, of 0.004.

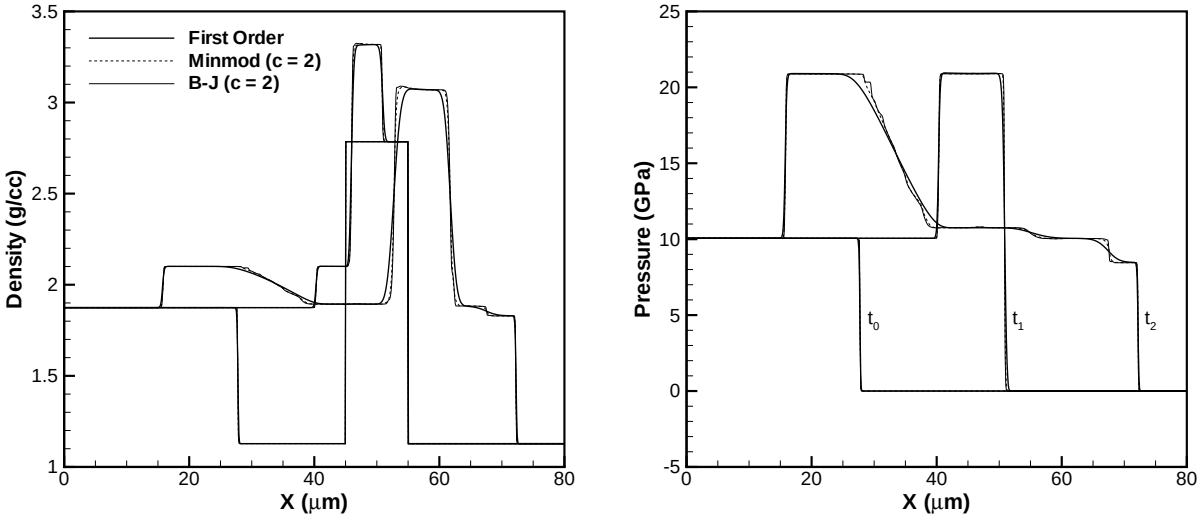

(a) Second-order compression factor of $c = 2$.

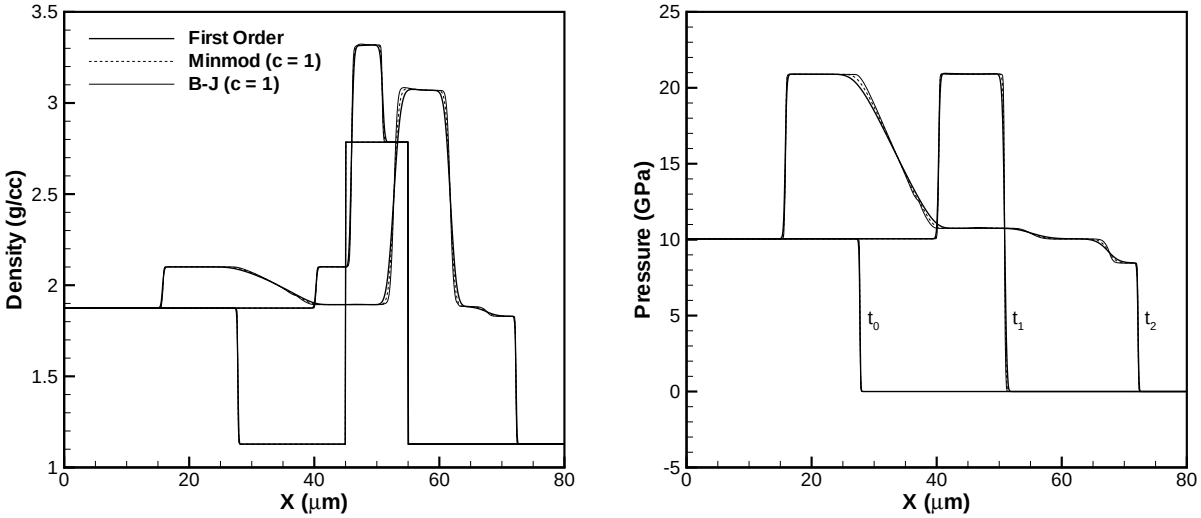

(b) Second-order compression factor of $c = 1$.

Figure 4.9: Solver comparison using various second-order compression factors for a 10.1 GPa inert nitromethane shock interaction with a 10 μm aluminum slab. Results are shown at three different times ($t_2 > t_1 > t_0$).

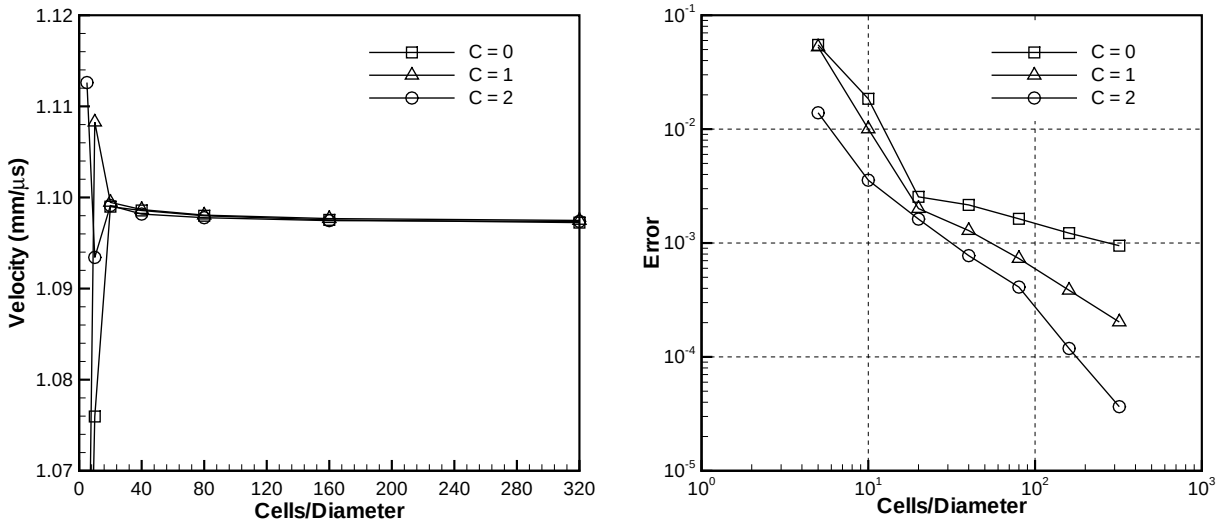

(a) Mesh convergence study for velocity.

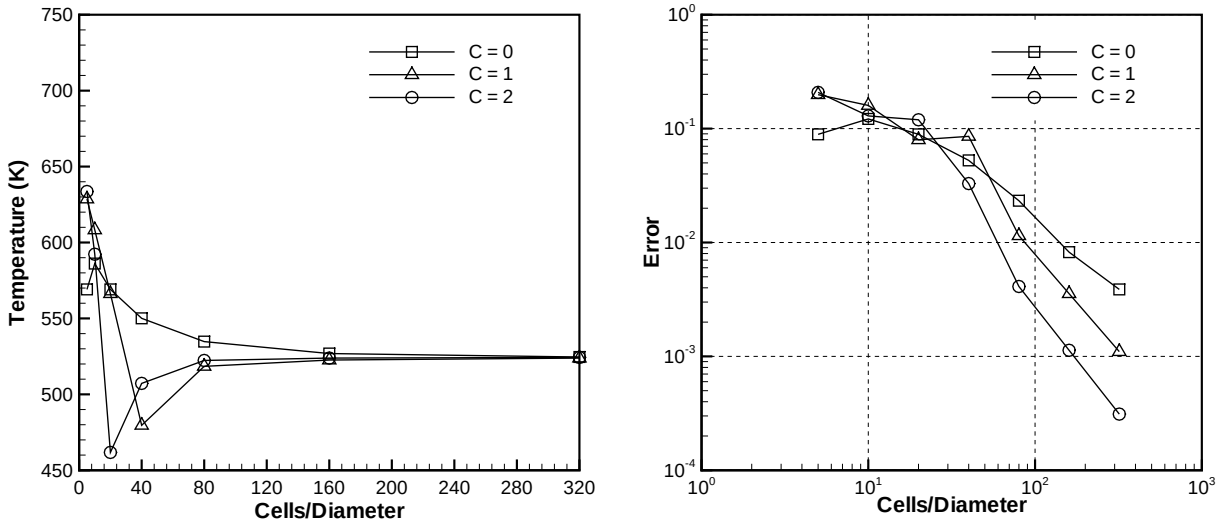

(b) Mesh convergence study for temperature.

Figure 4.10: Convergence of particle velocity and temperature during shock transmission resulting from interaction of a 10.1 GPa nitromethane shock with an aluminum particle.

4.4.4 Nitromethane detonation

Before the reaction model for nitromethane detonation can be validated, numerical stability and grid convergence are required. Sufficient numerical resolution is required to capture the detonation shock and reaction zone. Comparison to a thermochemical equilibrium calculation is conducted after investigating the grid convergence and timestep sensitivity.

Figure 4.11 shows the detonation shock and reaction zone for a sequence of increasing mesh resolutions with cell sizes ranging from 160 to 5 nm. Using finer resolutions increases the peak shock pressure and reduces the reaction-zone length due to the higher temperatures. Table 4.9 summarizes the detonation velocity, shock pressure, CJ flow pressure, reaction-zone length measured at the sonic point ($u_f = D_0 - a_f$), and the corresponding number of cells in the detonation reaction zone, N_R. Mesh resolutions with a computational cell size of $160 \geq \Delta x \geq 5$ nm (625 to 20,000 cells on a 100 μm long one-dimensional domain) correspond to the pressure wave profiles in Figure 4.11. A resolution of 10 nm, with 202 cells in the detonation reaction zone, was selected for the 3D mesoscale calculations.

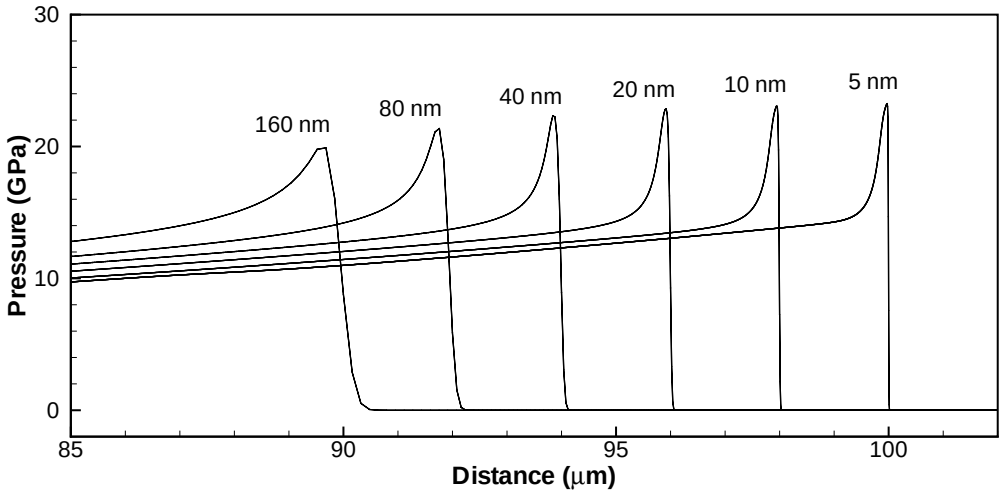

Figure 4.11: Effect of mesh resolution on the 1D nitromethane detonation reaction zone. Profiles plotted at arbitrary distance location for clarity.

The timestep stability is investigated by varying the Courant number. For inviscid flow, the Courant criterion [42] defines the maximum timestep, $\Delta t = \frac{CFL\Delta x}{|u|+a}$, where CFL is the Courant-Friedrich-Lewy number, or simply Courant number. Typically, for simple flows in one dimension, a Courant number of $CFL = 0.5$ is used. However, the multiple equations of state in combination with a reaction model generally require a smaller Courant number.

Table 4.9: Effect of mesh resolution on the nitromethane detonation reaction zone after a running distance of 100 μm.

Δx (nm)	D_0 (mm/μs)	P_{VN} (GPa)	P_{CJ} (GPa)	L_R (μm)	N_R
160	6.640	19.89	13.45	3.76	24
80	6.665	21.36	13.66	2.88	36
40	6.680	22.33	13.71	2.12	53
20	6.690	22.85	13.77	2.05	102
10	6.695	23.06	13.80	2.02	202
5	6.700	23.22	13.84	1.99	398

Figure 4.12 highlights the effect of increasing the Courant number. For $CFL = 0.3$, small oscillations begin in the Taylor expansion. For larger Courant numbers of $CFL = 0.5$ and 0.7, oscillations enter the reaction zone which affects the shock velocity and peak pressure causing instability in the detonation front. Small Courant numbers result in longer simulation times and, therefore, should remain as large as practical. A Courant number of $CFL = 0.25$ was chosen for stability in the calculations involving reactive flow. Inert shock calculations employed $CFL = 0.4$.

Behind the sonic point (i.e., the CJ point), the solution is unsteady with a self-similar Taylor expansion wave. Inside the detonation zone, the flow is subsonic and steady in the shock frame of reference. Formation of a stable reaction zone occurs over a running distance of at least 10 reaction-zone lengths [132]. Figure 4.13 illustrates the detonation wave profiles after running a distance of 100 reaction-zone lengths.

Figure 4.14 illustrates the $p - \nu$ process for the detonation wave. Beginning at State 0, the shocked liquid nitromethane follows a path along the reactants Hugoniot to the von Neumann pressure at which point the chemical reaction begins. In reality, the reaction path taken is along the Rayleigh line; however, in the numerical model the shock process occurs over a few computational cells, each containing an intermediate state that must satisfy the Mie-Grüniesen EOS (see Ripley et al. [163]). During the Arrhenius reaction, the M-G reactants are transformed into the JWL products, which expand from the CJ point to State 1 at the tail of the Taylor wave.

Table 4.10 compares the CJ state calculated using Cheetah to the results of the numerical model. The CJ state in the numerical model was measured where $u_f = D - a_f$. The agreement is deemed acceptable.

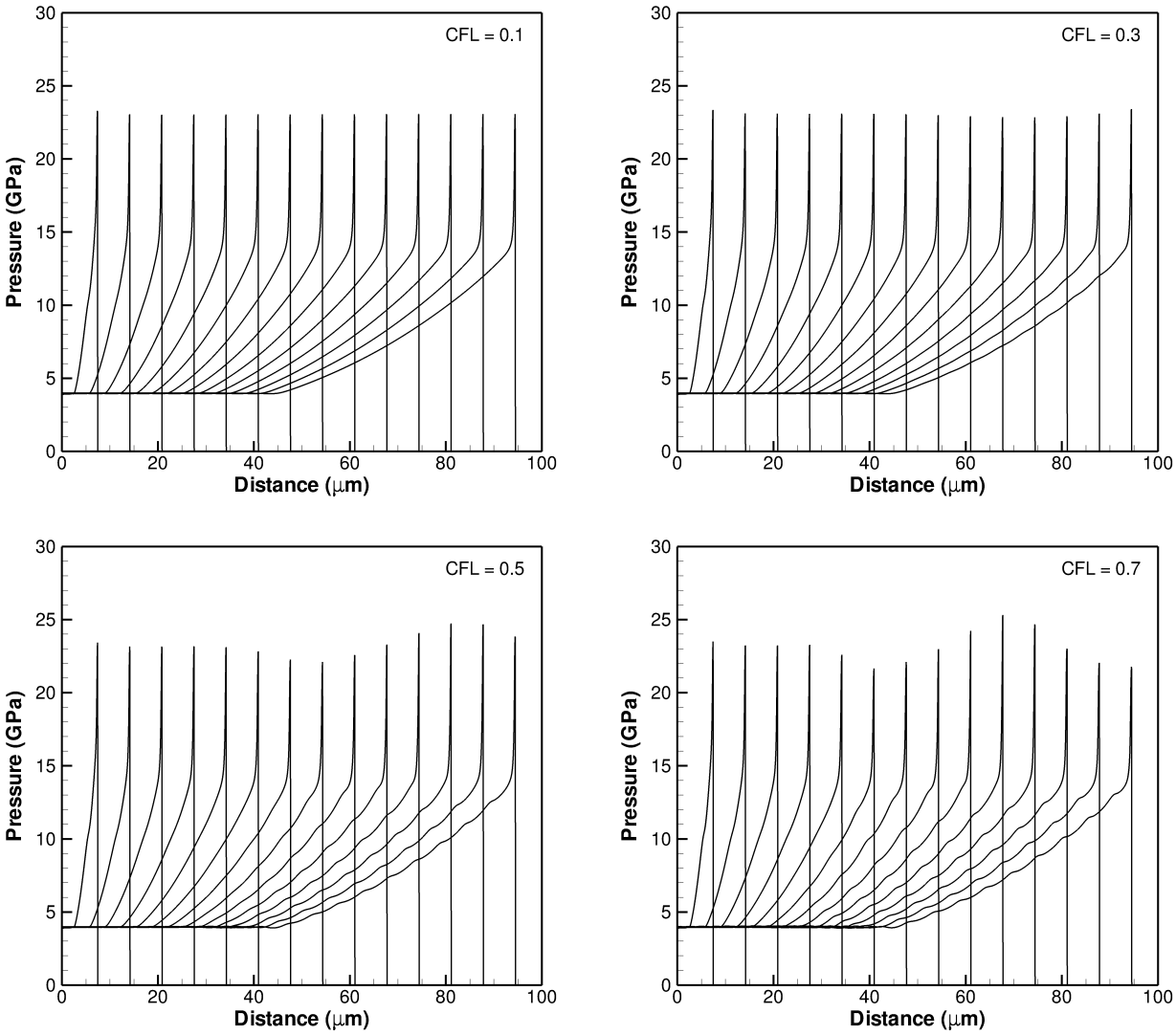

Figure 4.12: Effect of Courant number on the stability of the nitromethane detonation solution.

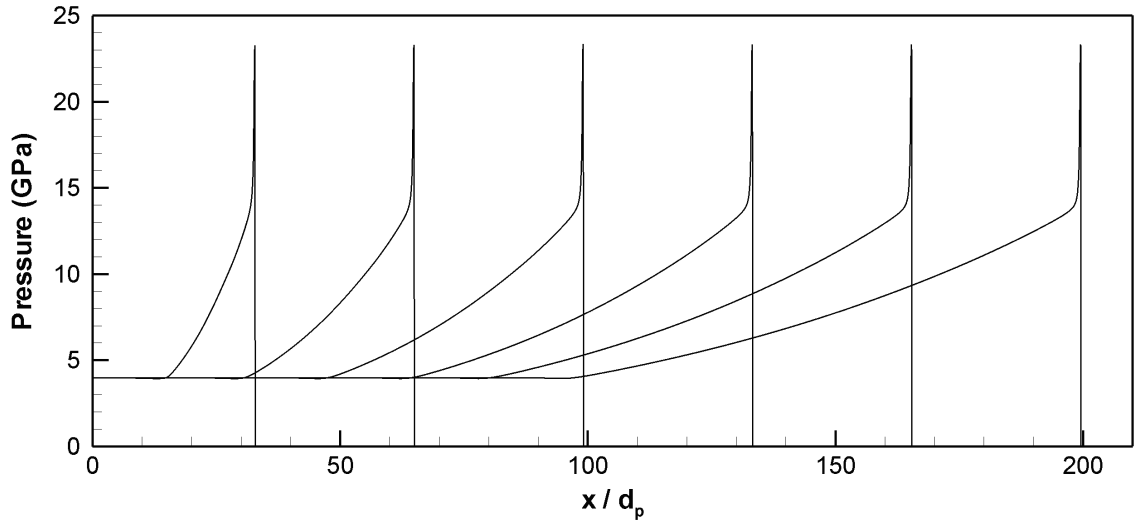

Figure 4.13: Pressure wave pressure profiles with a closed boundary at $x = 0$. For $d_p = 1$ μm, the one-dimensional resolution corresponds to 100 cells/d_p with a total of 20,000 cells in the 1D domain.

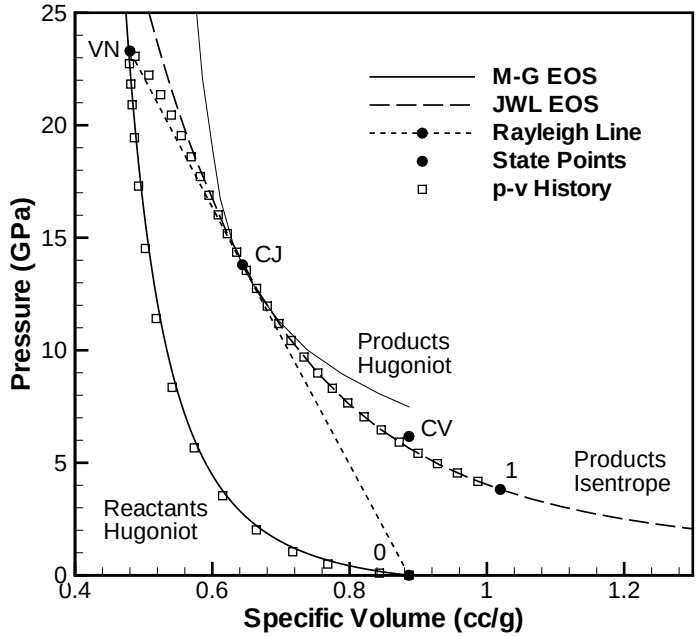

Figure 4.14: Detonation process (numerical $p - \nu$ history) overlaid on the model equations of state and key state points.

Table 4.10: Comparison of the Chapman-Jouguet state from the numerical model to Cheetah (BKWS library).

CJ State Parameter	Cheetah	Numerical
Detonation Velocity (mm/μs)	6.612	6.690
Density (g/cc)	1.538	1.551
Pressure (GPa)	13.16	13.80
Temperature (K)	3628	3657
Gas Velocity (mm/μs)	1.742	1.827
Sound Speed (mm/μs)	4.847	4.867

4.5 Problem configuration

4.5.1 Initial particle packing configurations

Ordered matrices of spherical aluminum particles saturated with liquid nitromethane are simulated at the mesoscale for various particle spacings covering an order-of-magnitude range of volume fractions from $0.065 \leq \phi_{s0} \leq 0.740$. Three packing configurations were considered, as illustrated in Figure 4.15. The close-packed configuration (face-centered cubic lattice arrangement) was selected for most of the calculations since it provides the densest loading conditions. Table 4.11 compares the solid volume fraction for the various packing configurations. The dilute limit ($\phi_{s0} \to 0$) is simulated using a 2D axi-symmetric model of a single spherical particle, while the dense limit ($\phi_{s0} \to 1$) is simulated using a 1D model of a semi-infinite solid slab.

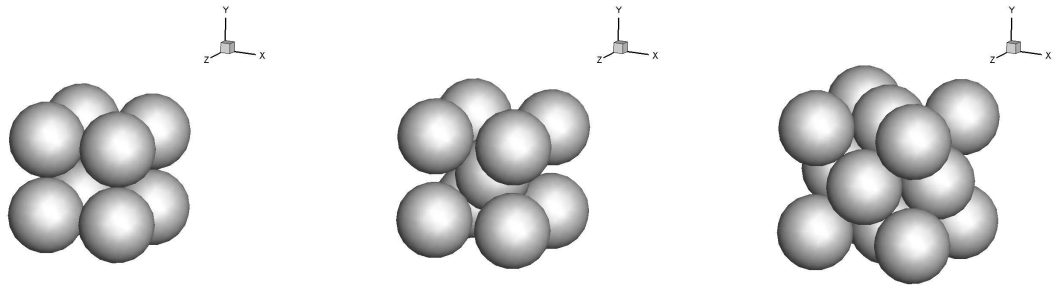

Figure 4.15: Geometric arrangements of packed spherical particles: simple cubic (SC); $\phi_{packed} = 0.52$ (left); body-centred (BC), $\phi_{packed} = 0.68$ (centre); and, close packed (CP), $\phi_{packed} = 0.74$ (right).

Table 4.11: Theoretical and experimental volume fractions of packed particle beds.

Packing Configuration	Volume Fraction, ϕ_{packed}	
	Theoretical	Approximate
Simple cubic (SC)	$\pi/6$	0.52
Body-centred cubic (BC)	$\sqrt{3}\pi/8$	0.68
Close-packed (CP), also called face-centred cubic packing	$\sqrt{2}\pi/6$	0.74
Random packing	-	0.58 - 0.62
Loose powder	-	0.5 (typ.)

Table 4.12: Volume fraction as a function of particle spacing in various matrix configurations from Ripley et al. [168].

Inter-particle Spacing, s	Face-Centred (Close Packed)	Body-Centred Packing	Simple-Cubic Packing
0	0.740	0.680	0.520
$0.1d_p$	0.556	0.511	0.391
$0.2d_p$	0.428	0.394	0.301
$0.4d_p$	0.270	0.248	0.190
$0.8d_p$	0.127	0.117	0.089
∞	0.000	0.000	0.000

4.5.2 Particle spacing and volume fraction

The spacing between the surfaces of two spheres (i and j) positioned at (x_i, y_i, z_i) and (x_j, y_j, z_j) is defined as:

$$s_{ij} = \sqrt{(x_i - x_j)^2 + (y_i - y_j)^2 + (z_i - z_j)^2} - \frac{d_i + d_j}{2} \tag{4.17}$$

The matrix volume fraction for mono-sized spheres with spacing, s, is:

$$\phi_{matrix} = \phi_{packed} \left(\frac{d_p}{d_p + s} \right)^3 \tag{4.18}$$

Table 4.12 summarizes the volume fractions for various inter-particle spacing distances and particle packing configurations, which are independent of material type.

The solid mass fraction is more commonly used in experiments since it can be measured directly. The relationship between volume and mass fraction is $Y_j = \rho_j \phi_j / \rho_{mix}$, where

the bulk mixture density is $\rho_{mix} = \sum_j \rho_j \phi_j$. Table 4.13 summarizes the volume fraction, mass fraction, and bulk mixture density for various particle spacings in a nitromethane/aluminum matrix.

Table 4.13: Solid fraction and bulk density for close-packed particle matrices of aluminum particles saturated with nitromethane.

Inter-particle Spacing, s	**Volume Fraction, ϕ_{s0}**	**Mass Fraction, Y_{s0}**	**Bulk Density ρ_{mix} (g/cc)**
0	0.740	0.875	2.354
$d_p/20$	0.639	0.814	2.187
$d_p/10$	0.556	0.756	2.049
$d_p/5$	0.428	0.649	1.837
$d_p/2$	0.219	0.409	1.491
d_p	0.093	0.202	1.282

4.6 Computational domain

The primary computational domains for the mesoscale calculations employ 3D Cartesian grids that contain the packed particle beds. The mesh is uniform in the vicinity of the shock and the particles; geometrically-expanding meshes are used to extend the domain upstream and downstream of the region of interest. The limiting case of a single particle utilizes a 2D axi-symmetric mesh, and the solid limit involves a 1D planar domain – both employ the same mesh resolution and expanding mesh away from the region of interest. This section describes the computational domain, boundary conditions, initial conditions, mesh resolutions, and mesh decomposition for parallel computing used in this work.

4.6.1 Representative volume element

Mesoscale domains are typically very small (1 μm – 1 cm) and contain $\mathcal{O}(100)$ grains or particles. For the model results to be representative of the larger heterogeneous material, Markov [138] introduced the concept of a representative volume element (RVE). The mesoscale domain must describe a small but representative region of material that is sufficiently large to capture the statistical response. For realistic heterogenous matter, Baer [7] suggests at least four grains (particles) across the width of a domain. However,

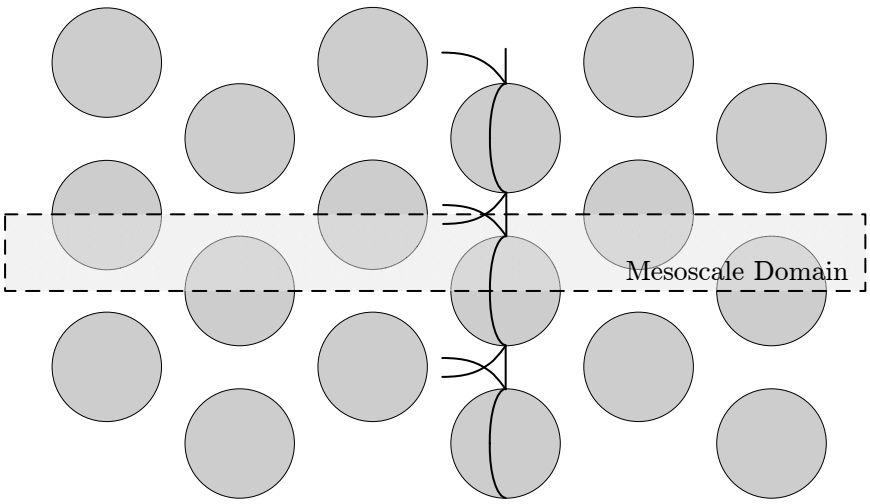

Figure 4.16: Minimum mesoscale domain size in a regular geometric arrangement of particles with symmetric shock interaction. Two dimensions shown for simplicity.

since the particles in the present work are mono-sized and arranged in a regular geometric pattern, the solution is periodic in the transverse direction. Therefore, a significantly smaller domain can be investigated, as illustrated in Figure 4.16. Prescribing reflective boundary conditions to the mesoscale domain enforces symmetry and provides a periodic solution.

In three dimensions, the mesoscale domain boundaries cut through the spherical particles. The particles are one-quarter sphere segments aligned on orthogonal symmetry planes, representative of spherical particles in a semi-infinite matrix. A total of 20 – 40 spherical particles are included. The dimensions of the domain are therefore proportional to the particle diameter and inter-particle spacing. For 1 μm particles with a 1 μm spacing in a close-packed matrix, the domain dimensions are $15.0 \times 1.41 \times 1.41$ μm.

4.6.2 Initial conditions

Various initial conditions are required to evaluate the different detonation interaction regimes (see Section 2.5). These include inert Heaviside shocks for the small particle limit, reactive Heaviside shocks in the large particle limit, and detonation wave profiles for the intermediate regime. The limiting interaction regimes are established using jump conditions applied to a region ahead of the particle bed, as shown in Figure 4.17. An inflow boundary condition upstream of the particles provides the piston effect that supports the rear shocked flow. This is different from the initial conditions normally used in shock tubes,

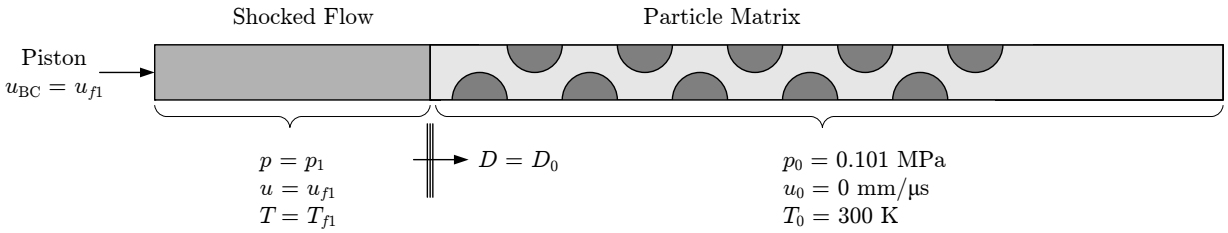

Figure 4.17: Typical problem setup for the limiting interaction regimes.

since both the shock and post-shock flow are initialized with their respective velocities. Furthermore, since the CJ shock also features a material interface, the reaction model is used but with an infinite reaction rate to provide an instantaneous conversion from reactants to products within the shock front. Table 4.14 summarizes the jump conditions for the four initial discontinuities that utilize the Heaviside shock conditions.

Table 4.14: Jump conditions for initial Heaviside discontinuities in nitromethane.

Property	**8.58 GPa Shock**	**10.1 GPa Shock**	**CJ Shock**	**VN Shock**
D_0 (mm/μs)	4.454	4.769	6.690	6.690
ρ_{f1} (g/cc)	1.833	1.875	1.538	2.085
p_1 (GPa)	8.58	10.1	13.8	22.8
u_{f1} (mm/μs)	1.710	1.884	1.758	3.046
T_{f1} (K)	1181	1336	3592	2790
Shocked material	Liquid	Liquid	Gas	Liquid

For the cases involving detonation interaction with the particle matrices, a detonation wave profile is first computed in 1D and then mapped onto the 3D domain. Prior to the detonation wave entering the packed particle matrix, the detonation is run out to a distance of 1.0 mm. This was done to reduce the gas expansion rate in the Taylor wave during the interaction with metal particles, as shown in Figure 4.18.

With the Taylor expansion effect minimized, a 1D spatial wave distribution is selected to initialize 3D meshes of the same resolution containing the particle bed. The resulting initial condition on the 3D mesh contains the same detonation wave profile from the 1D mesh. Therefore, the 3D detonation wave is initially perfectly planar. This initialization method is fully conservative since the meshes have identical resolutions. Figure 4.19 shows the detonation wave profile (from $t = 970\tau$ in Figure 4.18) applied to a three-dimensional mesh as the initial conditions for studying the detonation wave interaction with the particle matrix.

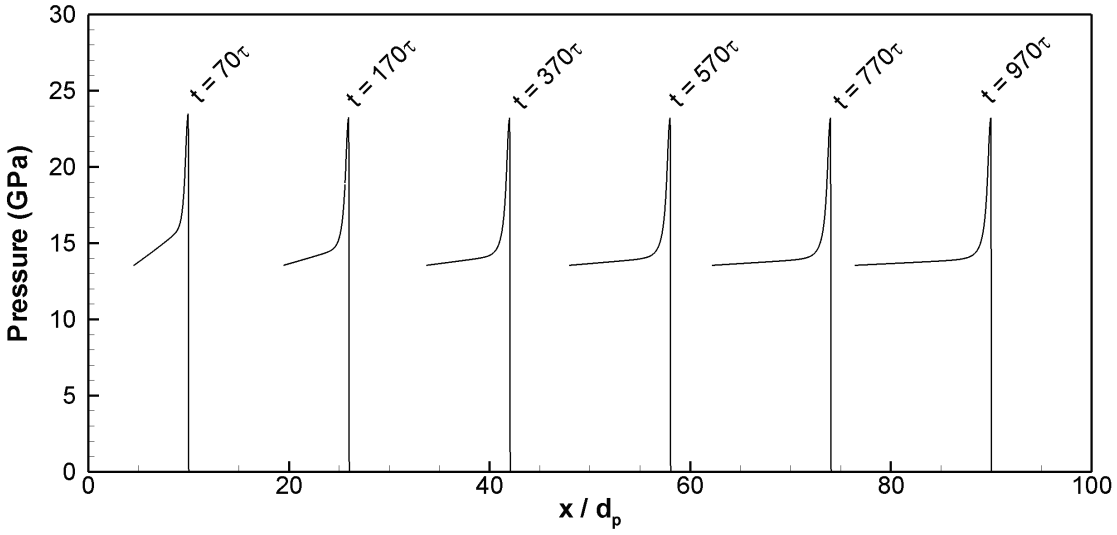

Figure 4.18: Effect of detonation running distance on reducing the Taylor wave expansion. One-dimensional profiles obtained using 100,000 cells over a 1 mm long mesh. Profiles plotted at arbitrary x locations for clarity ($d_p = 1$ μm).

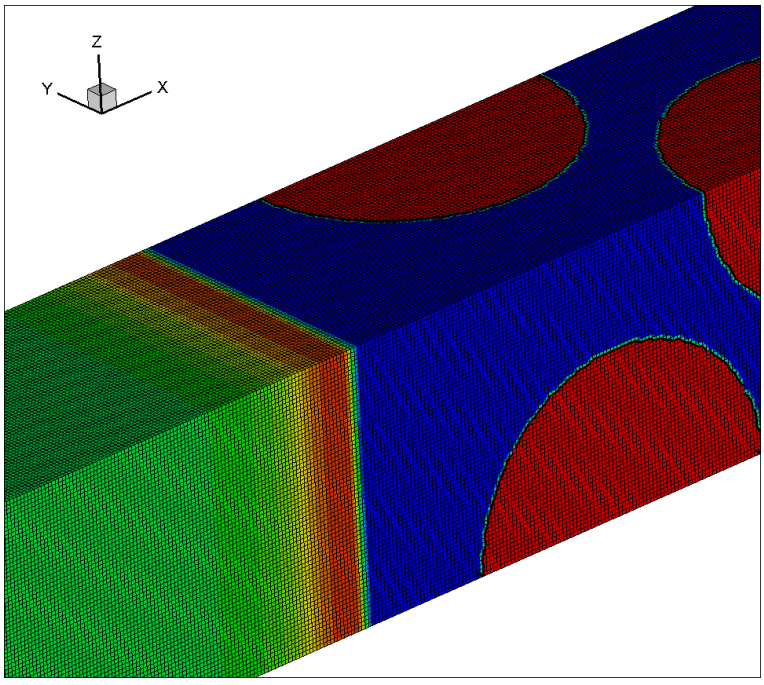

Figure 4.19: Initialized 3D mesoscale domain for detonation conditions and close-packed particle arrangement. Colour contours represent material density. Black lines show the elements of the hexahedral mesh (mesh resolution of 80 cells / particle diameter).

Table 4.15: Computational mesh details for 80 cells per particle diameter employed in Ripley et al. [169].

Inter-particle Spacing, s	Volume Fraction, ϕ_{s0}	Number of Cells per Direction ($X \times Y \times Z$)	Total Number of Cells	Number of CPU
0	0.74	$869 \times 56 \times 56$	2,725,184	16
0	0.74	$1669 \times 56 \times 56$	5,233,984	32
$0.2d_p$	0.428	$1069 \times 68 \times 68$	4,943,056	32
$0.5d_p$	0.219	$1069 \times 85 \times 85$	7,723,525	16
d_p	0.093	$1269 \times 113 \times 113$	16,203,861	16

Table 4.16: Computational mesh details for 100 cells per particle diameter employed in Ripley et al. [170].

Inter-particle Spacing, s	Volume Fraction, ϕ_{s0}	Number of Cells per Direction ($X \times Y \times Z$)	Total Number of Cells	Number of CPU
0	0.74	$1075 \times 71 \times 71$	5,419,075	100
$0.2d_p$	0.428	$1269 \times 85 \times 85$	9,168,525	100
$0.5d_p$	0.219	$1319 \times 106 \times 106$	14,820,284	100
d_p	0.093	$1569 \times 142 \times 142$	31,637,316	100

4.6.3 Resolution and domain decomposition

The early work of Mader [132] used only five mesh points across particle inclusions. In 2D calculations, Zhang et al. [229] used 20 cells and Milne [144] used 50 cells across the particle diameter. Here, resolutions of 40, 80 and 100 cells per particle diameter were considered for both 2D and 3D calculations. As shown in §4.4.3, these resolutions are in the asymptotic grid convergence region with an acceptable error magnitude. The resulting high-resolution 3D meshes contained up to 32 million cells, which required the use of parallel computing on a distributed memory network. The Message Passing Interface (MPI) was used for up to 100 CPU. Tables 4.15 and 4.16 summarize the computational mesh details. Figure 4.20 shows a typical example of the parallel domain decomposition obtained using simple geometric division. Each partition contains between 50,000 and 300,000 computational cells.

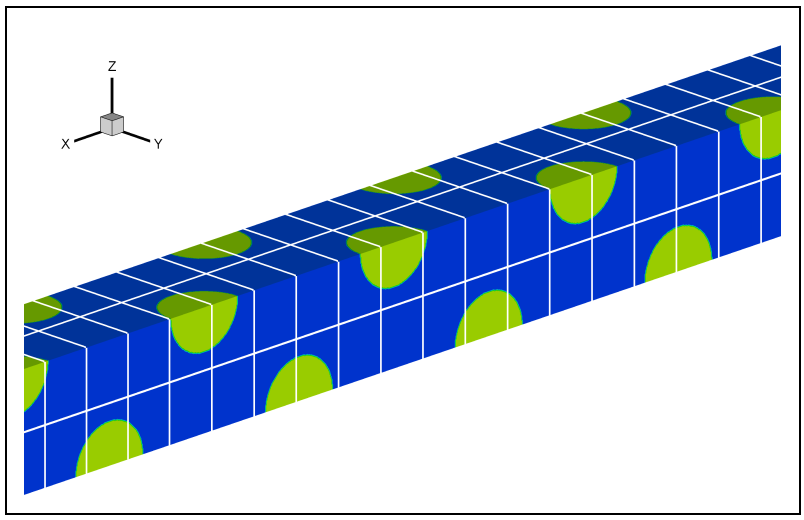

Figure 4.20: Parallel partitioning of the 3D mesoscale domain: 25 × 2 × 2 partitions configured for 100 CPU parallel computation. Partition boundaries shown by white lines.

4.7 Diagnostics

The large data size generated using the 3D meshes prevented frequent output of the volumetric data. Numerical gauges were embedded in the flow to report the local conditions at a high frequency. Gauge data were output at every numerical timestep, which is very small. Further, on-the-fly analysis of a candidate particle was performed and the reduced data were recorded. This analysis has an associated computational cost; therefore, it was only conducted at a lower frequency, typically at 10 – 20 times per shock interaction time.

Candidate particles were studied 6 – 8 layers into the matrix, where the interaction became quasi-steady in the absence of starting and end effects [169]. Figure 4.21 shows a typical particle matrix with the location of numerical gauges and highlights the candidate particle. The gauges provide pressure, temperature, and flow velocity output. The wave propagation velocity through the matrix can be measured using the time of arrival between consecutive gauges. Additional gauges were located at the mass-centre, side edge, leading edge, and trailing edge of the particles, but were only used for limited scoping studies.

4.7.1 Particle acceleration and heating

Results from mesoscale calculations were used to observe the behaviour of each particle under shock and detonation conditions, and in various particle packing densities and configurations. The theoretical mass of an individual particle is: $m_p = \rho_s \frac{\pi}{6} d_p^3$. For

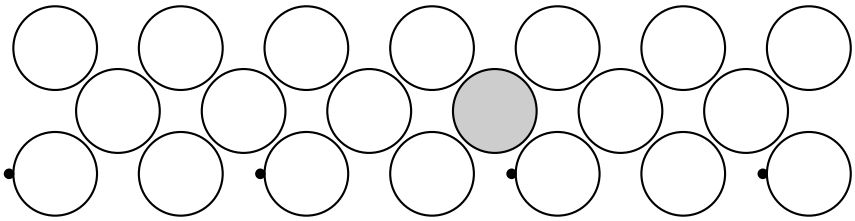

(a) Gauges at the particle leading edges.

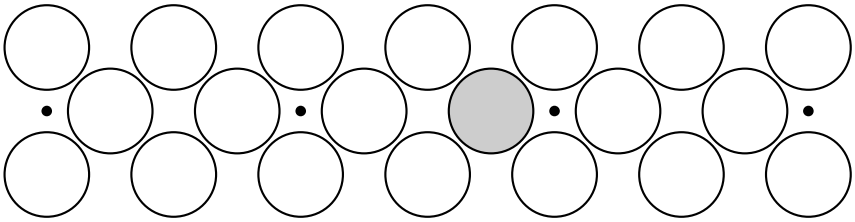

(b) Gauges located in voids between particles.

Figure 4.21: Diagnostics in the mesoscale model: location of gauges embedded in the particle matrices and candidate particle highlighted.

deforming particles in the mesoscale calculation, where the mass distribution within the particle varies during shock compression, the time-dependent local particle mass is calculated by integrating over the cells ($i = 0 \ldots N$) in the mesoscale mesh; each cell has a volume $\mathrm{d}V = \Delta x \Delta y \Delta z$.

The specific candidate particle (see Figure 4.21) is uniquely initialized with a passively-advected scalar, Y_p, such that its mass, velocity, and temperature could be measured independently of other particles. For the mass integration:

$$m_p(t) = \iiint_V \rho Y_p \mathrm{d}V = \sum_i^N \rho_i Y_i \Delta x \Delta y \Delta z \tag{4.19}$$

The time-dependent, mass-averaged velocity and temperature were examined by integrating in discrete form:

$$u_p(t) = \frac{1}{m_p} \iiint_V \rho_p u_p Y_p \mathrm{d}V = \frac{1}{m_p} \sum_i^N (\rho_p u_p Y_p)_i \Delta x \Delta y \Delta z \tag{4.20a}$$

$$T_p(t) = \frac{1}{m_p} \iiint_V \rho_p T_p Y_p \mathrm{d}V = \frac{1}{m_p} \sum_i^N (\rho_p T_p Y_p)_i \Delta x \Delta y \Delta z \tag{4.20b}$$

Figures 4.22 and 4.23 show a comparison of local velocity and temperature measurements to the mass-averaged values. The velocity and temperature measurements at the

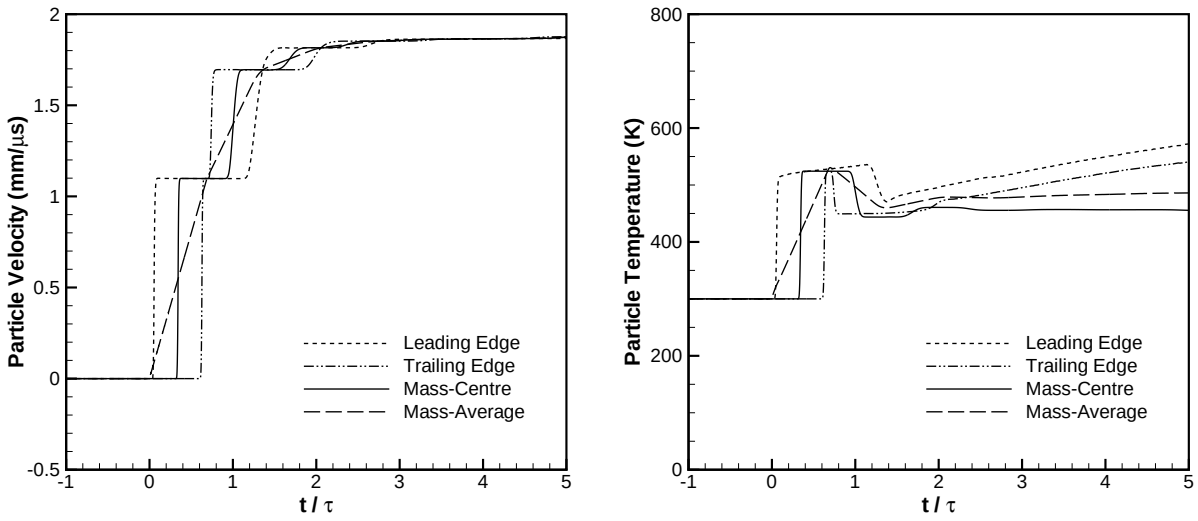

Figure 4.22: Comparison of mass-averaged particle velocity (left) and temperature (right) with local measurement points in a single slab particle ($d_p = 10$ μm). Gauges located at the leading edge, mass centre, and trailing edge.

leading, trailing, and side edges demonstrate the significant influence of the complex wave interactions at the edge of the particle. The mass-averaged velocity and temperature are representative of a composite measurement of the various locations including the mass-centre gauge. The mass-averaged quantity integrated over the entire volume of the particle tends to smooth the discontinuities (internal shocks and expansions) and provide a bulk response for the mesoscale behaviour.

4.8 Summary of modeling approach

In this chapter, the modeling assumptions and simplifications were justified using evidence from the literature. This includes using inert, spherical, mono-sized particles that are not melted or damaged within the detonation interaction timescale. The prototype heterogeneous explosive, consisting of aluminum particles saturated with liquid nitromethane, was analyzed both at the individual constituent level, and together as an explosive system. The behaviour and timescales present in the prototype explosive system were further used to confirm the assumptions. The numerical model for mesoscale simulation was presented; this included the governing equations, equations of state, and detonation reaction model. Validation of the method was performed using a benchmark test case, followed by a grid convergence study and evaluation of the order of accuracy, and

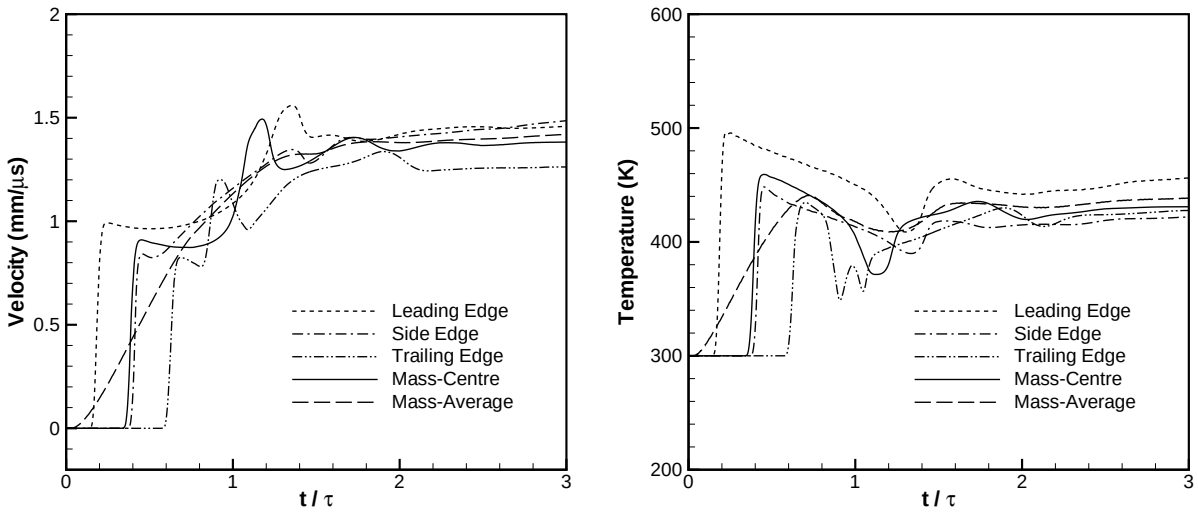

Figure 4.23: Comparison of mass-averaged particle velocity (left) and temperature (right) with local measurement points in a single spherical particle (d_p = 30 μm). Gauges at the leading edge, side edge, mass centre, and trailing edge.

the effect of mesh resolution and timestep sensitivity on the detonation reaction model. The computational domain for the mesoscale simulations was presented, including the geometric arrangement and spacing between the particles, mesh resolution requirements, initial and boundary conditions, and domain decomposition for parallel computing. Finally, the diagnostic methods were explained along with a comparison of measurement locations and techniques.

Chapter 5

Results of continuum modeling of particles at the mesoscale

This chapter investigates and quantifies the velocity and temperature transmission factors during shock compression using continuum modeling. Mesoscale simulations of single particles and matrices of packed particles are conducted to determine the particle acceleration and heating during shock and detonation interaction. The effect of impedance ratio is investigated using inert shocks in simple slab models. The effect of the explosive-to-solid density ratio, previously identified by Zhang et al. [229], is reproduced using inert shock interaction with single particles of magnesium, aluminum, copper, titanium, and tungsten. The remaining calculations focus exclusively on the nitromethane/aluminum system, including reactive shock and detonation wave interaction. The full range of volume fraction is studied by varying the spacing between particles, and considering the limiting cases of a single particle (dilute limit, $\phi_{s0} \to 0$) and wave transmission into a semi-infinite slab (dense limit, $\phi_{s0} \to 1$). The full range of the ratio of particle diameter to detonation reaction-zone length, $\delta = d_p/L_R$, is also studied by considering the small particle limit using inert shock interaction, and the large particle limit using CJ shock interaction. The intermediate regime of δ is investigated by varying the particle diameter for a fixed detonation reaction-zone length. At the end of this chapter, velocity and temperature transmission factors are compiled and presented in terms of the volume fraction and the ratio of particle diameter to detonation reaction-zone length. Finally, the free-edge condition is investigated as a boundary condition using two-dimensional cylindrical particles.

5.1 Results for planar slab particles

Shock and detonation interaction with semi-infinite slabs, single slab particles, and layers of slab particles provide a clear illustration of the fundamental physics without the complexities of packed matrices by removing three-dimensional and curvature effects. Slab calculations are performed using one-dimensional domains of comparable mesh resolution to the primary 3D models. The slab models demonstrate shock transmission and reflection, and the resulting single particle acceleration and heating. The effect of impedance ratio is illustrated using characteristic wave diagrams and records of particle velocity and temperature. The interactions between slab particles and arrays of slab particles highlight the multiple particle/wave interactions that occur in more complicated three-dimensional matrices.

5.1.1 Shock interaction with a single slab

Liquid shock interaction with a single particle slab illustrates and quantifies the important wave physics. The incident shock transmits into the particle and reflects from the leading edge. Velocity and pressure are continuous at this interface (as in the Riemann solution [203, 128]). Once the transmitted shock reaches the trailing edge, the shock is further transmitted into the liquid downstream of the particle, and reflected within the particle towards the leading edge, thereby affecting the particle velocity and temperature. At later times, successive compressions and expansions reverberate within the particle, and interact with the material interfaces at the leading and trailing edges.

Figure 5.1 shows the shock interaction with a single aluminum slab particle ($d_p = 10$ μm) surrounded by liquid nitromethane. The spatial distribution of density, velocity, pressure, temperature, sound speed, and mass fraction are given at three key times: before, during, and after the primary shock interaction at the material interface. The resulting transmitted and reflected wave states are summarized in Table 5.1 for three cases: an inert 10.1 GPa shock, an inert 22.8 GPa von Neumann shock, and a 13.8 GPa reactive CJ shock. The results clearly demonstrate that the transmitted shock properties depend mainly on the incident shock pressure, but not on the incident shock temperature.

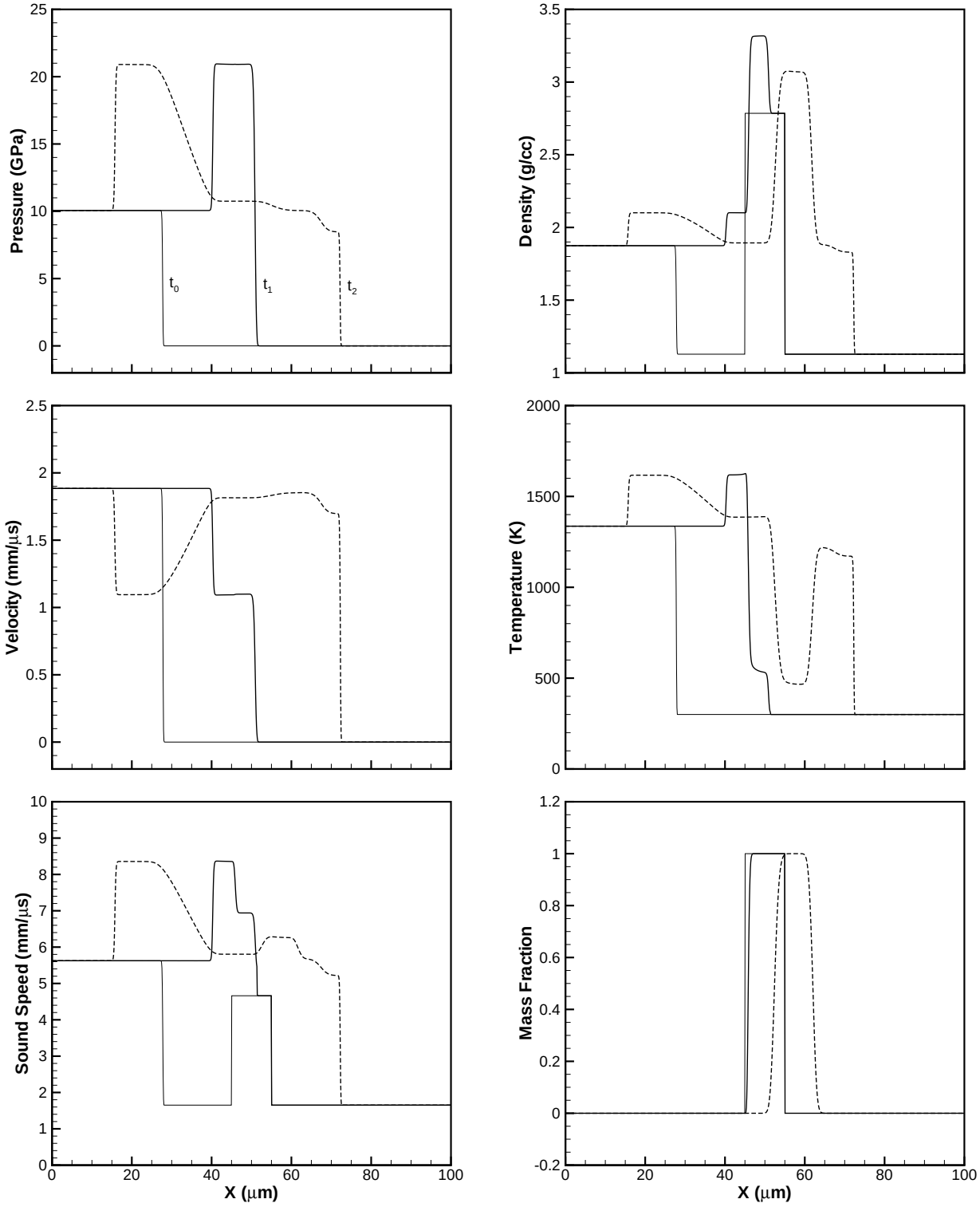

Figure 5.1: One-dimensional shock-particle interaction results using 100 cells / particle diameter (1000 cells total). Spatial distributions shown at three different times: t_0 - thin line, t_1 - thick line, t_2 - dashed line ($t_0 < t_1 < t_2$). Initial particle location for $45 \leq x \leq 55$ μm.

Table 5.1: One-dimensional wave transmission results calculated numerically.

	Incident (NM)	Reflected (NM)	Transmitted (Al)
10.1 GPa Inert Shock Interaction (D_0 = 4.769 mm/μs)			
Pressure (GPa)	10.1	20.9	20.9
Velocity (mm/μs)	1.884	1.094	1.098
Temperature (K)	1336	1619	524
Density (g/cc)	1.874	2.100	3.320
von Neumann Interaction (D_0 = 6.690 mm/μs)			
Pressure (GPa)	22.8	46.0	46.0
Velocity (mm/μs)	3.046	2.032	2.038
Temperature (K)	2790	3233	1112
Density (g/cc)	2.085	2.298	3.722
CJ Shock Interaction (D_0 = 6.690 mm/μs)			
Pressure (GPa)	13.3	19.4	19.4
Velocity (mm/μs)	1.756	1.018	1.034
Temperature (K)	3591	4357	503
Density (g/cc)	1.530	1.773	3.289

5.1.2 Detonation interaction with a semi-infinite slab

Figure 5.2 illustrates a NM detonation wave interacting with a semi-infinite slab of aluminum, where the material interface is initially located at $x/d_p = 1$. The initial response is similar to the inert shock result, where the incident wave is both transmitted and reflected from the material interface boundary. However, in the case of a detonation wave, the expansion in the reaction zone also interacts with the material interface, and both the transmitted and reflected wave strengths decay behind the leading shock fronts. Since the Taylor wave expansion length scale is much greater than the detonation reaction-zone length, the transmitted shock attenuation is limited, and at later times, shows a sustained shock traveling in the semi-infinite slab of aluminum.

5.1.3 Effect of shock impedance

The shock impedance is defined as $Z = \rho D$. If the impedances are matched for two materials in contact, an incident shock wave is transmitted perfectly across the interface and there is no reflected shock. In general, this is not the case (i.e., $Z_p \neq Z_f$), and a reflected wave component exists. Courant and Friedrichs [42] reviewed the various shock interaction cases. If a shock wave enters a higher impedance medium, the reflected wave

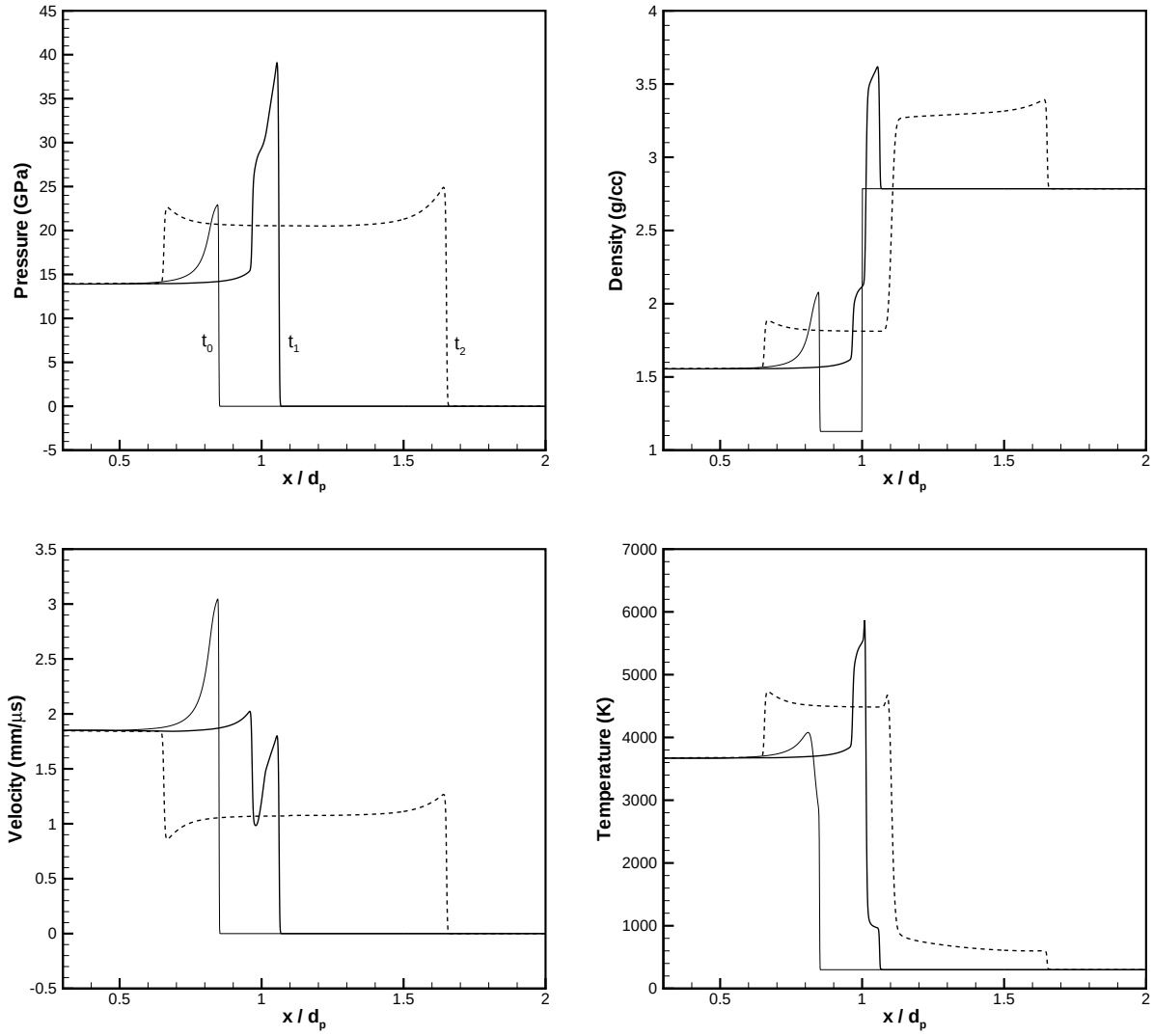

Figure 5.2: One-dimensional NM detonation interaction with a semi-infinite aluminum slab. Spatial distributions shown at three different times: t_0 - thin line, t_1 - thick line, t_2 - dashed line ($t_0 < t_1 < t_2$). Initial slab interface is at $x/d_p = 1$.

is a shock wave. Conversely, if a shock wave enters a lower impedance medium, the reflected wave is a rarefaction. The interaction physics are illustrated on characteristic wave diagrams in Figure 5.3. The main features of the shock interaction with a metal particle are illustrated, including: transmission and reflection of the incident shock at the leading edge; retransmission and reflection of the shock at the trailing edge; and, wave reverberation within the particle. Several states are identified in Figure 5.3 for later discussion of a quantitative example.

Typical one-dimensional model results for a 10.1 GPa inert shock pressure are considered as quantitative examples of the effect of impedance ratio. Figure 5.4 shows the high-impedance-ratio case ($Z_p > Z_f$) of a nitromethane shock interacting with an aluminum slab particle; Figure 5.5 illustrates the low-impedance-ratio condition ($Z_p < Z_f$) by considering an aluminum shock interacting with a nitromethane slug. In both cases, the particle size is 10 μm. The transmitted shock states for both cases are summarized in Table 5.2.

In the case of a 10.1 GPa NM shock interacting with an Al particle, the transmitted wave speed in the metal is greater than the incident shock; state $p1$ represents the 1D wave transmission. At the trailing edge on the far side of the particle, the transmitted shock is subsequently retransmitted into the liquid explosive and a rarefaction forms that travels upstream in the metal particle. Following the shock interaction time, τ_S, the mass centre of the particle is in state $p2$, where the velocity is 90.0% of the shocked fluid velocity in state $f1$. After two or three shock interaction times, during which additional wave reverberations occur inside the metal particle, the mass-centre velocity reaches state $p5$, which is 98.8% of the shocked fluid velocity.

For comparison, the low-impedance-ratio example has a 10.1 GPa shock in aluminum interacting with a slug of nitromethane. In this case, the transmitted shock is much slower than the incident shock. Similar to the high-impedance-ratio condition, after a few internal wave reverberations the mass-centre particle velocity approaches the shocked fluid velocity. Whereas the high-impedance case shows a monotonic increasing particle velocity during successive reverberations (Figure 5.4), the low-impedance case demonstrates a damped oscillation of the particle velocity (Figure 5.5). Further, the transmitted temperature ratio of the low-impedance case is reversed to that of the high-impedance condition; that is, the transmitted temperature into a nitromethane slug was greater than the shocked temperature of the host aluminum material (see Table 5.2). Note that $T_{f1,\mathrm{NM}} = 1336$ K, whereas $T_{f1,\mathrm{Al}} = 379$ K.

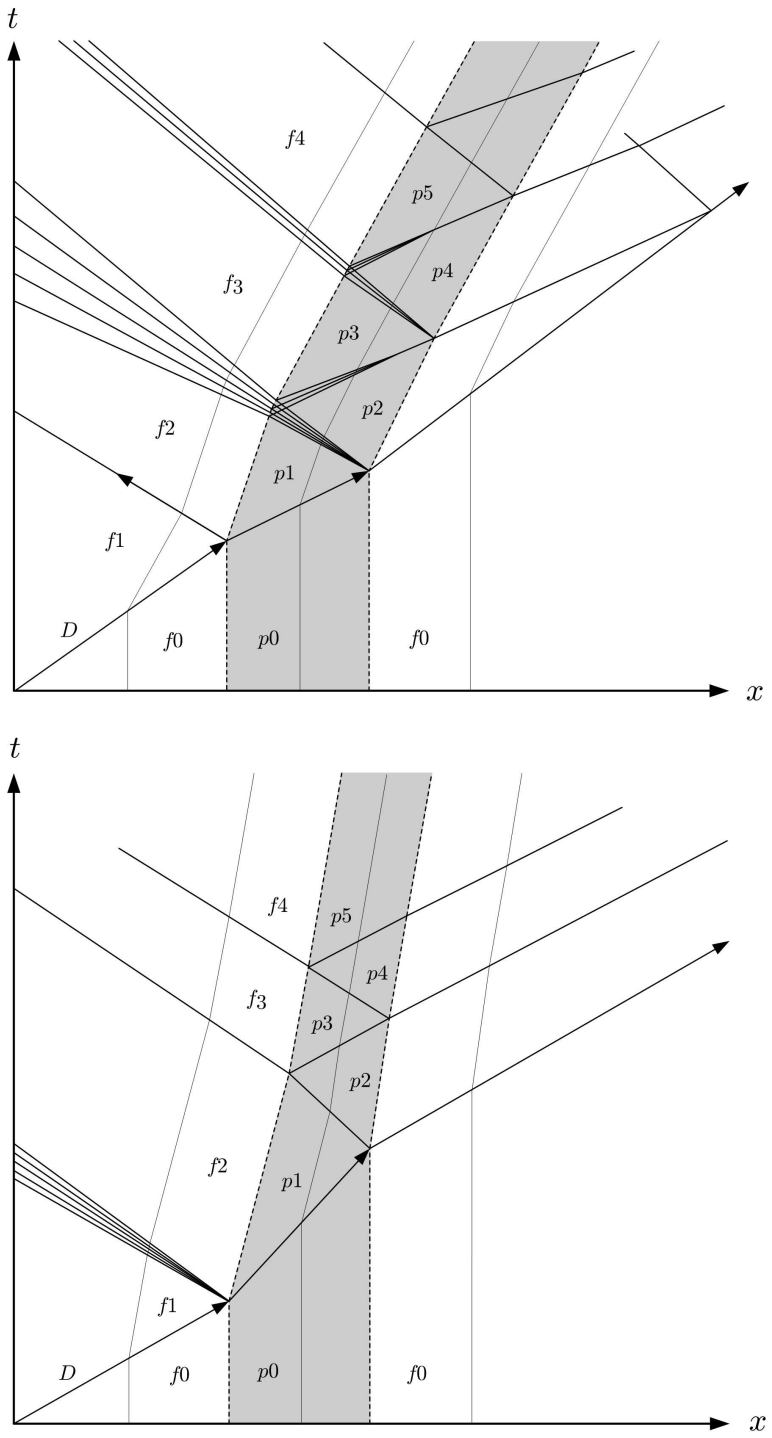

Figure 5.3: Characteristic wave diagrams for one-dimensional shock-particle interaction in the $x - t$ plane: $Z_p > Z_f$ (upper) and $Z_p < Z_f$ (lower). The shaded region indicates the particle location with the material interface identified using a dashed line; thin lines denote streamlines.

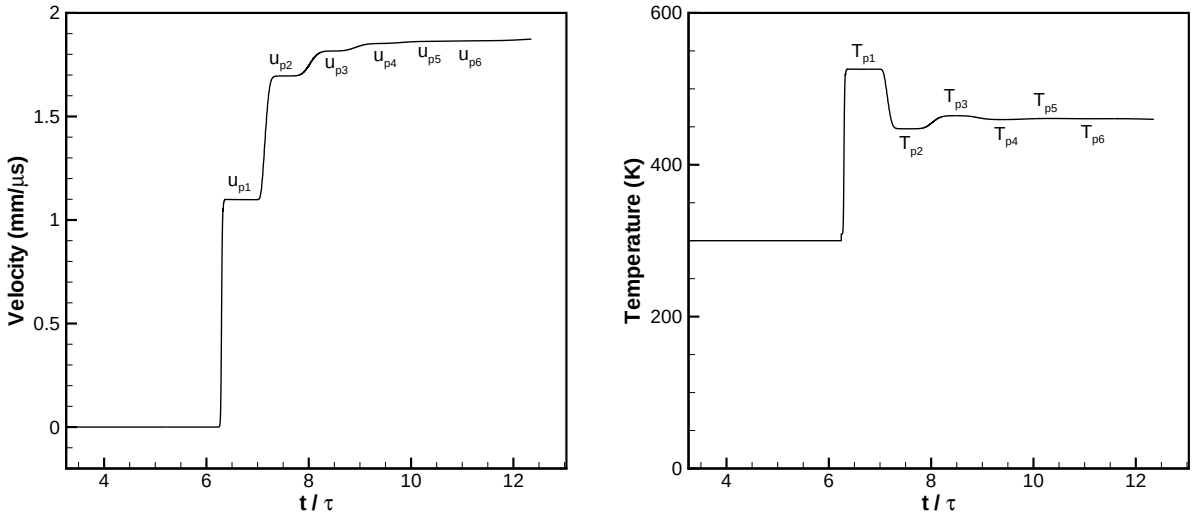

Figure 5.4: Velocity and temperature history of a high-impedance aluminum slab particle resulting from a 10.1 GPa incident shock in nitromethane ($Z_p > Z_f$).

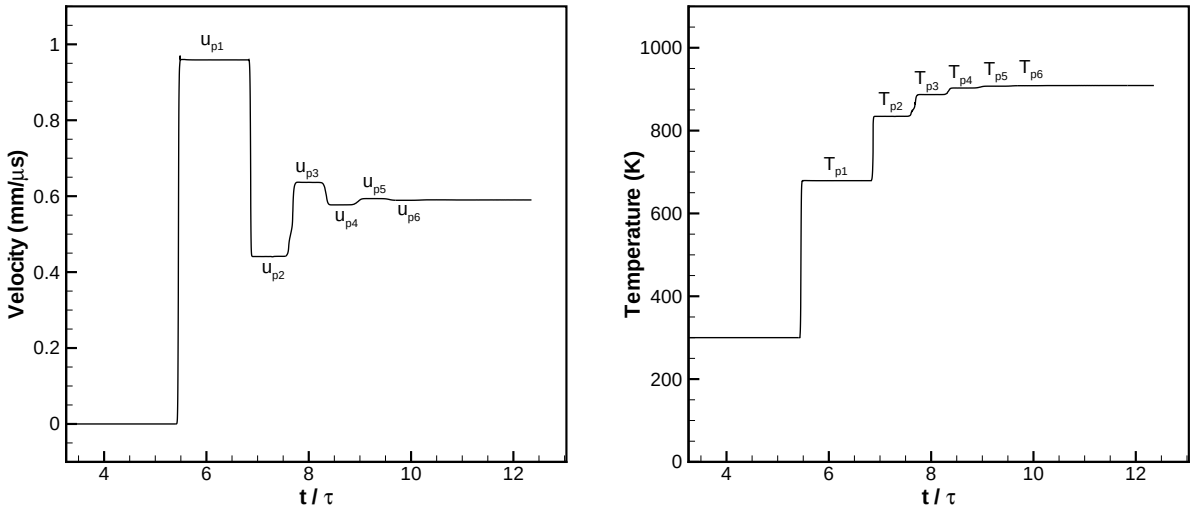

Figure 5.5: Velocity and temperature history of a low-impedance nitromethane particle slug resulting from a 10.1 GPa incident shock in aluminum ($Z_p < Z_f$).

Table 5.2: Transmitted velocity and temperature ratios during internal shock reflections for two shock impedance ratios.

State	Case 1: NM-Al-NM ($Z_p > Z_f$)		Case 2: Al-NM-Al ($Z_p < Z_f$)	
	u_p/u_{f1}	T_p/T_{f1}	u_p/u_{f1}	T_p/T_{f1}
p_1	0.582	0.393	1.625	1.792
p_2	0.900	0.333	0.746	2.202
p_3	0.963	0.347	1.078	2.340
p_4	0.983	0.340	0.978	2.382
p_5	0.988	0.344	1.007	2.394
p_6	0.990	0.343	0.998	2.397

5.1.4 Effect of edge condition

Based on wave transmission physics, the downstream particle interface affects the particle acceleration and heating, comparable to the incident wave effect. The material downstream of an aluminum particle (called the backing material) is varied using three conditions, one of which is nitromethane as demonstrated above. The case of perfect impedance matching is considered by backing the particle with aluminum. A free-edge interface is also considered by backing the particle with gas ($\rho_{gas} = 0.0012$ g/cc, assuming air at 300 K).

Figure 5.6 compares the resulting velocity and temperature recorded in the aluminum particle from an incident 8.5 GPa nitromethane shock. For the aluminum backing condition with perfect impedance matching, there is no rarefaction wave generated at the trailing edge. The nitromethane backing features an expansion wave at the trailing edge as previously discussed. The air backing introduces a very large density ratio at the trailing edge ($\rho_{\mathrm{Al}}/\rho_{\mathrm{gas}} \approx 2300$) and results in a very strong expansion wave and weak transmission into the gas. The upstream traveling expansion wave accelerates the particle to a high velocity while significantly reducing its temperature. These extreme conditions are expected to occur at the edge of an explosive charge.

5.1.5 Effect of neighbouring particles

Particles located upstream or downstream of a candidate particle introduce additional material interfaces that both transmit and reflect shocks. Figure 5.7 plots the complex interaction between a pair of slab aluminum particles in liquid nitromethane subjected to

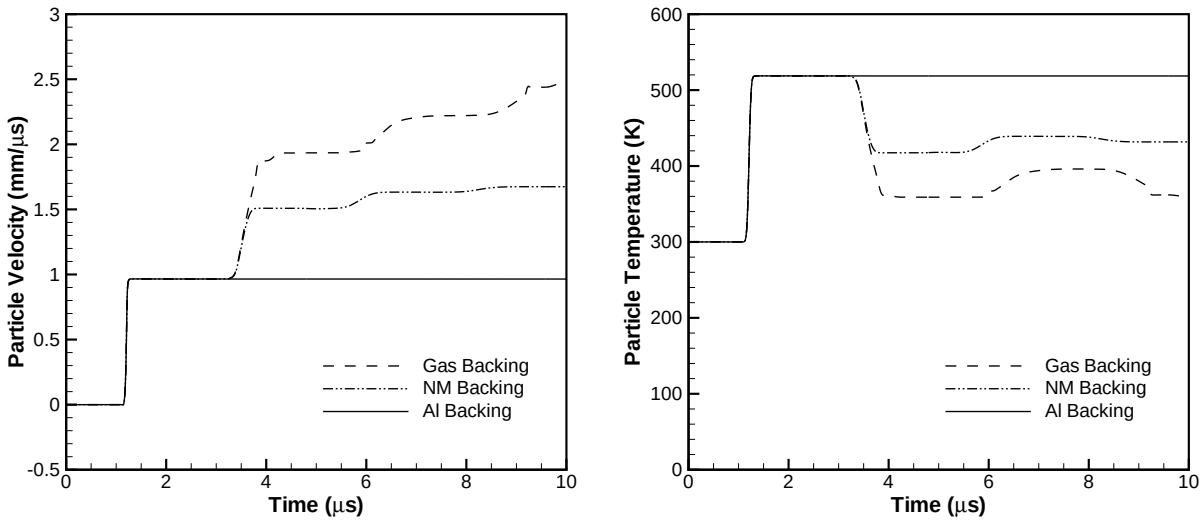

Figure 5.6: Effect of backing material on the edge rarefaction wave and resulting particle acceleration and heating.

an incident 10.1 GPa shock. Two different separation distances are shown to highlight the effect of the gap spacing. Considering a pair of slab particles, the incident shock transmitted through the upstream particle is subsequently re-transmitted into the liquid between the particles. Following shock traversal across the gap between the particles, the shock is both reflected and transmitted at the leading edge of the downstream particle. The reflected shock travels upstream and interacts with the first particle which reduces the upstream particle velocity. The transmitted shock in the second particle reflects as an expansion wave at trailing edge; this expansion travels upstream and transmits through the gap space and into the leading particle, thereby accelerating the first particle later in time.

The main influence of the gap size is on the arrival time of the upstream traveling reflected shock, which decreases the upstream particle velocity. For small gap spacings, the upstream traveling shock arrives coincident with the upstream traveling rarefaction, further reducing the particle velocity. For larger gap spacings, the upstream traveling shock may collide with the wave reverberating inside the particle, thus competing with the shocked particle velocity.

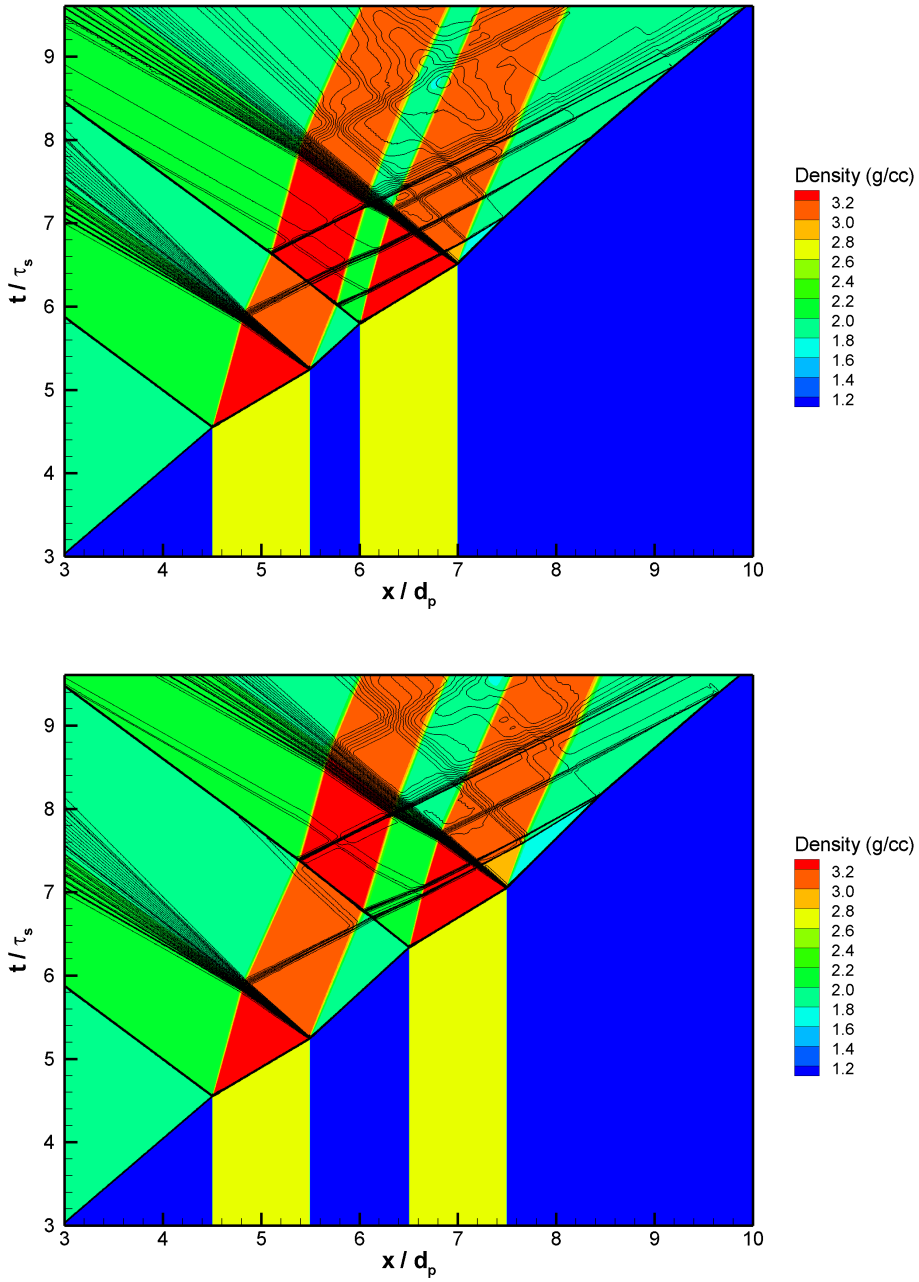

Figure 5.7: Effect of gap space size on shock interaction between a pair of slab particles: $s = 0.5d_p$ (upper) and $s = 1d_p$ (lower). Colour contours: density; and, black lines: isobars (pressure from $10^5 - 10^{10}$ Pa shown in log scale).

5.1.6 Array of slab particles

The neighbouring particle analysis is extended further by studying a semi-infinite array of slab particles separated by gaps filled with liquid explosive, as shown schematically in Figure 5.8. The gap spacing, s, is varied parametrically for a fixed particle diameter, d_p. As shown for a pair of slab particles, the spacing between particles affects the arrival of the reflected shock from the downstream particle. The upstream traveling shock returns to the particle and reduces its velocity. This process is repeated in both the upstream and downstream directions for an array of slab particles.

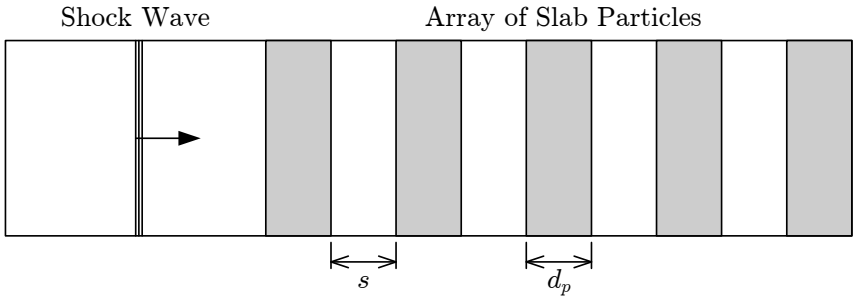

Figure 5.8: One-dimensional model to study the effect of particle spacing with liquid explosive filling the gaps.

Each layer of slab particles influences the other particles, although the effect of distant particles is greatly attenuated. The influence of the immediate upstream and downstream particles occurs when shock and expansion waves are transmitted or reflected from material interfaces. The timing of subsequent shock interactions depends on the gap size and particle diameter. The gap size is related to the volume fraction using $\phi_{s0} = d_p/(d_p + s)$ for slab particles.

Figure 5.9 presents the results recorded in the first particle in an array of slab aluminum particles subjected to a shock of 10.1 GPa in liquid nitromethane. For the first particle of an array, the maximum particle velocity was observed for infinite spacing (dilute flow, $\phi_{s0} \to 0$), which behaves essentially as a single particle. The lowest particle velocity occurred for $s = 0$, representative of a semi-infinite slab (dense volume fraction limit, $\phi_{s0} \to 1$). The particle velocity for the various gap spacings ($0 \leq s \leq 1$) are bound by these two limits. In the absence of a downstream particle (e.g., infinite spacing), the particle velocity increases with time until equilibrium is reached since there are no waves traveling upstream.

In the next example, the second particle in the semi-infinite array is considered, for

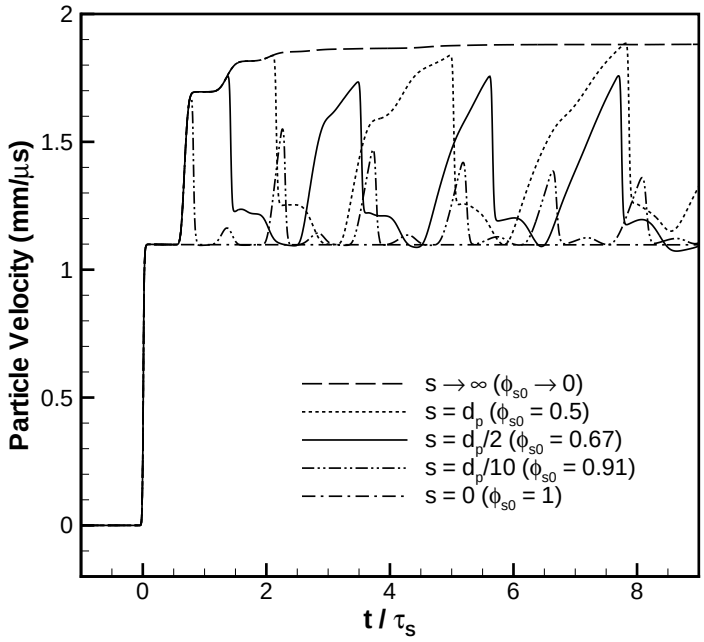

Figure 5.9: Effect of downstream particle spacing on the mass-centre transmitted velocity history of the leading particle in an array of slab particles.

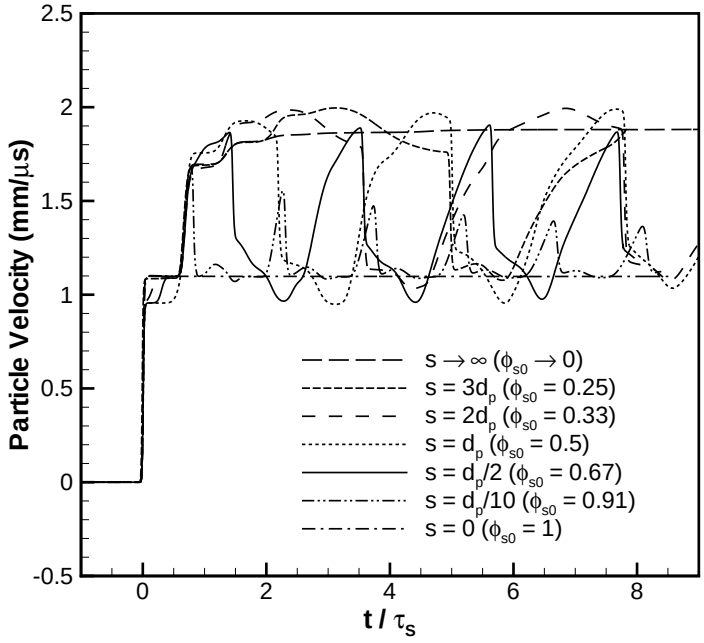

Figure 5.10: Effect of upstream and downstream particles on the mass-centre transmitted velocity history of the second particle in an array of slab particles.

which the gap spacing has two influences on the downstream particles. First, the shock strength arriving at the leading edge of the second particle depends on the gap space upstream. For small upstream gap spacings, the shock reverberates within the gap in a timescale less than the shock transmission through the particle. For larger upstream gap spacings, the shocks transmitted from the upstream particle coalesce and strengthen before entering the downstream particle. Figure 5.10 shows the results recorded in the second particle in the array of slab particles.

The second effect is coherent wave transmission. Compared to the upstream particle, the peak velocity of the downstream particle is no longer bound by the dilute and dense limits. When considering the downstream particle, the local particle velocity extends below the dense limit and above the dilute limit. Figure 5.10 shows that for volume fractions less than 0.5, the peak velocity exceeds the single particle value. The maximum velocity occurred for $\phi_{s0} = 0.25$. The lowest peak transmitted velocity into the downstream particle occurred for the limit of no gaps ($\phi_{s0} \to 1$). In this case, perfect transmission occurs and the downstream particle velocity is the same as for the upstream particle.

The particle velocity achieved in the downstream particle exhibits a slight inverted U-shaped functional dependence based on the volume fraction, whereas the upstream particle velocity is a monotonic decreasing function of volume fraction. The results of maximum particle velocity in an array of slab particles are summarized in Figure 5.11.

5.2 Single spherical particle results

The one-dimensional slab particle analogues have indicated the primary shock interaction physics, particularly wave transmission and reflection at the particle interface. The canonical system involving spherical particles is inherently three dimensional with curved interfaces along the particles. Shock and detonation interaction with a single spherical particle is considered here, and is representative of the dilute limit ($\phi_{s0} \to 0$). Simulation of the single particle is performed using a two-dimensional axisymmetric model (see Figure 5.12) of comparable resolution to the final 3D packed particle matrices.

5.2.1 Inert shock interaction with a single particle

Now that the shock impedance effect and spacing between particles has been analyzed, the effect of density ratio is evaluated. The effect of density ratio is investigated in the small

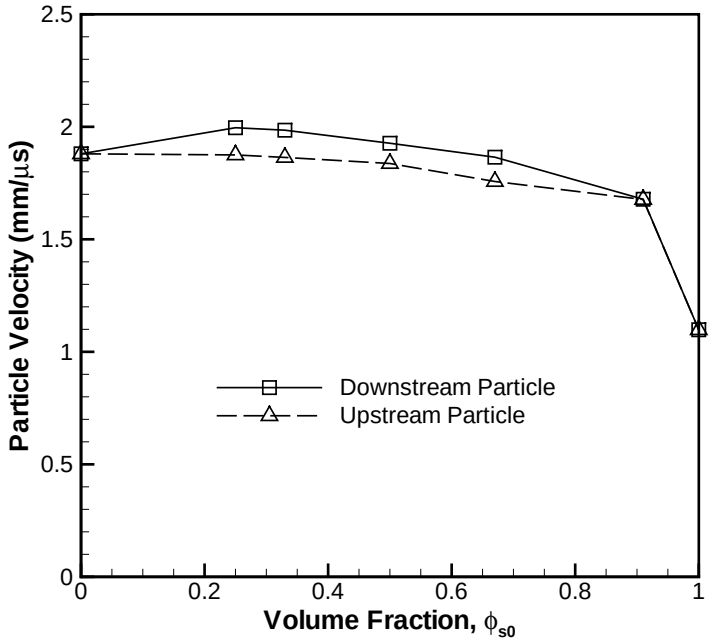

Figure 5.11: Peak velocity of a slab particle in an array due to various gap spacings reported as volume fraction.

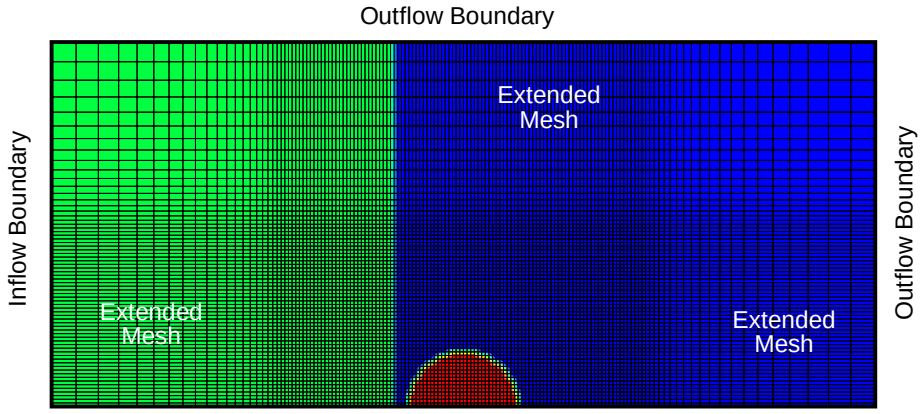

Figure 5.12: Mesoscale configuration for 2D axisymmetric model for single spherical particle interaction, schematically illustrating mesh density, initial conditions and boundary conditions.

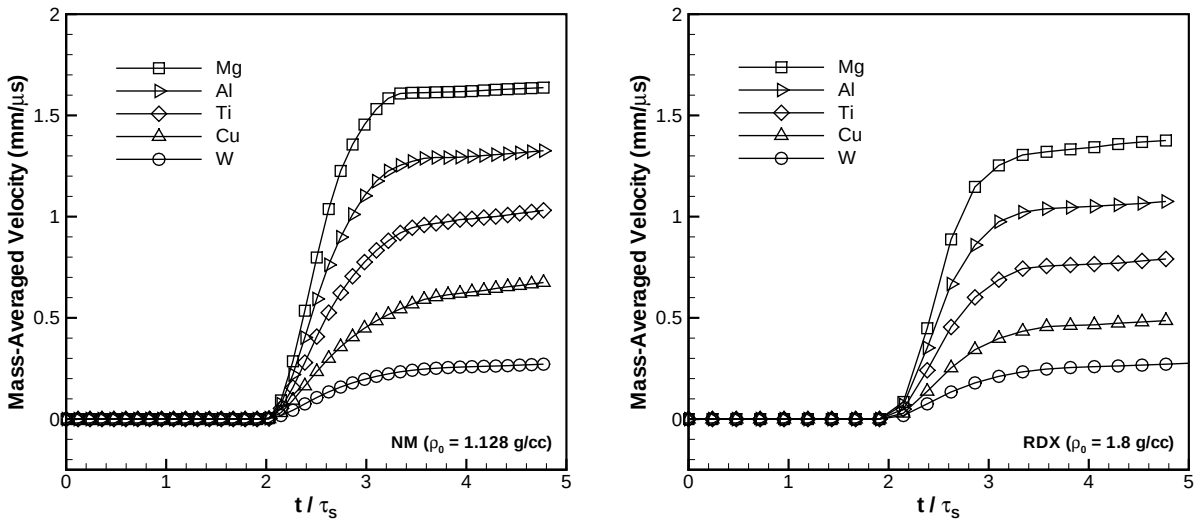

Figure 5.13: Single particle velocity during a 10.1 GPa inert shock interaction: (left) metal particles in NM explosive (ρ_{f0} = 1.128 g/cc); and (right) metal particles in RDX explosive (ρ_{f0} = 1.8 g/cc).

particle limit for a shock pressure of 10.1 GPa, following the work of Zhang et al. [229]. Table 5.3 summarizes the solid density for particles of magnesium, aluminum, titanium, copper, and tungsten, along with the corresponding density ratio when saturated in RDX and NM explosives, that are used to study the particle acceleration.

Table 5.3: Density ratio of explosive to solid for various metal particles and explosive matter.

Metal	Solid Density,	Density Ratio, ρ_{f0}/ρ_{s0}	
	ρ_{s0} (g/cc)	NM (ρ_{f0} = 1.128 g/cc)	RDX (ρ_{f0} = 1.8 g/cc)
Magnesium	1.780	0.6337	1.0112
Aluminum	2.875	0.3923	0.6261
Titanium	4.528	0.2491	0.3975
Copper	9.920	0.1137	0.1815
Tungsten	19.30	0.0585	0.0933

The resulting particle velocity during the shock interaction is recorded for a single particle of different metals, listed in Table 5.3, subjected to an inert shock. Figure 5.13 plots the mass-averaged particle velocity history during several shock interaction times. The measurement frequency indicated by the data points is coarse in these early calculations; subsequent computations employed an output frequency at least ten times greater.

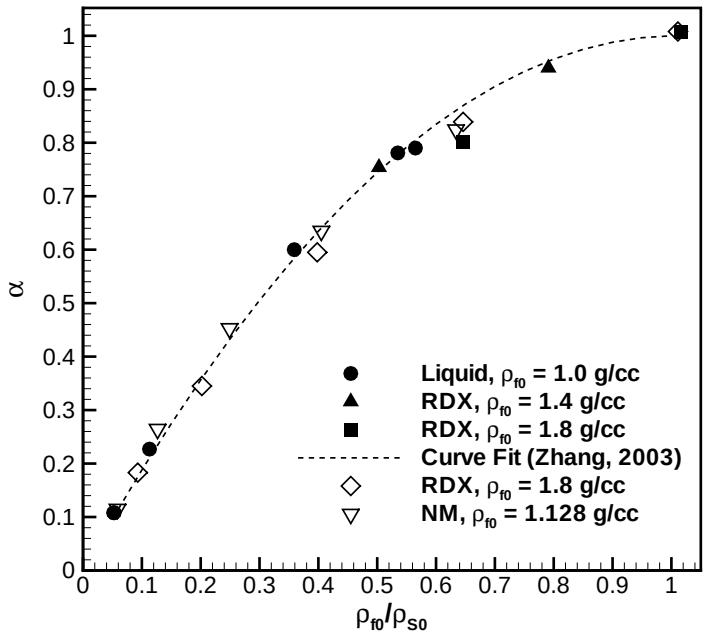

Figure 5.14: Single particle velocity transmission factors measured at $1\tau_S$ for various density ratios. Solid symbols indicate data from Zhang et al. [229]. Open symbols are the present results using a similar 10.1 GPa incident shock.

The shock-compressed particle velocity is measured after one shock interaction time, τ_S, and then it is used to define the velocity transmission factor, $\alpha = u_p(\tau_S)/u_{f1}$ (for neat NM, $\rho_{f0} = 1.128$ g/cc and $u_{f1} = 1.884$ mm/μs; for pure RDX, $\rho_{f0} = 1.8$ g/cc and $u_{f1} = 1.170$ mm/μs). Figure 5.14 summarizes the velocity transmission factor to quantify the shock compression acceleration of single particles. The results are plotted against the initial density ratio of explosive to solid particle, ρ_{f0}/ρ_{s0}, and compared to the numerical results and curve fit of Zhang et al. [229], who used particles of magnesium, beryllium, aluminum, nickel, uranium, and tungsten. The agreement is very good, and reinforces the fact that the density ratio is one of the most significant factors affecting particle acceleration.

5.2.2 Detonation interaction with a single particle

Computation of diffraction of a detonation wave over a single particle in a 2D mesh (Figure 5.15) shows that the shock is both transmitted into the metal at the particle leading edge, and also reflected back into the reaction zone thereby increasing the reaction rate. A Mach stem forms as the shock in the explosive diffracts over the particle. Depending on the impedance ratio, the shock inside the metal particle may travel ahead of the incident shock,

transmitting an oblique shock into fresh explosive ahead of the detonation front. Behind the diffracting detonation shock, expansion of the flow on the backside of the particle causes the local reaction-zone length to increase. At the particle trailing edge, either the diffracted shock arrives first or the converging shock inside the particle is retransmitted into the fresh explosive behind the trailing edge. This can initiate the explosive locally ahead of the detonation shock. Subsequently, a strong rarefaction forms within the metal particle contributing to both a large acceleration and a decrease in temperature.

Interaction of a nitromethane detonation wave with single aluminum particles of various diameters (i.e., various $\delta = d_p/L_R$) are computed. The mass-averaged particle velocity history achieved during detonation interaction with a single particle is illustrated in Figure 5.16. Since a fixed numerical mesh resolution was maintained (100 cells/μm), such that the number of cells in the ideal detonation reaction zone ($N_R = 200$) was unchanged, the number of cells across the particle diameter increased with δ and the corresponding computational effort increased exponentially. Thus for large δ, limited duration particle velocity histories are available. For $\delta < 0.5$ the peak particle velocity exceeds the CJ value, illustrating a significant influence of the VN spike on the particle acceleration. For $t/\tau_S \gg 1$ the particle velocity equilibrates below the CJ value ($u_{\mathrm{CJ}} = 1.827$ mm/μs, see Table 4.10) due to the influence of the Taylor expansion.

Figure 5.16 shows the mass-averaged shock compression temperature for a single particle for various δ. Smaller particles achieve higher temperatures, although the maximum temperature during shock interaction is much less than the CJ flow temperature ($T_{\mathrm{CJ}} = 3657$ K). Oscillations in the temperature histories are caused by successive compressions and expansions due to wave reverberation inside the particle. Note that the temperature calculations in this work address the shock compression heating within a timescale on the order of one shock interaction time, the long time temperature equilibrium between the particle and detonation products will rely on other heat transfer mechanisms such as convective heating behind the detonation shock.

5.3 Matrix particle results

5.3.1 Results for the small particle limit ($d_p/L_R \ll 1$)

Figure 5.17 illustrates the particle deformation in a 3D particle matrix ($d_p = 10$ μm, $d_p/L_R \to 0$) resulting from a 10.1 GPa inert Heaviside step shock traveling from left

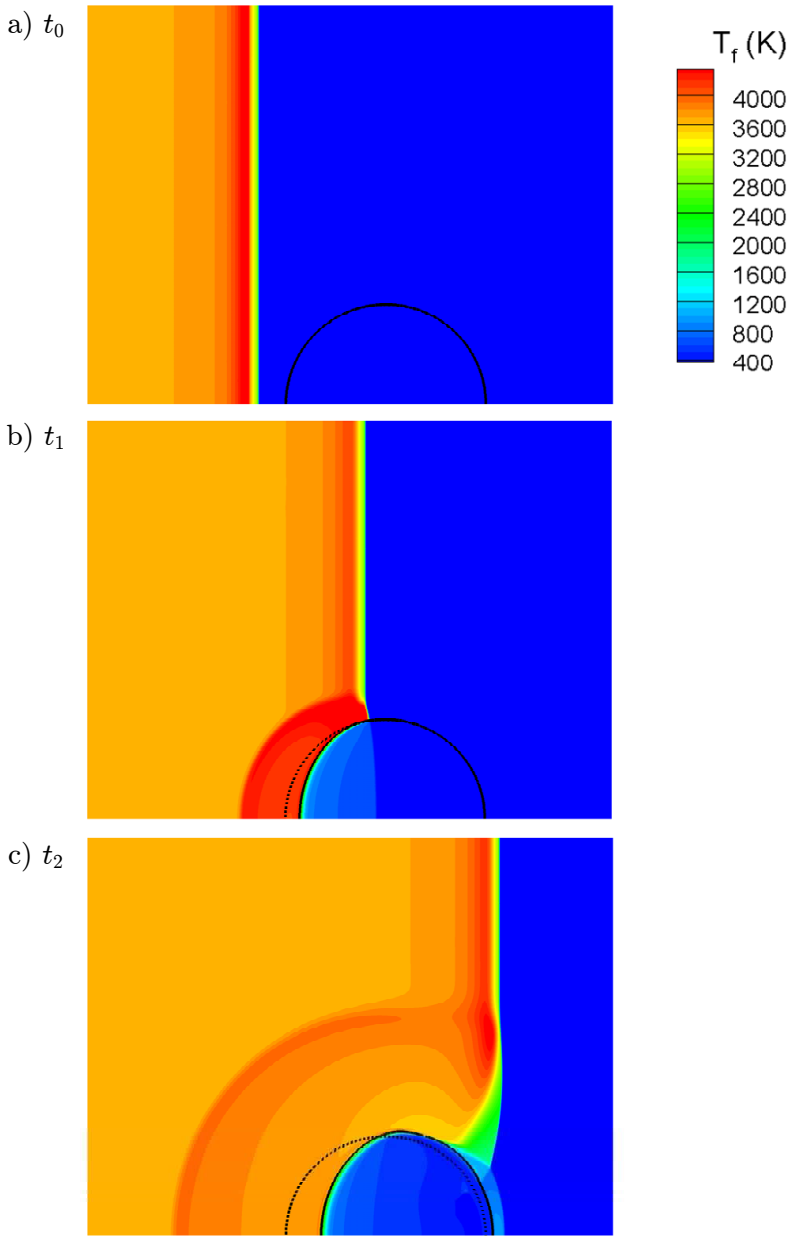

Figure 5.15: Temperature field during detonation wave interaction with a deformable metal particle ($\delta = 0.5$). Solid line is the particle-explosive interface; dotted line denotes the initially undeformed particle boundary.

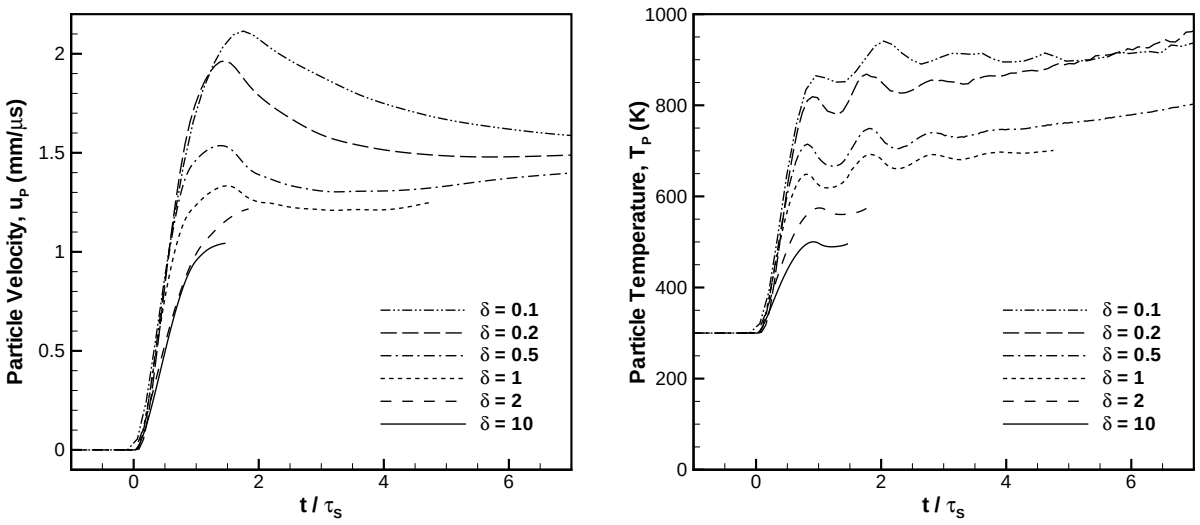

Figure 5.16: Particle velocity and temperature during nitromethane detonation interaction with a single aluminum particle computed for various $\delta = d_p/L_R$.

to right. The deformed particles resemble a saddle shape and, due to the inviscid hydrodynamics, are strongly influenced by the complex shock reflections from neighbouring particles. The deformation of the first layer is different because the reflected shock wave is not subsequently re-reflected from upstream particles. The severe deformation in the rear flow indicates that the aluminum particles will likely be damaged or fragmented if material shear stress and failure are considered.

Figure 5.18 (left) shows the pressure histories at the leading edges of the first eight layers of packed particles. The peak pressure reaches the perfect reflection value of 45.4 GPa and rapidly expands to less than half this value. The reverberating pressure oscillates with a period of $0.5\tau_S$ corresponding to the wave transit time within the interstitial pores contained between packed particles. There is a sustained quasi-steady pressure plateau centred below the 1D wave transmission value of 20.9 GPa.

Figure 5.18 (right) shows the mass-averaged particle velocity for three packing configurations. Within $1\tau_S$, the velocity in all three matrices exceeds the 1D wave transmission value of 1.094 mm/μs (see Table 5.1) due to the internal rarefaction as the wave exits the trailing edge of the particle. Subsequent shock reflection and interaction with neighbouring particles causes velocity fluctuations proportional to the particle spacing that vary with packing configuration. A timescale of $2\tau_S$ is sufficient to capture one full interaction cycle that includes the internal wave reverberation, and successive expansions and compressions from upstream, downstream, and neighbouring particles. The severe

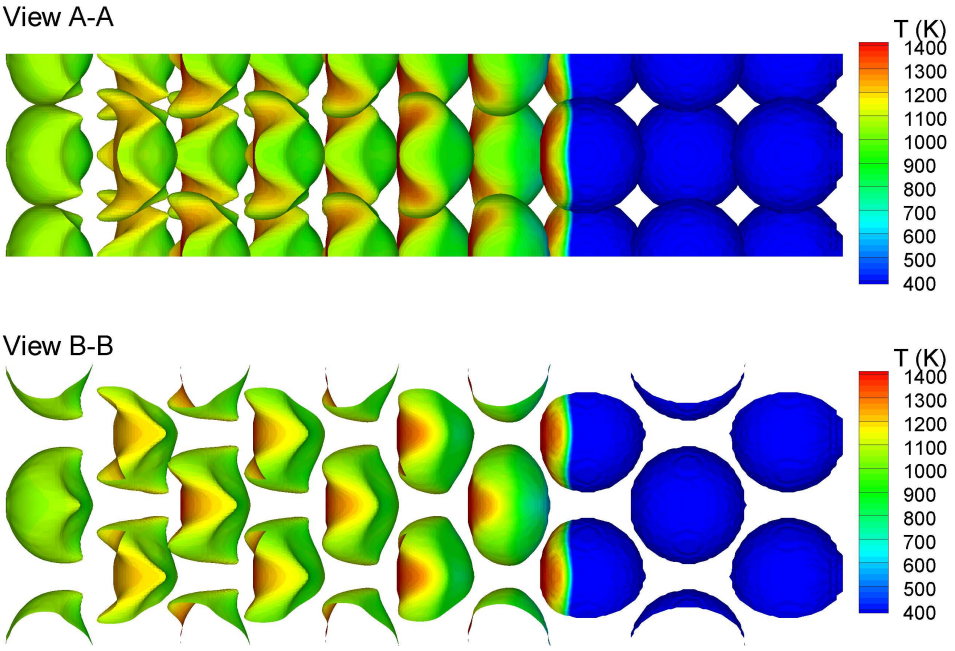

Figure 5.17: Inert shock interaction in a close-packed matrix of aluminum particles: resulting deformation and temperature distribution with $\phi_{s0} = 0.428$. Matrix viewed on the [100] plane (upper) and matrix viewed on the [110] plane (lower).

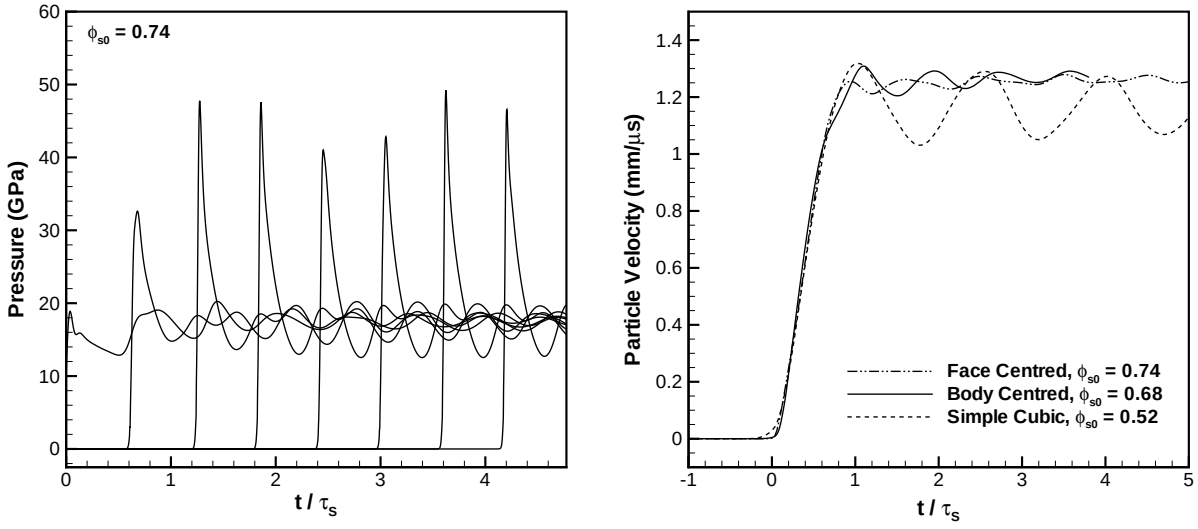

Figure 5.18: Results in the small particle limit: particle leading edge pressure histories for a close-packed matrix (left) and mass-averaged particle velocity for various matrices of packed spherical particles (right).

particle deformation observed in Figure 5.17 occurs after $2\tau_S$. Since the severe particle deformation occurs after the shock interaction timescale in the rear flow, it does not influence the evaluation of the velocity and temperature transmission factors within the shock interaction time.

Figure 5.19 illustrates the effect of particle spacing in a face-centred cubic matrix on the mass-averaged particle velocity. For large distances between particles ($\phi_{s0} \to 0$) the particle response appears as a step shock interacting with a single particle monotonically increasing towards the limit of the shocked fluid velocity. As the volume fraction increases, the velocity rise time (acceleration) decreases. For close spacing between particles, the reflections from neighbouring particles influence the particle response, which is exhibited as an oscillation in the shocked particle velocity. The oscillation frequency increases as the spacing between particles is reduced. This indicates that the reverberation period is proportional to the spacing between particles, which is characterized by shocks transiting the gaps between particles. Unlike the monotonic velocity increase in the case of single particle interaction, as the solid volume fraction increases in the particle matrix, the velocity profile after the initial acceleration within $1\tau_s$ approaches a plateau with smaller oscillations.

Figure 5.20 provides a summary of the velocity and temperature transmission results (α and β, respectively) for the small particle limit using a 10.1 GPa inert shock. The transmission factors are evaluated at an interaction time of $2\tau_S$ to include expansion from the particle tailing edge and wave interactions from neighboring particles. A mean transmission value measured at $2\tau_S$ is obtained using slope fitting to smooth the oscillation effect. One can also choose an average over a period of oscillation after the initial rise within $1\tau_S$, but the difference to the $2\tau_S$ values are not essential, particularly as the solid volume fraction increases, as demonstrated in Figure 5.19.

The results in Figure 5.20 were recorded in the fourth particle layer, as discussed in Ripley et al. [168]. Comparison of the packing configurations shows that the transmission factors for the simple cubic packing were considerably different. This is primarily due to this particular packing matrix that provides two propagation channels: one through the linear array of stacked particles, and the other uninhibited through the column of liquid in the void space. The simple cubic packing is an unrealistic configuration in practice, and is not given further consideration. The present 3D results are compared to 2D cylindrical results of Zhang et al. [229]. The agreement is improved for a lower number of 2D cylinders, despite the fact that a higher number of 2D cylinders better approximates an infinite array of particles as in the 3D configuration.

Both the velocity and temperature transmission factors for the close-packed and body-

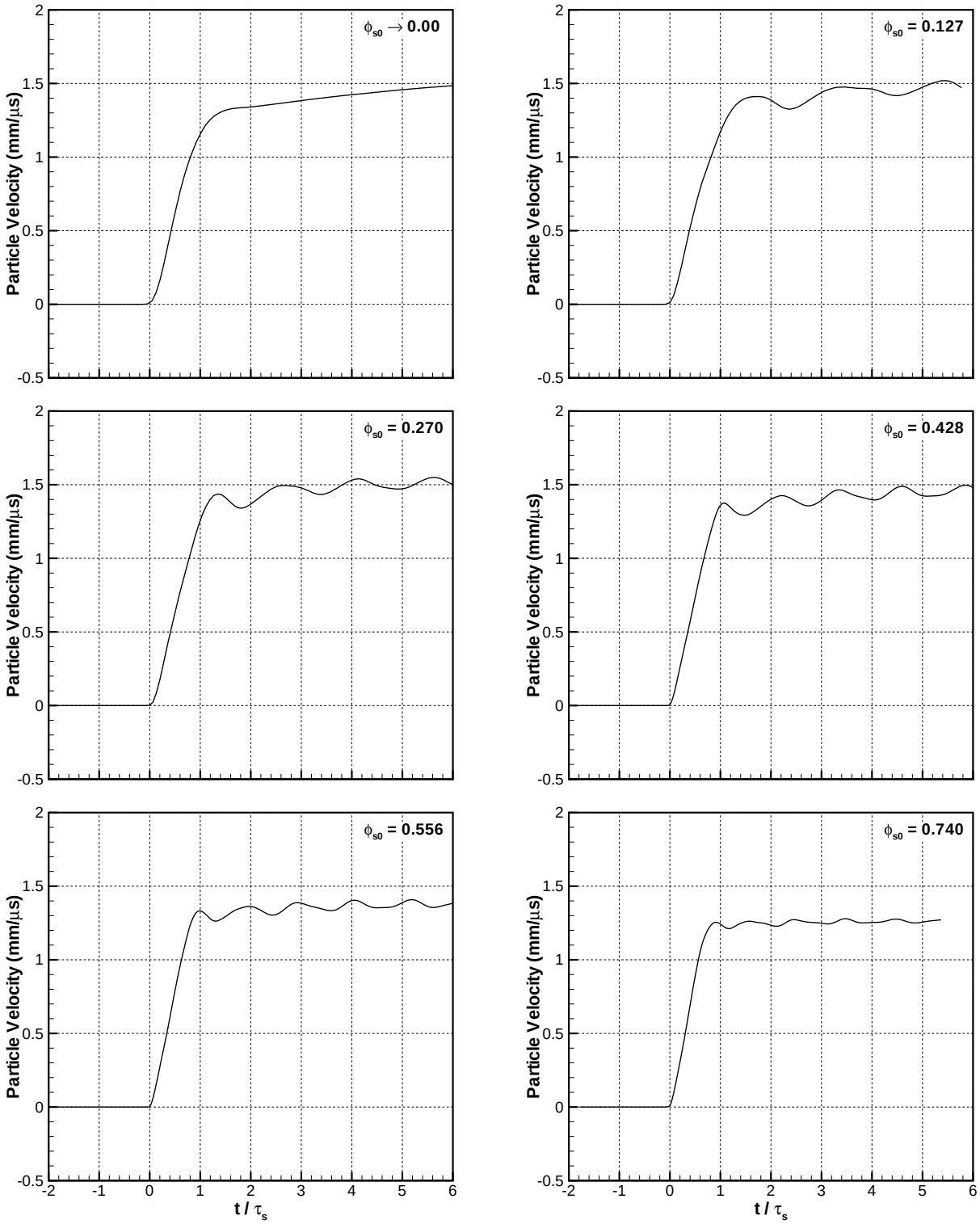

Figure 5.19: Mass-averaged velocity history for an aluminum particle in a 10.1 GPa inert nitromethane shock for face-centred cubic particle matrices with various volume fractions.

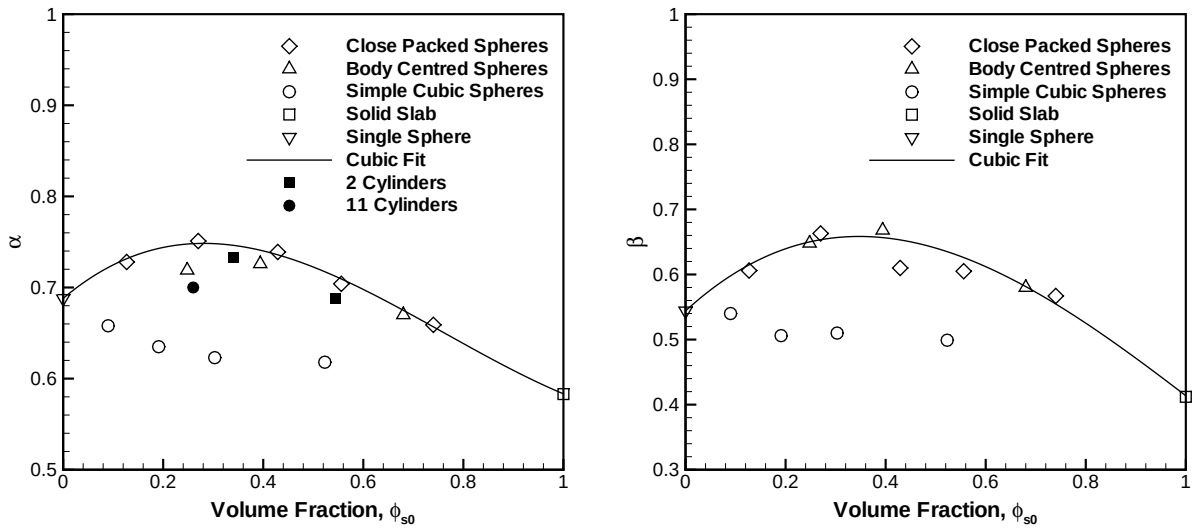

Figure 5.20: Velocity, α (left), and temperature, β (right), transmission factors for a 10.1 GPa inert shock interaction with packed particle matrices. Cylinder results (solid symbols) are from Zhang et al. [229].

centred matrices follow an inverted U-shaped function that follows a cubic curve fitting. The maximum transmission factors occurred for $0.25 \lesssim \phi_{s0} \lesssim 0.40$, while the minimum transmission factors resulted at the dilute limit ($\phi_{s0} \to 0$) and high volume fraction limit ($\phi_{s0} \to 1$). In between the volume fraction limits, the spacing of the particles affects the arrival time and magnitude of reflected waves from upstream, downstream, and lateral particles, in addition to affecting the local flow diffraction. The maximum transmission factors are a result of superposition of transmitted shock waves that act in a coherent manner.

The remainder of the mesoscale results focus exclusively on the close-packed (face-centred cubic lattice arrangement) configurations. Figure 5.21 shows the results for von Neumann shock interaction with packed particle matrices. The shock interaction consists of a 22.8 GPa inert shock in nitromethane. The response is similar to the results above, except that the magnitude of the particle velocity is increased significantly.

The temperature field shown in Figure 5.22 indicates localized hot spots in the interstitial fluid sites between particles in the matrix. In other calculations [166], the peak fluid temperature found at the particle leading edge is 3828 K in the close-packed configuration, while it reaches only 2383 K for the simple cubic packing. The hot spots persist for a few shock interaction time scales. For reactive host matter, this behaviour will significantly affect the detonation process.

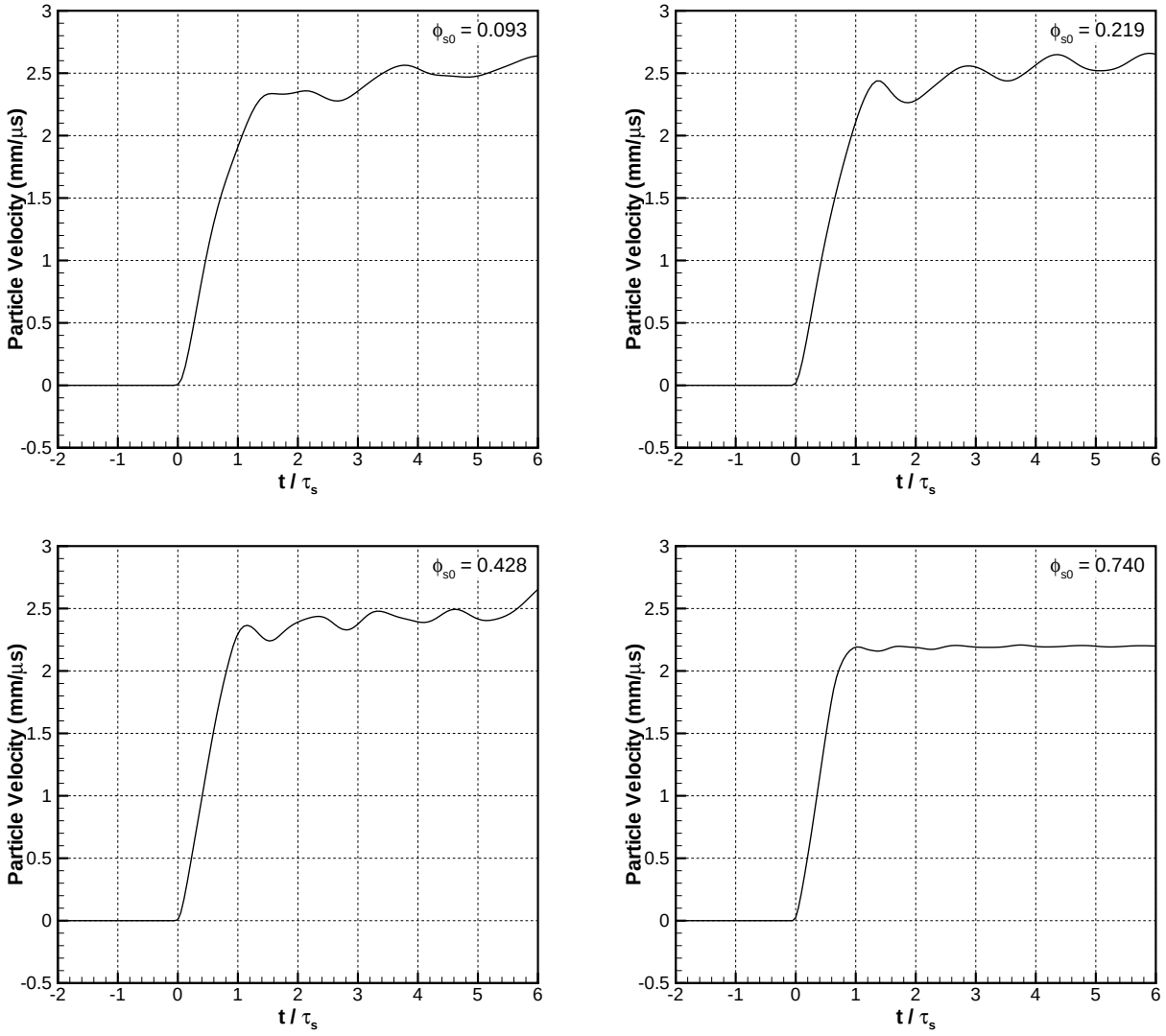

Figure 5.21: Mass-averaged particle velocity in a 22.8 GPa VN shock in nitromethane for different volume fractions.

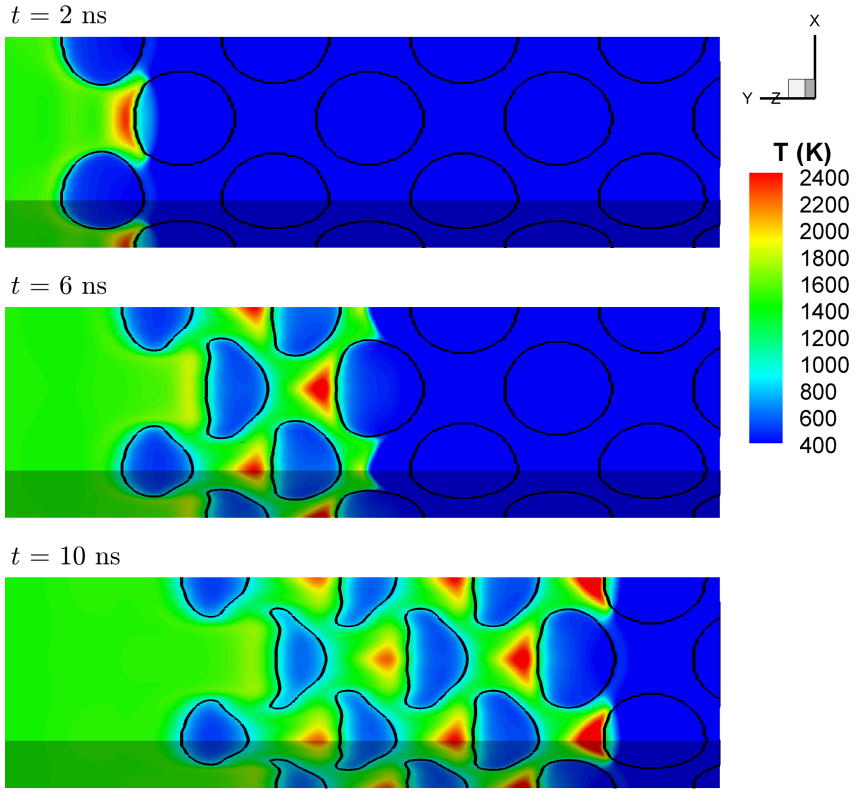

Figure 5.22: Inert shock interaction illustrating hot spots at the particle leading edges for a 10.1 GPa shock in nitromethane. Shock wave traveling from left to right.

5.3.2 Results for the large particle limit ($d_p/L_R \gg 1$)

In the $d_p/L_R \gg 1$ case, early simulation results (see Ripley et al. [166]) for the detonation wave over a single aluminum particle indicated that the particle velocity is first increased as the detonation front crosses the particle and is then reduced, subject to the Taylor expansion flow conditions. The Taylor expansion after the thin detonation front reduces the detonation flow velocity, thus changing the direction of the drag and reversing the momentum transfer direction from the particles to the detonation expansion flow. The large particle limit was studied preliminarily using $d_p = 30$ μm (see Ripley et al. [169]), which corresponds to $d_p/L_R = 15$. The unsteady Taylor expansion effect was minimized by running the detonation sufficiently far from the initiation location. For large detonation running distances, applicable to large explosive charges, the Taylor expansion effect is insignificant relative to the particle size.

For $d_p/L_R \gg 1$, the VN shock can be neglected and the detonation interaction with particle matrices can be better represented by a CJ shock. The jump condition in the host liquid does not follow the Hugoniot because the shock is reactive; that is, the chemical reaction rate is essentially infinite and the post-shock flow contains hot expansion products. Figure 5.23 illustrates a CJ shock ($D_0 = 6.69$ mm/μs, $P_{\rm CJ} = 13.8$ GPa, $u_{f1,\rm CJ} = 1.827$ mm/μs and $\rho_{f1,\rm CJ} = 1.551$ g/cc) traveling through an NM/Al matrix. For a particle spacing of $1d_p$, the volume fraction is $\phi_{s0} = 0.093$ and the CJ shock front profile tends to approach that of a planar wave prior to arrival at successive particle leading edges; this leads to a flattening of the particles during deformation.

The particle velocity and temperature histories are shown in Figure 5.24. Within $2\tau_S$ both the incident shock and internal rarefaction accelerate the particle, while an increase in particle temperature due to shock compression is followed by a decrease from the rarefaction expansion before lateral compression continues the particle heating. Figure 5.24 (upper) illustrates a decrease in particle velocity over $3 - 4$ τ_S as a result of a reflected wave returning from the downstream particles. Further particle acceleration must be influenced by viscous drag which is beyond the scope of the present work. Similarly, the particle heating is only affected by shock compression in the non-heat-conducting assumption, which is valid within the timeframe considered, although the NM detonation products are hot ($T_{f1,\rm CJ} = 3657$ K).

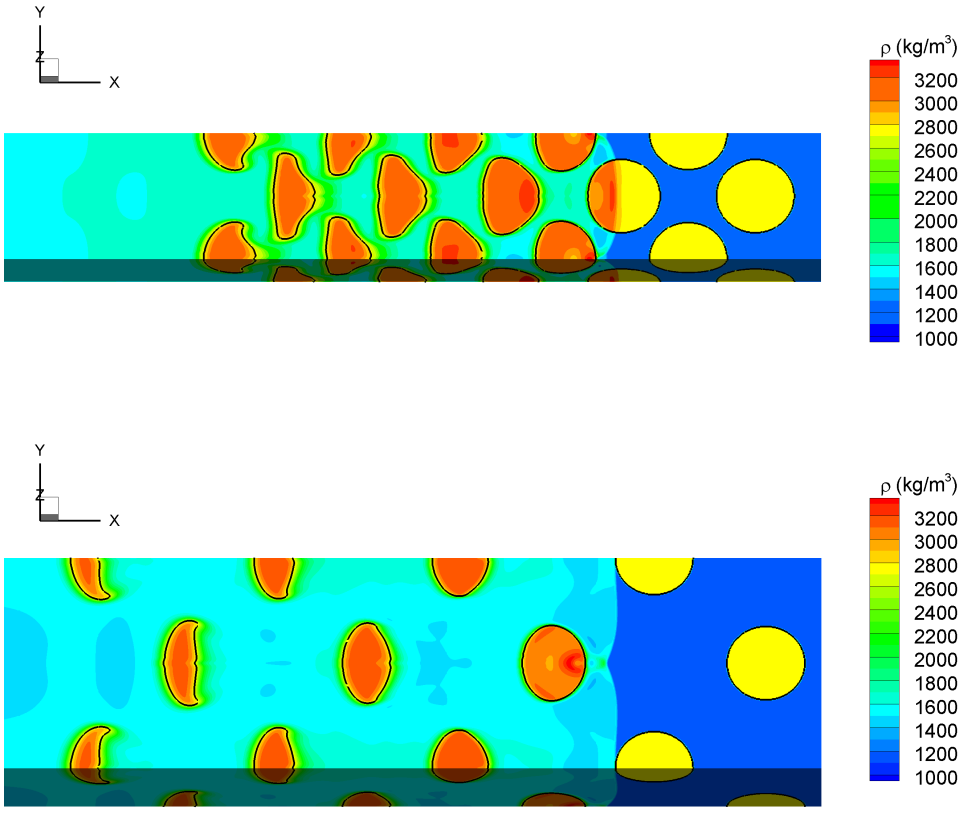

Figure 5.23: Fluid and particle density distribution and particle deformation for CJ shock propagation through a particle matrix: $\phi_{s0} = 0.520$ (upper) and $\phi_{s0} = 0.093$ (lower).

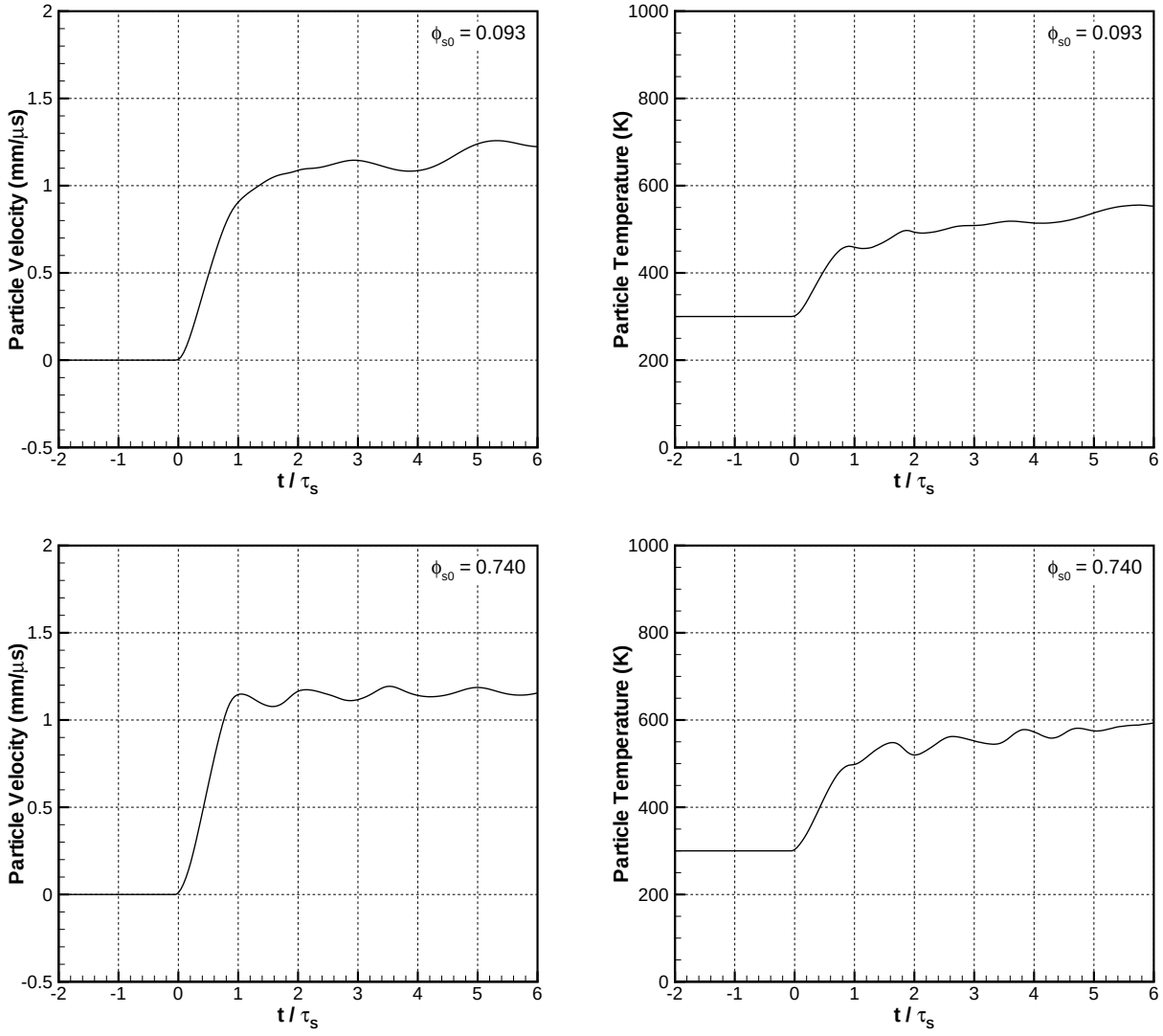

Figure 5.24: Mass-averaged particle velocity and temperature for CJ shock interaction at the large particle limit: $\phi_{s0} = 0.093$ (upper) and $\phi_{s0} = 0.740$ (lower).

5.3.3 Results for the intermediate regime ($d_p/L_R \sim 1$)

Detonation interaction in the intermediate regime was shown for single particles ($\phi_{s0} \to 0$) in §5.2.2. For packed particle matrices, the situation is more complex with reverberating waves and lateral expansions that further influence the particle and surrounding flow. Figure 5.25 illustrates the irregular propagation pattern of the detonation front in an NM/Al matrix ($d_p = 1$ μm, $d_p/L_R = 0.5$), where the detonation travels within the explosive contained in the voids and narrow channels between particles in addition to shock propagation within the metal. In close-packed matrices, transmission of the shock through the particle can subsequently pre-compress and initiate detonation in the fresh explosive on the far side of the particle prior to the diffracted shock arrival (hot-spot mechanism). For the conditions depicted in Figure 5.25, the NM behind the particle trailing edge reaches 800 K due to shock transmission and prior to reaction.

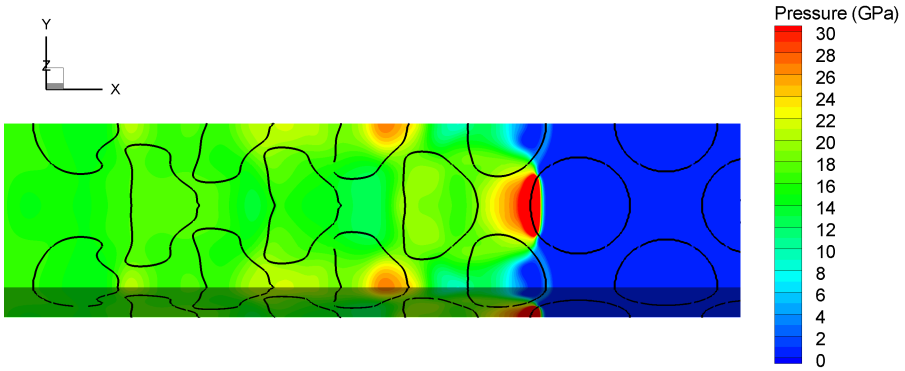

Figure 5.25: Pressure distribution and particle deformation for detonation ($d_p/L_R = 0.5$) through a packed particle matrix ($\phi_{s0} = 0.428$).

Figure 5.26 shows numerical pressure gauge results for detonation in a close-packed matrix, with the peak reflected VN shock pressure followed by oscillations at a frequency proportional to particle diameter and later by the Taylor wave expansion. Figure 5.26 (left) shows a precursor shock with magnitude of about 10 GPa (temperature approximately 1300 K) that was transmitted through the particle trailing edge into the void prior to arrival of the diffracted VN shock. Figure 5.26 (right) shows a smaller precursor shock exiting the trailing edge and a larger peak pressure due to collision of the diffracted shocks behind the particle trailing edge.

Figure 5.27 shows the particle velocity and temperature histories in a packed particle matrix for $d_p/L_R = 0.2$ where the detonation reaction zone is larger than the particle size.

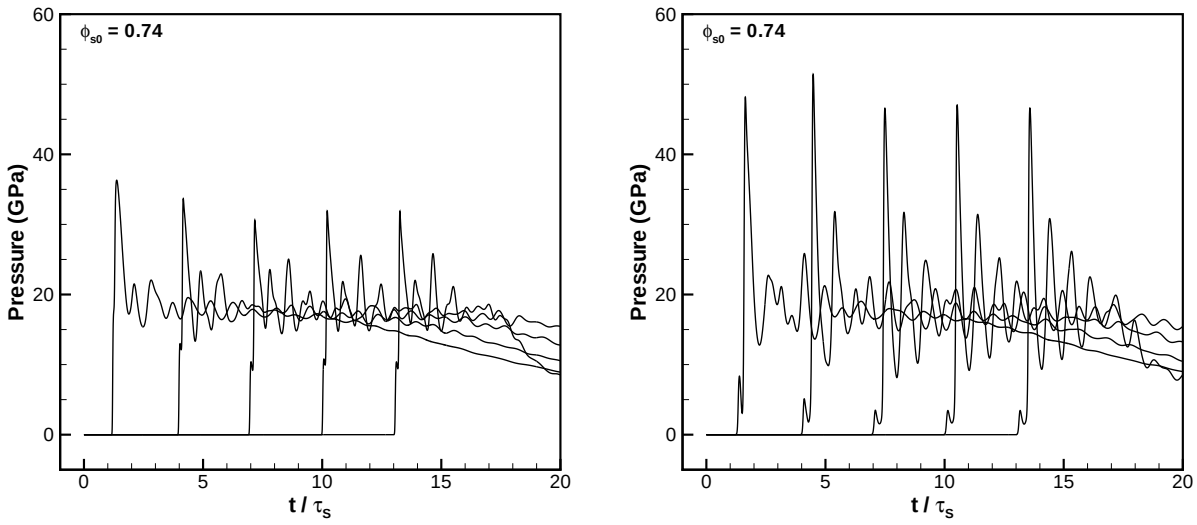

Figure 5.26: Gauge histories from nitromethane detonation ($d_p/L_R = 0.5$) in a close-packed matrix ($\phi_{s0} = 0.74$) with 20 layers of aluminum particles: pressure at particle leading edge (left) and pressure in voids behind trailing edges (right). Each curve presents successive results from the 1^{st}, 5^{th}, 9^{th}, 13^{th} and 17^{th} layers.

This is evident in the particle velocity history result, where the velocity first increases during interaction with the VN shock, and then decreases mainly over $5\tau_S$ during the expansion inside the reaction zone. The $2\tau_S$ assumption (§2.6) is especially justified by the temperature history where the first peak is reached between $1\tau_S$ and $2\tau_S$.

5.3.4 Additional detonation phenomena

Figure 5.28 (left) shows the detonation velocity through the packed particle matrices saturated with liquid explosive. The bulk shock propagation velocity was measured using wave time of arrival between consecutive numerical gauge stations located in an array perpendicular to the averaged detonation wave front. Under the detonation conditions studied here (i.e., aluminum particles in nitromethane), shock waves reflected from the leading edge of the particles cause an increase in the local NM density and pressure, thereby increasing the detonation velocity. Furthermore, waves traveling within the metal particle are transmitted into the fresh liquid explosive ahead of the detonation wave diffracting around the curved particle surface, thereby pre-compressing the explosive and increasing the local detonation velocity. Both of these local hot-spot factors contribute to bulk propagation speeds in excess of the CJ value in neat NM. In the present numerical

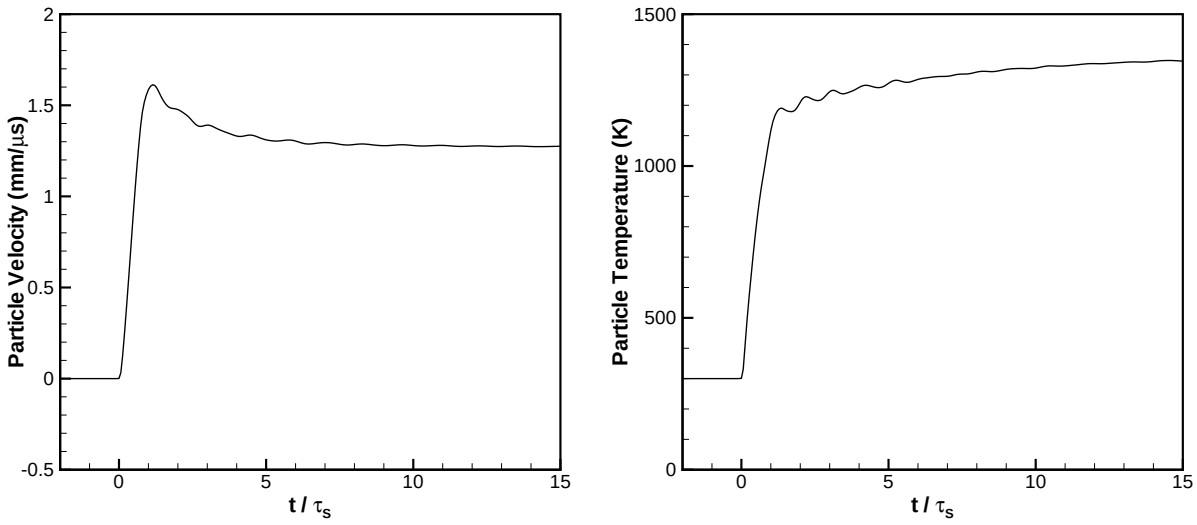

Figure 5.27: Particle velocity and temperature histories for nitromethane detonation in a dense matrix of aluminum particles with $d_p/L_R = 0.2$ and $\phi_{s0} = 0.74$.

calculations, the greatest bulk propagation velocities (up to 7.4 mm/μs) were observed for the highest metal mass fraction condition in combination with the smallest particle diameter (or longest reaction zone) within the region of the first particle layer. Afterwards, the momentum and energy transferred into the particles within the detonation zone compete with the local hot-spot factors, resulting in a quasi-steady propagation velocity with a deficit. The velocity deficit increases with an increase in solid volume fraction and a decrease in particle diameter. The maximum velocity deficit corresponds to a wave speed of 5.3 mm/μs and occurs for the small particle limit.

Figure 5.28 (left) shows increasing instability in the detonation front velocity for higher solid volume fractions, which is an expected feature due to high momentum and heat loss. The initially transient shock velocity becomes quasi-steady after traveling a distance of $6d_p$ into the matrix. Figure 5.28 (right) illustrates the quasi-steady detonation shock velocity as a function of increasing metal mass fraction. In comparison to Cheetah chemical equilibrium predictions using inert aluminum, where velocity and temperature equilibrium are assumed for all phases (see Fried et al. [68]), the mesoscale results for detonation shock velocity are consistently higher since the relative velocity of the solid phase remains below the flow velocity following the shock interaction. Similarly, the Cheetah equilibrium temperature is also lower than the mesoscale detonation results due to the same phase-non-equilibrium nature.

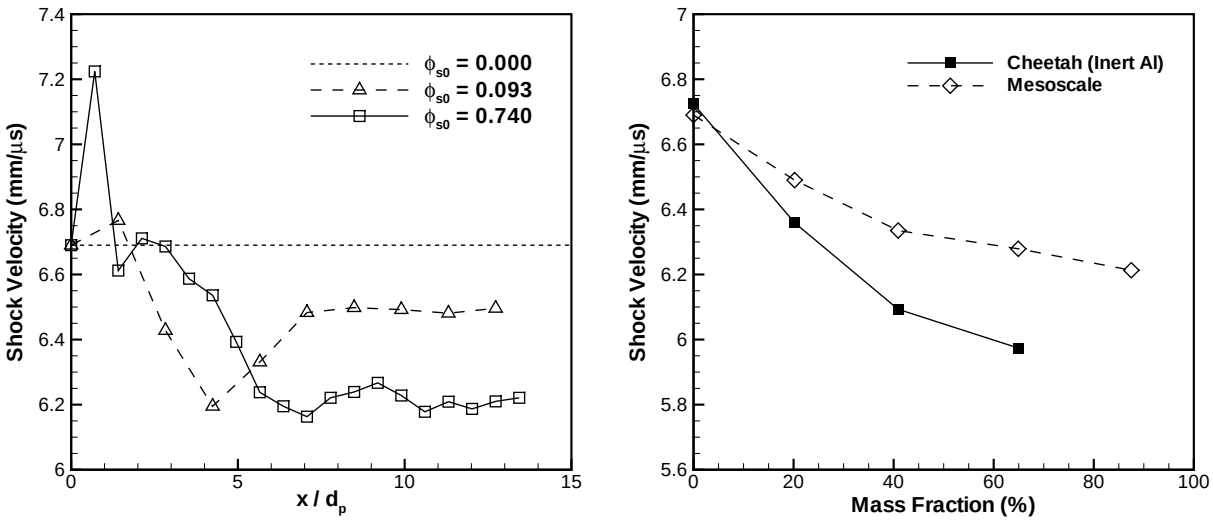

Figure 5.28: Detonation velocity through packed particle matrices ($d_p = 1$ μm; $L_R = 2$ μm): unsteady propagation velocity through several layers of aluminum particles with distance measured from the first layer (left) and quasi-steady propagation velocity for various aluminum mass fractions (right).

5.4 Shock compression transmission factors

The velocity and temperature transmission factors, α and β, were defined in Equations (2.19) and (2.20). For inert shocks, the effect of density ratio of explosive to solid particle on velocity transmission was presented in §5.2.1; the effect of packing configuration was evaluated in §5.3.1. The remaining influences of the volume fraction and detonation reaction-zone length on the velocity and temperature transmission factor are summarized in this section. They are evaluated for both a single particle and a matrix of particles.

5.4.1 Particle acceleration

Figure 5.29 shows the mesoscale results of the single particle velocity and corresponding transmission factor as a function of $\delta = d_p/L_R$. Both the velocity and the velocity transmission factor decrease from VN to CJ mainly over the interval from $0.1 \leq \delta \leq 1$. The single particle acceleration results are bound by the small particle limit ($\delta \to 0$) and the large particle limit ($\delta \to \infty$). The resulting velocity transmission factor was fit to the sigmoidal function:

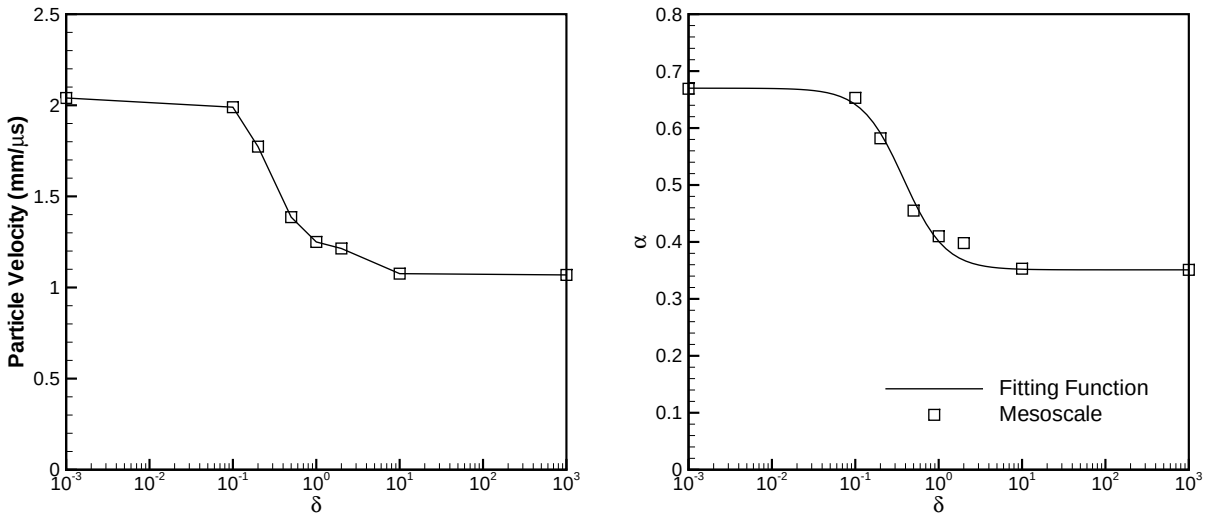

Figure 5.29: Shock compression acceleration of a single particle ($\phi_{s0} \to 0$) in a detonation flow: mass-averaged velocity for various particle diameters (left) and velocity transmission factor versus δ (right).

$$\alpha = \alpha_{\mathrm{CJ}} + \frac{\alpha_{\mathrm{VN}} - \alpha_{\mathrm{CJ}}}{1 + \exp\left[\dfrac{-\log(\delta/\delta_0)}{w}\right]} \tag{5.1}$$

The fitting function is plotted in Figure 5.29, where $\delta_0 = 0.38$ and $w = 0.25$. In Equation (5.1), $\alpha_{\mathrm{CJ}} = \alpha(\delta \to \infty) = 0.351$ and $\alpha_{\mathrm{VN}} = \alpha(\delta \to 0) = 0.669$.

Figure 5.30 summarizes the particle velocity and velocity transmission factors for the nitromethane/aluminum matrix. The results are plotted as a function of volume fraction, where $\phi_{s0} = 0$ represents the single particle results and $\phi_{s0} = 1$ represents the semi-infinite slab results. The remaining points are taken from the mesoscale results that employed close-packed spheres; the volume fraction was adjusted by changing the inter-particle spacing. For the various $\delta = d_p/L_R$ considered, there is weak similarity in the results, which are bound by limiting cases of $\delta \to 0$ for VN shock interaction and $\delta \to \infty$ for CJ shocked flow conditions. The velocity and velocity transmission factor exhibit an inverted U-shaped dependence on volume fraction for the various δ considered. From Figure 5.30, the maximum α generally occurs at $\phi_{s0} = 0.219$ ($s = 0.5d_p$), above which the transmission decreases linearly for increasing ϕ_{s0}. The regime of primary interest for dense granular flow in condensed explosives is from $0.2 \lesssim \phi_{s0} \lesssim 0.6$.

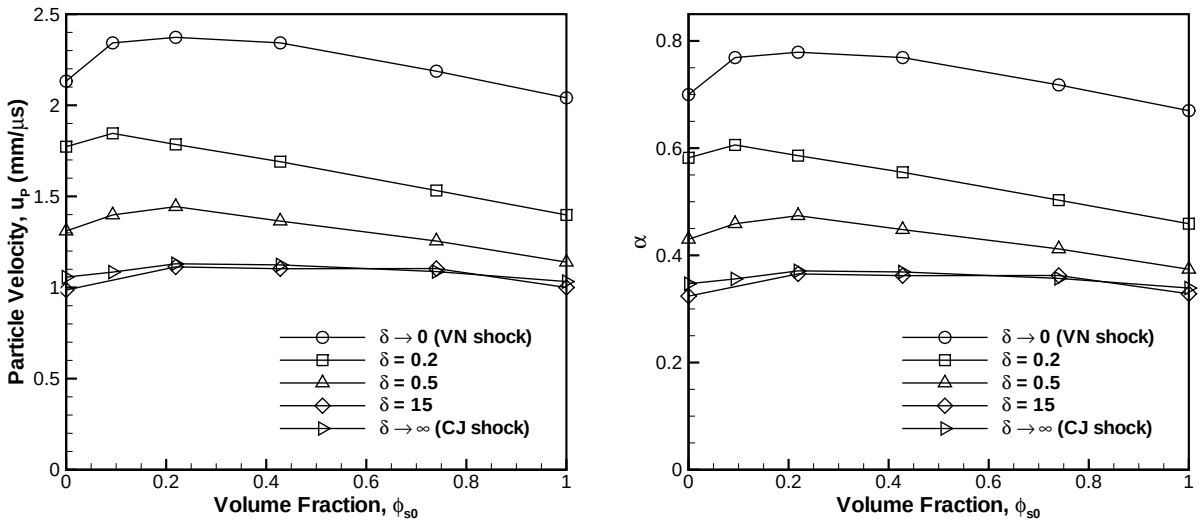

Figure 5.30: Shock compression acceleration results in a particle matrix: range of transmitted velocity between the interaction limits (left) and the corresponding velocity transmission factors (right).

The velocity transmission factor results were fit to a function of volume fraction and detonation reaction-zone length: $\alpha = \alpha(\phi_{s0}, \delta)$. The volume fraction effect was represented by a second-order polynomial function of ϕ_{s0}. The reaction-zone-length influence is exhibited as a shift in the velocity transmission factor, which was represented using an exponential function of δ and a fixed offset. The resulting function contains five fitting constants, as follows:

$$\alpha = c_1\phi_{s0}^2 + c_2\phi_{s0} + c_3\exp(-c_4\delta) + c_5 \tag{5.2}$$

where $c_1 = 0.2$, $c_2 = 0.1$, $c_3 = 0.4$, $c_4 = 3.3$ and $c_5 = 0.36$. Physically, two of the coefficients are interpreted as follows:

$$\begin{aligned} c_3 &= (\alpha_{\rm VN} - \alpha_{\rm CJ})_{\max} = \alpha(\phi_{s0} = 0.25, \delta \to 0) - \alpha(\phi_{s0} = 0.25, \delta \to \infty) \\ c_5 &= (\alpha_{\rm CJ})_{\max} = \alpha(\phi_{s0} = 0.25, \delta \to \infty) \end{aligned}$$

A comparison of the fitting function to the mesoscale results is given in Figure 5.31. The agreement is reasonable for $\delta < 1$. The largest differences occurred for high volume fractions in the large particle limit.

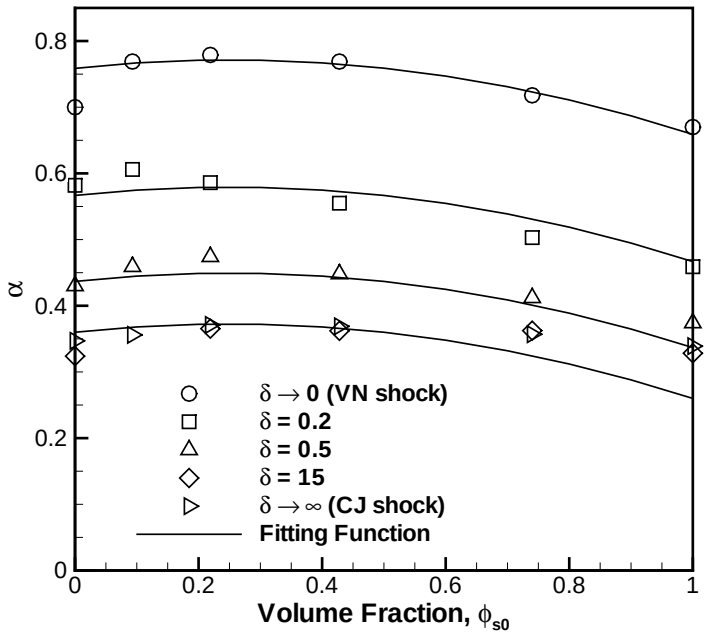

Figure 5.31: Multi-variable fitting for velocity transmission factor.

5.4.2 Particle heating

Figure 5.32 shows the mesoscale results of the single particle temperature and corresponding transmission factors, β, which are monotonic decreasing functions for increasing $\delta = d_p/L_R$. Both the temperature and the temperature transmission factor decrease from the VN to CJ limiting values mainly over the interval from $0.1 \leq \delta \leq 10$. Similar to the velocity transmission factor, the temperature transmission factor for a single particle is fit to the sigmoidal function:

$$\beta = \beta_{\mathrm{CJ}} + \frac{\beta_{\mathrm{VN}} - \beta_{\mathrm{CJ}}}{1 + \exp\left[\dfrac{-\log(\delta/\delta_0)}{w}\right]} \tag{5.3}$$

The fitting function is plotted in Figure 5.32, where $\delta_0 = 0.70$, $w = 0.45$, $\beta_{\mathrm{CJ}} = 0.170$, and $\beta_{\mathrm{VN}} = 0.337$.

Figure 5.33 shows the particle temperature and corresponding β transmission factors in the nitromethane/aluminum matrix as a function of volume fraction. The results are bound by the small particle limit ($\delta \rightarrow 0$) and large particle limit ($\delta \rightarrow \infty$). For a given volume fraction, β increases with the reaction-zone length (decreasing δ). Furthermore, the

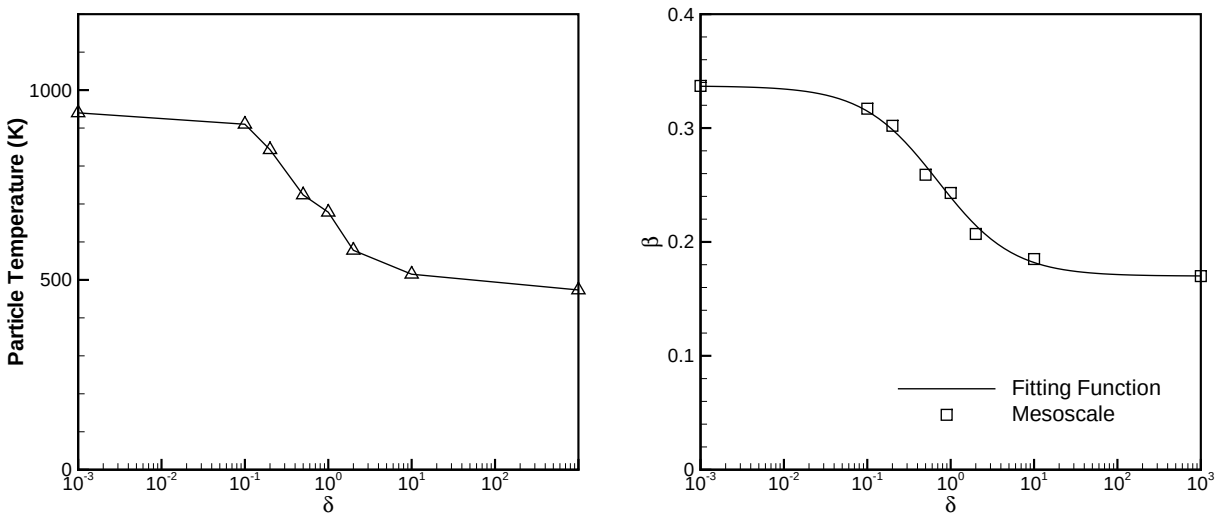

Figure 5.32: Shock compression heating of a single particle ($\phi_{s0} \rightarrow 0$) in detonation flow: mass-averaged temperature of single particles of various diameters (left) and the corresponding temperature transmission factors (right).

peak β value occurs at higher solid volume fractions as the reaction-zone length increases (decreasing δ). Although the temperature transmission factor exhibits an inverted U-shaped functional dependance on volume fraction in general, there is insufficient similarity in the solution for a fitting function to be determined.

5.4.3 Correlation of the transmission factors

The detonation reaction-zone length has a significant influence on the velocity and temperature transmission factors. Physical interpretation of the interaction of the particle with the detonation flow is briefly considered in this section, in an attempt to reduce the range of α and β between the interaction limits.

In the intermediate regime, the particle diameter and detonation reaction zone have comparable length scales. However, particles of different diameters are subjected to local detonation flow conditions ranging from the VN to CJ states with various degrees of reaction in between. As illustrated in Figures 5.22, 5.23, 5.25, and 5.26, the *in situ* wave is unsteady and multi-dimensional. Therefore, the reference shocked fluid state for the velocity and temperature transmission factors, α and β, in Equations (2.19) and (2.20) will be re-defined here. This is achieved by integrating the material velocity and temperature profile over an ideal 1D ZND detonation structure from the leading shock to a distance

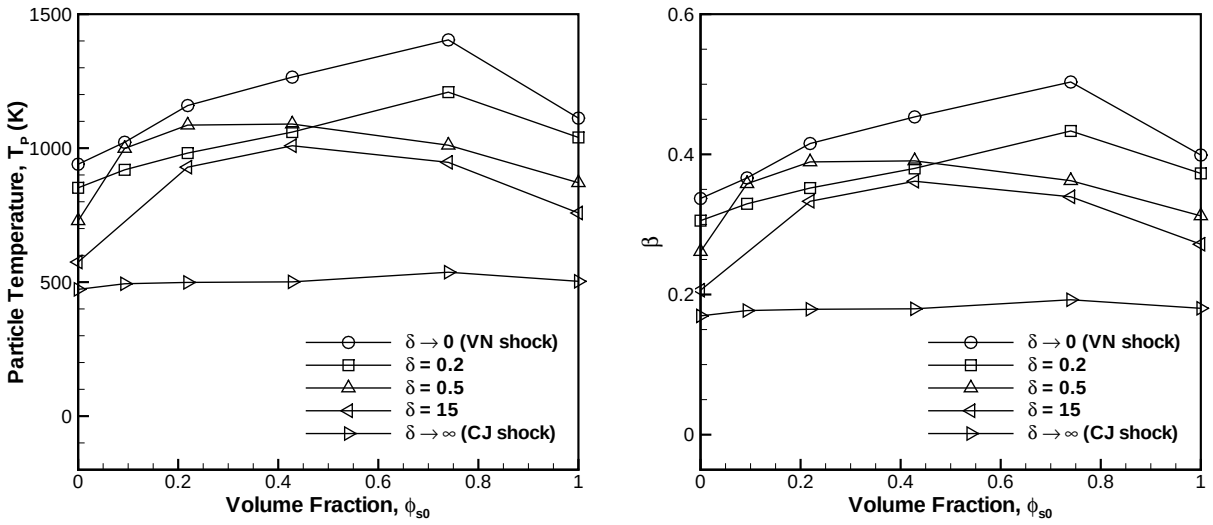

Figure 5.33: Shock compression heating results in a particle matrix: range of transmitted particle temperature between the interaction limits (left) and corresponding temperature transmission factors (right).

corresponding to the particle diameter, and then dividing it by the particle diameter:

$$\overline{u_f} = \frac{1}{d_p}\int_0^{d_p} u_f(\ell)d\ell, \quad \overline{T_f} = \frac{1}{d_p}\int_0^{d_p} T_f(\ell)d\ell, \tag{5.4}$$

where ℓ is the position along the integration length. For the inert Heaviside step shock in the small particle limit ($\delta = d_p/L_R \ll 1$), $u_f(\ell) = u_{f1}$ = constant and $T_f(\ell) = T_{f1}$ = constant; thus, Equation (5.4) results in $\overline{u_f} = u_{f1}$ and $\overline{T_f} = T_{f1}$. For $\delta = 1$, the resulting integrated fluid velocity of $\overline{u_f} = 2.006$ mm/μs is between the VN and CJ flow speeds, while the integrated temperature of $\overline{T_f} = 3740$ K is above both the VN and CJ temperatures. As shown by Mader [133], the Grüneisen parameter for the condensed explosive affects the reaction-zone length and can result in maximum temperatures within the reaction zone that are above the CJ value.

Single particle results

When using a constant shocked fluid velocity, $u_{\rm VN} = 3.046$ mm/μs, as the reference, the velocity transmission factor decreases from VN to CJ mainly over the interval from $0.1 \le \delta \le 1$, as shown in Figure 5.34(left). Changing the reference velocity to $\overline{u_f}$, the velocity transmission values are less dependent on δ. The resulting range of α for a single particle is reduced to 0.61 – 0.72.

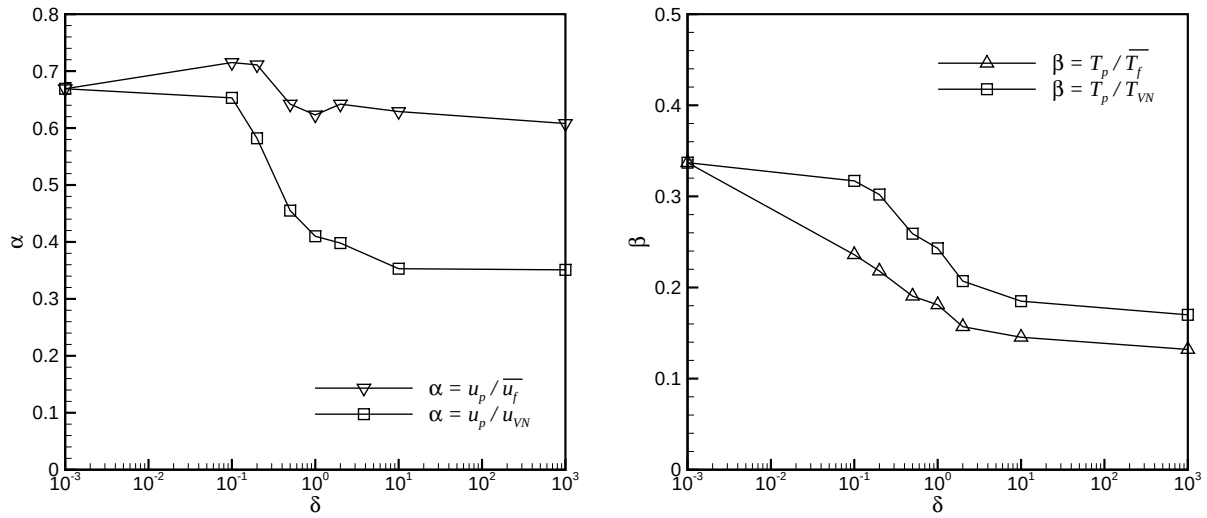

Figure 5.34: Shock compression acceleration and heating of a single particle ($\phi_{s0} \to 0$) in a detonation flow: velocity transmission factors (left) and temperature transmission factors (right) versus δ for various scaling methods.

Figure 5.34(right) illustrates that the temperature transmission factors scaled using T_{VN} are greater than those obtained using $\overline{T_f}$. This is an expected result since the shocked fluid is unreacted at the VN point. For $\delta \to 0$, $\overline{T_f} \to T_{\mathrm{VN}}$ and the transmission factors for both scalings become identical. Using $\overline{T_f}$ as the reference temperature reduced the range of β in the intermediate regime ($\delta \sim 1$). The temperature transmission factor with respect to the integrated reference value $\overline{T_f}$ decreases exponentially with an increase in δ, as shown by the linear trend when plotted on log scale.

Matrix particle results

Figure 5.35 shows that the velocity transmission factors collapse into a band approximately 0.14 wide when using the integrated shocked fluid velocity scaling. The results displayed in Figure 5.20 are included, as indicated by the line of $\delta \to 0$ (Inert Shock), which further demonstrates the collapsing of the velocity transmission factor. The remaining scatter may also be related to the other factors, such as shock strength and particle deformation. The change in fluid material due to reaction may also provide an additional effect. Further, the reference velocity was based on the ideal steady detonation wave in the absence of a particle bed and velocity deficit caused by momentum and heat transfer to the particles; therefore, local changes to reaction-zone length due to hot spots may also play a role.

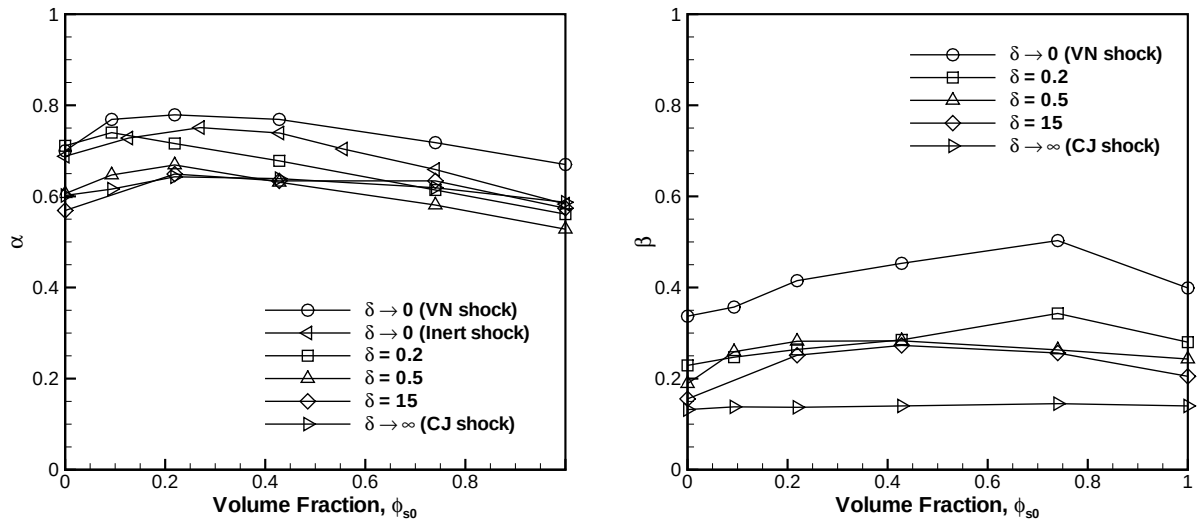

Figure 5.35: Shock compression acceleration and heating results in a particle matrix: reduction of the velocity transmission factor and temperature transmission factor when using integrated velocity, $\overline{u_f}$ (left), and temperature, $\overline{T_f}$ (right).

Figure 5.35 shows the particle temperature and corresponding β transmission factors in the nitromethane/aluminum matrix as a function of volume fraction. The temperature transmission factors are scaled using the integrated fluid temperature $\overline{T_f}$. Similar to particle acceleration, the particle heating is bound between the small particle and large particle limiting cases, and the effect of solid volume fraction on β is reduced for larger particles ($\delta \to \infty$). For volume fractions relevant to dense granular flow in condensed explosives (i.e., $0.2 < \phi_{s0} < 0.6$), the range of β is limited to 0.25 – 0.35 across two orders of magnitude for the ratio of $\delta = d_p/L_R$ (i.e., for $0.2 \leq \delta \leq 15$).

5.5 Free-edge condition

The preceding results were inertially confined, assuming infinite-diameter conditions. When the detonation reaches the edge of the charge, the explosive products break-out, expanding and driving a shock into the surrounding environment, while an expansion wave travels back into the charge. The free-edge provides a boundary condition at which the flow begins to transition from the detonation regime to the dense dispersal regime.

Considering a small but representative piece of the free edge of the charge, the explosive/air interface is assumed to be planar at the mesoscale. The free-edge was

preliminarily investigated using a 1D slab particle in Section 5.1.4. The edge condition is further investigated in 2D using cylindrical 'particles', as shown in Figure 5.36. Considering a reactive shock propagating into a NM/Al charge, the full inviscid model results in a flow similarity in which the flow field for any diameter of particles is scaled to the flow field at a given diameter of particles (see Sections 2.5.1 and 2.5.2). A 5 mm particle diameter is therefore chosen to facilitate the simulation. An inter-particle spacing of 1 mm in a hexagonal packing configuration results in a solid volume fraction of 0.63. The conditions for the reactive shock in NM are: $p = 13.3$ GPa and $D_0 = 6.690$ mm/μs. The particles are numbered in terms of layers, beginning at the outer edge of the charge. Layer 1 is closest to the free surface; Layer 5 is furthest from the edge of the charge (see Figure 5.36).

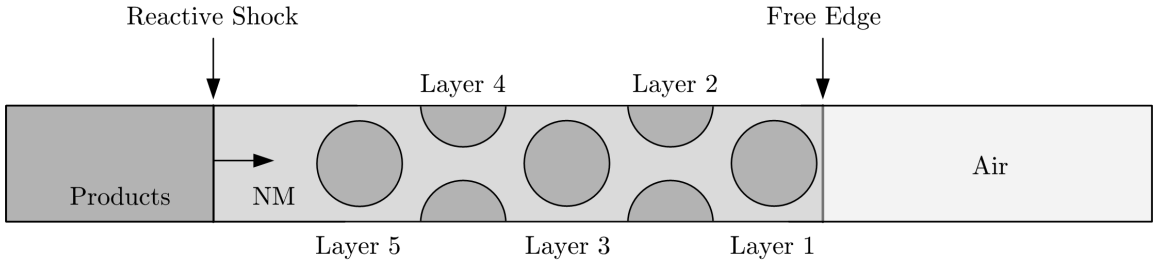

Figure 5.36: Two-dimensional mesoscale configuration for an inert shock interacting with a particle matrix at the free edge of the charge.

Figure 5.37 shows a slice (cut through the centre of Layers 2 and 4) of the spatial pressure distribution during shock interaction with particles at the free edge of the charge. The interaction of the shock with the particles has a two-dimensional structure with transverse waves, which is represented by the oscillating pressure in the matrix. When the shock reaches the edge of the charge, a strong rarefaction wave travels back into the mixture of NM detonation products and aluminum particles.

The mass-centre particle velocity results show a transmitted shock with a material velocity of 1.2 mm/μs as shown in Figure 5.38, followed by acceleration to above 2.5 mm/μs in the rarefaction expansion. Reflection of the shock from the upstream and downstream particles causes fluctuations in the particle velocity before the edge rarefaction takes over. Layer 1 does not have a downstream particle or condensed matter backing, and is therefore subject to a much stronger rarefaction which accelerates the particle, as explained in Section 5.1.4. The edge rarefaction travels upstream, accelerating the particles layer by layer. The greatest particle velocity occurred in the outermost layer due to the free-edge condition.

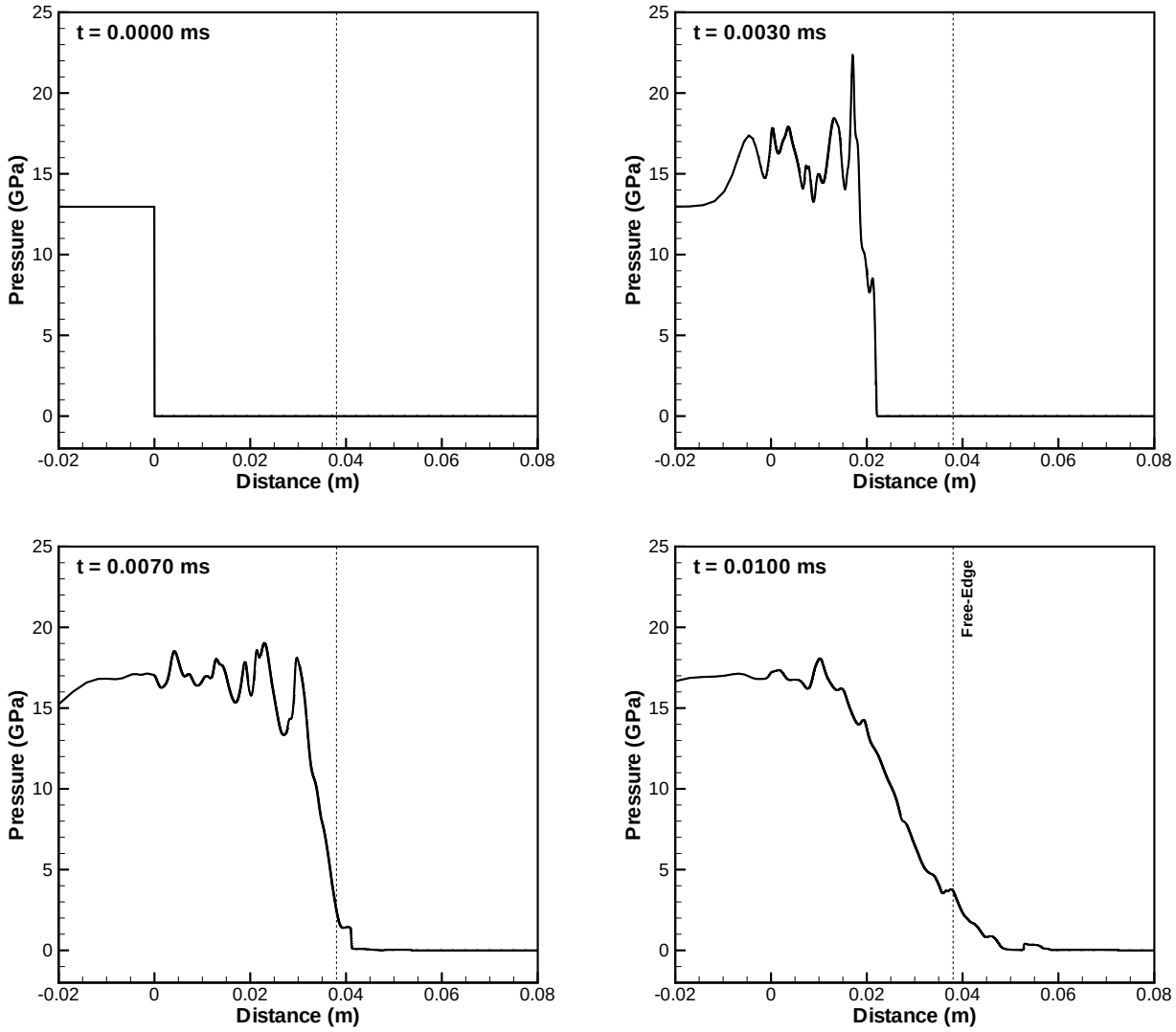

Figure 5.37: Pressure-distance profiles during free-edge expansion.

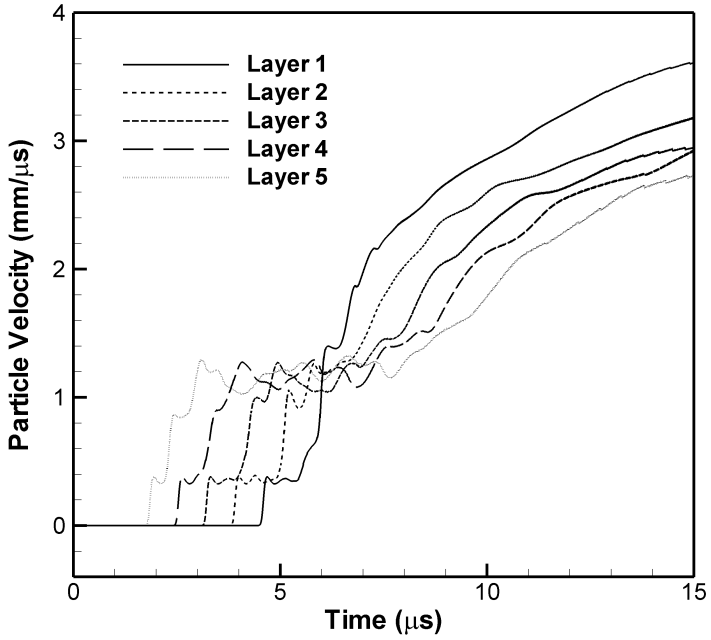

Figure 5.38: Mass-centred particle velocity near the free edge of the charge.

5.6 Summary of mesoscale results

Continuum modeling of particles at the mesoscale provided the key results for shock and detonation conditions. One-, two- and three-dimensional mesoscale simulations were employed to study interactions across the full range of volume fraction and various particle packing configurations. Shock physics were demonstrated using pressure, velocity, and temperature measurements in the explosive and solid particles. Detonation in matrices of packed aluminum particles saturated with nitromethane was studied, where the shock interaction timescale was resolved. The three-dimensional structure of detonation including hot spots and transverse waves were observed and related to detonation instability and velocity deficit. The resulting momentum and heat transfer to the particles were quantified in terms of the relevant parameter groups. Particle acceleration and heating within the shock and detonation zone are expressed in terms of shock compression velocity transmission factors $\alpha = u_{p1}/u_{f1}$ and temperature transmission factors $\beta = T_{p1}/T_{f1}$. In addition to the Mach number, the transmission factors are a function of the solid volume fraction, the density ratio of explosive to solid particle, and the ratio of particle diameter to detonation reaction zone length.

Chapter 6

Application to macroscopic modeling

Detonation of multiphase or slurry explosives involves rapid acceleration and heating of solid particles due to shock compression. The resulting momentum and energy exchange affects the detonation performance of the explosive, and also the dispersal and subsequent reaction of metal particles. Physical models are therefore formulated to represent the effects of the microscopic interaction of the detonation shock with the particles. They are applicable to an engineering modeling scale so that this acceleration and heating mechanism can be realized in practical problems.

In this chapter, the shock transmission factors from the mesoscale calculations are applied to formulate macroscopic functions for drag force and heat transfer rate. The macroscopic framework is first explained, which is suitable for implementation of the new models as source terms. The resulting new shock compression models are formulated as a drag coefficient and Nusselt number, which are then explored analytically. The shock compression acceleration and heating correlations are applied to two sets of challenging tests: first, heterogeneous detonation is considered for aluminum particles saturated with liquid nitromethane; and second, inert particle dispersal is studied using a spherical charge containing steel beads saturated with nitromethane.

6.1 Macroscale framework

The macroscale framework given below describes the conservation laws for a generalized two-phase flow, which is representative of a dense flow of particles in condensed explosives. At the macroscale, continuum theory is assumed for the particle phase where the number

density is above 10^{10} m^{-3} for a dense flow of particles smaller than 100 μm. The basic two-phase governing equations (Equations 3.40 – 3.42) can be re-written by employing some of the assumptions and simplifications from Chapters 3 and 4. In particular, the viscous and conduction terms are removed for high-Reynolds-number flow (i.e., $Re \to \infty$). The resulting set of governing equations, therefore, describes an inviscid and non-heat-conducting fluid flow. Exchange of mass, momentum, and energy occur through the multiphase source terms. An explicit dynamic compaction source term has been omitted (see Baer and Nunziato [10]); the compaction effect on the solid volume fraction is included in the shock compression momentum and heat transfer coefficients obtained from the mesoscale calculations. The macroscopic two-phase equations are summarized as follows:

Fluid Phase:

$$\begin{aligned}
\frac{\partial(\sigma_f)}{\partial t} + \frac{1}{r^n}\frac{\partial}{\partial r}(r^n \sigma_f u_f) + \frac{\partial}{\partial y}(\sigma_f v_f) &= -J_p \\
\frac{\partial}{\partial t}(\sigma_f u_f) + \frac{1}{r^n}\frac{\partial}{\partial r}\left[r^n(\sigma_f u_f^2 + p_f\phi_f)\right] + \frac{\partial}{\partial y}(\sigma_f u_f v_f) &= -J_p u_p - F_{pr} \\
\frac{\partial}{\partial t}(\sigma_f v_f) + \frac{1}{r^n}\frac{\partial}{\partial r}(r^n \sigma_f u_f v_f) + \frac{\partial}{\partial y}(\sigma_f v_f^2 + p_f\phi_f) &= -J_p v_p - F_{py} \\
\frac{\partial}{\partial t}(\sigma_f E_f) + \frac{1}{r^n}\frac{\partial}{\partial r}\left[r^n(\sigma_f u_f E_f + p_f\phi_f u_f)\right] + \frac{\partial}{\partial y}(\sigma_f v_f E_f + p_f\phi_f v_f) &= -J_p(E_p + Q_p) \\
&\quad -F_{pr}u_p - F_{py}v_p + Q_R \\
\frac{\partial \sigma_f Y_{fj}}{\partial t} + \frac{1}{r^n}\frac{\partial}{\partial r}(r^n \sigma_f u_f Y_{fj}) + \frac{\partial}{\partial y}(\sigma_f v_f Y_{fj}) &= -\omega_j
\end{aligned} \tag{6.1}$$

Particle Phase:

$$\begin{aligned}
\frac{\partial(\sigma_p)}{\partial t} + \frac{1}{r^n}\frac{\partial}{\partial r}(r^n \sigma_p u_p) + \frac{\partial}{\partial y}(\sigma_p v_p) &= J_p \\
\frac{\partial}{\partial t}(\sigma_p u_p) + \frac{1}{r^n}\frac{\partial}{\partial r}(r^n \sigma_p u_p^2) + \frac{\partial}{\partial y}(\sigma_p u_p v_p) &= J_p u_p + F_{pr} \\
\frac{\partial}{\partial t}(\sigma_p v_p) + \frac{1}{r^n}\frac{\partial}{\partial r}(r^n \sigma_p u_p v_p) + \frac{\partial}{\partial y}(\sigma_p v_p^2) &= J_p v_p + F_{py} \\
\frac{\partial}{\partial t}(\sigma_p E_p) + \frac{1}{r^n}\frac{\partial}{\partial r}(r^n \sigma_p u_p E_p) + \frac{\partial}{\partial y}(\sigma_p v_p E_p) &= J_p(E_p + Q_p) + F_{pr}u_p + F_{py}v_p \\
\frac{\partial n_p}{\partial t} + \frac{1}{r^n}\frac{\partial}{\partial r}(r^n n_p u_p) + \frac{\partial}{\partial y}(n_p v_p) &= N_p
\end{aligned} \tag{6.2}$$

The macroscale equations are presented for a generalized two-dimensional framework, although they can be directly extended to three dimensions. For 2D flow, the radial

symmetry coordinate system is planar for $n = 0$ and cylindrical for $n = 1$. For spherical problems modeled in 1D, $n = 2$; the details on radial symmetry can be found in [62] and [128].

In the governing equations, J_p is the mass transfer source term ($J_p = 0$ is assumed for inert particles without evaporation phase change), F_p is the momentum transfer force, and Q_p is the rate of heat transfer between phases. For the fluid phase, Q_R is a chemical reaction source term and ω_j are the reaction rates. The source term N_p represents the rate of change in the number of particles ($N_p = 0$ is assumed for no agglomeration/fragmentation). Particle acceleration and heating are, therefore, the dominant interaction exchange terms considered in this work. Using the standard definition for drag force on a spherical particle, and multiplying by the number of particles (n_p) within a macroscale control volume, the momentum source term is:

$$F_p = \frac{\pi d_p^2}{8} n_p \rho_f |u_f - u_p|(u_f - u_p) C_d \tag{6.3}$$

where C_d is the drag coefficient. The traditional convective heat transfer equation, multiplied by the number of particles, is used for the macroscopic model of the energy source term:

$$Q_p = \pi d_p n_p k_f (T_f - T_p) Nu \tag{6.4}$$

where k_f is the thermal conductivity of the fluid and Nu is the Nusselt number. Equations of state are required to close the system of equations (Equations 6.1 and 6.2). In addition, the monodisperse particle size assumption is used to relate the particle diameter to the number density: $n_p = 6\phi_p / \pi d_p^3$.

This type of multiphase model framework is based on the two-phase fluid-dynamic model of Kuo et al. [117] (see Kuo [116]). The model has been extended by Oran and Boris [153] for deflagration-to-detonation transition (DDT) in propellants, and by Baer and Nunziato [10] and Zhang et al. [226, 231] to model detonation in porous media and later particle dispersal.

6.2 Macroscopic model formulation

As discussed in Chapter 2 and 3, the traditional drag coefficient and Nusselt number correlations are not applicable in the shock compression regime in condensed matter.

Models for the acceleration and heating during the timescale for the detonation shock crossing the particle are required. As shown in Equations (3.18) and (3.39), these models are a function of the solid volume fraction of particles, density ratio of explosive to solid particles, ratio of particle size to detonation reaction-zone length, and Mach number. These functions have been quantitatively studied in the mesoscale simulations; the development of the macroscopic model is based primarily on the mesoscale shock compression results from Chapter 5. Additional details may be found in Ripley et al. [171].

6.2.1 Shock compression acceleration

The particle acceleration during the shock interaction can be obtained by differentiating the particle velocity with respect to time. The mesoscale results showed that the mass-averaged particle velocity was approximately linear during the shock interaction timescale (see Figures 5.19, 5.21, and 5.24). Figure 6.1 reproduces a typical mesoscale particle velocity history, superimposed with four options for representing the particle acceleration at the macroscale. The options, labeled Models a – d, are presented in Equations (6.5) – (6.8).

Model a:

$$u_p(t) = u_{p0} + (u_{p1} - u_{p0})\frac{t - t_0}{2\tau_S}, \quad \text{for } t_0 \le t \le t_0 + 2\tau_S, \tag{6.5}$$

Model b:

$$u_p(t) = \begin{cases} u_{p0} + [u_p(\tau_S) - u_{p0}]\,\frac{t-t_0}{\tau_S} & t_0 \le t \le t_0 + \tau_S \\ u_p(\tau_S) + [u_{p1} - u_p(\tau_S)]\,\frac{t-t_0-\tau_S}{\tau_S} & t_0 + \tau_s \le t \le t_0 + 2\tau_S \end{cases} \tag{6.6}$$

Model c:

$$u_p(t) = \begin{cases} u_{p0} + [u_{p1} - u_{p0}]\,\frac{t-t_0}{\tau_S} & t_0 \le t \le t_0 + \tau_S \\ u_{p1} & t_0 + \tau_s \le t \le t_0 + 2\tau_S \end{cases} \tag{6.7}$$

Model d:

$$u_p(t) = u_{p1}, \quad \text{for } t_0 \le t \le t_0 + 2\tau_S, \tag{6.8}$$

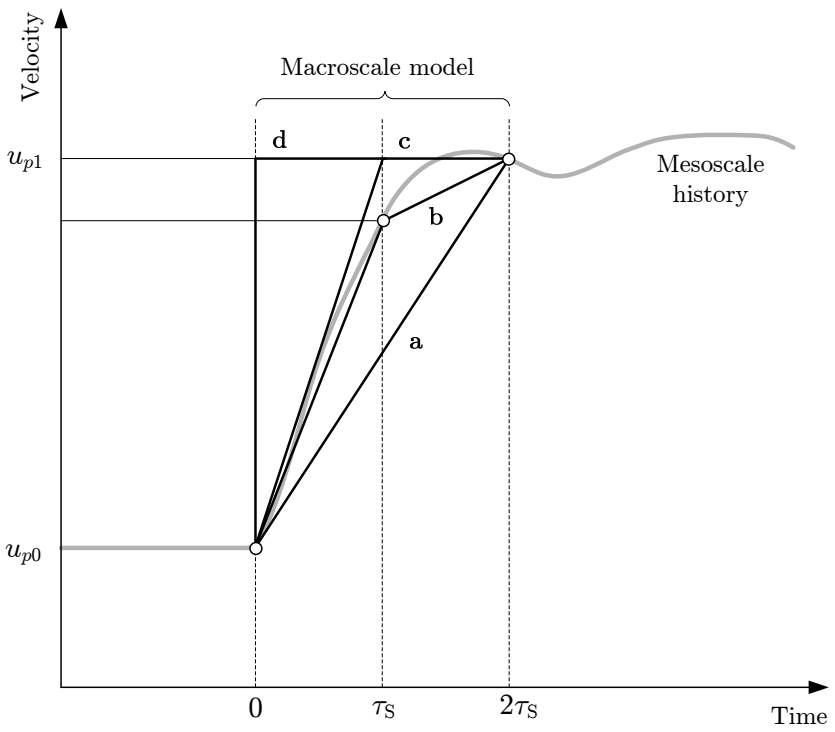

Figure 6.1: Macroscopic model options for particle acceleration compared to mesoscale particle velocity history.

where t_0 is the shock arrival time at the particle leading edge, and τ_S is the shock interaction time.

In Models a – d, $\tau_S = d_{p0}/D_0 =$ constant, $u_p(\tau_S) =$ constant, and $u_{p1} = u_p(2\tau_S) =$ constant, as determined from the mesoscale results. Note also that $u_p(t) = u_{p0}$ for $t < t_0$. With the exception of Model b, a simple acceleration can therefore be assumed as follows:

$$u_p(t) = u_{p0} + (u_{p1} - u_{p0})\frac{t - t_0}{\tau}, \quad \text{for } t_0 \leq t \leq t_0 + \tau, \tag{6.9}$$

where τ is the macroscale interaction time. For Model a, $\tau = 2\tau_S$; for Model c, $\tau = \tau_S$; and, for Model d, $\tau \to 0$, which may be represented by a Heaviside function. For the remainder of the model development, Model c is chosen since it best represents the mesoscale behaviour.

Employing the generalized particle velocity function in Equation (6.9) with $\tau = \tau_S$, the acceleration process can then be approximated assuming a constant acceleration over the interval as follows:

$$\frac{\mathrm{d}u_p}{\mathrm{d}t} \approx \frac{\Delta u_p}{\Delta t} = \frac{u_{p1} - u_{p0}}{\tau_S} \tag{6.10}$$

Since $u_{p1} = \alpha u_{f1}$ and $u_{p0} = 0$, the particle acceleration is then:

$$\frac{\mathrm{d}u_p}{\mathrm{d}t} = \frac{\alpha u_{f1}}{\tau_S} \tag{6.11}$$

Newton's law relating the force to the acceleration, written for a collection of n_p particles,

$$F_p = n_p \frac{\pi d_{p0}^3 \rho_{s0}}{6} \frac{\mathrm{d}u_p}{\mathrm{d}t} \tag{6.12}$$

is combined with Equation (6.3) for the standard definition for drag force on spherical particles, which gives the drag coefficient in terms of particle acceleration:

$$C_d = \frac{4\rho_{s0} d_{p0}}{3\rho_f |u_f - u_p|(u_f - u_p)} \frac{\mathrm{d}u_p}{\mathrm{d}t} \tag{6.13}$$

Substituting Equations (6.9) and (6.11) into Equation (6.13), while assuming $u_f \approx u_{f1}$, $u_{f1} > u_p(t)$ for $t \leq \tau_S$, and $\rho_f \approx \rho_{f1}$, an "effective" drag coefficient is obtained for the shock compression interaction:

$$C_d(t) = \frac{4\rho_{s0} d_{p0}}{3\rho_{f1}} \frac{\alpha u_{f1}}{\tau_S \left(u_{f1} - \frac{t-t_0}{\tau_S} u_{p1}\right)^2} \tag{6.14}$$

Finally, substituting $\tau_S = d_{p0}/D_0$ and $u_{p1} = \alpha u_{f1}$, the "effective" drag coefficient becomes:

$$C_d(t) = \frac{4\rho_{s0} D_0}{3\rho_{f1} u_{f1}} \frac{\alpha}{\left(1 - \frac{t-t_0}{\tau_S}\alpha\right)^2}, \quad \text{for } t_0 \leq t \leq t_0 + \tau_S. \tag{6.15}$$

where $\alpha = f\left(\phi_{s0}, \rho_{f0}/\rho_{s0}, d_p/L_R, M_0\right)$ can be obtained from the mesoscale simulations described in Chapter 5.

In a general sense for physical parameters, C_d may be a function of other physical parameters that are time-dependent, but preferably should not show an explicit time-dependence itself. In Equation (6.15), the explicit time dependence is caused by the assumption of Equation (6.10) in a convenient way to facilitate the numerical implementation.

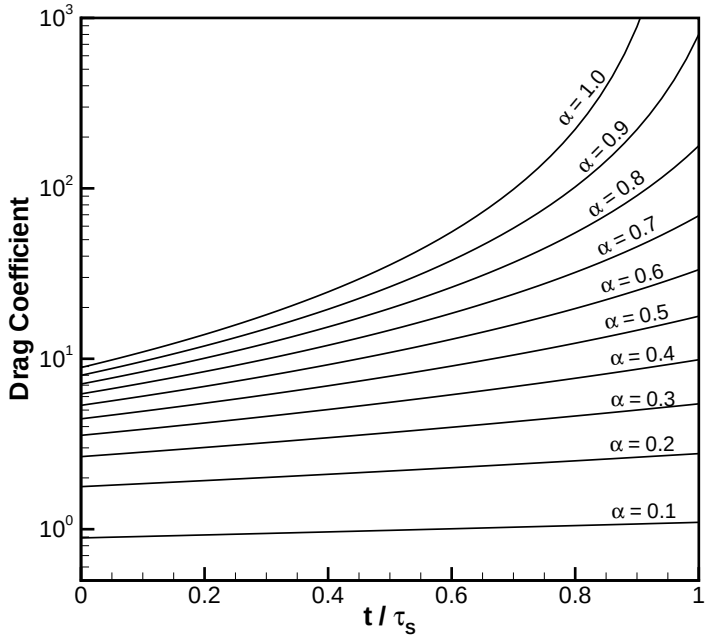

Figure 6.2: Shock compression effective drag coefficients for aluminum particles (ρ_{s0} = 2.700 g/cc) in a CJ shock in nitromethane (ρ_{f1} = 1.538 g/cc, D_0 = 6.612 mm/μs, u_{f1} = 1.742 mm/μs, using Cheetah with BKWS library and ρ_{f0} = 1.128 g/cc, T_{freeze} = 2145 K).

The resulting drag coefficient can be plotted for various velocity transmission factors, $0 \leq \alpha \leq 1$, during the shock interaction time, where $t_0 = 0$ for simplicity. Figure 6.2 shows the effective drag coefficient calculated from Equation (6.15) for aluminum particles in a CJ nitromethane shock flow. The effective drag coefficient model in Equation (6.15) is applicable to other condensed explosives containing metal particles.

For $\alpha = 0$, there is no shock compression acceleration and therefore $C_d(t) = 0$. As the value of α increases, there is a greater variation in C_d over the shock interaction time. For $\alpha = 1$, $C_d(t) \to \infty$ since $u_{p1} \to u_{f1}$ as $t \to \tau_S$.

6.2.2 Shock compression heating

Applying the same procedure to the particle heating, the Nusselt number for shock compression can be obtained. Similar to the acceleration, the particle heating rate in the mesoscale results is considered constant (see Figures 5.24 and 5.27) and, therefore, can be approximated by a linear function:

$$T_p(t) = T_{p0} + (T_{p1} - T_{p0})\frac{t - t_0}{\tau_S} \tag{6.16}$$

where t_0 is the shock arrival time at the particle leading edge. The heating process can then be approximated assuming a constant temperature rise over the interval as follows:

$$\frac{\mathrm{d}T_p}{\mathrm{d}t} \approx \frac{\Delta T_p}{\Delta t} = \frac{T_{p1} - T_{p0}}{\tau_S} \tag{6.17}$$

Since $T_{p1} = \beta T_{f1}$ and $T_{p0} \neq 0$, the particle heating rate is then:

$$\frac{\mathrm{d}T_p}{\mathrm{d}t} = \frac{\beta T_{f1} - T_{p0}}{\tau_S} \tag{6.18}$$

Combining the standard definition for convective heat transfer on spherical particles in Equation (6.4) with the heat transfer rate expression,

$$Q_p = n_p c_s \frac{\pi d_{p0}^3 \rho_{s0}}{6} \frac{\mathrm{d}T_p}{\mathrm{d}t} \tag{6.19}$$

gives the Nusselt number in terms of particle heating rate:

$$Nu = \frac{c_s \rho_{s0} d_{p0}^2}{6k_{f0}(T_f - T_p)} \frac{\mathrm{d}T_p}{\mathrm{d}t} \tag{6.20}$$

Substituting Equations (6.16) and (6.18) into Equation (6.20) and assuming $T_f \approx T_{f1}$, an "effective" Nusselt number is obtained for the shock compression interaction:

$$Nu(t) = \frac{c_s \rho_{s0} d_{p0}^2}{6k_{f0}} \frac{\beta T_{f1} - T_{p0}}{\tau_S \left[T_{f1} - T_p(t)\right]} \tag{6.21}$$

Finally substituting $\tau_S = d_{p0}/D_0$ and $T_{p1} = \beta T_{f1}$, the "effective" Nusselt number is then:

$$Nu(t) = \frac{c_s \rho_{s0} d_{p0} D_0}{6k_{f0}} \frac{\beta T_{f1} - T_{p0}}{\left(1 - \frac{t-t_0}{\tau_S}\beta\right) T_{f1} - \left(1 - \frac{t-t_0}{\tau_S}\right) T_{p0}}, \quad \text{for } t_0 \leq t \leq t_0 + \tau_S. \tag{6.22}$$

Figure 6.3 plots the resulting Nusselt number for various temperature transmission factors during one shock interaction time, where $t_0 = 0$ for simplicity. The Nusselt

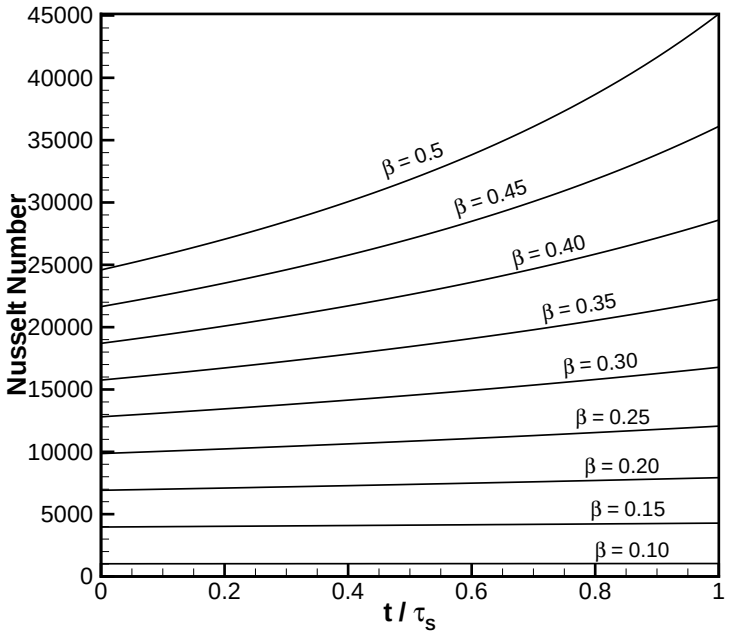

Figure 6.3: Shock compression effective Nusselt number ($d_p = 10$ μm) for aluminum particles ($\rho_s = 2.700$ g/cc, $c_s = 883$ J/kg-K) in a CJ shock in nitromethane ($\rho_{f1} = 1.538$ g/cc, $T_{f1} = 3628$ K, $D_0 = 6.612$ mm/μs, $u_{f1} = 1.742$ mm/μs, using Cheetah with BKWS library and $\rho_{f0} = 1.128$ g/cc, $T_{\text{freeze}} = 2145$ K).

number results plotted in Figure 6.3 are specific to aluminum particles in a constant CJ nitromethane detonation shocked flow, but can be recomputed for mixtures of other explosive and metal particles using Equation (6.22).

Since $T_{p0} = 300$ K, there is no shock compression heating for $\beta = T_{p0}/T_{f1}$ (i.e., $Nu(t) = 0$ when $T_{p0} = \beta T_{f1}$). In the above example, $Nu = 0$ for $\beta = 0.0827$. For $\beta < T_{p0}/T_{f1}$, $Nu(t) < 0$; therefore, $\beta = T_{p0}/T_{f1}$ sets a lower bound. For $\beta = 1$, $Nu(t) \to \infty$ since $T_{p1} \to T_{f1}$ as $t \to \tau_S$.

6.3 Verification of the shock compression model

Since the particle heating and acceleration were approximated as constant-rate processes during the shock compression, simple analytical and numerical evaluation of their implementation can be performed. The one-dimensional equation of motion and energy conservation can be readily discretized and integrated numerically:

$$u_p(t+\Delta t) = u_p(t) + \Delta t \left[\frac{3\rho_f}{4\rho_s d_p} |u_{f1} - u_p(t)|(u_{f1} - u_p(t)) C_d(t) \right] \tag{6.23}$$

$$T_p(t+\Delta t) = T_p(t) + \Delta t \left[\frac{6k_f}{\rho_s c_s d_p^2} (T_{f1} - T_p(t)) Nu(t) \right] \tag{6.24}$$

The shock compression drag coefficient and Nusselt number correlations are applied only during two shock interaction timescales:

$$C_d(t) = \begin{cases} 0 & t < t_0 \\ C_d\left(\frac{\rho_{f0}}{\rho_{s0}}, \phi_{s0}, \delta, t\right) & t_0 \le t \le t_0 + 2\tau_S \\ C_d(Re, M_0, Pr, \phi_{s0}) & t > t_0 + 2\tau_S \end{cases} \tag{6.25}$$

and

$$Nu(t) = \begin{cases} 0 & t < t_0 \\ Nu\left(\frac{\rho_{f0}}{\rho_{s0}}, \phi_{s0}, \delta, t\right) & t_0 \le t \le t_0 + 2\tau_S \\ Nu(Re, M_0, Pr, \phi_{s0}) & t > t_0 + 2\tau_S \end{cases} \tag{6.26}$$

In Equations (6.25) and (6.26), the C_d and Nu models use Equations (6.15) and (6.22) for $t_0 \le t \le t_0 + \tau_S$, respectively; for $t > t_0 + 2\tau_S$, correlations for C_d and Nu applicable for $\phi_{s0} > 0$ are used (e.g., the Smirnov correlation examined in Section 2.2). For $t \gg \tau_S$ the flow may become dilute if $\phi_{s0} \to 0$. In this regime, Equations (6.25) and (6.26) are replaced with traditional dilute correlations applicable to single spherical particles in steady flow.

Dilute correlations provide an informative comparison to the shock compression models used in Equations (6.15) and (6.22). Representative dilute correlations are chosen among many available in the literature. For drag, the correlation of Gilbert et al. [80] was used:

$$C_d(Re) = 0.48 + (Re)^{-0.85} \tag{6.27}$$

For heat transfer, the Nusselt number correlation of Knudsen and Katz [113] was used:

$$Nu(Re, Pr) = 2 + 0.6 Re^{1/2} Pr^{1/3} \tag{6.28}$$

In Equations (6.27) and (6.28), the Reynolds number and Mach number are defined using the relative velocity between the phases:

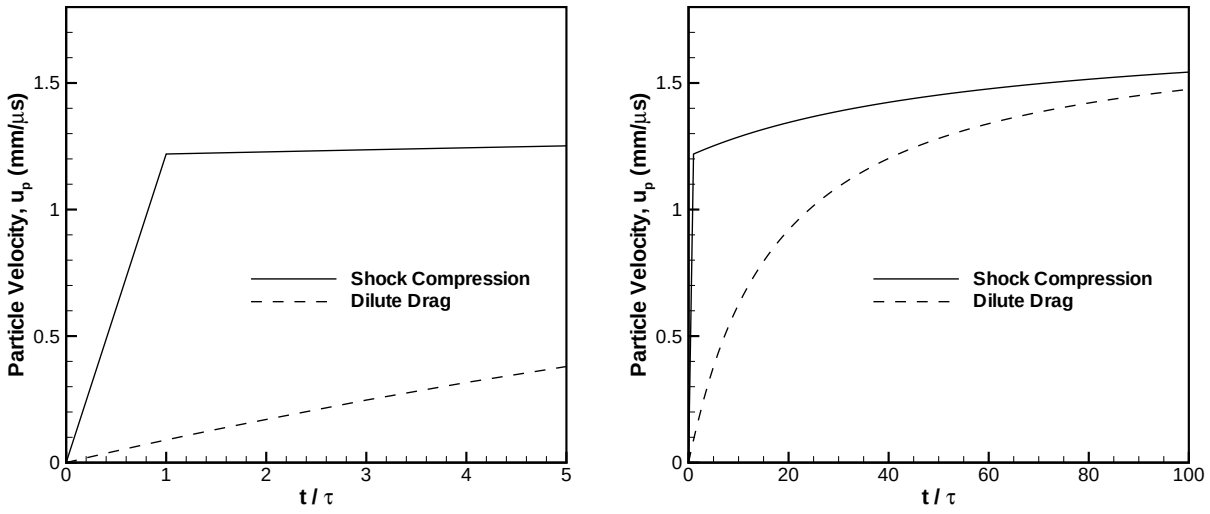

Figure 6.4: Response of the shock compression acceleration model ($\alpha = 0.7$, $\tau = \tau_S$) for particle velocity compared to dilute model: (left) zoom of shock interaction timescale; and, (right) late-time behaviour. Results for an aluminum particle ($\rho_{s0} = 2.700$ g/cc, $d_p = 10$ μm) in a CJ nitromethane shock ($D_0 = 6.612$ mm/μs, $u_{f1} = 1.742$ mm/μs, $\rho_{f1} = 1.538$ g/cc).

$$Re = \frac{\rho_f |u_f - u_p| d_p}{\mu_f}, \quad M = \frac{|u_f - u_p|}{a_f} \tag{6.29}$$

Figures 6.4 and 6.5 illustrate the resulting shock compression acceleration and heating for an aluminum particle in a constant CJ nitromethane detonation shocked flow. For this analysis, shock compression in a typical system with $\phi_{s0} = 0.25$ and $d_p/L_R = 0.1$, results in $\alpha = 0.7$ and $\beta = 0.2$ from the mesoscale results in Chapter 5. The shock compression models are compared to the standard dilute correlations (Equations 6.27 and 6.28). Using only the standard dilute drag, the particle velocity reaches the shock compression value after $40\tau_S$. Similarly for temperature, the shock compression particle temperature is reached after $20\tau_S$ using dilute heating. This example clearly demonstrates that the standard drag models fail to predict the acceleration and heating of particles in condensed matter subjected to a shock or detonation wave.

6.4 Application of shock compression models

This section provides a few examples of the application of the macroscopic shock compression models for effective drag coefficient and Nusselt number to practical problems

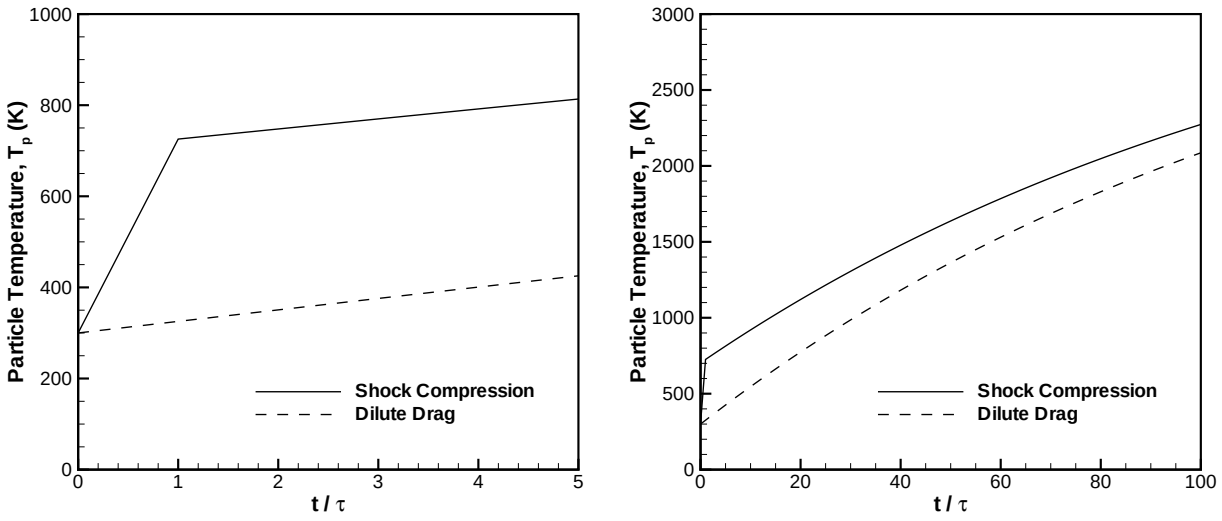

Figure 6.5: Response of the shock compression heating model ($\beta = 0.2$, $\tau = \tau_S$) for particle temperature compared to dilute model: (left) zoom of shock interaction timescale; and, (right) late-time behaviour. Results for an aluminum particle ($\rho_{s0} = 2.700$ g/cc, $d_p = 10$ μm, $c_s = 883$ J/kg-K) in a CJ nitromethane shock ($D_0 = 6.612$ mm/μs, $T_{f1} = 3628$ K, $\rho_{f1} = 1.538$ g/cc).

involving multiphase explosives. First, heterogeneous detonation of a cylindrical slurry explosive with metal particles is modeled for infinite diameter and finite diameter conditions. Second, dispersal of particles into air is demonstrated from detonation of a spherical charge of explosive and metal particles. In all the examples, the modeling results are compared with well-established experiments.

6.4.1 Heterogeneous detonation

Kato and Murata [105, 106] studied heterogeneous detonation of neat nitromethane saturating beds of metal particles in a sufficiently large cylindrical steel tube (with an inner diameter of 31 mm and a wall thickness of 3.5 mm). Detonation pressure was recorded using PVDF gauge measurements at a 1 ns time resolution. For aluminum, they showed increased detonation pressure for small particles, and decreased detonation pressure for large particles (see Figure 1.5). For all particle sizes tested, the reaction-zone length was longer than that of neat nitromethane, and the detonation propagated with a velocity deficit. For a range of intermediate particle sizes, there are secondary pressure waves behind the leading shock, indicating the reaction of aluminum particles.

Evaluation of the experimental data of Kato and Murata [105, 106] is given in Table

Table 6.1: Experimental configuration for detonation of nitromethane saturating beds of aluminum particles from Kato and Murata [105, 106], and corresponding velocity and temperature transmission factors selected from mesoscale calculations.

Experimental Configuration		Physical Interpretation			
d_p (μm)	ϕ_{s0}	δ	α	β	τ_S (ns)
3	0.35	0.01	0.77	0.44	0.5
5	0.38	0.02	0.76	0.45	0.8
8	0.46	0.03	0.74	0.46	1.3
14	0.53	0.05	0.70	0.48	2.2
35	0.44	0.12	0.65	0.32	5.5
108	0.51	0.36	0.45	0.27	17
350	0.44	1.17	0.40	0.21	55

6.1 where the particle diameter and volume fraction are from their experiments. Applying $L_R = 300$ μm for neat nitromethane from the high-resolution experiments of Sheffield et al. [185], $\delta = d_p/L_R$ can be calculated using the particle diameter. The curves in Figures 5.30 and 5.33 were used to select α and β, as summarized in Table 6.1. The microscopic interaction ranges from the small particle limit ($\delta \ll 1$), which involves essentially frozen von Neumann (VN) shock interaction with the particles, to the intermediate regime ($\delta \sim 1$) where L_R is comparable to d_p providing two characteristic length scales. The interaction time, τ_S, is estimated using the neat detonation velocity, $D_0 = 6.4$ mm/μs, from the experiments.

The shock compression models (Equations 6.15 and 6.22) are applied in the source terms of the macroscopic two-phase continuum model in Equations (6.1) and (6.2), to simulate heterogeneous detonation. A single-step Arrhenius rate law is used for the NM detonation, since the present focus is on the momentum and heat transfer models. The particles are modeled as an inert solid flow continuum in the Eulerian frame, where the particle number density is solved such that the size of particles relative to the mesh size only influences the source term rates. Since the individual particle response has been homogenized at the macroscopic level, the fluctuating pressure and localized hot spots due to shock interaction in interstitial pores are exhibited as increased bulk temperature and enhanced pressure, in agreement with observations using the current transducer resolutions of Kato and Murata [105, 106].

For these experiments with sufficiently large tubes providing heavy confinement, an infinite charge diameter is assumed in the modeling, and then the detonation can be

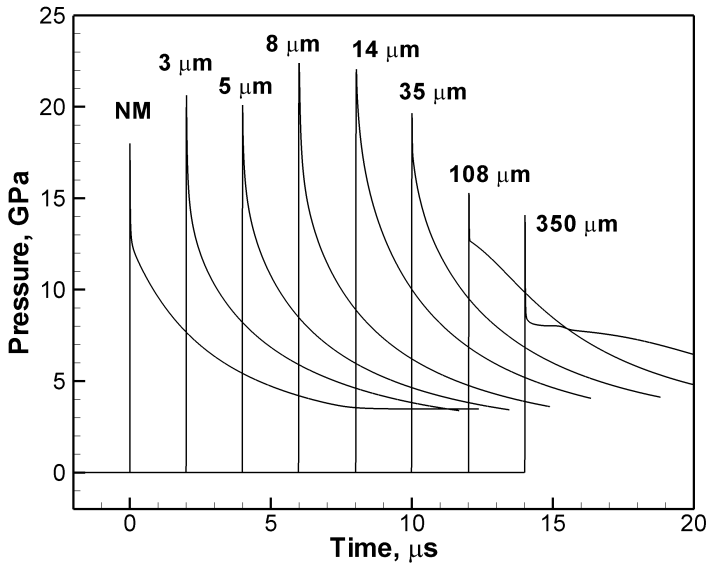

Figure 6.6: Infinite-diameter detonation pressure profiles for various particle sizes using a one-dimensional model. Detonation shocks located at arbitrary times for clarity.

considered using 1D calculations. Figure 6.6 shows the pressure histories for several particle sizes along with a baseline NM detonation, which are consistent with the results of Kato and Murata [105, 106] (reproduced in Figure 1.5). For 3 to 35 μm particles, both the peak shock and detonation flow pressure increase relative to the neat NM detonation. Also evident in Figure 6.6 is the increased steady zone behind the shock, which is consistent with Kato's observations of increased reaction-zone length in heterogeneous explosives. The rear unsteady flow differs from the experiment mainly due to lateral expansion effects and the inert particle assumption limiting reaction.

Table 6.2 summarizes the infinite-diameter numerical results using the macroscale model. The local shock propagation velocity in the particle bed appears as a reduced bulk detonation velocity when averaged at the macroscale. The detonation velocity deficit with respect to the neat NM detonation results from momentum and heat losses to the particles in the reaction zone. Variations are expected due to the solid volume fraction range of 0.35 – 0.53 used in the experiments (see Table 6.1).

The detonation velocity is less than the results of Kato and Murata [105, 106] despite showing good agreement in pressure. The experiment includes particles with a size distribution where the smallest particles may react in the detonation zone thereby supporting the shock velocity. As previously stated, the reaction of particles was not considered in the modeling. Furthermore, it is not known whether the detonation velocity

Table 6.2: Summary of numerical results for infinite-diameter heterogeneous detonation.

d_p (μm)	D_0 (mm/μs)	p_{CJ} (GPa)	p_{VN} (GPa)	u_{p1} (mm/μs)	T_{p1} (K)
NM	6.430	13.3	17.7	-	-
3	4.800	14.6	20.7	1.299	597
5	4.690	15.5	20.1	1.181	522
8	4.480	18.6	22.6	1.041	475
14	4.240	19.3	22.4	0.928	428
35	4.450	17.6	19.7	0.942	443
108	4.510	12.8	15.3	0.719	473

measured in the experiment reached a steady propagation velocity. The cylindrical explosive was only 150 mm long, and was initiated by solid explosive which typically overdrives the detonation.

Although equilibrium is not applicable to the two-phase flow, Cheetah calculations for nitromethane with inert aluminum show $D_{CJ} = 5.284$ mm/μs, $p_{CJ} = 7.12$ GPa, $u_{CJ} = 0.727$ mm/μs and $T_{CJ} = 1883$ K, which demonstrates the limiting case for small particles.

6.4.2 Detonation failure diameter

Detonation failure for NM/Al in light cylindrical casing has been studied experimentally. Frost et al. [74] used Al particles saturated with sensitized NM contained in thin glass tubes; Kato and Murata [105, 106] studied Al particles saturated with neat NM contained in thin PVC tubes. Figure 6.7 shows the experimental relationship between charge diameter and particle diameter for detonation failure in lightly-cased cylindrical explosives. For both glass and PVC casing, the detonation failure curve for aluminum is U-shaped, where the critical diameter increases in both the small particle limit and large particle limit. The small difference between the two curves indicates that the reactivity of the liquid explosive (sensitized or neat NM) may play a less important role than the particle interactions on detonation failure. Particles result in hot spots that promote detonation ignition, as well as momentum and heat losses that desensitizes detonation.

Detonation failure was investigated for lightly-cased cylinders using a 2D axisymmetric model. The casing was modeled using a hydrodynamic model; the casing material was PVC ($\rho = 1.2$ g/cc) and was 3.5 mm thick. A numerical mesh resolution of 10 μm was used with the Arrhenius rate law, as in the infinite diameter calculations. Figure 6.8 illustrates the cylindrical charge detonation results for a 20 mm ID tube, with 1000 mesh

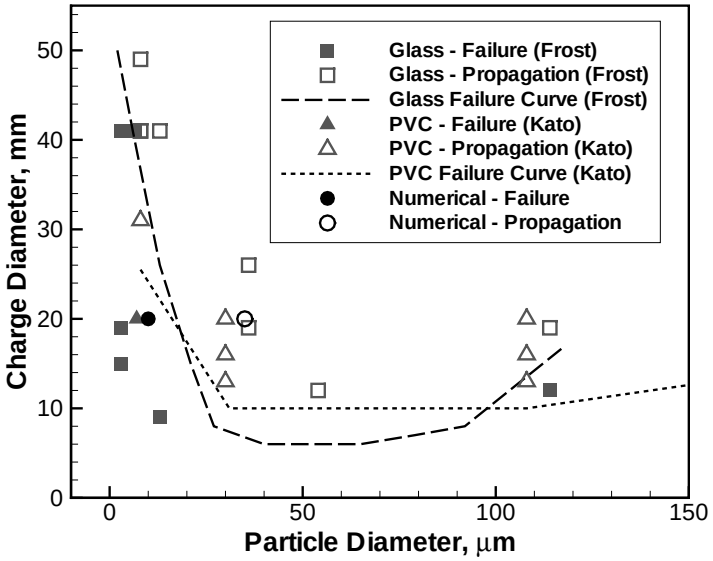

Figure 6.7: U-shaped detonation failure diameter curves: numerical results using shock compression models compared to experimental data in Frost et al. [74] and Kato and Murata [105, 106].

points in the charge radius and another 350 through the casing thickness. The detonation front curvature and detonation reaction zone are resolved. For 35 μm particles, steady detonation propagation is achieved, whereas for 8 μm particles the shock compression losses in the lengthening reaction zone lead to detonation failure beginning at the inner casing wall.

The present numerical results for 20 mm diameter charges are included in Figure 6.7 showing that the critical diameter for detonation failure in the small particle regime is consistent with experimental data. It should be noted that the overall computational mesh contained over 30 million computational points and required several days of parallel computing effort; therefore, only limited configurations were tested. Additional calculations should be conducted to complete the failure diameter curve. The reaction model should also be tested for its ability to predict the failure diameter of the pure explosive. A more sophisticated reaction model may be required, such as two- or three-step ignition and growth type models (see discussion in §4.3.4).

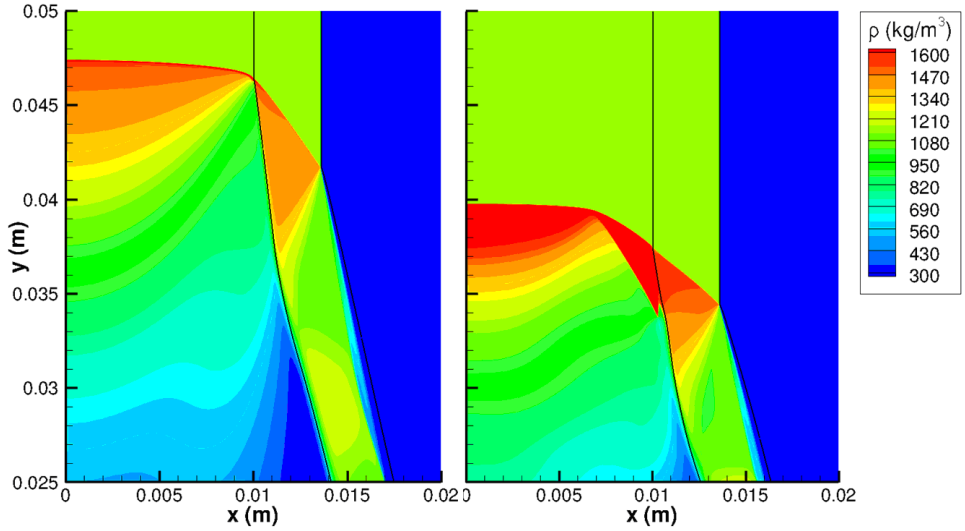

Figure 6.8: Heterogeneous detonation of 20 mm diameter cylindrical NM/Al charges in 3.5 mm thick PVC casing: 35 μm particles with detonation propagation (left) and 8 μm particles with detonation failure (right). Detonation shock propagation is from bottom to top.

6.4.3 Explosive dispersal of particles

The experimental configuration for explosive dispersal of particles is described in detail by Zhang et al. [226] and Frost et al. [75]. The relevant configuration details are summarized here. The spherical charge, contained in a thin glass casing, consists of a packed bed of inert particles saturated with liquid nitromethane sensitized by 10% triethylamine (TEA). Spherical steel beads from Draiswerke Inc. [49] were sieved to a size distribution of 463±38 μm ($\rho_{s0} = 7.850$ g/cc and $c_s = 460$ J/kg-K). The charge size was 11.8 cm in diameter and was centrally initiated by 7 g of solid explosive. The heterogeneous mixture consisted of 434 g NM with 10% TEA plus 4400 g of steel beads [226, 75]. The initial steel mass fraction of 0.92 corresponds to a solid volume fraction of 0.62. In the macroscale simulation, the particles were modeled as monodisperse ($d_p = 463$ μm), the thin glass casing was not included, and the booster explosive was replaced by nitromethane.

Before considering multiphase dispersal, the numerical method was first validated for the pure explosive. As in the experiments of Zhang et al. [226], an 11.8 cm diameter homogeneous charge of nitromethane was simulated as a baseline. The explosive contained 1080 g of NM with 10% TEA by mass. The results are shown in Figure 6.9 with excellent agreement to both experiments and calculation results of Zhang et al. [226].

Figure 6.10 gives some exploratory results for the heterogeneous charge of nitromethane

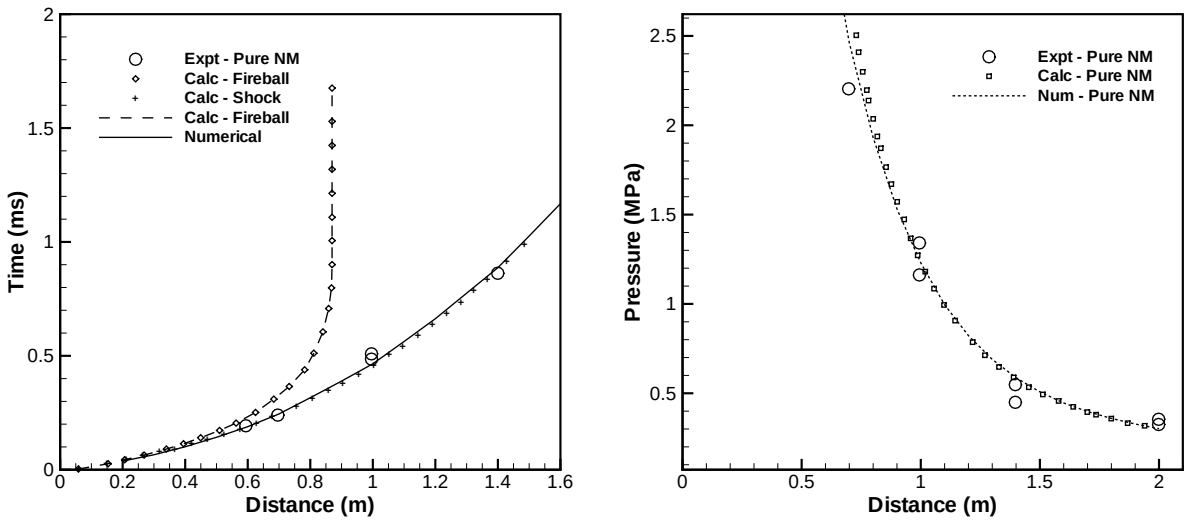

Figure 6.9: Validation of the homogeneous explosion model without particle additives for shock velocity and blast pressure resulting from an 11.8 cm spherical explosive containing NM/TEA (present numerical results compared to the experiment and calculation results from Zhang et al. [226]).

with steel beads. First, the inert particle dispersal was simulated using the standard dilute drag (Equation 6.25), which shows an overprediction of the shock speed with a severely delayed particle front velocity. This can be compensated for by using an *ad hoc* momentum enhancement factor. The numerical results of Zhang et al. [226] employed a momentum enhancement factor of 6 for the first 0.4 ms. In a similar attempt, the second simulation shows the particle dispersal for a momentum enhancement factor of 10 applied over the first 0.2 ms, with good agreement to the experiment.

In order to replace these *ad hoc* corrections with physics-based models, the above simulation is reconsidered using the macroscopic shock compression acceleration and heating models (Equations 6.15 and 6.22 described in Section 6.2). The present configuration of large steel particles in sensitized nitromethane falls in the large particle regime ($d_p/L_R \gg 1$). Therefore, the transmission factors required for Equations (6.15) and (6.22) must be generated for steel particles. The single steel particle results from Figure 5.14 in Section 5.2.1, gives $u_{p1} = 0.488$ mm/μs and $\alpha = 0.28$ for an initial density ratio of explosive to solid particles of $\rho_{f0}/\rho_{s0} = 0.144$. However, this result is for the small particle limit which demonstrated the highest transmission factors. Additional mesoscale calculations were necessary for the large particle limit. To obtain simple yet representative results, 2D mesoscale calculations were conducted for steel beads in nitromethane. Further,

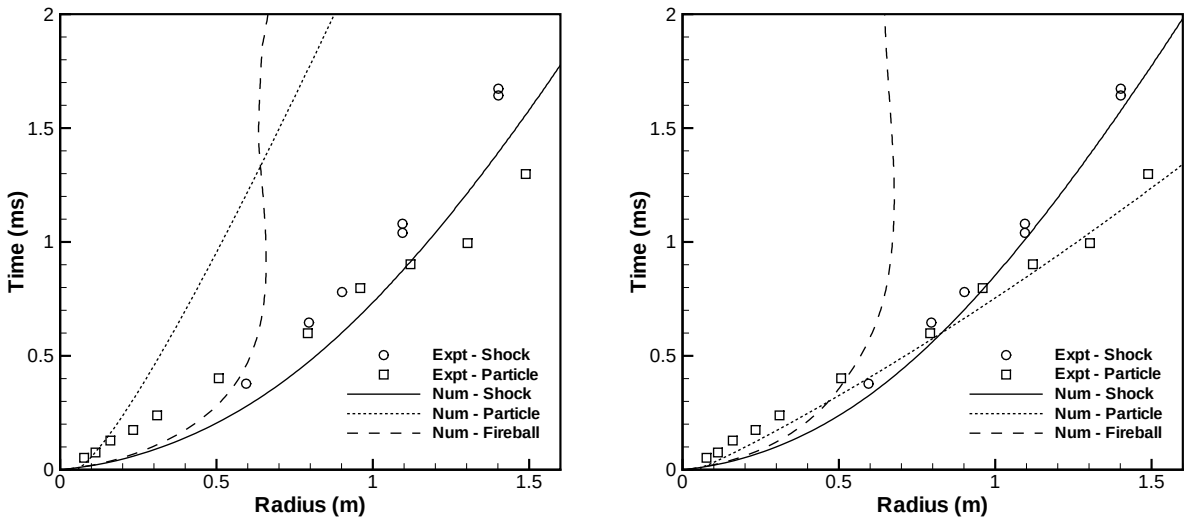

Figure 6.10: Effect of drag model on inert particle dispersal trajectory and shock velocity from an 11.8 cm diameter spherical explosive containing steel beads saturated with nitromethane. Comparison of standard dilute drag (left) to *ad hoc* enhanced drag with a factor of 10 applied for 0.2 ms (right) from Ripley et al. [165].

the free-edge of the charge was also included to investigate the particle acceleration during the edge expansion. The 2D configuration employing cylindrical 'particles' was discussed in Section 5.5, where the setup was shown in Figure 5.36. Here, a resolution of 100 cells/diameter was used. Figure 6.11 illustrates the results for steel particles undergoing shock compression followed by edge expansion.

Due to the low density ratio of the liquid explosive to steel particles, minimal acceleration and heating occur as the detonation shock passes. Figure 6.11 shows that an initial velocity of approximately 0.150 mm/μs is transmitted into the particle by the detonation shock, corresponding to a trivial shock compression factor of $\alpha = 0.08$. In contrast, during the edge expansion, a significant acceleration of the particles is achieved. In the outer layers of particles, the particle velocity exceeds 1.0 mm/μs after a few shock interaction timescales. Therefore, at the outer edge of the charge (i.e., between $0.95R_0 \leq R \leq R_0$), a velocity transmission factor of $\alpha = 0.60$ was applied for $5\tau_S$, which corresponds to the values in the mesoscale observations.

From the 2D mesoscale calculations of shock interaction with packed steel particles saturated with sensitized NM, the shocked particle temperature was $T_{p1} = 388$ K for a CJ shock representative of the large particle limit; this gives $\beta = 0.107$. The subsequent rarefaction in the particle reduces the transmitted temperature, followed by edge expansion

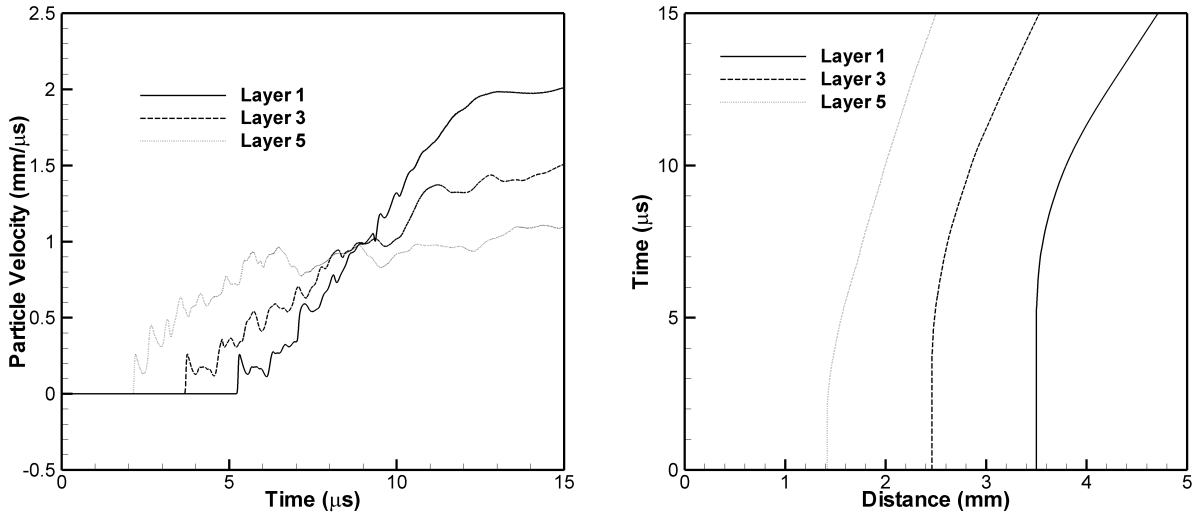

Figure 6.11: Mesoscale particle velocity and trajectory for 'cylindrical' steel beads at the charge edge (arbitrary zero time and distance).

further reducing the particle temperature at the edge of the explosive. Overall, the shock compression heating effect is insignificant for the system of steel particles in nitromethane.

Figure 6.12 provides the macroscale results for detonation and dense dispersal using the macroscopic shock compression model (Equation 6.15). During the detonation stage, only very little particle velocity ($u_{p1} \sim 0.100$ mm/μs) is achieved due to the high solid particle density as explained above. Due to the rapid and significant momentum transfer required for the heavy particle acceleration, the detonation products gas velocity is substantially retarded behind the reaction zone. As the detonation shock transmits into the air at the charge edge, the enhanced drag (Equation 2.17) during the edge expansion rapidly accelerates the particles. For a particle front solid concentration of 1 mg/m^3, the particle velocity achieved is 1.540 mm/μs at a radius of 7.5 cm. This is consistent with the mesoscale particle velocity measured in the outer layers at the edge of the charge (see Figure 6.11). The particle velocity profile contains a kink at 0.525 mm/μs, which corresponds to a solid concentration of 1 kg/m^3 and defines the boundary between the spall layer and dense particle flow lagging behind.

The solution in Figure 6.12 is used to initialize a larger domain to study the later-time particle dispersal. The Smirnov drag correlation (Equation 2.17) was used, although the flow quickly becomes dilute. Figure 6.13 shows the subsequent dispersal process using spatial velocity distributions. The particle velocity is compared to the gas velocity for several instances in time. Although initially the gas velocity is very high, it quickly decays

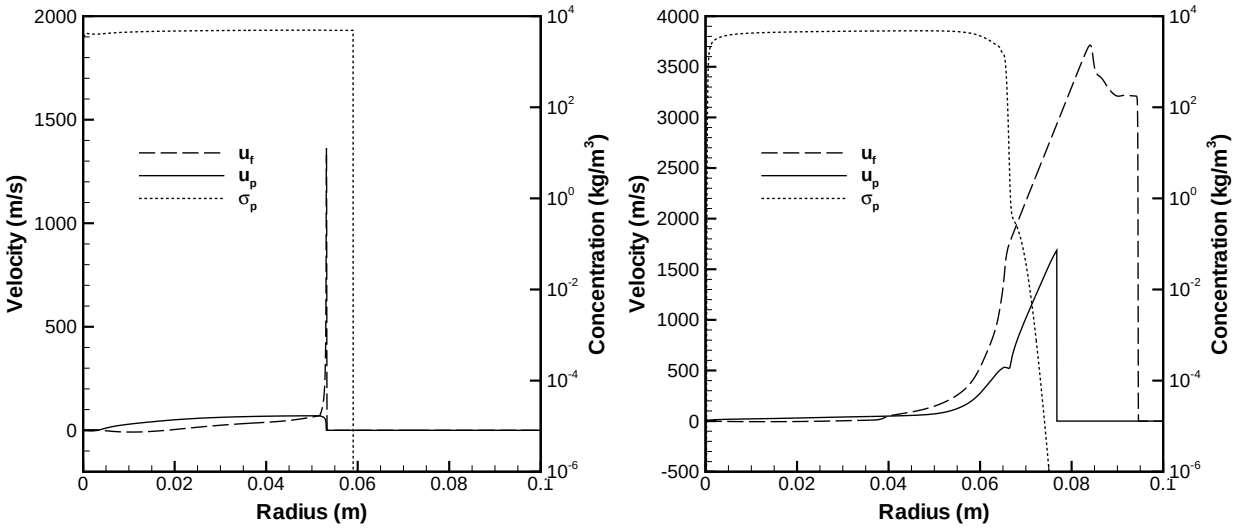

Figure 6.12: Macroscale particle and gas velocity during detonation at $t = 10$ μs (left) and early dense dispersal at $t = 19$ μs (right) of an 11.8 cm spherical explosive containing steel beads saturated with nitromethane. Results using a mesh resolution of 0.03 mm.

in the spherical expansion. The large dense particles are inertially dominated at later times and overtake the gas shock.

Figure 6.14 gives a comparison of the present numerical results for the shock, fireball, and particle dispersal trajectories against published experimental and calculation data [226]. The benchmark data points forming the particle trajectory are a composite of several experimental trials. In the early time, the particle trajectory was measured using radiographs of three separate trials [69]. In the later dispersal, the particle position was measured from high-speed cinematography. Air-blast overpressure was measured outside the fireball which provided the time of arrival of the primary shock front. The fireball trajectory was calculated using modeling approaches reported in Zhang et al. [226]. Overall, the results displayed in Figure 6.14 demonstrate excellent agreement between the present model and the experimental data.

6.5 Validation of particle heating

Diagnostic techniques for determining particle temperature in condensed matter detonation remain a challenge for experimentalists. Direct measurements are impractical; therefore, non-evasive methods have typically been used. In situ measurements of particle tem-

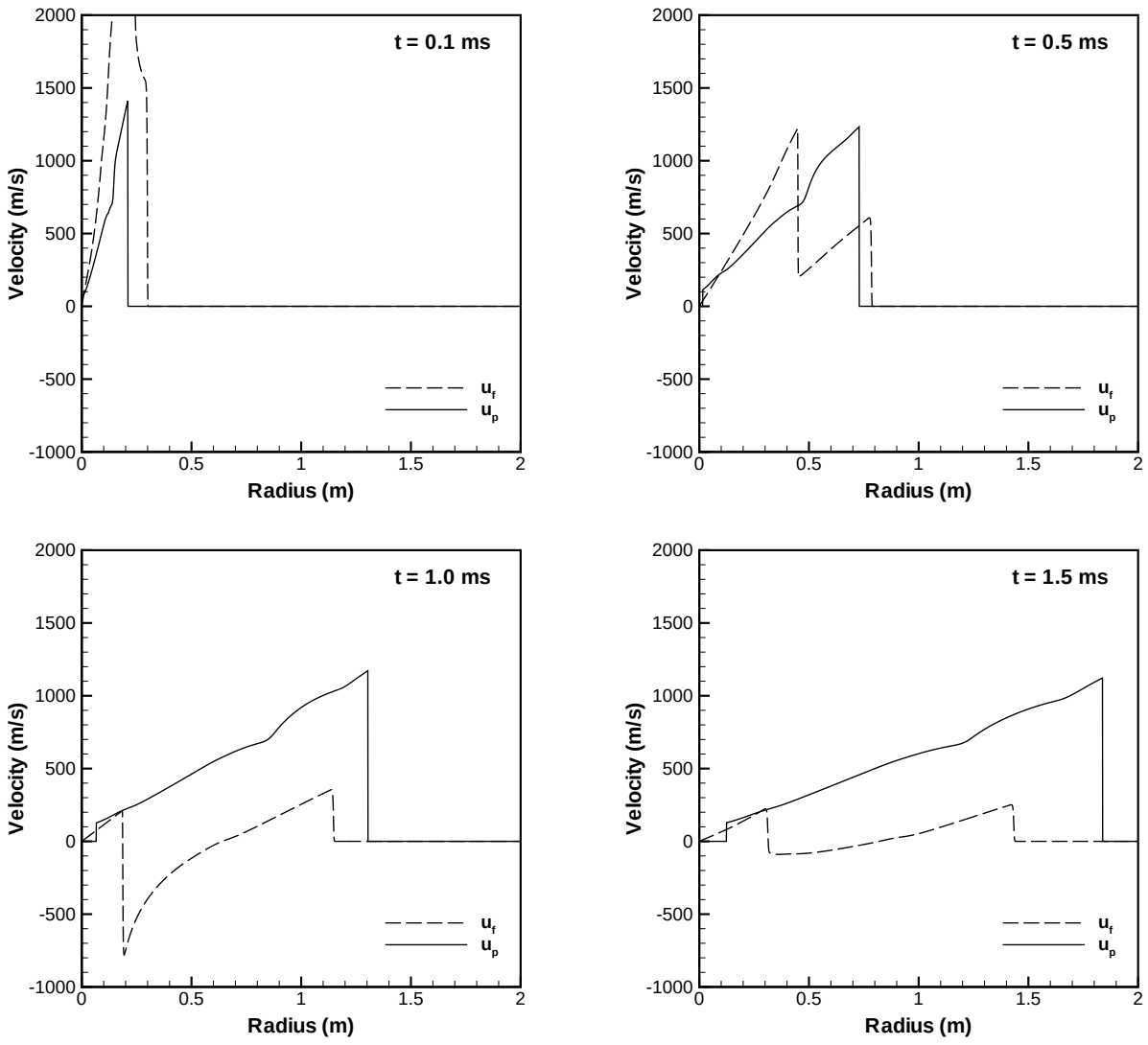

Figure 6.13: Distribution of particle and gas velocity for macroscale inert particle dispersal from an 11.8 cm spherical explosive containing steel beads saturated with nitromethane. Results shown at four different times (mesh resolution of 1 mm).

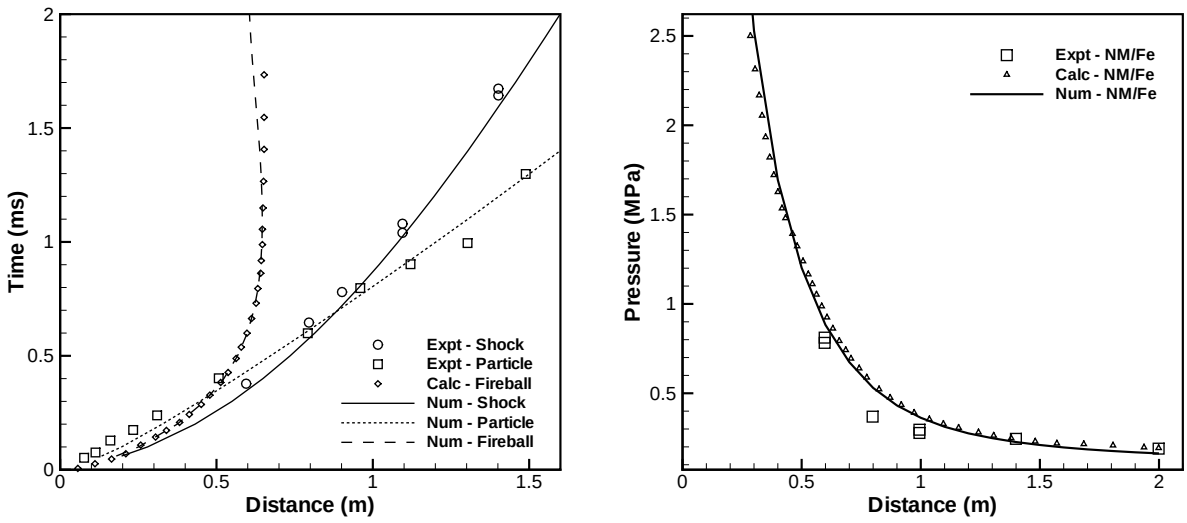

Figure 6.14: Explosive dispersal of inert particles from an 11.8 cm spherical explosive containing steel beads saturated with nitromethane: shock velocity (left) and blast pressure (right). Comparison of present numerical results to published data. Symbols (experimental and calculation results) are from Zhang et al. [226].

perature during detonation are not currently possible. For post-detonation observations, approaches include thermocouple, optical pyrometry, and high-speed spectroscopy.

Goroshin et al. [88, 89] and Frost et al. [73] fielded optical pyrometry to measure the temperature of a multiphase fireball. Particle temperature during inert dispersal is preferable for validation of the shock compression heating. However, for the dispersal to effectively be inert, large particles are required. Trials involving dispersal of 114 μm aluminum particles [74] featured delayed reaction with the potential to provide suitable information for the dispersed particle temperature. Unfortunately, Frost [69] indicated that temperature data for these trials was not viable because the inert particle emission was below the lower threshold, since the signal levels were set for reacting particles ($T \sim 3400$ K, the adiabatic flame temperature of Al in air). Similarly, Carney et al. [36] and Grégoire et al. [91] investigated spectroscopy with the goal of measuring reacting particle signatures. Since detecting particle combustion is usually the focus of spectroscopy, emission of the AlO and Al_2O_3 bands was measured, rather than atomic Al emission which is indicative of particle temperature. Again, particle temperature prior to ignition and reaction is not available due to weak signals [35].

Since experimental data on particle temperature due to shock compression and dense dispersal are not directly available, anecdotal evidence may be inferred from particle

burning. Thermocouple measurements [73] of the air temperature in the multiphase flow field may provide some information. Limitations include a stationary gauge, measurement of the shock-heated air and combustion gases, and lagged thermal response. Unfortunately, the thermal lag of even the smallest thermocouples limits the particle temperature data, and this method may only be applicable to reactive particles.

Reactive particle dispersal test cases feature a critical charge diameter for particle ignition [77, 74], where there is competition between particle heating in the hot detonation products and gas expansion cooling. For charge diameters above the critical diameter, particle reaction indicates that particle heating from shock compression and dense dispersal was sufficient to reach the ignition. Therefore, an ignition delay time could be used to infer particle heating rates. Unfortunately, there is considerable uncertainty in the chemical kinetics of particle ignition and reaction (see Zhang et al. [227]). Even for aluminum, which is perhaps the most commonly studied reactive metal, the particle temperature for ignition is the subject of wide debate [109], and ranges from the melting temperature of pure aluminum (933 K) up to the melting temperature of the aluminum oxide (Al_2O_3) coating (2150 K) [204].

Modeling of spherical reactive particle dispersal [122] and cylindrical reactive particle dispersal [164] demonstrated that the particle size distribution, particle reaction mechanism, and casing influence are among the uncertainties that prevent these test cases from being used to verify the shock compression heating models in a rigorous manner. Future work may provide a consistent and independent method of validation for the particle temperature in condensed matter subjected to shock and detonation waves.

6.6 Discussion of macroscale application

Macroscopic models for shock compression drag and heating were developed and implemented into a macroscopic framework via two-phase source terms. They were developed as effective drag coefficients and Nusselt numbers applied during the shock interaction timescale. The macroscopic models employed the velocity and temperature transmission factors that were determined from the mesoscale simulations in Chapter 5. The resulting new models for shock compression were applied to macroscale test cases involving heterogeneous detonation and explosive dispersal of particles. Comparison to available experimental data showed comparable results for detonation velocity deficit, enhanced detonation flow pressure, extended steady zone, and detonation failure diameter.

Momentum and heat loss in the detonation reaction zone were determined to the detonation and edge expansion regimes showed excellent agreement for particle front trajectory and blast pressure, as compared to experimental data. Validation of the particle temperature remains a challenge due to the lack of experimental data.

Chapter 7

Conclusions

Condensed explosives containing metal particles provide a fundamental system for investigating detonation and explosion physics. In particular, shock and detonation interaction with metal particles are responsible for several multi-scale phenomena that are related to momentum loss and heat transfer. The objective of this thesis was to develop novel physical models for acceleration and heating of metal particles in condensed explosive detonation. A quantitative description of the resultant momentum and heat transfer was determined, and the principal shock interaction mechanisms were interpreted. These physics-based models were employed to explore and understand the mechanisms responsible for the slurry detonation and explosive particle dispersal phenomena observed in experiments.

Dimensional analysis showed that the particle acceleration and heat transfer during detonation shock compression in a dense solid particles-condensed explosive system are a function of the material density ratio of explosive to particle, ρ_{f0}/ρ_{s0}, the volume fraction, ϕ_{s0}, and the ratio of particle diameter to detonation zone length, $\delta = d_p/L_R$, which are distinct from Reynolds number, Re, Prandtl number, Pr, and Mach number, M_0. While viscosity and heat conduction are important later in the detonation and explosion process, they can be neglected when compared with the other parameters during the shock compression time scale. Thus, the acceleration force and heat transfer can be described by an effective drag coefficient, $C_d = f(\rho_{f0}/\rho_{s0}, \phi_{s0}, d_p/L_R, M_0)$, and the heat transfer is represented by an effective Nusselt number, $Nu = f(\rho_{f0}/\rho_{s0}, \phi_{s0}, d_p/L_R, M_0)$. Mesoscale simulations of spherical aluminum particles saturated with liquid nitromethane were conducted by varying ϕ_{s0} and $\delta = d_p/L_R$ at a given M_0 and ρ_{f0}/ρ_{s0}, which were known important parameters. The full range of ϕ_{s0} and δ were studied, where δ ranged between

the small particle limit, with essentially inert shock interaction, to the large particle limit, with infinitely thin detonation front diffraction followed by detonation products expansion flow.

Features of heterogeneous detonation were explored including: detonation instability and velocity deficit; pressure front fluctuations with peaks up to four times the CJ detonation pressure and periods proportional to the particle size; and, transverse waves and hot spots characteristic of locally enhanced pressure and temperature fronts. These physics are consistent with macroscopic phenomena observed in published experiments. Detonation failure was not considered in the mesoscale study since these calculations assumed infinite diameter conditions (no charge edge effects). From the mesoscale simulations, a shock compression velocity transmission factor, $\alpha = f(\rho_{f0}/\rho_{s0}, \phi_{s0}, d_p/L_R, M_0)$, and temperature transmission factor, $\beta = f(\rho_{f0}/\rho_{s0}, \phi_{s0}, d_p/L_R, M_0)$, were obtained to summarize the acceleration and heating behaviour within a detonation shock interaction time. The maximum particle acceleration occurred at $\phi_{s0} = 0.25$; whereas the maximum shock compression heating occurred over a wider range of solid volume fraction, within $\phi_{s0} = 0.4 - 0.74$. The acceleration and heating rates of 1 – 10 μm particles were measured to be $\mathcal{O}(10^{12} - 10^{13})$ m/s^2 and $\mathcal{O}(10^{12} - 10^{13})$ K/s, respectively, and occurred within the shock interaction timescale $\mathcal{O}(10^{-10} - 10^{-9})$ s.

Scaling of the velocity and temperature transmission factors using the post-shock (von Neumann) state appears to be the most convenient since it is easily obtained from analytical shock relationships; however, this scaling showed a strong dependence on the ratio of particle diameter to reaction-zone length. Shock compression transmission factors, scaled with the ideal ZND detonation wave fluid velocity integrated over the particle diameter, indicated a weak dependence on the ratio of particle diameter to detonation reaction-zone length for momentum, and an exponentially decreasing dependence for temperature. For a matrix of aluminum particles saturated with nitromethane, 36 – 78% of the shocked fluid velocity and 18 – 50 % of the shocked fluid temperature were achieved by the particles, depending on the ratio of particle diameter to detonation reaction-zone length.

Overall, velocity and temperature transmission factors can be simplified using an appropriate choice of scaling value; reduction of α and β in this fashion allows a practical model to be implemented without *a priori* knowledge of the reaction-zone length or the *in situ* detonation wave profile. As an example, the results were applied to formulate functions for macroscopic momentum and energy transfer between the two phases during detonation shock compression. These functions can then be used as the inter-phase exchange source terms applied to macroscopic continuum modeling of practical problems such as detonation

of a multiphase explosive or shock propagation in a dense particle-fluid system.

7.1 Practical considerations

Without losing generality for the outcome in condensed matter, a prototype system of liquid nitromethane explosive saturating solid aluminum particles was studied. A monodisperse distribution and ordered packing of spherical particles was considered as a simplification of the problem. Real slurry explosives contain a particle size distribution spanning two orders of magnitude in size, a random packing structure, non-spherical particle shapes, and some particles have an oxide coating. Three-dimensional mesoscale approaches, such as those employed in the present work, are capable of describing this type of system; however, increased resolution would be required to capture smaller particle diameters in the distribution and the thin oxide coatings. A larger representative volume element (mesoscale domain size) would also be needed to describe a random packing in a statistically representative manner. Both requirements significantly increase the computational effort. In the present calculations, the high resolutions and long runtimes reached the limit of available computational resources. During the course of this project, a ten-fold increase in computer resources was developed (presently 160 CPU), indicating that more detailed calculations may be realizable in the near future. The largest mesoscale calculations by Baer have currently reached 20,000 CPU [8].

The present study, considering monodisperse particles, demonstrated the effect of particle size on acceleration and heating throughout the range of $\delta = d_p/L_R$ considered. When a polydisperse particle size distribution is included, the relative acceleration of the particles will ultimately lead to particle/particle collisions in the detonation flow, resulting in additional forces acting between particles. This external surface force would necessitate the use of collision/contact algorithms (e.g., [29]). The multiple particle size distribution and random packing configuration would decrease the ordered structure to the matrices and effectively dampen the resonant fluctuations of pressure in the system. Non-spherical particles add the complexity of additional contact points, increased shear, and rigid-body rotation. Baer [6] simulated randomly oriented cubical crystals, and showed reduced pressure fluctuations and increased material deformation.

Establishing the initial packing configuration for such slurry explosive systems with polydisperse size distributions and non-spherical particle shapes is also a challenge. Arbitrary distributions may be achieved using filling methods that use gravitational

settling with rigid-body collision and frictional contact to establish the initial packing. Baer employed a statistical-mechanical method based on Monte Carlo and molecular dynamics with a densification algorithm to generate an ensemble of packed particles [6]. Computerized topography [215, 179] has been used to digitally initialize the 3D domains. Similarly, it is possible to use the micrographs of metal particles to describe the initial size, shape, orientation, and packing of the metal particles in a real slurry explosive system.

In the present mesoscale simulations, the single-step reaction model did not resolve the induction-zone length in the detonation wave. The effect of including the induction zone would increase the length of the von Neumann pressure plateau following the leading detonation shock. This would tend to shift the velocity and transmission factors toward the small particle limit since the particles would interact with an extended shock region before entering the expanding flow in the reaction zone. Sheffield et al. [185] measured the nitromethane induction zone as 1 – 3 ns in duration, in agreement with calculations of Tarver [196]. This represents an induction-zone length of about 6.3 – 19 μm, compared to the measured overall reaction-zone length of 300 μm. For nitromethane with a short induction zone, the resulting shift in $\delta = d_p/L_R$ would be small. The increased effort of high resolutions and additional reaction mechanisms do not warrant such an investigation for the liquid nitromethane explosive used in the present study. Other explosives, with elongated induction zones, may necessitate this type of analysis.

7.2 Future work

Extension of the present calculations to include the later-time viscous flow following shock compression calls for interface improvements and the addition of particle strength models. Interface resolution may be improved using adaptive mesh refinement (AMR) techniques; however, the complex shock reflections and fluctuating pressure fields would result in excessive refinements effectively giving a uniform mesh of a higher resolution. Lagrangian interface trackers used in ALE codes offer an alternative – these methods were not adopted for this study, since shock compression temperature and detailed detonation reaction models were not available. Material interface trackers are recommended and consist of two aspects: front tracking and interface reconstruction. Front tracking is achieved using the level set method (see Sethian [183], Osher and Sethian [155], and Glimm [83]). Three-dimensional interface reconstruction methods include first-order schemes, such as SLIC (Simple Line Interface Calculation) [150], and second-order methods like SMYRA (Sandia Modified Young's Reconstruction Method) [23]. For the flow regime following

shock compression, immersed boundary methods (IBM) are already in use for mesoscale studies of the viscous flow and wake interactions of dense particles (see Xu et al. [221, 220]).

Non-spherical particles and a particle size distribution with increased shear, rotation, and collision will require strength models for the solid. Application to thin particle flakes, such as in the experiments of Yoshinaka et al. [222] and mesoscale simulations of Cooper et al. [40], further warrants failure models for particle damage, break-up, and fragmentation. The Johnson-Cook [101] strength model has been widely adopted in the literature.

7.3 Closing remarks

Acceleration and heating of metal particles in condensed matter detonation were studied using a theoretical and numerical investigation. The range of parameters examined was influenced by experimental observations from the literature. The present study demonstrated the importance of the relative size of particles to the detonation reaction-zone length, particle packing configuration, and volume fraction of particles. This was achieved using mesoscale modeling of a prototype system of spherical aluminum particles saturated with liquid nitromethane, the results of which may be extended to other slurry explosives. The mesoscale results generated a tremendous volume of data and are rich in physics. Highly fluctuating pressure fields, transverse waves, extended steady zone, hot spots, detonation instability, and detonation velocity deficit are among the key detonation physics observed in the mesoscale results. It is hoped that future mesoscale studies may include shock initiation, detonation failure, reactive particles, and solid heterogeneous explosives.

Results for particle acceleration and heating were correlated into fitting functions of the relevant parameters to facilitate their use. Implementation into a macroscopic model framework required developing shock compression source term models for drag force and heat transfer rate during the shock interaction time. Application of the macroscopic models to slurry detonation and explosive particle dispersal demonstrated not only the utility of approach, but correctly represented the physical interactions from the underlying mesoscale. Detonation velocity deficit, enhanced detonation flow pressure, extended steady zone, and detonation failure diameter were achieved using macroscopic modeling with the newly-developed shock compression models. Momentum and heat loss in the detonation reaction zone are the mechanisms responsible for the observed detonation phenomena. Furthermore, shock compression acceleration applied to explosive dispersal of solid particles

displayed physically-accurate particle front trajectory and blast pressure, as compared to experimental data. Further work is recommended to employ the shock compression models in cylindrical explosive dispersal, and investigation of critical diameter for particle ignition.

Permissions

Figure 1.2 was reprinted from Thermochimica Acta, Volume 384, M. R. Baer, "Modeling heterogeneous energetic materials at the mesoscale", Page 355, Copyright (2002), with permission from Elsevier.

Figure 1.4(left) was reprinted with permission from AIP Conference Proceedings, Shock Compression of Condensed Matter, "The effect of additives on the detonation characteristics of a liquid explosive" by Haskins, Cook, and Briggs, Copyright 2002, American Institute of Physics.

Figure 2.4 was reproduced with kind permission from Springer Science+Business Media: Shock Waves an International Journal, "Experimental and numerical investigation of the shock-induced fluidization of a particles bed", Volume 8, 1998, Page 35, Figure 9, by Rogue, Rodriguez, Haas, and Saurel.

Figures 1.6, 1.7, 1.8 and 2.13 are property of the Government of Canada, and were used with permission from Defence R&D Canada – Suffield.

References

[1] Anderson, J. D. *Modern Compressible Flow: With Historical Perspective*, third ed. McGraw-Hill, New York, NY, 2003.

[2] Argonide Corp. Electro-exploded nanopowders [online]. http://www.argonide.com/nanopowders.html, Accessed October 2008.

[3] Arrhenius, S. über die reaktionsgeschwindigkeit bei der. inversion von rohrzucker durch säuren (On the reaction rate of the inversion of non-refined sugar upon souring). *Z. Phys. Chem. 4* (1889), 226–248.

[4] Askeland, D. R. *The Science and Engineering of Materials*, third ed. Chapman and Hall, 1996.

[5] Baer, M. *Shock Wave Science and Technology Reference Library*, 2 ed. Springer, 2007, ch. Mesoscale modeling of shocks in heterogeneous reactive materials, pp. 321–356.

[6] Baer, M. R. Modeling heterogeneous energetic materials at the mesoscale. *Thermochimica Acta 384* (2002), 351–367.

[7] Baer, M. R. Personal communication, July 2005.

[8] Baer, M. R. Personal communication, July 2009.

[9] Baer, M. R., Hertel, E. S., and Bell, R. L. Multidimensional DDT modeling of energetic materials. In *Proceedings of the Conference of the American Physical Society topical group on shock compression of condensed matter* (1996), S. Schmit and W. Tao, Eds., American Institute of Physics, pp. 433–436.

[10] Baer, M. R., and Nunziato, J. W. A two-phase mixture theory for the deflagration-to-detonation transition (DDT) in reactive granular mixtures. *International Journal of Multiphase Flow 12*, 6 (1986), 861–889.

[11] Baer, M. R., and Trott, W. M. Mesoscale descriptions of shock-loaded heterogeneous porous materials. In *Proc. 12th APS Shock Compression of Condensed Matter* (Atlanta, GA, 2002), M. Furnish, N. Thadhani, and Y. Horie, Eds., American Institute of Physics, Melville, NY, pp. 713–716.

[12] Baker, W. E. *Explosions in Air*. University of Texas Press, Austin, TX, 1973.

[13] Baker, W. E., Westine, P. S., and Dodge, F. T. Similarity methods in engineering dynamics. Tech. rep., South West Research Institute, San Antonio, Texas, 1981.

[14] Bardenhagen, S. G., and Brackbill, J. U. Dynamic stress bridging in granular material. *Journal of Applied Physics 83*, 11 (1998), 5732–5740.

[15] Barth, T. J., and Jesperson, D. C. The design and application of upwind schemes on unstructured meshes. In *AIAA Paper 89-0366* (1989).

[16] Bastea, S. Transport properties of fluid mixtures at high pressures and temperatures. application to the detonation products of HMX. In *12th International Detonation Symposium* (San Diego, CA, 2002), Office of Naval Research, Arlington, VA, pp. 576–583.

[17] Batten, P., Clarke, N., Lambert, C., and Causon, D. M. On the choice of wavespeeds for the HLLC Riemann solver. *SIAM Journal of Scientific Computing 18*, 6 (1997), 1553–1570.

[18] Baudin, G., Lefrancois, A., Bergues, D., Bigot, J., and Champion, Y. Combustion of nanophase aluminium in the detonation products of nitromethane. In *11th International Detonation Symposium, ONR 33300-5* (Arlington, VA, 1998), Office of Naval Research, pp. 989–997.

[19] Bdzil, J. B. Perturbation methods applied to problems in detonation physics. In *6th Symposium (International) on Detonation* (Washington, DC, 1976), pp. 352–370.

[20] Bdzil, J. B., Aslam, T. D., Henninger, R., and Quirk, J. J. High-explosives performance: Understanding the effects of a finite-length reaction zone. *Los Alamos Science LANL–28–12*, 28 (2003).

[21] Bdzil, J. B., Menikoff, R., Son, S. F., Kapila, A. K., and Stewart, D. S. Two-phase modeling of a deflagration-to-detonation transition in granular materials: a critical examination of modeling issues. *Physics of Fluids 11*, 2 (1999), 378–402.

[22] Bdzil, J. B., and Stewart, D. S. Modeling two-dimensional detonation with detonation shock dynamics. *Physics of Fluids A: Fluid Dynamics 1*, 7 (1989), 1261–1267.

[23] Bell, R. L., and Hertel Jr., E. S. An improved interface reconstruction algorithm for Eulerian codes. Tech. Rep. SAND92-1716, Sandia National Laboratories, Albuquerque, NM, 1992.

[24] Benson, D. J. Computational methods in Lagrangian and Eulerian hydrocodes. *Computer Methods in Applied Mechanics and Engineering 99*, 2–3 (1992), 235–394.

[25] Bertin, J. J. *Hypersonic Aerothermodynamics*, third ed. AIAA Education Series, Washington, DC, 1994.

[26] Blais, N. C., Engelke, R., and Sheffield, S. A. Mass spectroscopic study of the chemical reaction zone in detonating liquid nitromethane. *Journal of Physical Chemistry A 101*, 44 (1997), 8285–8295.

[27] Bouyer, V., Sheffield, S. A., Dattelbaum, D. M., Gustavsen, R. L., Stahl, D. B., and Doucet, M. Experimental measurements of the chemical reaction zone of detonating liquid explosives. In *16th APS Topical Conference on Shock Compression of Condensed Matter* (Nashville, TN, 2009), M. L. Elert, W. T. Buttler, M. D. Furnish, W. W. Anderson, and W. G. Proud, Eds., American Institute of Physics, Melville, NY, pp. 177–180.

[28] Bridgman, P. W. Recent work in the field of high pressures. *Reviews of Modern Physics 18*, 1 (1946).

[29] Brilliantov, N. V., and Poschel, T. *Kinetic Theory of Granular Gases*. Oxford University Press, Oxford, UK, 2004.

[30] Brousseau, P., and Anderson, C. J. Nanometric aluminum in explosives. *Propellants, Explosives, Pyrotechnics 27*, 5 (2002), 300–306.

[31] Buckingham, E. On physically similar systems; illustrations of the use of dimensional equations. *Physical Review 4*, 4 (1914), 345–376.

[32] Callister, W. D. *Materials Science and Engineering*, fourth ed. John Wiley & Sons, New York, 1997.

[33] Campbell, A. W., Davis, W. C., and Travis, J. R. Shock initiation of detonation in liquid explosives. *Physics of Fluids 4*, 4 (1961), 498–510.

[34] Campbell, A. W., Malin, M. E., and Holland, T. E. Detonation in homogeneous explosives. In *Second ONR Symposium on Detonation AD–52144* (Washington, DC, 1955), Office of Naval Research, pp. 336–359.

[35] Carney, J. R. Personal communication, June 2009.

[36] Carney, J. R., Wilkinson, J., and Lightstone, J. M. Time-resolved optical measurements of detonation and combustion products. In *15th APS Topical Conference on Shock Compression of Condensed Matter* (Kohala Coast, HI, 2007), M. Elert, M. D. Furnish, R. Chau, N. C. Holmes, and J. Nguyen, Eds., American Institute of Physics, Melville NY, pp. 1225–1228.

[37] Chapman, D. L. On the rate of explosion in gases. *Philosophical Magazine 47*, 284 (1899), 90–104.

[38] Combustion Dynamics Ltd. SuperSTATE theory manual. Tech. rep., Combustion Dynamics Ltd, Medicine Hat, AB, 1998.

[39] Cook, M. D., Haskins, P. J., and Stennett, C. Development and implementation of an ignition and growth model for homogeneous and heterogeneous explosives. In *Proceedings of the 11th International Detonation Symposium* (Snowmass, CO, 1998), Office of Naval Research, Arlington, VA, pp. 589–598.

[40] Cooper, M. A., Baer, M. R., Schmitt, R. G., Kaneshige, M. J., Pahl, R. J., and DesJardin, P. E. Understanding enhanced blast explosives: a multi-scale challenge. In *19th Military Aspects of Blast and Shock* (Calgary, AB, 2006).

[41] Cooper, P. W. *Explosives Engineering*. Wiley-VCH, New York, 1996.

[42] Courant, R., and Friedrichs, K. O. *Supersonic Flow and Shock Waves*. Interscience Publishers, New York, 1948.

[43] Cowan, R. D., and Fickett, W. Calculation of the detonation properties of solid explosives with the Kistiakowsky-Wilson equation of state. *J. Chem. Phys. 24*, 5 (1956), 932.

[44] Davis, W. C. Introduction to detonation phenomena. Tech. Rep. LA-UR-79-2880, Los Alamos Scientific Lab., 1979. U. S. Army Research Office Working Group Meeting on Detonation Phenomena, Menlo Park, CA, October 23-24.

[45] Davydov, V. Y., Grishkin, A. M., and Feodoritov, I. I. Experimental-theoretical investigation of the oxidation of aluminum in detonation waves. *Combustion, Explosion, and Shock Waves 28*, 5 (1992), 564–568.

[46] Department of the Army. Military explosives, army technical manual. Tech. Rep. TM-9-1300-214, Department of the Army, 1984.

[47] Dobratz, B. M., and Crawford, P. C. LLNL explosives handbook - properties of chemical explosives and explosive simulants. Tech. Rep. UCRL-52997-Rev2, Lawrence Livermore National Laboratories, Livermore, CA, January 1985.

[48] Döering, W. On detonation processes in gases. *Ann. Phys. 43* (1943), 421–436.

[49] Draiswerke Inc. Drais grinding media [online]. http://www.draiswerke-inc.com /media.htm, Accessed June 2009.

[50] Drake, R. M. Discussion on G. C. Vliet and G. Leppert forced convection heat transfer from an isothermal sphere to water. *ASME Journal of Heat Transfer 83*, 2 (1961), 170–179.

[51] Dremin, A. N. Toward detonation theory. In *High pressure shock compression of condensed matter*. Springer, New York, NY, 1999.

[52] Dremin, A. N., and Rozanov, O. K. On the detonation of nitromethane acetone mixtures. *Dokl Akad. Nauk. SSSR 139*, 1 (1961), 137–139. [cited in Dremin (1999)].

[53] Dremin, A. N., Rozanov, O. K., and Trofimov, V. S. On the detonation of nitromethane. *Combustion and Flame 7*, 2 (1963), 153–162.

[54] Dremin, A. N., Savrov, S. D., Trofimov, V. S., and Shvedov, K. K. *Detonatsionnye Volny v Kondensirovannykh Sredakh (Detonation Waves in Condensed Media)*. Izd-vo Nauka, Moscow, 1970. Translated from Russian by Foreign-Technology Division, Wright-Patterson AFB, OH, August 1972, FTD-HT-23-1889-71 [cited in Fickett and Davis (1979)].

[55] Drumheller, D. S. *Introduction to Wave Propagation in Nonlinear Fluids and Solids*. Cambridge University Press, New York, NY, 1998.

[56] Elperin, T., Igra, O., and Ben-Dor, G. Rarefaction waves in dusty gases. *Fluid Dynamics Research 4* (1988), 229–238.

[57] Engelhardt, C. Numerical modeling of heterogeneous high explosives. In *38th AIAA Fluid Dynamics Conference and Exhibit, AIAA-2008-3921* (Seattle, WA, 2008).

[58] Engelke, R. Effect of a physical inhomogeneity on steady-state detonation velocity. *Physics of Fluids 22*, 9 (1979), 1623–1630.

[59] Engelke, R., and Bdzil, J. B. A study of the steady-state reaction-zone structure of a homogeneous and a heterogeneous explosive. *Physics of Fluids 26*, 5 (1983), 1210–1221.

[60] Erpenbeck, J. J. Detonation stability for disturbances of small transverse wavelength. *Physics of Fluids 9*, 7 (1966), 1293–1306.

[61] Eyring, H., Powell, R. E., Duffey, G. H., and Parlin, R. B. The stability of detonation. *Chemical Reviews 45*, 1 (1949), 69–181.

[62] Ferziger, J. H., and Peric, M. *Computational Methods for Fluid Flow and Heat Transfer*. Springer, New York, NY, 1999.

[63] Fickett, W. *Introduction to Detonation Theory*. University of California Press, Berkeley, CA, 1985.

[64] Fickett, W., and Davis, W. C. *Detonation*. University of California Press, Berkeley, CA, 1979.

[65] Fordham, S. *High Explosives and Propellants*, second ed. Pergamon Press, Oxford, England, 1980.

[66] Fourier, J. B. J. *Analytical Theory of Heat*. Cambridge University Press, London, 1878. Translated, with notes, by A. Freeman.

[67] Fox, T. W., Rackett, C. W., and Nicholls, J. A. Shock wave ignition of magnesium powders. In *Proc. 11th Int. Symp. Shock Tubes and Waves* (Seattle, 1978), B. Ahlborn, A. Hertzberg, and D. Russell, Eds., University of Washington Press, pp. 262–268.

[68] Fried, L. E., Howard, W. M., and Souers, P. C. Cheetah 2.0 user's manual. Tech. Rep. UCRL-MA-117541 Rev. 5, University of California, Lawrence Livermore National Laboratory, Livermore, CA, 1998.

[69] Frost, D. L. Personal communication, July 2009.

[70] Frost, D. L., Aslam, T., and Hill, L. G. Application of detonation shock dynamics to the propagation of a detonation in nitromethane in a packed inert particle bed. In *11th APS Topical Meeting on Shock Compression of Condensed Matter* (Snowbird, UT, 1999), M. D. Furnish, L. C. Chhabildas, and R. S. Hixson, Eds., American Institute of Physics, Melville NY, pp. 821–824.

[71] Frost, D. L., Cairns, M., Goroshin, S., and Zhang, F. Reaction of titanium and zirconium particles in cylindrical explosive charges. In *15th APS Topical Conference on Shock Compression of Condensed Matter* (Kohala Coast, HI, 2007), M. Elert, M. D. Furnish, R. Chau, N. C. Holmes, and J. Nguyen, Eds., American Institute of Physics, Melville NY, pp. 781–784.

[72] Frost, D. L., Cairns, M., Goroshin, S., and Zhang, F. Effect of particle morphology on the reactivity of explosively dispersed titanium particles. In *16th APS Topical Conference on Shock Compression of Condensed Matter* (Nashville, TN, 2009), M. L. Elert, W. T. Buttler, M. D. Furnish, W. W. Anderson, and W. G. Proud, Eds., American Institute of Physics, Melville NY, pp. 157–160.

[73] Frost, D. L., Goroshin, S., Cairns, M., Ripley, R., and Zhang, F. Temperature measurements in a multiphase fireball. In *22nd International Colloquium on the Dynamics of Explosions and Reactive Systems* (Minsk, Belarus, 2009).

[74] Frost, D. L., Goroshin, S., Levine, J., Ripley, R., and Zhang, F. Critical conditions for ignition of aluminum particles in cylindrical charges. In *14th APS Topical Group Meeting on Shock Compression of Condensed Matter* (Baltimore, MD, 2005), M. Furnish, M. Elert, T. Russell, and C. White, Eds., American Institute of Physics, Melville NY, pp. 972–975.

[75] Frost, D. L., Ornthanalai, C., Zarei, Z., Tanguay, V., and Zhang, F. Particle momentum effects from the detonation of heterogeneous explosives. *Journal of Applied Physics 101* (2007), 113529.

[76] Frost, D. L., and Zhang, F. *Shock Wave Science and Technology Reference Library: Heterogeneous Detonation*, vol. 4. Springer-Verlag, Berlin Heidelberg, 2009, ch. Slurry Detonation, p. 217.

[77] Frost, D. L., Zhang, F., Murray, S. B., and McCahan, S. Critical conditions for ignition of metal particles in a condensed explosive. In *12th International Detonation Symposium* (San Diego, CA, 2002), pp. 693–701.

[78] Gertsman, V. Y., and Kwok, Q. S. M. TEM investigation of nanophase aluminum powder. *Microscopy and Microanalysis 11* (2005), 410–420.

[79] Gibbs, T. R., and Popolato, A. *LASL Explosive Property Data*. University of California Press, Berkeley, CA, 1980.

[80] Gilbert, M., Davis, L., and Altman, D. Velocity lag of particles in linearly accelerated combustion gases. *Jet Propulsion 25* (1955), 26–30.

[81] Glassman, I. *Combustion*. Academic Press, New York, 1977.

[82] Glassman, I. *Combustion*, 3rd ed. Academic Press, San Diego, CA, 1996.

[83] Glimm, J., Grove, J. W., Li, X. L., Shyue, K. M., Zhang, Q., and Zeng, Y. Three dimensional front tracking. *SIAM Journal on Scientific Computing 19*, 3 (1998), 703–727.

[84] Godunov, S. K. A difference scheme for numerical computation of discontinuous solution to hydrodynamic equations. *Math. Sbornik 47* (1959), 271–306.

[85] Gogulya, M. F., Dolgoborodov, A. Y., Brazhnikov, M. A., and Baudin, G. Detonation waves in HMX/Al mixtures. In *11th International Detonation Symposium ONR 33300-5* (Snowmass, CO, 1998), Office of Naval Research, Arlington, VA, pp. 979–988.

[86] Gonthier, K. A., and Rumchik, C. G. Theory and analysis of non-ideal detonation for RDX/dilute metal mixtures. In *13th International Detonation Symposium* (Norfolk, VA, 2006), Office of Naval Research, Arlington, VA, pp. 176–186.

[87] Gordon, S., and McBride, B. J. Computer program for calculation of complex equilibrium compositions and applications. Tech. Rep. RP-1311, NASA, 1994.

[88] Goroshin, S., Frost, D. L., Levine, J., Yoshikana, A., and Zhang, F. Optical pyrometry of fireballs of metallized explosives. In *Proc. of 18th International Symposium on the military Aspects of Blast and Shock* (Bad Reichenhall, Germany, 2004).

[89] Goroshin, S., Frost, D. L., Levine, J., Yoshinaka, A., and Zhang, F. Optical pyrometry of fireballs of metalized explosives. *Propellants, Explosives, Pyrotechnics 31*, 3 (2006), 169–181.

[90] Gover, J. E. Shock wave physics. Tech. Rep. SNLA Classnotes, 1980. [cited in Cooper (1998)].

[91] Grégoire, Y., Sturtzer, M.-O., Khasainov, B. A., and Veyssiere, B. Investigation of the behaviour of aluminium particles in the burnt products of heterogeneous explosives. In *21st International Colloquium on the Dynamics of Explosions and Reactive Systems* (Poitiers, France, 2007).

[92] Hardesty, D. R. An investigation of the shock initiation of nitromethane. *Combustion and Flame 27*, 2 (1976), 229–251.

[93] Harten, A. High resolution schemes for hyperbolic conservation laws. *Journal of Computational Physics 49* (1983), 357–393.

[94] Haskins, P. J., Cook, M. D., and Briggs, R. I. The effect of additives on the detonation characteristics of a liquid explosive. In *Shock Compression of Condensed Matter - 2001* (Atlanta, GA, 2002), M. D. Furnish, N. N. Thadhani, and Y. Horie, Eds., American Institute of Physics, Melville, NY, pp. 890–893.

[95] Hayes, B. On electrical conductivity in detonation products. In *Fourth Symposium (International) on Detonation, ACR-126* (Silverspring, MD, 1965), Office of Naval Research, White Oak, MD, pp. 595–601.

[96] Hobbs, M. L., and Baer, M. R. Calibrating the BKW-EOS with a large product species data base and measured C-J properties. In *10th International Detonation Symposium* (Boston, MA, 1994), Office of Naval Research, Arlingtion, VA, pp. 409–418.

[97] Igel, E. A., and Seely, L. B. J. The detonation behavior of liquid TNT. In *Second ONR Symposium on Detonation* (Washington, DC, 1955), Office of Naval Research, pp. 321–335.

[98] Incropera, F. P., and DeWitt, D. P. *Introduction to Heat Transfer*, fourth ed. Wiley, New York, NY, 2002.

[99] Jenkins, C. M., Horie, Y., Ripley, R. C., and Wu, C.-Y. Imaging high speed particles in explosive driven blast waves. In *16th APS Topical Conference on Shock Compression of Condensed Matter* (Nashville, TN, 2009), American Institute of Physics, Melville, NY, pp. 635–638.

[100] Johansson, C. H., and Persson, P. A. *Detonics of High Explosives*. Academic Press, New York, NY, 1970.

[101] Johnson, G. R., and Cook, W. H. A constitutive model and data for metals subjected to large strains, high strain rates and high temperatures. In *Proceedings of the 7th International Symposium on Ballistics* (The Hague, The Netherlands, 1983), p. 541547.

[102] Jouguet, E. On the propagation of chemical reactions in gases. *Journal de Mathematiques Pures et Appliquees 1* (1905), 347–425.

[103] Kato, Y., and Brochet, C. Cellular structure of detonation in nitromethane containing aluminum particles. In *Proc. 6th Symposium (International) on Detonation* (Coronado, CA, 1976), pp. 124–132.

[104] Kato, Y., Kato, H., Murata, K., and Itoh, S. Overdriven detonation in high density explosives containing tungsten powder. In *13th International Detonation Symposium* (Norfolk, VA, 2006), J. Kennedy and J. Schelling, Eds., Office of Naval Research, pp. 196–203.

[105] Kato, Y., and Murata, K. Detonation in packed beds of metal particles saturated with nitromethane. In *Proceedings of Europyro 2007 - 34th International Pyrotechnics Seminar* (Beaune, France, 2007).

[106] Kato, Y., and Murata, K. Detonation characteristics of packed bed of metal particles saturated with nitromethane. In *7th International Symposium on Hazards, Prevention and Mitigation of Industrial Explosions* (St. Petersburg, Russia, 2008), pp. 260–269.

[107] Kato, Y., Murata, K., and Itoh, S. Detonation characteristics of packed beds of aluminum saturated with nitromethane. In *13th International Detonation*

Symposium (Norfolk, VA, 2006), J. Kennedy and J. Schelling, Eds., Office of Naval Research, Arlington, VA, pp. 187–195.

[108] Kennedy, B. *Surface Mining*, second ed. Port City Press, Baltimore, MD, 1990.

[109] Kim, K., Wilson, W., Peiris, S., Needham, C., Watry, C., Ortley, D. J., and Zhang, F. Effects of particle damage during detonation of thermobarics on subsequent reactions. In *21st International Colloquium on the Dynamics of Explosions and Reactive Systems* (Poitiers, France, 2007).

[110] Kinney, G. F., and Graham, K. J. *Explosive Shocks in Air*, second ed. Springer-Verlag, Berlin Heidelberg, 1985.

[111] Kipp, M. E., and Nunziato, J. W. Numerical simulation of detonation failure in nitromethane. In *Seventh Symposium (International) on Detonation* (Boston, MA, 1981), Office of Naval Research, Arlington, VA.

[112] Kistiakowsky, G. B., and Wilson, E. B. Report on the prediction of detonation velocities of solid explosives. Tech. Rep. OSRD-69, Office of Scientific Research and Development, 1941.

[113] Knudsen, J. G., and Katz, D. L. *Fluid Mechanics and Heat Transfer*. McGraw-Hill, New York, NY, 1958.

[114] Kopyshev, V. P., Medvedev, A. B., and Khrustalev, V. V. Model estimation of the viscosity of explosion products of condensed explosives. *Combustion, Explosion, and Shock Waves 40*, 200 (2004).

[115] Korobeinikov, V. P., Levin, V. A., Markov, V. V., and Chernyi, G. G. Propagation of blast waves in combustible gas. *Astronautica Acta 17* (1972), 529–537.

[116] Kuo, K. K. *Principles of Combustion*, 2nd ed. John Wiley and Sons, Toronto, ON, 2005.

[117] Kuo, K. K., Koo, J. H., Davis, T. R., and Coates, G. R. Transient combustion in gas-permeable propellants. *Acta Astronautica 3* (1976), 573–591.

[118] Kurangalina, R. K. Critical diameter of liquid explosives as a function of powder content. *Zhurnal Prikladnoi Mekhaniki i Tekhnicheskoi Fiziki 10*, 4 (1969), 133–136.

[119] Kury, J. W., Breithaupt, R. D., and Tarver, C. M. Detonation waves in trinitrotoluene. *Shock Waves 4*, 9 (1999), 227–237.

[120] Lanovets, V. S., Levich, V. A., Rogov, N. K., Tunik, Y. V., and Shamshev, K. N. Dispersion of the detonation products of a condensed explosive with solid inclusions. *Combustion, Explosion, and Shock Waves 29*, 5 (1993), 638–641.

[121] Laurence, S. J., Deiterding, R., and Hornung, H. G. Proximal bodies in hypersonic flow. *Journal of Fluid Mechanics 590* (2007), 209–237.

[122] Leadbetter, J., Ripley, R. C., and Zhang, F. Explosive dispersal of metal particles in urban street structures. In *Proceedings of the International Symposium on the Effects of Munitions with Structures 12.1* (Orlando, FL, 2007).

[123] Lee, E., Finger, M., and Collins, W. JWL equation of state coefficients for high explosives. Tech. Rep. UCID-16189, Lawrence Livermore National Laboratory, Livermore, CA, 1973.

[124] Lee, E. L., Hornig, H. C., and Kury, J. W. Adiabatic expansion of high explosive detonation products. Tech. Rep. UCRL-50422, University of California, Livermore, CA, 1968.

[125] Lee, E. L., and Tarver, C. M. Phenomenological model of shock initiation in heterogeneous explosives. *Physics of Fluids 23*, 12 (1980), 2362–2372.

[126] Lee, J. J., Brouillette, M., Frost, D. L., and Lee, J. H. S. Effect of diethylenetriamine sensitisation on detonation of nitromethane in porous media. *Combustion and Flame 100* (1995), 292–300.

[127] Lee, J. J., Frost, D. L., Lee, J. H. S., and Dremin, A. Propagation of nitromethane detonation in porous media. *Shock Waves 5*, 1/2 (1995), 115–119.

[128] LeVeque, R. J. *Finite Volume Methods for Hyperbolic Problems*. Cambridge University Press, Cambridge, UK, 2002.

[129] Liou, M.-S., and Steffen, C. J. A new flux splitting scheme. *Journal of Computational Physics 107* (1993), 251–278.

[130] Lutz, A. E., Kee, R. J., and Miller, J. A. CHEMKIN-II. Tech. Rep. SAND87-8248, Sandia National Labs, Albuquerque, NM, 1987.

[131] Mader, C. L. The hydrodynamic hot spot and shock initiation of homogeneous explosives. Tech. Rep. LA-2703, Los Alamos Scientific Laboratory of the University of California, Los Alamos, NM, 1962.

[132] Mader, C. L. *Numerical Modeling of Detonation*. University of California Press, Berkeley, CA, 1979.

[133] Mader, C. L. *Numerical Modeling of Explosives and Propellants*, second ed. CRC Press, Boca Raton, FL, 1998.

[134] Mader, C. L., and Forest, C. A. Two-dimensional homogeneous and heterogeneous detonation wave propagation. Tech. Rep. LA-6259, Los Alamos Scientific Laboratory, NM, 1976.

[135] Mader, C. L., and Kershner, J. D. Three-dimensional modeling of shock initiation of heterogeneous explosives. In *19th Symposium (International) on Combustion* (Pittsburg PA, 1982), pp. 685–690.

[136] Mader, C. L., and Kershner, J. D. The heterogeneous explosive reaction zone. In *9th Symposium (International) on Detonation* (Portland OR, 1989), pp. 693–700.

[137] Mallory, H. D. Detonation reaction time in nitromethane. *Physics of Fluids 19*, 9 (1976), 1329–1331.

[138] Markov, K. Z. *Heterogeneous media micromechanics modeling methods and simulations*. Birkhauser, Boston, MA, 2000, ch. Elementary micromechanics of heterogeneous media, pp. 1–146.

[139] Marsh, S. P. *LASL Shock Hugoniot Data*. University of California Press, Berkeley, CA, 1980.

[140] Martec Ltd. Chinook theory manual. Tech. Rep. SM-07-01, Martec Ltd, Halifax, NS, 2007.

[141] McGlaun, J. M., and Thompson, S. L. CTH: A three-dimensional shock wave physics code. *International Journal of Impact Engineering 10* (1990), 351–360.

[142] McQueen, R. G., and Marsh, S. P. Equation of state for nineteen metallic elements from shock-wave measurements to two megabars. *Journal of Applied Physics 31*, 7 (July 1960), 1253–1269.

[143] Menikoff, R. Compaction wave profiles in granular HMX. In *12th APS Shock Compression of Condensed Matter - 2001, Atlanta, GA* (Atlanta, GA, 2002), M. D. Furnish, N. N. Thadhani, and Y. Horie, Eds., American Institute of Physics, Melville, NY, pp. 979–982.

[144] Milne, A. M. Detonation in heterogeneous mixtures of liquids and particles. *Shock Waves 10* (2000), 351–362.

[145] Milne, A. M., Cargill, S., Bennett, K., and Longbottom, A. W. Modelling of enhanced blast and heterogeneous explosives. In *19th International Military Aspects of Blast and Shock* (Calgary, AB, 2006).

[146] Milne, A. M., Longbottom, A. W., Evans, D. J., Haskins, P. J., Cook, M. D., and Briggs, R. I. The burning rate of aluminium particles in nitromethane in cylinder tests. In *12th International Detonation Symposium* (San Diego, CA, 2006), Office of Naval Research, Arlington, VA.

[147] Mochalova, V. M., Utkin, A. V., Garanin, V. A., and Torunov, S. I. Structure of detonation waves in tetranitromethane and its mixtures with methanol. *Combustion, Explosion, and Shock Waves 45*, 3 (2009), 320–325.

[148] Mulford, R. N., and Swift, D. C. Mesoscale modeling of shock initiation in HMX-based explosives. In *12th APS Shock Compression of Condensed Matter - 2001* (Atlanta, GA, 2002), M. D. Furnish, N. N. Thadhani, and Y. Horie, Eds., American Institute of Physics, Melville NY, pp. 415–418.

[149] Nahmani, G., and Manheimer, Y. Detonation of nitromethane. *Journal of Chemical Physics 24* (1956), 1074–1077.

[150] Noh, W. F., and Woodward, P. SLIC (simple line interface calculation). In *Proc. 5th Int. Conf. on Numerical Methods in Fluid Dynamics* (Enschede, Netherlands, 1976), pp. 330–340.

[151] Nunziato, J. W., Kennedy, J. E., and Hardesty, D. R. Modes of shock wave growth in the initiation of explosives. In *6th Symposium (International) on Detonation* (Coronado, CA, 1976), Office of Naval Research, Washington, DC, pp. 47–59.

[152] Oppenheim, A. K., Kuhl, A. L., and Kame, M. M. On self-similar blast waves headed by the Chapman-Jouguet detonation. *Journal of Fluid Mechanics 55*, 5 (1972), 257–270.

[153] Oran, E. S., and Boris, J. P. *Numerical Simulation of Reactive Flow*. McGraw-Hill, New York, NY, 1987.

[154] Oseen, C. W. über die stokessesche formel und über eine verwandte aufgabe inder hydrodynamik. *J. Ark. Mat. Astron. Fys. 6*, 29 (1910).

[155] Osher, S., and Sethian, J. A. Fronts propagating with curvature dependent speed: algorithms based on Hamilton-Jacobi formulations. *Journal of Computational Physics 79*, 1 (1988), 12–49.

[156] Ottosen, N. S., and Petersson, H. *Introduction to the Finite Element Method*. Prentice-Hall, London, 1992.

[157] Petel, O. E., Mack, D., Higgins, A. J., Turcotte, R., and Chan, S. K. Comparison of the detonation failure mechanism in homogeneous and heterogeneous explosives. In *13th International Symposium on Detonation* (Norfolk, VA, July 2006), pp. 2–11.

[158] Phillips, R., Brady, J., and Bossis, G. Hydrodynamic transport properties of hard-sphere dispersions. I. Suspensions of freely mobile particles. *Physics of Fluids 31*, 12 (1988), 3462–3472.

[159] Plaksin, I., Campos, J., Ribeiro, J., Mendes, R., Gois, J., Protugal, A., Simoes, P., and Pedroso, L. Detonation meso-scale tests for energetic materials. In *12th APS Shock Compression of Condensed Matter - 2001, Atlanta, GA* (Melville NY, 2002), M. D. Furnish, N. N. Thadhani, and Y. Horie, Eds., American Institute of Physics, pp. 922–925.

[160] Powers, J. M., Stewart, D. S., and Krier, H. Theory of two-phase detonation – Part I: Modeling. *Combustion and Flame 80* (1990), 264–279.

[161] Richards, D. W., De Angelis, R. J., Kramer, M. P., House, J. W., Cunard, D. A., and Shea, D. P. Shock-induced deformation of tungsten powder. *Adv. X-ray Analysis 47* (2004), 351–356.

[162] Ripley, R. C. Unstructured-grid methods for numerical simulation of shock wave interaction with bodies and boundary layers. Master's thesis, University of Waterloo, Waterloo, ON, 2002.

[163] Ripley, R. C., Donahue, L., and Zhang, F. A hybrid equation-of-state detonation model for homogeneous explosives. In *Combustion Institute / Canadian Section - Spring Technical Meeting* (Halifax, NS, 2005).

[164] Ripley, R. C., Leadbetter, J., Donahue, L., and Zhang, F. Acceleration, heating and reaction of aluminum particles in condensed explosive dispersal. In *20th Military Aspects of Blast and Shock* (Oslo, Norway, 2008).

[165] Ripley, R. C., Leadbetter, J., Donahue, L., Zhang, F., and Frost, D. L. Acceleration of solid particles in explosive dispersal. In *27th International Symposium on Shock Waves* (St. Petersburg, Russia, 2009).

[166] Ripley, R. C., Lien, F.-S., and Yovanovich, M. M. Numerical simulation of shock diffraction on unstructured meshes. *Computers and Fluids 35* (2005), 1420–1431.

[167] Ripley, R. C., Whitehouse, D. R., and Lien, F.-S. Effect of mesh topology on shock wave loading computations. In *11th Annual Conference of the CFD Society of Canada* (Vancouver, BC, 2003).

[168] Ripley, R. C., Zhang, F., and Lien, F.-S. Shock interaction of metal particles in condensed explosive detonation. In *14th APS Shock Compression of Condensed Matter* (Baltimore, MD, 2005), M. D. Furnish, M. Elert, T. Russell, and C. White, Eds., American Institute of Physics, Melville, NY, pp. 499–502.

[169] Ripley, R. C., Zhang, F., and Lien, F.-S. Detonation interaction with metal particles in explosives. In *13th International Detonation Symposium* (Norfolk, VA, 2006), J. Kennedy and J. Schelling, Eds., Office of Naval Research Report ONR 351-07-01, Arlington, VA, pp. 214–223.

[170] Ripley, R. C., Zhang, F., and Lien, F.-S. Acceleration and heating of metal particles in condensed explosive detonation. In *15th APS Shock Compression of Condensed Matter* (Kohala Coast, HI, 2007), M. Elert, M. D. Furnish, R. Chau, N. Holmes, and J. Nguyen, Eds., American Institute of Physics, Melville, NY, pp. 409–412.

[171] Ripley, R. C., Zhang, F., and Lien, F.-S. Momentum and heat transfer models for detonation in nitromethane with metal particles. In *16th APS Topical Conference on Shock Compression of Condensed Matter* (Nashville, TN, 2009), M. L. Elert, W. T. Buttler, M. D. Furnish, W. W. Anderson, and W. G. Proud, Eds., American Institute of Physics, Melville, NY, pp. 331–334.

[172] Rogue, X., Rodriguez, G., Haas, J. F., and Saurel., R. Experimental and numerical investigation of the shock-induced fluidization of a particles bed. *Shock Waves 8*, 1 (1998), 29–45.

[173] Rudinger, G. Experiments on shock relaxation in particle suspensions in a gas and preliminary determination of drag coefficients. In *ASME Multiphase Flow Symposium* (New York, NY, 1963).

[174] Rudinger, G. Some properties of shock relaxation in gas flows carrying small particles. *Physics of Fluids 7*, 5 (1964), 658–663.

[175] Rudinger, G. Effective drag coefficient for gas-particle flow in shock tubes. *Trans. ASME Journal of Basic Engineering D 92* (1970), 165–172.

[176] Rudinger, G. *Fundamentals of Gas-Particle Flow*. Elsevier, New York, 1980.

[177] Sachs, P. G. The dependence of blast on ambient pressure and temperature. Tech. Rep. BRL Report No 466, Aberdeen Proving Ground, Maryland, 1944.

[178] Saito, T. Numerical analysis of dusty-gas flows. *Journal of Computational Physics 176* (2002), 129–144.

[179] Sakellariou, A., Sawkinsa, T. J., Sendena, T. J., and Limayeb, A. X-ray tomography for mesoscale physics applications. *Physica A: Statistical Mechanics and its Applications 339*, 1-2 (2004), 152–158. Proceedings of the International Conference New Materials and Complexity.

[180] Sauer, F. M. Convective heat transfer from spheres in a free-molecular flow. *Journal of Aerospace Science and Technology 18* (1951), 353–354.

[181] Schlichting, H. T. *Boundary Layer Theory*, 7th ed. McGraw-Hill, Toronto, ON, 1979.

[182] Sedov, L. Propagation of strong shock waves. *Journal of Applied Mathematics and Mechanics 10* (1946), 241–250.

[183] Sethian, J. A. *Level set methods and fast marching methods. Evolving interfaces in computational geometry, fluid mechanics, computer vision, and materials science*, second ed., vol. 3 of *Cambridge Monographs on Applied and Computational Mathematics*. Cambridge University Press, 1999.

[184] Shchelkin, K. I. Unidimensional instability of detonation. *Dokl. Aka. Nauk SSSR (Phys. Chem. Sect.) 160* (1965), 1144–1146. [cited in Fickett and Davis (1979)].

[185] Sheffield, S., Engelke, R., Alcon, R., Gustavsen, R., Robins, D., Stahl, D., Stacy, H., and Whitehead, M. Particle velocity measurements of the reaction zone in nitromethane. In *12th International Detonation Symposium* (San Diego CA, 2002), pp. 159–166.

[186] Smirnov, N. Combustion and detonation in multi-phase media: Initiation of detonation in dispersed-film systems behind a shock wave. *International Journal of Heat and Mass Transfer 31*, 4 (1988), 779–793.

[187] Sommerfeld, M., and Decker, S. On the importance of the Basset history term on the particle motion induced by a plane shock wave. In *Proceedings of the 19th ISSW, vol. III* (Marseille, France, 1993), pp. 37–42.

[188] Soo, S. *Fluid Dynamics of Multiphase Systems*. Blaisdell Publishing Company, Waltham, MA, 1967.

[189] Stewart, D. S. Towards the miniaturization of explosive technology. *Shock Waves 11*, 6 (2002), 467–473.

[190] Stewart, D. S., and Bdzil, J. B. The shock dynamics of stable multidimensional detonation. *Combustion and Flame 72* (1988), 311–323.

[191] Stewart, D. S., and Bdzil, J. B. Modeling unit cell interactions for the microstructure of a heterogeneous explosive: Detonation diffraction past an inert sphere. In *16th APS Topical Conference on Shock Compression of Condensed Matter* (Nashville, TN, 2009), M. L. Elert, W. T. Buttler, M. D. Furnish, W. W. Anderson, and W. G. Proud, Eds., American Institute of Physics, Melville NY, pp. 117 – 120.

[192] Strehlow, R. A. *Combustion Fundamentals*. McGraw-Hill, New York, NY, 1984.

[193] Sun, M., Saito, T., Takayama, K., and Tanno, H. Unsteady drag on a sphere by shock wave loading. *Shock Waves 14* (2005), 3–9.

[194] Tam, C. K. W. The drag on a cloud of spherical particles in low Reynolds number flow. *Journal of Fluid Mechanics 38* (1969), 537–546.

[195] Tanguay, V., Higgins, A. J., and Zhang, F. A simple analytical model for reactive particle ignition in explosives. *Propellants, Explosives, Pyrotechnics 32*, 5 (2007).

[196] Tarver, C. M. Chemical energy release in self-sustaining detonation waves in condensed explosives. *Combustion and Flame 46* (1982), 157–176.

[197] Tarver, C. M. Chemical reaction and equilibration mechanisms in detonation waves. In *10th Topical Conference on Shock Compression of Condensed Matter* (Amherst, MA, 1997), S. C. Schmidt, D. P. Dandekar, and J. W. Forbes, Eds.

[198] Tarver, C. M. Detonation reaction zones in condensed explosives. In *14th APS Shock Compression of Condensed Matter* (Baltimore, MD, 2005), M. D. Furnish, T. R. M. Elert, and C. White, Eds., American Institute of Physics, Melville, NY, pp. 1026–1029.

[199] Tarver, C. M., Tao, W. C., and Lee, C. G. Sideways plate push test for detonating solid explosive. *Propellants, Explosives, Pyrotechnics 21* (1996), 238–246.

[200] Taylor, G. I. The formation of a blast wave by a very intense explosion. I. Theoretical discussion. *Proceedings of the Royal Society of London. Series A, Mathematical and Physical Sciences 201*, 1065 (1950), 159–174.

[201] Taylor, J. *Detonation in Condensed Explosives*. Oxford University Press, London, UK, 1952.

[202] Thomas, P. On the influence of the Basset history force on the motion of a particle through a fluid. *Physics of Fluids A 4*, 9 (1992), 2090–2093.

[203] Toro, E. F. *Riemann Solvers and Numerical Methods for Fluid Dynamics*. Springer-Verlag, Berlin, 1997.

[204] Trunov, M. A., Schoenitz, M., Zhu, X., and Dreizin, E. L. Effect of polymorphic phase transformations in Al_2O_3 film on oxidation kinetics of aluminum powders. *Combustion and Flame 140* (2005), 310–318.

[205] Urtiew, P. From cellular structure to failure waves in liquid detonations. *Combustion and Flame 25* (1975), 241–245.

[206] Valimet Inc. Spherical metal powders [online]. http://www.valimet.com/, Accessed October 2008.

[207] van Leer, B. Towards the ultimate conservative difference scheme V. a second order sequel to Godunov's method. *Journal of Computational Physics 32* (1979), 101–136.

[208] Vargaftik, N. B., Filippov, L. P., Tarzimanov, A. A., and Totskii, E. E. *Handbook of Thermal Conductivity of Liquids and Gases*. CRC Press, Boca Raton, FL, 1993.

[209] von Neumann, J. Theory of detonation waves. In *John von Neumann, Collected Works*, L. A. J. Taub, Ed., vol. 6. Pergamon Press, Oxford, UK, 1942.

[210] von Neumann, J. *John von Neumann. Collected Works*, vol. 6. Permagon Press, Elmsford, NY, 1963, ch. The point source solution, pp. 219–237.

[211] Walker, F. E. Initiation and detonation studies in sensitized nitromethane. *Acta Astronautica 6* (1979), 807–813.

[212] Walsh, J. M., and Christian, R. H. Equation of state of metals from shock wave measurements. *Physical Review 97*, 6 (1955), 1544–1556.

[213] Walsh, J. M., Rice, M. H., McQueen, R. G., and Yarger, F. L. Shock-wave compressions of twenty-seven metals. *Physical Review 108*, 2 (1957), 196–216.

[214] Weast, R. C., Astle, M. J., and Beyer, W. H. *CRC Handbook of Chemistry and Physics*, 66th ed. CRC Press, Boca Raton FL, 1986.

[215] Wellington, S. L., and Vinegar, J. J. X-ray computed tomography. *Journal of Petrolium Technology 39* (1987), 885–898.

[216] White, F. M. *Viscous Fluid Flow*, 2nd ed. McGraw-Hill, Toronto, ON, 1991.

[217] White, F. M. *Fluid Mechanics*, 3rd ed. McGraw-Hill, New York, NY, 1994.

[218] Williams, F. A. *Combustion Theory*. Addison-Wesley, Reading, MA, 1965.

[219] Williamson, R. Parametric studies of dynamic powder consolidation using a particle-level numerical model. *Journal of Applied Physics 68*, 3 (1990), 1287–1296.

[220] Xu, T., Ji, H., Lien, F.-S., and Zhang, F. Drag-force in supersonic dense gas-solid flow. In *27th International Symposium on Shock Waves* (St. Petersburg, Russia, 2009).

[221] Xu, T., Ji, H., Lien, F.-S., and Zhang, F. Numerical simulations with an immersed boundary method pertinent to multiphase turbulent flows. In *17th Annual Conference of the CFD Society of Canada* (Ottawa, ON, 2009).

[222] Yoshinaka, A., Zhang, F., and Wilson, W. Effect of shock compression on aluminum particles in condensed media. In *15th APS Shock Compression of Condensed Matter* (Kohala Coast, HI, 2007), M. Elert, M. Furnish, R. Chau, N. Holmes, and J. Nguyen, Eds., American Institute of Physics, Melville, NY, pp. 1057–1060.

[223] Zarei, Z., Frost, D. L., and Timofeev, E. V. Particle entrainment in supersonic flow. In *27th International Symposium on Shock Waves* (St. Petersburg, Russia, 2009).

[224] Zel'dovich, Y. B. On the theory of the propagation of detonation in gaseous systems. *Zh. Eksp. Teor. Fiz. 10* (1940), 542–568.

[225] Zel'dovich, Y. B., and Kompaneets, S. A. *Theory of Detonations*. Academic Press, New York, NY, 1960.

[226] Zhang, F., Frost, D. L., Thibault, P. A., and Murray, S. B. Explosive dispersal of solid particles. *Shock Waves 10* (2001), 431–443.

[227] Zhang, F., Gerrard, K., and Ripley, R. C. Reaction mechanism of aluminum-particle–air detonation. *Journal of Propulsion and Power 25*, 4 (2009), 845–858.

[228] Zhang, F., Murray, S. B., and Gerrard, K. B. Aluminum particles-air detonation at elevated pressures. *Shock Waves* (2006).

[229] Zhang, F., Thibault, P. A., and Link, R. Shock interaction with solid particles in condensed matter and related momentum transfer. *Proceedings of the Royal Society of London A*, 459 (2003), 705–726.

[230] Zhang, F., Thibault, P. A., Link, R., and Gonor, A. Momentum transfer during shock interaction with metal particles in condensed explosives. In *12th APS Shock Compression of Condensed Matter, Atlanta GA* (Atlanta, GA, 2002), M. Furnish, N. Thadhani, and Y. Horie, Eds., American Institute of Physics, Melville, NY, pp. 934–937.

[231] Zhang, F., Tran, D., and Thibault, P. A. Multiphase models for detonations and explosions in a dusty or porous medium. In *Proc. Combustion Canada '96* (Ottawa, ON, 1996).

[232] Zhang, F., and Wilson, W. Reaction of fragments from cased explosive charges. In *Proc. 20th International Symposium on the military Aspects of Blast and Shock* (Oslo, Norway, 2008).

[233] Zhang, F., Yoshinaka, A., Frost, D. L., Ripley, R. C., Kim, K., and Wilson, W. Casing influence on ignition and reaction of aluminum particles in an explosive. In *13th International Detonation Symposium* (Norfolk, VA, 2006), Office of Naval Research, Arlington, VA, pp. 233–244.

[234] Zhang, F., Yoshinaka, A., Murray, S. B., and Higgins, A. Shock initiation and detonability of isopropyl nitrate. In *12th International Detonation Symposium* (San Diego CA, 2002), Office of Naval Research, Arlington, VA, pp. 781–790.

[235] Zuber, N. On the dispersed two-phase flow of the laminar flow regime. *Chemical Engineering Science 19* (1964), 897–917.